Nuclear Magnetic Resonance studies of controlled drug release devices

Perkins, Emily

Award date:
2009

Awarding institution:
University of Bath

Nuclear Magnetic Resonance Studies of Drug Release Devices

Emily Louise Perkins

A thesis submitted for the degree Doctor of Philosophy

University of Bath
Department of Chemical Engineering

January 2009

Abstract

In this work the techniques of NMR cryoporometry and cryodiffusometry are developed and applied to the investigation of porous systems for controlled drug release devices. Both sol-gel silicas and PLGA microspheres are investigated. The cryoporometry method is developed from that described in the literature and a robust method for pore size determination is established. Cryoporometry investigations on sol-gel silicas are compared to data from other more traditional and better understood porosimetry techniques in order to determine the cause of hysteresis seen between the freezing and thawing process of an imbibed liquid. The causes of hysteresis are determined to be both pore shape and pore network related. Percolation theory is applied to the freezing process within the sol gel silica and shows that the freezing process occurs as a freezing front that begins in the bulk and progresses in toward the centre of the pellet. Thus, the freezing curve can be used to determine the size of the pore entrances. NMR diffusometry techniques are applied to PLGA microspheres at room temperature and during the freeze-thaw process in cryoporometry, a technique called cryodiffusometry. These investigations provide information about the micrometer scale pores within the microspheres and also the characteristics of the polymer matrix structure at the nanometer scale. Time-resolved cryodiffusometry studies of the PLGA microspheres show changes in the polymer matrix nominal pore neck and pore body sizes, tortuosity, and connectivity. These changes can be qualitatively discussed in terms of the drug release mechanism. The development of this technique and its application to nanometer scale porosity evolution in polymer matrices is novel and has advanced the understanding of the freezing process of a liquid imbibed in a porous solid.

Acknowledgements

Firstly I should like to thank my supervisors, Dr Sean Rigby and Dr Karen Edler for their support and advice over the last three years. Your guidance, knowledge and enthusiasm for science has helped to make my time back in Bath both enjoyable and stimulating, with lengthy, and at times, animated discussions and suggestions.

Much gratitude is bestowed upon Dr John Lowe, NMR spectroscopist, whose enthusiasm and plethora of NMR knowledge has been greatly received. Thank you for your support in my desire to push the boundaries of what can be done with our NMR spectrometers, enabling me to make significant developments to the cryodiffusometry techniques used.

Thank you to the members of the Rigby and Edler groups for all the discussions (some about work), help to find things in the lab, or just knowing who to ask about the little things, without which the big things can't happen. Thanks to the technical and support staff of both the Chemical Engineering and Chemistry Departments for your support and experience.

Thank you to my parents who supported my decision to return to university. Without their hard work and never-ending patience I would not have had the opportunities that I have had, and would not be the person that I am. I should also like to thank my brother for his words of experience and brutal honesty about the life of a PhD student, ensuring that I kept focused, and for his technical help on finalising the layout of my thesis.

Special thanks go to the friends I have made here, for your friendship and many happy times. Finally, thank you to my boyfriend, Adrian, for the calming influence and encouragement offered in times of stress and for always being able to make me smile.

Contents

List of Figures

List of Tables

Nomenclature

Acronym	Definition
PLGA	Poly(lactic-co-glycolic acid)
NMR	Nuclear Magnetic Resonance
PFG	Pulsed Field Gradient
FID	Free induction delay
PGSE	Pulsed Gradient Spin Echo
PGSTE	Pulsed Gradient Stimulated Echo
LED	Longitudinal Eddy Delay
BPLED	Bipolar Longitudinal Eddy Delay
CPMG	Carr-Purcell Meiboom-Gill pulse sequence
r.m.s.	Root mean square
5-FU	5-Fluorouracil, model drug used for drug encapsulation within microspheres
5-FD	5-Fluoro-5'Deoxyuridine
TMFU	4-(trifluoromethyl)umbelliferone
TMS	Tetramethylsilane
DCM	Dichloromethane
PVA	Polyvinyl alcohol
SEM	Scanning Electron Microscope

Symbol	Definition
β	Critical exponent, percolation theory
γ	Gyromagnetic ratio of observed nucleus
γ_l	Surface tension of adsorbate in liquid form
γ_{ls}	Surface tension between liquid and solid
δ	Length of gradient pulse(s)
δ_s	Difference in chemical shift between methanol peaks in low temperature methanol calibration equation (ppm)
Δ	Diffusion time(s)
ϵ_p	Voidage or porosity of material(no units)
ζ	As defined in text,$\gamma^2 g^2 \delta^2 (\Delta - \delta/3 - \tau/2)(sm^{-2})$
Θ	Contact angle(degrees)
κ	Integral mean surface curvature of pore
ν	Critical exponent, percolation theory
ν	Degrees of freedom, statistical analysis
ρ	Surface relaxivity
ρ_s	Density of solid
σ_{sl}	Surface energy at solid liquid interface
τ	Time for correction between bipolar gradient pulses(s)
τ_i	Tortuosity for component i (-)
τ_m	Tortuosity of matrix structure (-)
τ_p	Particle tortuosity, or pore network tortuosity (-)
τ_w	Weighted tortuosity (-)
ϕ	Contact angle(degrees)
χ^2_R	Reduced chi-squared ,goodness of fit, as defined in text(-)

Symbol	Definition
a	Salt content adjustment factor for diffusion coefficient(-) calculation
a_s	Separation distance between parallel plates(m)
A, B, C, D, E, F, G	Fitting parameters
A_m	Molecular cross sectional area of adsorbate(Å ^{2})
c	BET constant
d	Crystal size(m)
d_i	Diameter of ,molten pores(m)
D	Diffusion coefficient(m^2/s)
D_d	Diffusion coefficient of water in deuterated water(m^2/s)
D_e	Effective diffusion coefficient(m^2/s)
D_i	Diffusion coefficient of component i(m^2/s)
D_w	Self diffusion coefficient of water i(m^2/s)
D_0	Intra-particle diffusion coefficient, diffusion coefficient in matrix (m^2/s)
D_B	Bulk diffusion coefficient of water at experiment temperature (m^2/s)
D_P	Diffusion coefficient for motion perpendicular to the applied magnetic field(m^2/s)
D_s	Diffusion coefficient of water in salt solution(m^2/s)
D_{PFG}	Diffusion coefficient calculated from PFG experiment(m^2/s)
D'_{PFG}	Diffusion coefficient calculated from PFG experiment adjusted for salt content(m^2/s)
E	Expected value determined from model calculation
f	Fraction of occupied bonds
f_c	Critical fraction of occupied bonds or percolation threshold value
f_d	Fraction of deuterated water
f_w	Fraction of water
F	Fraction of occupied bonds in the percolation cluster
g	Gradient pulse strength(G/m)
G	Gradient pulse strength(G/cm)
ΔH_f	Bulk enthalpy of fusion per gram of material
i	Intercept
I	NMR signal intensity (arbitrary unit)
I_a	Absolute NMR signal intensity (arbitrary unit)
I_{adj}	Temperature adjusted NMR signal intensity (arbitrary unit)
I_m	Matrix contained water NMR signal intensity (arbitrary unit)

Symbol	Definition
I_{min}	Minimum absolute NMR signal intensity (arbitrary unit)
I_0	Reference NMR signal intensity (arbitrary unit)
I_p	NMR signal intensity for powder silica sample (arbitrary unit)
I_r	Relative NMR signal intensity (arbitrary unit)
I_T	NMR signal intensity at temperature T (arbitrary unit)
I_w	NMR signal intensity for whole silica pellet sample(arbitrary unit)
k	Model parameter defined in text
k_{GT}	Gibbs-Thomson parameter(nmK)
K	Model parameter defined in text
l_i	Average pore length(m)
L	Average linear dimension of a bond, percolation theory
L_{95}	Lower 95 % confidence interval
$M(\Delta, K)$	Echo signal intensity for a given value of Δ and K
n	Number of observations
n_i	Number of molten pore
N_A	Avogadro's constant
N_b	Number of occupied bonds(below freezing point)
N_f	Number of occupied bonds in percolation cluster(frozen)
N_p	Number of pores
N_T	Total number of bonds, percolation theory
O	Observed value from experiment
p	Pressure
p_0	Saturation pressure
p_f	Number of fitting parameters
p_i	Fraction of water in component i(-)
$p(d)$	Pore size distribution
P_s	Capillary pressure
P_{cx}	Pressure on convex side of meniscus
P_{cv}	Pressure on concave side of meniscus
q	Model parameter defined in text
r_c	Core radius(m)
r_{cavity}	Cavity radius determined by PFG(m)

Symbol	Definition
r_p	Pore radius(m)
$r_{p,ave}$	Average pore radius(m)
r_p^U	Upper pore radius estimate(m)
r_p^L	Lower pore radius estimate(m)
r_{rms}	Root mean square displacement(m)
R	Universal gas constant
s	Slope, gradient
se	Standard error
S	Surface area of pores (m^2)
S_a	Specific surface area of solid (m^2g^{-1})
t	Thickness of unfrozen layer(nm)
$t_{stat}^{5,\nu}$	Value of 't' statistic for 5 % two-tailed test with ν degrees of freedom
T	Temperature(K or °C)
T_{ref}	Reference temperature(K or °C)
T_m	Bulk melting point(K or °C
$T_m(d)$	Melting point of crystals size d(K or °C
ΔT_m	Melting point depression(K or °C
ΔT_f	Freezing point depression(K or °C
T_1	Longitudinal relaxation parameter
T_2	Transverse relaxation parameter
T_2^*	Transverse relaxation parameter in an inhomogeneous field
$T_{2,bulk}$	Bulk fluid transverse relaxation parameter
U_{95}	Upper 95 % confidence interval
V	Volume of pores, or liquid (m^3)
V_i	Volume of liquid in pores (m^3)
V_m	Molar volume of adsorbate in liquid form (m^3)
V_N	Normalised volume (m^3)
V_0	Total volume (m^3)
W_{ps}	Reversible work required to separate unit area of solid from the pore wall
x	Pore diameter, pore size(m)
x_m	Monolayer capacity(cm^3)
Z	Coordination number, percolation theory

Chapter 1

Introduction

1.1 Drug delivery

For centuries man has used elixirs, potions and ointments to treat ailments and diseases. In recent times, as mans' understanding of human biology, immunology and disease have increased, so too, has the sophistication of the medicinal treatments being employed. Practices in modern medicine are improving all the time, reducing the number of premature deaths caused by disease and sustaining those with long term health problems to live longer. Alongside the advances in surgical techniques are the ever increasing number and complexity of the drugs available for treatment. The means by which a drug is administered is also evolving, from traditional methods such as oral administration in tablet or liquid form, sub-cutaneous or intravenous injection, pessary, diffusion through the skin, inhalation, and more recently controlled drug release from the implantation of a removable device, to transfer of drugs to the skin released from a patch, biodegradable implants that release the contained drug over time, bioadhesive materials that release drugs at a target area, or bio-reactive materials that respond to a given condition, such as pH or glucose level, within the body and then release contained drug. These systems are referred to as controlled drug delivery systems, DDS, whereby the release of drug can be prolonged over a period of time, or targeted to a specific site or condition within the body. A controlled drug delivery device is defined as a device that releases the treatment over a long period of time, greater than one day, and at a controlled rate (Saltzmann, 2001). All of these delivery methods are used, or proposed for use, to administer the continually growing list of pharmaceuticals approved for human use today. The method of administration is often dependent on the characteristics of the drug molecule: hydrophobicity or hydrophilicity, size, shape, active group, pH stability, toxicity.

The advantages offered by these advanced DDS are significant to those with long term treatment needs and those with the need for acute short term intensive targeted treatments. For long term treatment controlled DDS offer a reduction in the number of times the patient must have the drug administered and, therefore, reducing the disruption to the patients lifestyle and can increase patient compliance, which will also improve the stability of the patients condition. Examples of long term treatments that could benefit from such systems include the treatment of high cholesterol, blood disorders and epilepsy. The advantages of targeted drug delivery include a reduced dosage, since all the drug is delivered to the required site, therefore, only affecting the area requiring treatment, also reducing the side effects seen by the patient, an example of which includes chemotherapy drugs for cancer treatment. The targeting of a particular tissue can be done by means of direct injection or implantation of the device at the target area, or bioadhesion of the device to specific cells or mucus. These methods offer an attractive means of concentrating the drug release at the target area. Bio-reactive systems could allow for more efficient treatment of conditions such as diabetes, where the presence of glucose at a specified levels causes the DDS to release insulin in sufficient quantity, reducing the reliance on the patient continually monitoring their blood sugar level.

The burst release seen in some biodegradable systems could be both an advantage or disadvantage depending on the treatment, for some drug therapies, it is necessary to have a higher initial dose to begin the treatment, whereas for others the initial burst may be toxic, or may just cause unnecessary additional dumping of a costly active ingredient. One concern with regards to DDS is the possibility of dose dumping if the system fails, that is when the entire dosage of drug contained within the system is released at one time, this could be toxic, or reduce the effectiveness of the treatment, necessitating repeated administration. The hazards of dose dumping may be reduced by using many small devices as opposed to one large delivery device, if one micro-device fails the dose dumping effect should be small and managed within safe guidelines for any toxicity effects. Controlled delivery devices in addition to being used in-vivo have attracted attention for the potential to deliver bioactive molecules during the in-vitro growth of tissue within the field of tissue engineering.

Although the number of potential uses for drug delivery systems is great, the actual number of products on the market are limited due to a lack of thorough understanding of the mechanism by which the drug is released. In this work Nuclear Magnetic Resonance techniques are developed and applied to silica and polymer materials to determine structural characteristics that influence the mechanism of release of an encapsulated molecule.

1.2 Nuclear Magnetic Resonance (NMR)

Since the first detection of a Nuclear Magnetic Resonance (NMR) signal in 1945 achieved by Felix Bloch and Edward Purcell, who both received the Nobel prize for Physics in 1952 (Blumich, 2005), NMR techniques have been developed from simple scientific applications too many complex and varied applications. Probably the most recognised application is the multi-dimensional magnetic resonance imaging (MRI) for medicinal applications. NMR is observed if the nuclei having magnetic properties are excited within a magnetic field, a resonance signal is emitted as the nuclei relax. The observed resonance signal is dependent on the environment in which the nucleus is situated and can, therefore, be used to probe that environment. NMR can be used to determine the identity of a chemical compound by observing it's NMR spectrum, or collection of signals from nuclei of different environments. NMR diffusion studies can be used to determine the diffusion coefficient of a nucleus within a molecule based on the loss of signal detected due to the motion of the molecule over a given diffusion time. The relaxation behaviour of a nucleus in a solid is different to that of the liquid, therefore, a change of state can be observed by either an increase or decrease in the observed signal intensity. The design of modern NMR experiments comes from manipulation of these characteristics by utilising different pulse sequences, ie. changes to the way in which the nuclei are excited and the conditions of the magnetic field the nuclei experience. In this work the ability to monitor diffusion and the change of liquid to solid to liquid are utilised, the great potential of NMR is that these techniques can be combined and used at the same time.

1.3 Thesis structure

This thesis is divided into seven chapters:

- *Introduction*
- *Development of cryoporometry method*
  This chapter discusses the work done to develop the cryoporometry method for the investigation of materials for drug delivery. After a critical review of the technique information available in the literature, it was found that some work was required to establish a robust method for sample temperature measurement and sample equilibration. Preliminary experiments are carried out on sol-gel silica materials to determine if information could be gained from the freezing curve in addition to the melting curve of the cryoporometry cycle, which had been the focus of previously published

work. To verify the applicability of the cryoporometry freeze-thaw hysteresis as a characterisation technique, a comparison with mercury porosimetry data was made.

- *Application of cryodiffusometry to silica materials*
  Further investigations are carried out on silica materials combining cryoporometry and diffusometry to gain an understanding of the freezing mechanism of the imbibed liquid. Comparing cryoporometry data with nitrogen sorption and mercury porosimetry has provided an understanding of the causes for the hysteresis seen in cryoporometry freeze-thaw cycles, the contributions of different effects are discussed. Percolation theory is applied to the freezing process within the sol-gel silica to determine if the mechanism of freezing can be described in terms of a freezing front that penetrates the porous material from the bulk toward the centre of the pellet. The interpretation of cryodiffusometry applied to silica can be made with the support of nitrogen sorption and mercury porosimetry, which are not suitable for investigation on the polymer microspheres discussed later. These investigations provide base ideas for the interpretation of the more complex and evolving polymer matrix structure determination.

- *Preparation and characterisation of PLGA microspheres*
  The structure of Poly(lactic-co-glycolic acid) microspheres and it's effect on the release profile of an encapsulated drug molecule is of great interest to improve the design of such drug delivery devices. Before a study of the structure is conducted, it is important to know how these microspheres are made and how the preparation method can effect the macroscale structure of the microspheres. The preparation methods used for PLGA microspheres are discussed in terms of the effects that the preparation parameters can have on the characteristics of the microspheres produced, such as microsphere diameter and pore diameter. Two variations of preparation techniques are trialled and a variation in preparation parameters are considered. The resulting microspheres are studied with Scanning Electron Microscopy (SEM) and typical SEM images are discussed. Some nuclear magnetic resonance (NMR) diffusometry experiments are carried out at ambient temperature and are discussed in terms of diffusion models within porous media available in the literature.

- *Cryoporometry of PLGA microspheres*
  This chapter describes the application of cryoporometry to investigate the longer term structural changes in the polymer matrix at the nanometer scale once immersed in aqueous media. Three batches of microspheres are made with and without encapsulated model drug and with both low and high molecular weight PLGA. These batches are investigated by cryoporometry over approximately one hundred days, results are

discussed in terms of structural changes to the nominal pore body and pore neck sizes determined from the melting and freezing curves. Shielding effects and percolation properties are also discussed in terms of drug mobility through the polymer matrix.

- *Cryodiffusometry of PLGA microspheres*
  NMR diffusometry experiments are conducted on the microsphere samples during the freezing and thawing process of cryoporometry cycles. The determination of appropriate diffusion models and interpretation of tortuosity within the polymer matrix structure are made. Changes in the observed diffusion characteristics are discussed in combination with cryoporometry derived pore sizes. The consequential effects of the changes seen during this time are discussed qualitatively in relation to the drug release mechanism.

- *Conclusions and further work*

References

B. Blumich. *Essential NMR*. Springer, 2005.

W. M. Saltzmann. *Drug Delivery Engineering Principles for drug therapy*. Oxford University Press, 2001.

Chapter 2

Development of the cryoporometry method

2.1 Background and theory

Nuclear Magnetic Resonance (NMR) cryoporometry is the investigation of pore size and pore size distribution by studying the melting or freezing characteristics of an imbibed liquid using NMR. It was first published by W. T. Thomson (Lord Kelvin) in 1871 (Thomson, 1871) that there are changes in physical properties of a fluid when it is contained within a porous solid. This theory was developed by J. J. Thomson (Thomson, 1888) and Gibbs (Gibbs, 1928) to produce the Gibbs-Thomson equation for melting point depression, 2.1*.

$$\Delta T_m = T_m - T_m(d) = \frac{4\sigma_{sl} T_m}{d\Delta H_f \rho_s} \tag{2.1}$$

where ΔT_m is the melting point depression in °C for a small crystal of size d in m, T_m is the bulk melting point and $T_m(d)$ is the melting point of crystals of size d, σ_{sl} is the surface energy of the solid-liquid interface, ΔH_f is the bulk enthalpy of fusion per g of material, and ρ_s is the density of the solid.

This equation, 2.1, describes the relationship between the melting point depression and small crystal diameter, for a crystal within a liquid. If the crystal is formed within a confined pore, i.e. when the crystal size is limited by the pore size, the wall effects must also be considered. In cryoporometry it is often assumed that the liquid has weak interaction with the solid in which it is confined and, therefore, that wall effects are negligible and pore dimension is the dominating parameter defining the melting point depression (Mitchell et al., 2008). However, this is not always the case. The phase change liquid to solid within a porous material can be considered analogous to evaporation of a liquid to a gas during

*As expressed in (Jackson and McKenna, 1990)

gas desorption from a solid porous material, see Section 3.2.3 on nitrogen adsorption and desorption. Assuming a cylindrical pore shape, the advancing meniscus between solid and liquid state is hemispherical. The core radius r_c is related to the pore radius r_p estimate by equation 2.2.

$$r_c = r_p \cos\phi \tag{2.2}$$

where ϕ is the contact angle of the meniscus with the solid wall and $0 \leq \phi \leq 180°$. Therefore, combining equations 2.1 and 2.2 gives the Gibbs-Thomson equation for melting point depression of a solid in confined cylindrical pore, equation 2.3

$$\Delta T_m = T_m - T_m(d) = -\frac{4\sigma_{sl} T_m}{d\Delta H_f \rho_s} \cos\phi \tag{2.3}$$

However, the contact angle, ϕ, is a function of the interactive forces between the liquid and the wall as described in the work of Young (Adam, 1957) and Dupré (1869), this relationship is described by equation 2.4.

$$\cos\phi = \frac{W_{ps}}{\sigma_{sl}} - 1 \tag{2.4}$$

where W_{ps} is the reversible work required to separate a unit area of solid from the pore wall.

Although contact angle varies for different systems and it is not always possible to measure due to small pore sizes and complex networks being investigated, it is often given an assumed value. For example, in thermoporometry the assumed value is 180 °for the solid-liquid phase change (Jackson and McKenna, 1990). Alternatively, it is incorporated into an empirically determined constant within the simplified version of equation 2.3 as in Strange et al. (2003), equation 2.5.

$$\Delta T_m = -\frac{k_{GT}}{x} \tag{2.5}$$

where k_{GT} is the Gibbs-Thomson parameter and x is the pore diameter in metres.

To determine the pore size distribution within a solid using this relationship a method of determining the melting point of the imbibed liquid is required. Differential scanning

calorimetry (DSC) is one method that has been used; it relies on the measurement of energy released or absorbed during the phase transition and the overall technique is termed thermoporosimetry. Quinson and coworkers developed the technique to also include determination of the surface area of a porous material (Quinson et al., 1986; Quinson, 1987; Quinson and Brun, 1988). This method of thermoporosimetry has more recently been used to look at the structure of mesoporous materials, including silicas and polymeric gels (Jackson and McKenna, 1990; Sliwinska-Bartowiak et al., 2001; Schreiber et al., 2001; Iza et al., 2000).

Thermoporosimetry techniques evolved further in the early 1990s when NMR signal intensity was suggested as an alternative method for determining the molten fraction of imbibed liquid within a porous sample during the gradual freezing of the liquid (Strange et al., 1993). More recently, the advancement of temperature control within NMR systems has lead to the development of NMR cryoporometry (Webber, 2000; Strange et al., 2003).

Due to the significant reduction in transverse relaxation constant, T_2, between liquid and solid phase of a fluid (Topgaard and Soderman, 2002; Strange et al., 2003) it is possible to determine the change in the relative volume of molten liquid by measuring the change in NMR signal intensity. The short relaxation time of the solid results in a decrease of signal intensity as the temperature is decreased and the liquid begins to freeze, once all the liquid is frozen there is zero observable signal using certain pulse sequences in a liquid state probe. Therefore, from knowing the initial signal intensity for 100% liquid and the signal intensity for 100% solid, a relative value of the quantity of frozen material can be calculated for any temperature. NMR cryoporometry has become more widely used in the last 15 years, with studies of pore characteristics of silica gels (Mitchell et al., 2005; Hansen et al., 1996) and more recently polymer particles (Hansen et al., 2005; Petrov et al., 2006a). Recently a review of the technique has been published by Mitchell et al. (2008).

The number of published studies using NMR cryoporometry was limited at the start of this project, and with varying experimental details being used. It was, therefore, important to establish an experimental procedure that would produce accurate, reproducible results for the system being studied. Whilst DSC studies used ramped temperature profiles (Jackson and McKenna, 1990; Iza et al., 2000; Schreiber et al., 2001; Sliwinska-Bartowiak et al., 2001; Janssen et al., 2004), both ramped (Webber et al., 2001; Valiullin and Furo, 2002; Valckenborg et al., 2002; Dosseh et al., 2003; Hansen et al., 2005) and stepped, from 0.1—1.0 K/min (Valiullin and Furo, 2002a; Mikhalovska et al., 2006; Petrov and Furo, 2006) profiles have been used for cryoporometry. Equilibration times for step changes in temperature varied from 2 minutes (Hansen et al., 1996) to 10 minutes (Dosseh et al., 2003) and a variety of solvents have been used, including water (Schreiber et al., 2001; Janssen et al., 2004; Hansen et al., 2005), nitrobenzene (Valiullin and Furo, 2002), benzene and

cyclohexane (Strange et al., 1993; Dosseh et al., 2003; Petrov and Furo, 2006) and cyclooctane (Petrov and Furo, 2006). Studies have been done over a range of pore diameters from 12 Å (Hansen et al., 1996) to 500 nm (Gane et al., 2004).

In previous work varying estimates of k_{GT}, the Gibbs-Thomson parameter are given for water ranging from 420 KÅ (Hansen et al., 2005) to 850 KÅ (Valckenborg et al., 2002) with many giving a value of around 500 $\pm$50 KÅ (Schmidt et al., 1995; Hansen et al., 1996; Schreiber et al., 2001; Webber et al., 2001; Hansen et al., 2005; Petrov et al., 2006a) despite the variety of materials studied. However, for a detailed knowledge of pore structure, it is vital to know the exact temperature at which the imbibed liquid melts or freezes (Filippov and Skirda, 2000). It is critical, therefore, to determine the temperature calibration between the probe set temperature and the temperature experienced within the sample for the system being studied. Until recently (Mitchell et al., 2008) this subject was, at best, often only briefly described in the literature (Valckenborg et al., 2001) with temperatures taken as that of the temperature controller (Mikhalovska et al., 2006; Topgaard and Soderman, 2002; Mitchell et al., 2005) or referenced against one temperature such as the bulk freezing or melting point of the imbibed liquid (Petrov and Furo, 2006). The work described below shows that these are not accurate assumptions.

There is a variance in temperature between the NMR probe temperature controller and the temperature of the sample, and there is not a simple or predictable relationship between these two temperatures. Some effort has been made to relate temperature ramping and controller temperature to the actual sample temperature (Webber, 2000) but this is only true for samples immersed in the liquid due to the variation in heat transfer properties of liquids compared to gases. During the development of the experimental method for this work, described in Section 2.2, consideration to each of these details was made.

By comparing NMR cryoporometry results with those from more traditional, and better understood, porosimetry techniques it is hoped that a greater understanding of NMR cryoporometry can be made. Although the causes of NMR cryoporometry freeze-thaw hysteresis are currently not fully understood, a number of causes have been suggested in the literature, a more detailed description of which is given in Section 3.2.1, Chapter 3.

Mercury porosimetry has been a common method to analyse macroporous (> 50 nm) and mesoporous (2–50 nm) structures such as catalyst materials and rock. Mercury is a non-wetting liquid and, therefore, requires an applied pressure to force it into the pores of such a solid. Greater pressure is required to force mercury into smaller pores. The magnitude of the applied pressure relates to the size of the pores as described by the Washburn equation 2.6 (Washburn, 1921),

$$P_s = \frac{2\gamma_{ls}}{r_p} cos\Theta \tag{2.6}$$

where P_s is the capillary pressure, γ_{ls} is the surface tension of the liquid with the solid at a contact angle of Θ and r_p is the pore radius.

During the intrusion process, mercury is forced into the pores from the outside surface of the material. Any larger pore that are connected to the outside by a small pore or 'neck' will not be filled until the pressure is sufficient for the mercury to penetrate the smaller pore and the intrusion curve is thus susceptible to shielding effects.

Mercury porosimetry is also susceptible to hysteresis dependent on the pore network connectivity. During the extrusion of mercury, the pressure reaches a sufficient level to empty the small 'neck' pores but the pressure is too great for the mercury to empty from the inner larger pores and mercury is retained in the larger shielded pores. Once the mercury extrusion is disrupted, the mercury remains trapped inside the larger pore even at atmospheric pressure. Further discussion on the physical interpretation of mercury porosimetry, NMR cryoporometry and the causes of the freeze-thaw hysteresis can be found in Chapter 3.

2.2 Development of experimental procedure

2.2.1 Preliminary experimental tests on amorphous silica materials

To ensure the freezing point was observed, the first step in developing the experimental method was to determine the temperature range over which the proton spectra would be taken. To this end, a trial with one of the silica pellet samples, s980g, was carried out. The pellets were soaked in distilled water and excess water removed, by dabbing on wetted tissue, before they were placed in a 5 mm diameter NMR tube. Wetted tissue was used to ensure bulk water is removed without absorbing water contained within the pores. The sample was then placed in a Bruker 400 MHz NMR spectrometer and cooled by means of the thermal control system within the spectrometer, which allows the probe temperature to be adjusted to a set point and maintained at that temperature whilst a spectrum is collected. Cooling was performed in a stepped fashion, with 1 K steps, and a typical spectrum for the imbibed water signal is shown in Figure 2.1.

The broad nature of this spectrum, 8 ppm, compared to that of liquid only signal, 0.03 ppm, is due to the multiple solid-liquid-air interface susceptibility effects within the sample. This experiment gave an estimation of freezing and melting temperatures for the system,

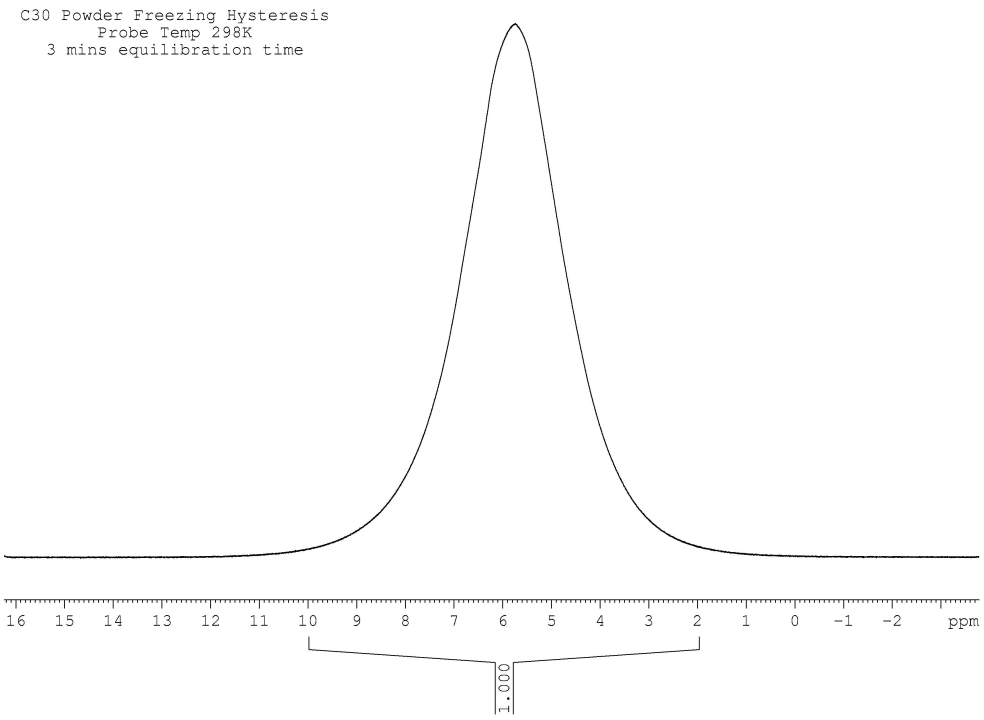

Figure 2.1: A typical NMR spectrum of water contained within the pores of silica pellet

and allowing for an uncorrected temperature calibration, the range of 298 K to 267 K was selected to show the freeze-thaw hysteresis of water in this porous silica sample. The silica samples s980g and c30 are known to have similar pore sizes of 20–40 nm and will, therefore, require similar temperature ranges to view the freeze-thaw hysteresis, an example of which can be seen Figure 2.2.

Once the temperature range was established, it was important to determine the required equilibration times for each temperature set point. The quasi equilibrium nature of the phase change being studied suggested the use of a step-wise temperature change would be the most suitable method to gain an accurate account of the quantity of material freezing at a given temperature. A heating rate of 8 K per hour was suggested (Hansen et al., 2005), this is equivalent to an equilibration time of 7.5 minutes per 1 K change. Using this as an estimate, acquisitions were taken using 3, 6, 9 and 12 minutes equilibration for each 1 K change in temperature. Therefore, the temperature profile was such that four spectra were collected at each temperature. This profile was used for both freezing and thawing the sample.

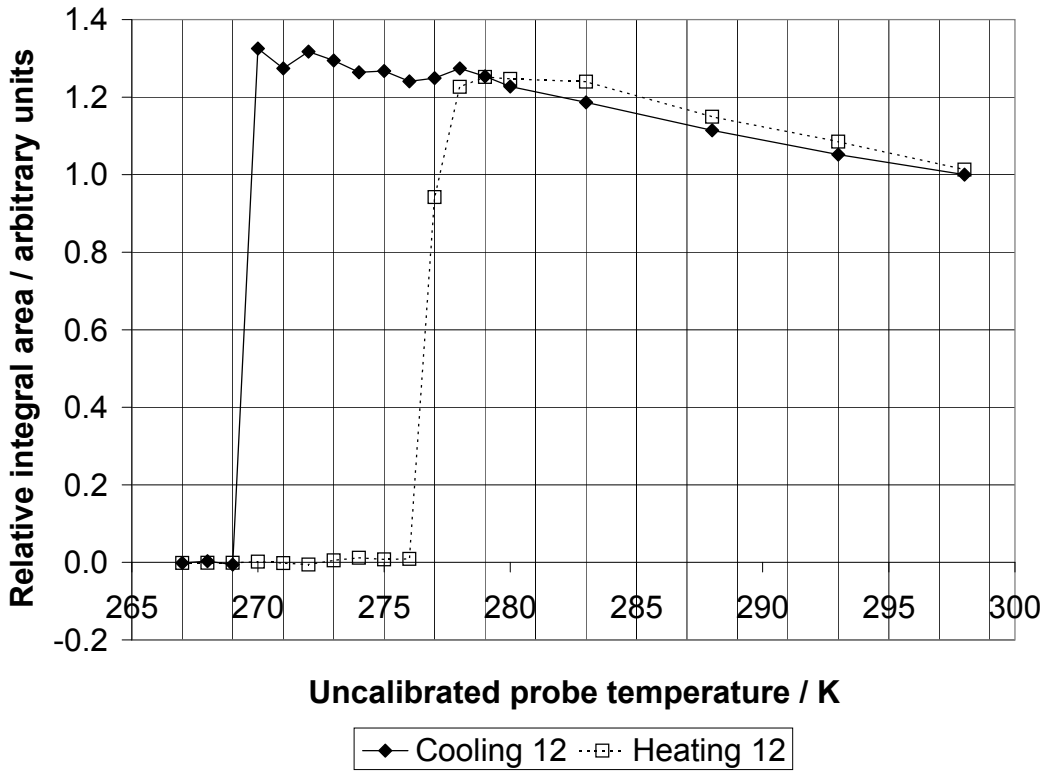

Figure 2.2: A typical freeze-thaw hysteresis for water contained in porous s980g silica pellet

The temperature control, time delays and spectra collection were automated using the program *multi_zgvt*, this program recalls a list of user defined temperatures and waits a user defined time delay before acquiring spectra. Thus, the program controls temperature and data collection at specified intervals after equilibration at a target temperature. This experiment showed that an equilibration of 6-9 minutes was required for freezing and 9-12 minutes for thawing, in close agreement with the literature (Hansen et al., 2005). Although the necessary equilibration time should be greatest for this test sample of the whole pellet sample, with the water within the central part of the pellet being most thermally shielded, for completeness the repetitions of four spectra at each temperature were initially used for all new samples. This would highlight any difference in equilibration times between whole, broken and powdered samples or between different samples. An example of multiple equilibration time freeze-thaw hystereses can be seen in Figure 2.3.

For each experiment, a large number of spectra were produced that all required processing. The software supplied with the NMR spectrometer (XWIN NMR and more recently TOPSPIN2) contains automatic programs (au programs) one of which will allow one or more commands to be carried out on multiple data sets, specifically *multicmd*. This program allows for each processing command to be completed on each data set in series.

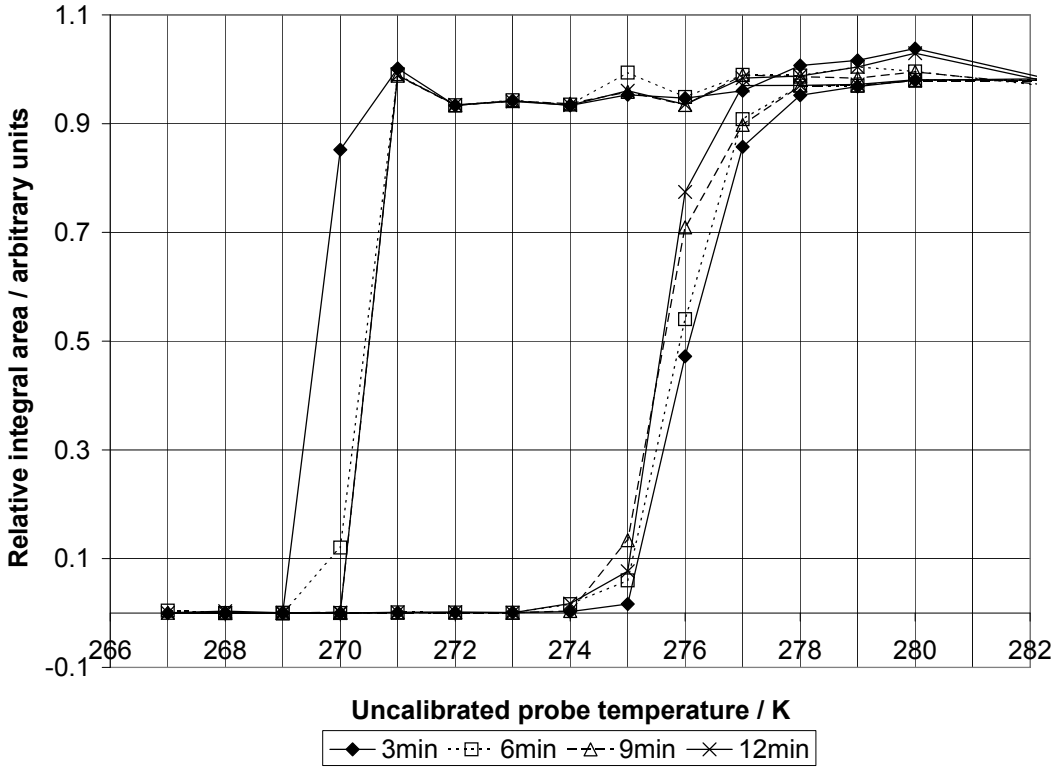

Figure 2.3: A typical freeze-thaw hysteresis for water contained in porous silica pellet at 3, 6, 9, and 12 minutes equilibration

In summary, the data processing steps for each spectrum include performing the Fourier Transform of the free induction decay, (FID)[†], carrying out a basic phase correction and baseline correction. Once processed, the region in which the water peak appears can be defined and all spectra integrated in this region, using the program *multi_integ*. The relative signal intensities for each temperature set point could then be calculated and plotted to show the phase transition.

Initially, a basic pulse and acquire sequence was used, however, this led to a low intensity broad peak for water, even after complete freezing, as the solid water was still being detected. In order to remove this broad peak a simple Hahn spin echo sequence was used, as suggested in the literature (Petrov and Furo, 2006). This sequence is a basic form of the Carr-Purcell Meiboom-Gill (CPMG) sequence, also used for cryoporometry (Hansen et al., 1996; Mitchell et al., 2005). The pulse sequences used are detailed in Appendix A.7.

[†]The FID is the raw data signal received by the NMR, this data is processed by Fourier Transform to give the NMR spectrum.

2.2.2 Temperature calibration using methanol

It was essential that the temperature inside the sample was known for each spectrum taken in order to establish the exact temperature at which any change of state occurred. The required accuracy of the sample temperature is dependent on the value of the Gibb-Thomson parameter, see equation 2.5, as the greater the accuracy the clearer the determination of pore diameter. The NMR temperature control unit (BVT3200) has the operating temperature range of 123–423 K with an accuracy of ± 0.1 K. It is, however, acknowledged that the probe thermocouple, used by the temperature control unit, does not give an accurate measure of the sample temperature due to the heat transfer effects within the probe and the sample itself (Fritsch, 2000). This temperature difference occurs as a result of the positioning of the thermocouple within the probe.

Calibrations to account for this difference are often carried out for liquid state NMR (Geet, 1970). The probe thermocouple is placed below the sample within the flow of gas used to control the probe temperature and has been calibrated to equate this temperature to the actual sample temperature for a liquid sample. A commonly used method for a low temperature calibration (below 298 K) of this thermocouple is a methanol calibration. An NMR tube containing methanol is placed in the spectrometer and the distance between the signal of the hydroxyl proton and the methyl protons is measured at different temperatures. As the temperature decreases, the distance between the 2 signals of the chemical shift increases according to the equation 2.7[‡].

$$T = -23.832\delta_s^2 - 29.46\delta_s + 403.0 \tag{2.7}$$

where T is the actual temperature in Kelvin and δ_s is the difference in chemical shift between the two methanol peaks in ppm. This equation is valid in the 180—300 K range. For a liquid sample the methanol calibration gives a sufficiently accurate sample temperature, however, when the sample is a combination of solid, liquid and gas phase, the heat transfer dynamics become more complex and the methanol calibration is no-longer adequate.

The following sequence of experiments was carried out as an investigation into the temperature calibration: Initially, to calibrate the temperature for this system, some of the silica pellets were soaked in methanol to simulate the experimental procedure and conditions of the standard water experiment, the experimental set-up for this is shown in Figure 2.4 A. In this way, an exact temperature profile experienced by the imbibed liquid could be calculated using the low temperature methanol calibration, equation 2.7.

[‡]As expressed in (Geet, 1970)

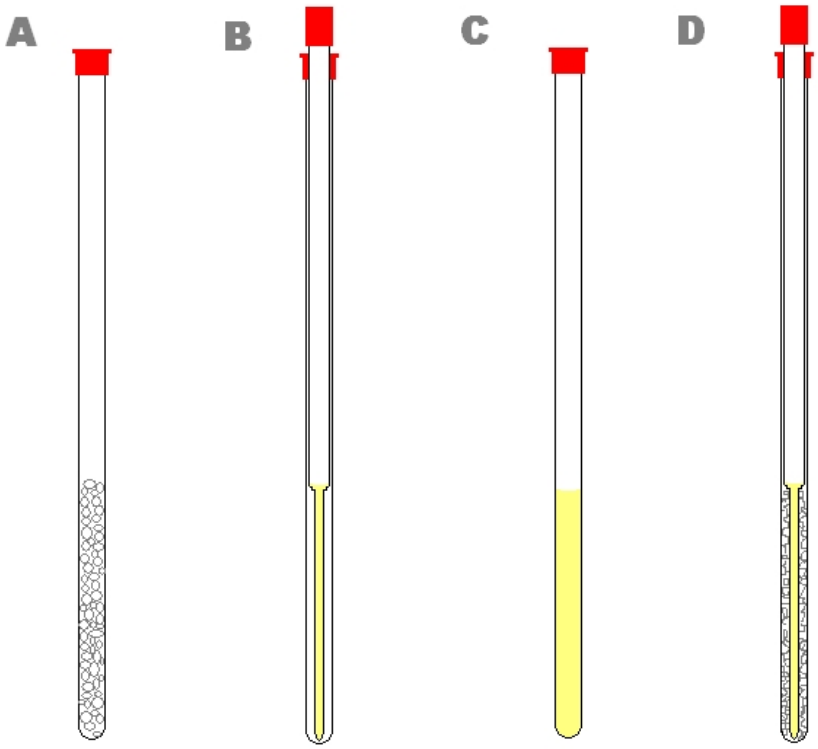

Figure 2.4: NMR experimental set up for calibration experiments 1

The results of this experiment can be seen in Figure 2.5. At low temperatures, within the range of interest for these experiments, it was found that calculated temperatures for the imbibed methanol were much lower than those suggested by the standard methanol calibration experiment, methanol in the NMR tube. If any difference was expected, it was that the imbibed methanol would be at a higher temperature, as the three-phase system was thought to introduce increased thermal shielding from the cold temperature gas flow used for temperature control. At this point it was thought that the methanol calibration equation 2.7 may not be valid for methanol confined within small pores.

The next calibration experiment used a methanol filled capillary of 2 mm outside diameter fitted along the central axis of the 5 mm outside diameter NMR tube. This set up introduced the additional heat transfer barriers of another layer of glass and air. The experimental set-up for this is shown in Figure 2.4 B. The simplicity of this set up provided easier shimming and removed the possible wall effects that may have influenced the results seen for methanol in the pellets. Results of this experiment also showed a difference from the standard calibration experiment as shown in Figure 2.5, however, it was seen that the methanol contained in the pellets and the capillary were in close agreement with each other. The results from the capillary experiments also showed some discrepancy between

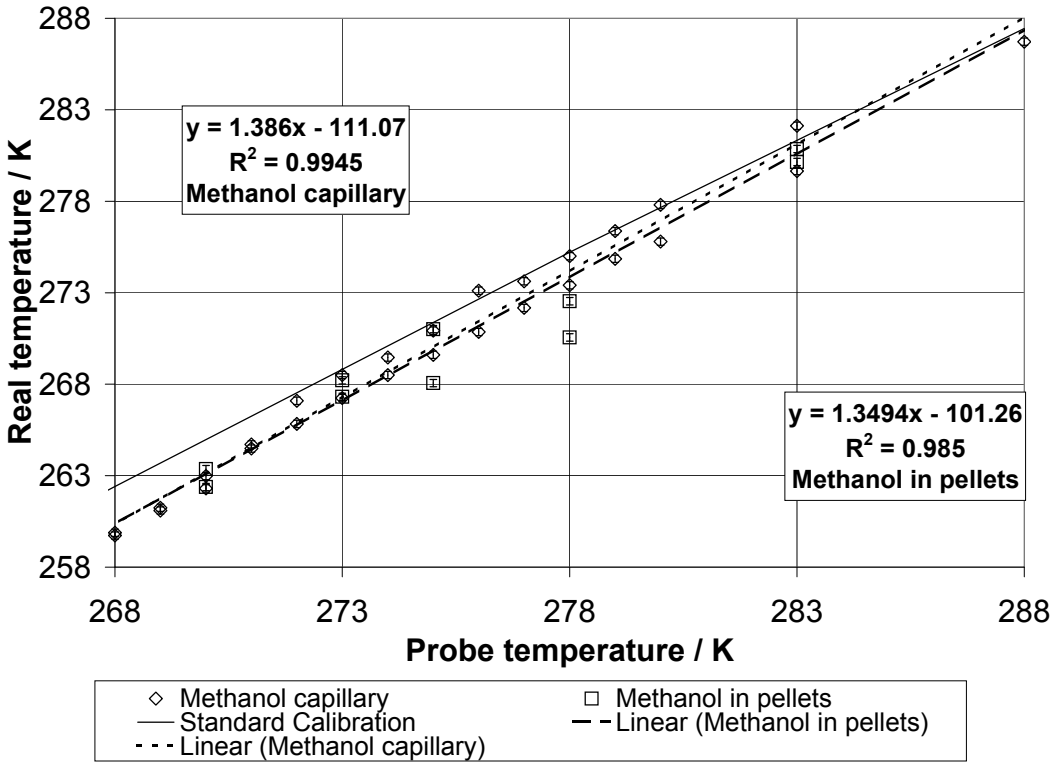

Figure 2.5: A comparison of methanol temperature calibration experiments conducted

the sample temperature and probe set temperature that was observed to be dependent on whether the sample was being cooled or heated, results are shown in Figure 2.6. A repeat of the standard calibration experiment, Figure 2.4 C, was conducted with methanol in an ordinary 5 mm diameter NMR tube. It was found that this experiment compared well the capillary experiment. The discrepancy between these results and the previous standard calibration experiment was found to be caused by varying the cooling rate and gas flow settings of the temperature control system. As a result of this finding, it was considered that the temperature experienced within the sample varied not only with the probe set temperature, but was also a function of the cooling rate, gas flow settings and probe heater power. Therefore, where practical the set points for cooling rate and gas flow should be kept constant, however, the probe heater power is the control for adjusting the temperature and, therefore, cannot be kept constant.

From these experiments, it was determined unfeasible to estimate an absolute temperature calibration for all possible experimental conditions, and it was decided that a better system would be to directly measure the sample temperature for each experiment. To do this using the methanol temperature calibration, both methanol and water have to be present in the same sample tube. To prevent methanol and water physically mixing, the

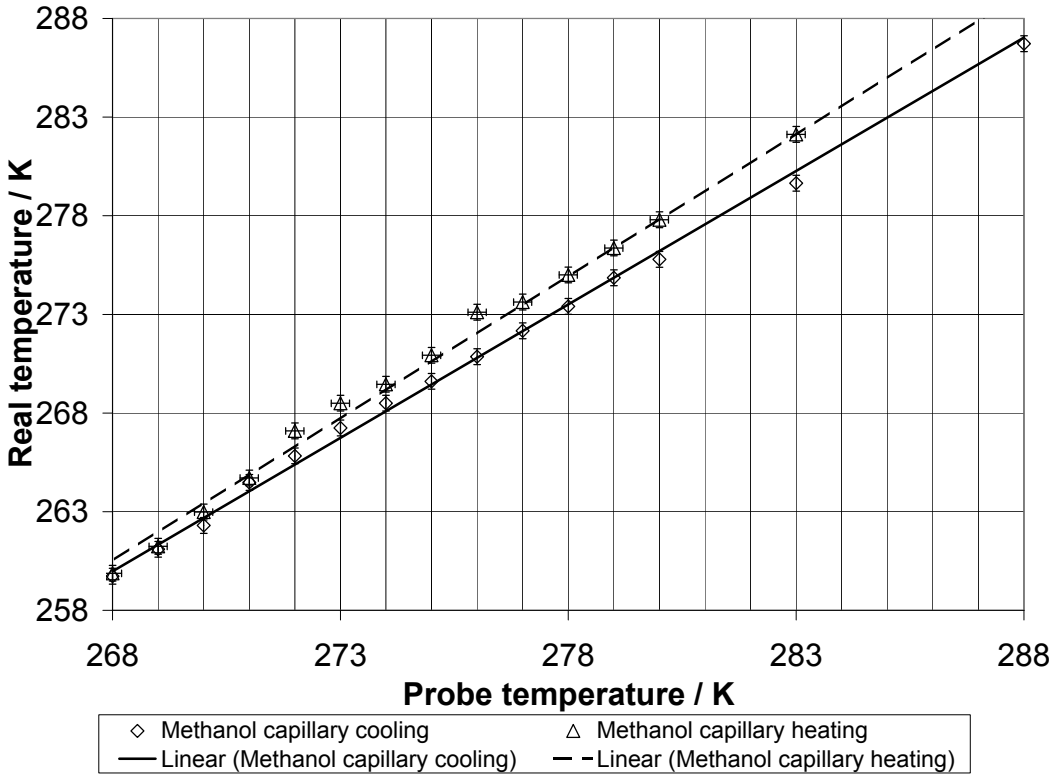

Figure 2.6: A comparison of heating and cooling temperature calibration for methanol capillary

experimental set-up proposed was a methanol capillary surrounded by broken pellet pieces imbibed with water, as shown in Figure 2.4 D. As discussed later in Section 2.3.2, there is no change in the freeze-thaw hysteresis of the water in broken pieces of pellet compared to that in a whole pellet, until the pieces are less than 30 μm in size. When the pellet pieces are below this size the internal pore network structure within the pellets is broken and the effects on the hysteresis change.

Additionally, this sample was difficult to shim and there was overlap of the water peak and one of the methanol peaks. To overcome this overlap, water was replaced with its deuterated form so that 2 individual FID signals could be measured. The spin echo pulse sequence used was modified to allow for a proton excitation at 400 MHz then a deuterium excitation at 61 Mhz to produce two spectra for each temperature set point. The results from this experiment can be seen in Figure 2.7, the methanol capillary experiment results are also shown for comparison.

One important observation from this experiment was that small adjustments in shimming these samples could change the apparent difference in chemical shift for the two methanol peaks, therefore, changing the observed temperature. These shimming effects are not relevant for water based freezing experiments as the exact position of the water

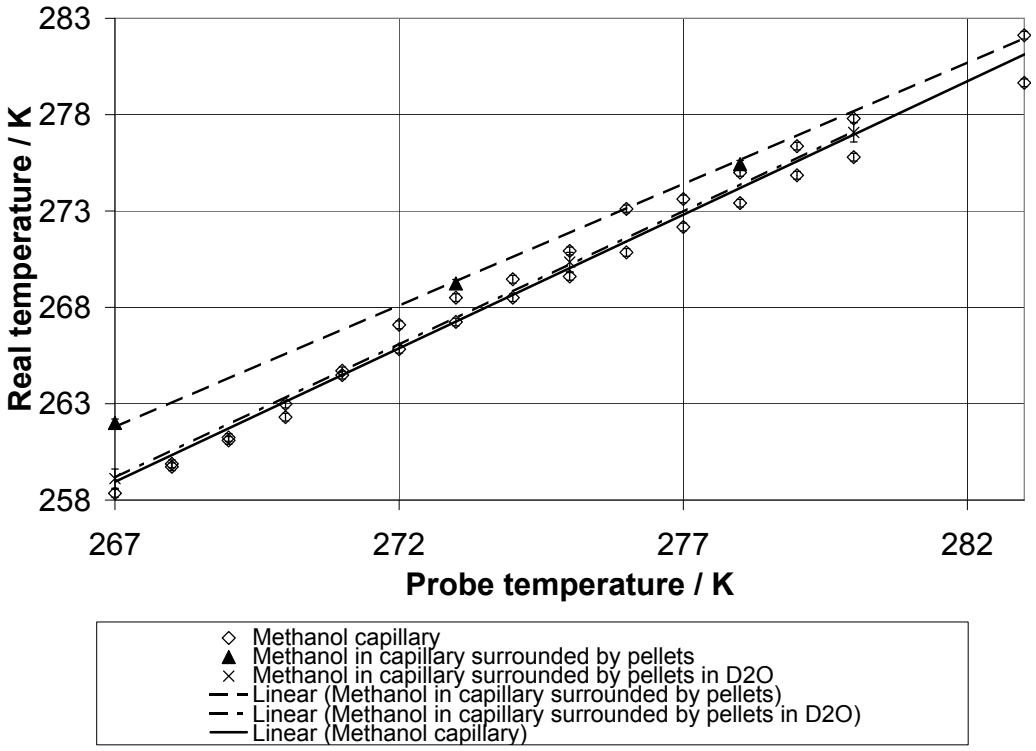

Figure 2.7: Methanol capillary surrounded by pellets temperature calibration

proton chemical shift is not important, only the strength of the signal required. However, the influence of these effects on the methanol temperature calibration render this method unreliable for these experiments and an alternative approach is required.

2.2.3 Temperature calibration using a thermocouple

The alternative approach considered was to use a thermocouple inserted into the sample during the acquisition of the spectra to measure the sample temperature directly. To this end a 't' type thermocouple, identical to that used within the probe, was sourced from the manufacturer of the spectrometer, Bruker. This copper-constantan thermocouple was calibrated against the expected freezing temperature for several water-glycerol mixtures, according to data from literature (Lane, 1925). The thermocouple was inserted into the NMR tube and connected directly into the control system, in place of the thermocouple normally used for temperature control, enabling the control of the temperature via the BVT3200 system by direct measurement of the sample temperature. Initially a sample of methanol was used to provide a reference to the temperature read by the thermocouple and that of the methanol. The thermocouple was placed a few millimeters into the top

of the sample, outside of the region of the detection coil, to avoid any interference within the collected FID or any shimming issues. There was agreement to within 0.5 K between the thermocouple temperature and the calculated temperature from the difference in the methanol chemical shift, with the main source of experimental error being determination of the tops of the two methanol peaks. From equation 2.7, peak position accuracy to 5 decimal places in ppm is required for 0.1 K temperature accuracy, realistically 4 decimal places can be determined from a spectrum which will give accuracy of ± 0.2 K.

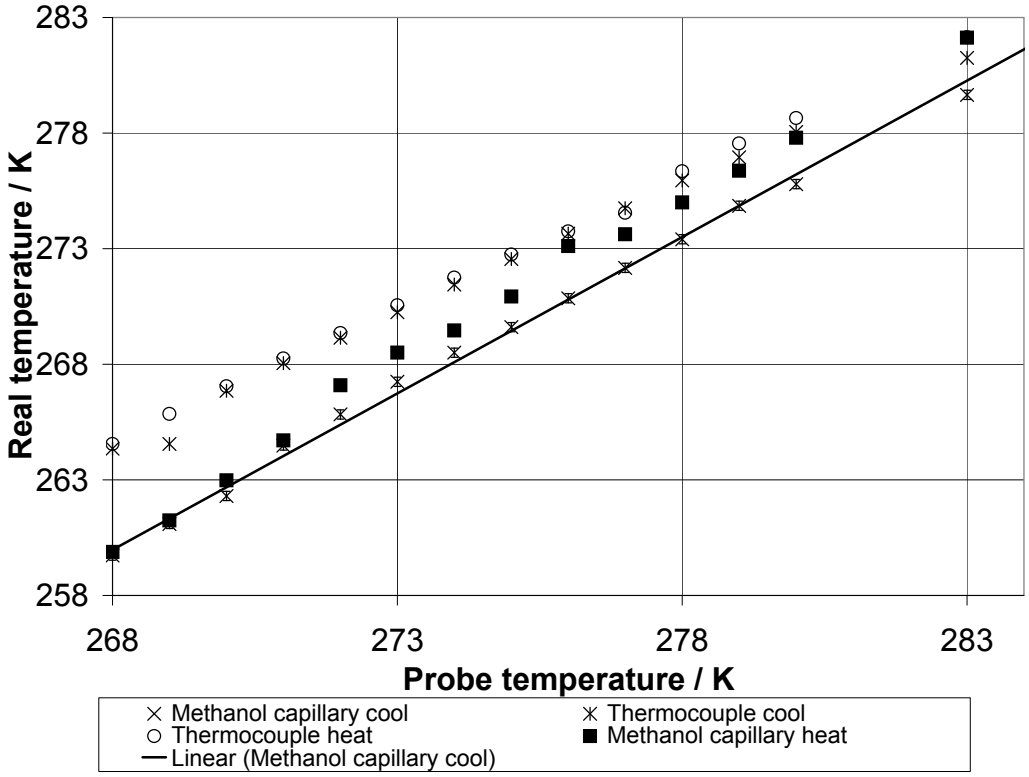

Figure 2.8: Thermocouple temperature calibration on cooling and heating the sample

A more significant practical issue arose from poor temperature control, the temperature control system took several minutes to reach a target temperature and would significantly over-shoot the target temperature. This was the result of the feedback control system assuming the placement of the thermocouple to be below the sample within the flow of cool nitrogen used to cool the sample. The insulated position of the thermocouple meant that the required temperature was overshot and the control system had a 'sluggish' response. Optimising the control system response parameters was not enough to manage accurate control and the set-up was changed. The probe thermocouple was used to manage the temperature control system and the second thermocouple within the sample was used as an independent system to monitor the sample temperature. A comparison of the thermocouple

temperature readings and the methanol capillary results for cooling and heating are shown in Figure 2.8. It can be seen that the thermocouple temperatures are consistent on cooling and heating the sample, whilst the methanol capillary experiments show discrepancies in temperature during cooling and heating.

2.2.4 Temperature gradient calibration

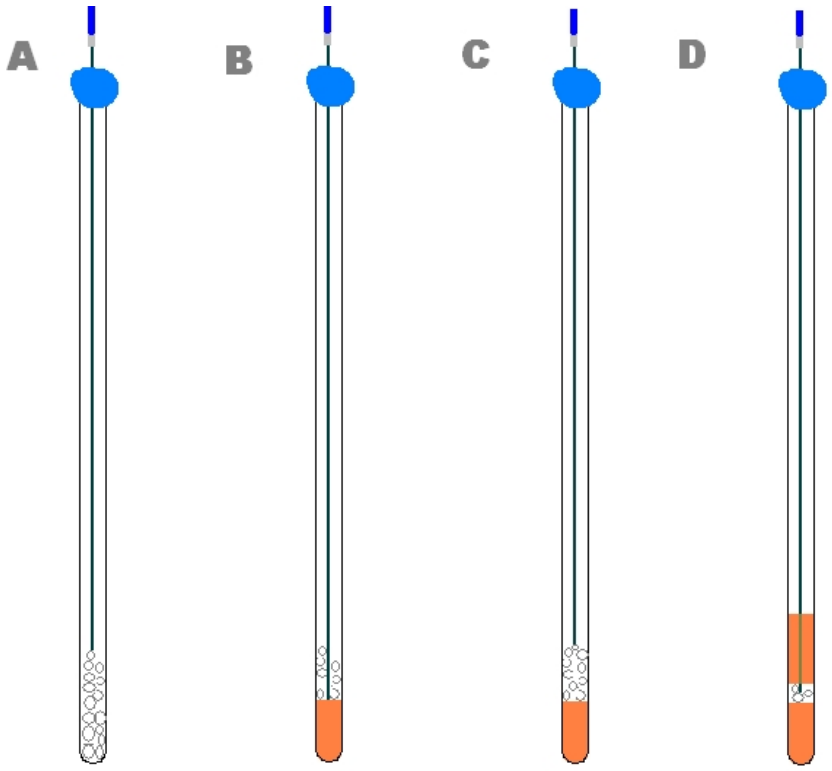

Figure 2.9: NMR experimental set up for calibration experiments 2

The mechanism of heat transfer between a fluid and solid is dependent on several parameters including the fluid dynamics and material properties of the system (Coulson and Richardson, 1999) and is, therefore, considered more complex than heat transfer within a liquid. Thus, investigations were carried out to determine the temperature gradient within the sample. The secondary thermocouple was placed on the surface of the silica pellet sample, as shown in Figure 2.9 A, to give an accurate temperature of the top of the sample at each probe set point temperature. A similar experiment, where the thermocouple was placed as the base of the sample, showed a 4 K temperature gradient through the sample. The heating and cooling of the sample is controlled by the cool nitrogen gas flow over the sample, which comes from below the NMR sample tube, causing a temperature gradient

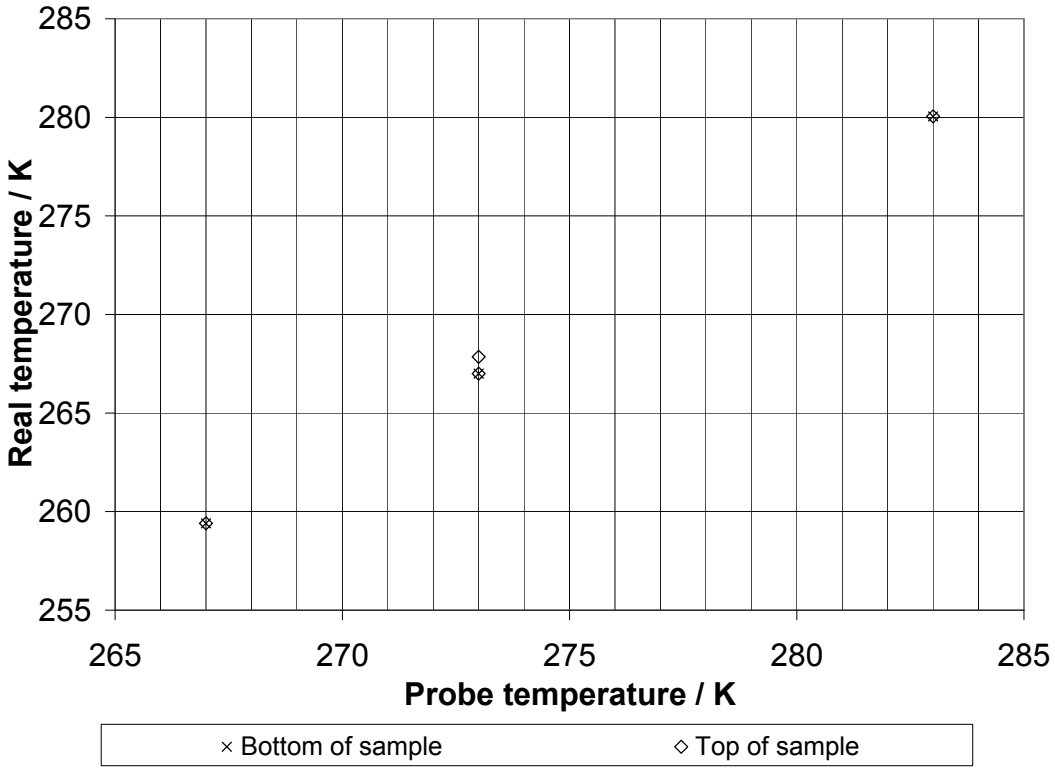

Figure 2.10: Results of measured temperatures for the top and bottom of insulated sample

along the axis of the NMR tube. To reduce this temperature gradient through the sample the lower end of the sample was insulated from the direct flow of the temperature controlling gas flow, by placing a susceptibility plug, made from a non-interfering material, beneath the silica pellets within the NMR tube. The temperature at the top and the bottom of the sample was measured for a series of probe set temperatures of both increasing and decreasing temperature as shown in Figures 2.9 B and C. The results for this experiment seen in Figure 2.10, show a temperature gradient of approximately 1 K over the sample for this set up. To further reduce this temperature gradient, a second susceptibility plug was placed on the top of the sample to cover the top end of the receiver coil and fewer pellets used, as shown Figure 2.9 D. This reduced the temperature gradient to 0.2 K.

2.2.5 Experimental procedure for silica pellet materials

The porous pellets were allowed to soak in laboratory standard deionised water until fully saturated, at least 20 minutes. Once all the pores were filled with water the pellets were dabbed onto wetted tissue paper to remove bulk water from the outside of the pellets. The wetted tissue was used to ensure that excess bulk water was removed, but water within the

pores was not drawn out from the internal pellet structure. A few of the pellets were then carefully placed inside a 5 mm outer diameter NMR tube on top of the first susceptibility plug, the second susceptibility plug was then placed on top with the thermocouple securely positioned to record the sample temperature. Once the experiment was completed, the whole pellets were broken and powdered using a mortar and pestle and pieces soaked again in deionised water and dabbed on wetted tissue. The presence of bulk water would reduce the relative magnitude of the signal recorded from the water entrapped in the pellets and upon freezing the presence of too much bulk water could cause the NMR tube to shatter as the water solidifies and expands. It was, therefore, essential that the excess bulk water was removed as much as possible from the outside of the pieces of sample.

The samples were studied with a Bruker 400 MHz NMR spectrometer. A simple spin echo sequence was used and the automated temperature adjustment program, *multi_zgvt*, was used to follow a sequence of decreasing and increasing temperatures. The temperature sequence used for the experiments was such that four acquisitions were made at each temperature, with an equilibration time of 3 minutes between each listed temperature. This effectively gave equilibration times of 3, 6 , 9 and 12 minutes for each temperature on both cooling and heating, as described earlier in this chapter.

The spectra were processed as described in Section 2.2.1, and results were transferred into excel where signal intensity versus temperature plots could be displayed, thus showing the freeze-thaw hysteresis. For the experiments described in this chapter, where actual pore size calculations were not required, the probe temperature was considered adequate for proof of concept.

2.3 Results and discussion

The results included here are preliminary results that were collected before the temperature gradient along the axis of the NMR tube was discovered. The work described in Chapter 3 uses the experimental method that was developed here.

2.3.1 The equilibration time

Figures 2.11 and 2.12 show the freeze-thaw hystereses for 3 and 12 minutes for two different sol-gel silica pellets with similar pore sizes, s980g and c30 respectively. It can be seen that there is a need to allow the sample to equilibrate at a given temperature for a period of time before taking the spectrum. This is to allow for the sample temperature to reach equilibrium and to allow time for the formation of, or melting of, ice crystals of the imbibed liquid, the

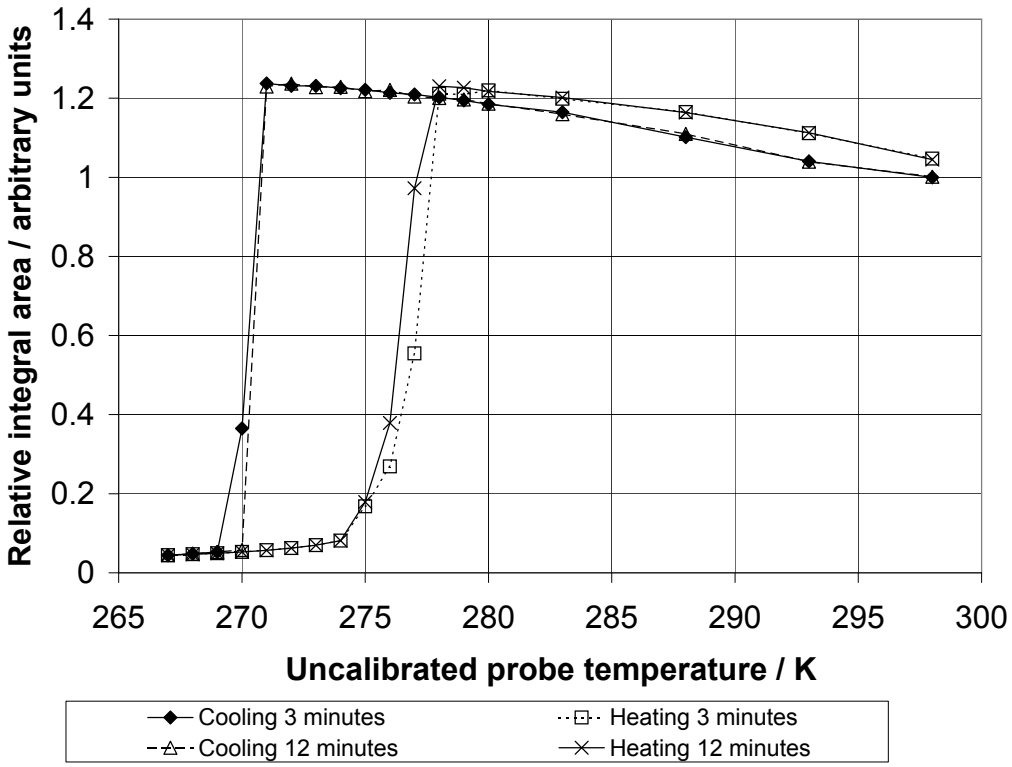

Figure 2.11: Whole s980g pellet freeze-thaw hysteresis at 3 and 12 minutes equilibration times

system thus reaching a steady state. These experiments show that changes within the peak intensity between 9 and 12 minutes were small, within experimental uncertainty, therefore, equilibration times of 9–12 minutes were appropriate for these systems. As previously mentioned in Section 2.2 this equilibration time is close to that suggested by the literature for an equivalent heating rate of 8 K per hour (Hansen et al., 2005).

2.3.2 Freeze-thaw hysteresis

Figures 2.11 and 2.12 show that there is a hysteresis between the freezing and thawing of the imbibed liquid in the silica pellets. It is thought that this hysteresis is the result of the difference in the freezing and melting mechanism due to the restrictions of the pore structure and pore network.

To demonstrate the effect of pore network restrictions on the freezing and thawing of imbibed liquid, a series of experiments were conducted with whole, broken and powdered samples of the two types of silica pellet. By breaking up the pellet the pore network should be disrupted and the hysteresis should change accordingly, the results for these experiments are shown in Figures 2.13 and 2.14, in which the curves for 12 minutes equilibration are

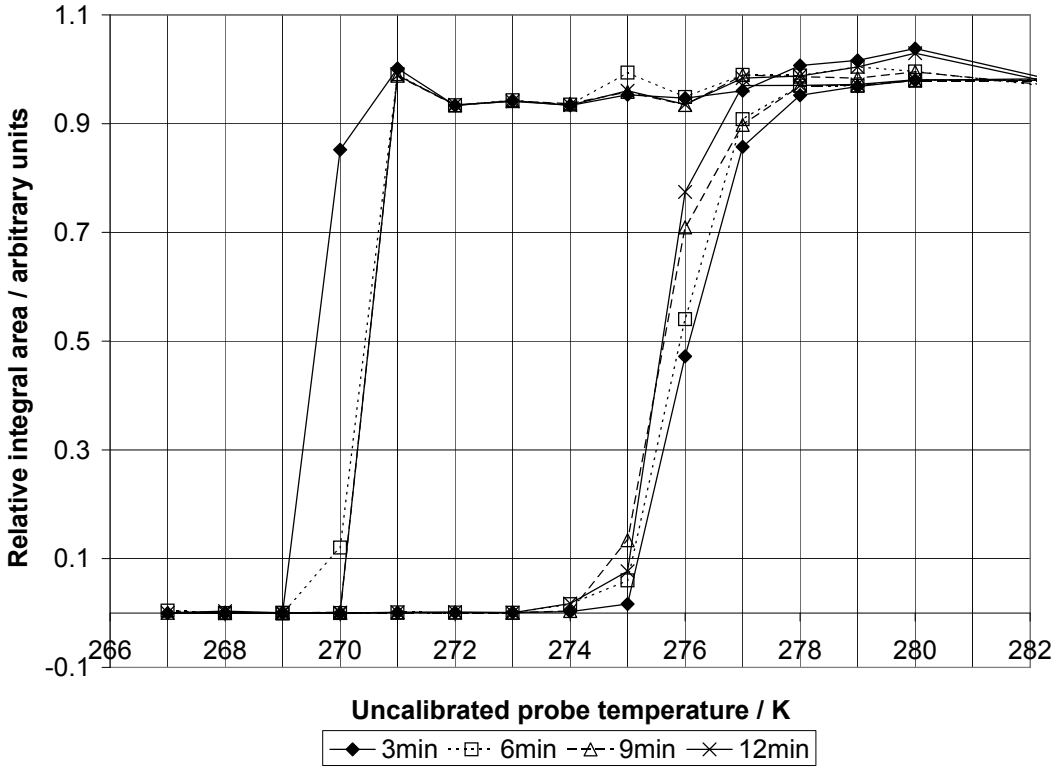

Figure 2.12: Whole c30 pellet freeze-thaw hysteresis at 3 and 12 minutes equilibration times

shown. Data was also collected at 3, 6 and 9 minutes equilibration showing equilibration was achieved. It can be seen in Figure 2.13 that the freeze-thaw hysteresis for broken pellets does not differ from that of whole pellets. This is in agreement with previous work on similar materials (Rigby et al., 2008) which suggests that there is a threshold size for the pellet piece, below which pore network shielding effect can be removed and above which no change is seen in the hysteresis. This is useful for experiments where small volumes of 'whole' pellets are required, broken pieces may be used. Once the pore structure has been broken up sufficiently, as in the powdered samples, it can be seen that there is a shift in the freezing point of the liquid within the powdered sample from that of the liquid within the whole or broken pellet pieces.

2.3.3 Freezing mechanism

Figures 2.13 and 2.14 show liquid freezing at 2–3 K higher for the powder samples than for whole pellet samples, suggesting larger pores are present in the powder samples, both samples whole and powder samples contain the same sizes of pores, however, their arrangement with respect to the bulk water has changed. In the whole pellet the required temperature

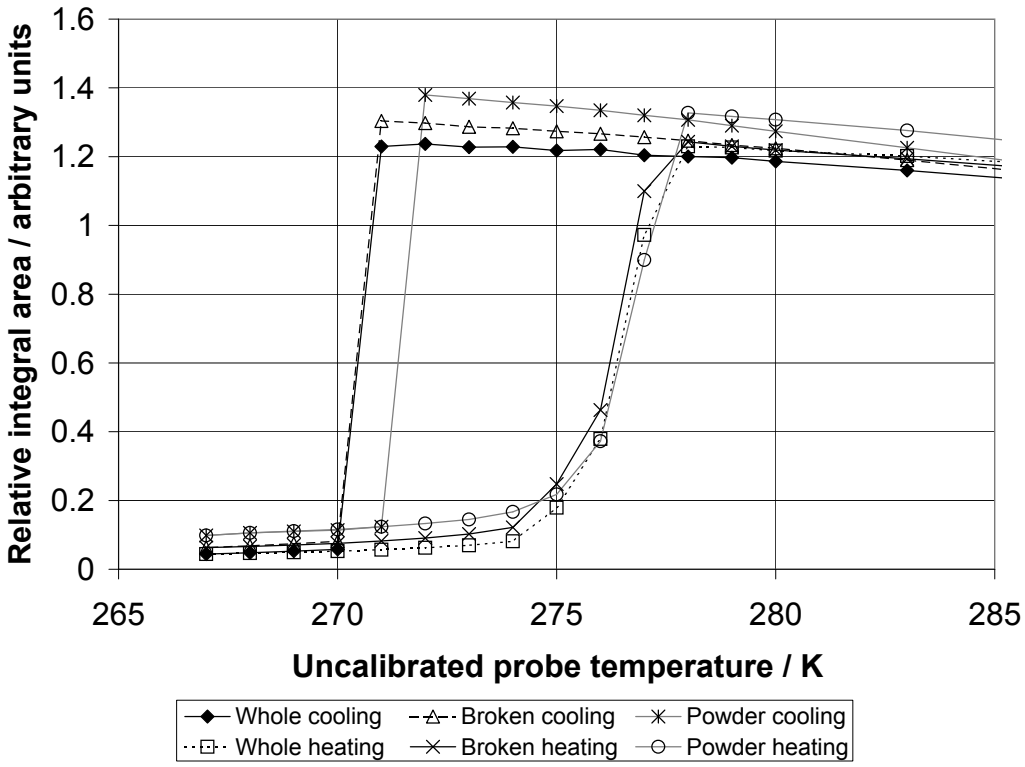

Figure 2.13: Whole, broken and powdered s980g pellet freeze-thaw hysteresis at 12 minutes equilibration time

for the freezing of the imbibed liquid in the smaller external pores is expected to be lower than that for the larger internal pores and, therefore, requires a lower temperature for the freezing to progress into the whole pellet pore structure. These results suggest the freezing mechanism for the imbibed liquid is in some part heterogeneous nucleation, with the freezing front moving into the pellet from the surface. When the pore structure is broken and all the pores are exposed to the external surface in the powder sample, heterogeneous nucleation can occur at a higher temperature, as there are no longer narrow pores shielding the progression of the freezing front into the larger internal pores. The shielding effects of the smaller pore entrances to the main pore structure have been removed in the powder samples. It is, however, not possible at this stage to completely rule out that there may be some contribution of homogeneous nucleation occurring within the pores. As previously mentioned these results were conducted before the discovery of the temperature gradient along the axis of the NMR tube, it is however hoped that this effect is seen when repeated following the final experimental procedure, Section 2.2.5.

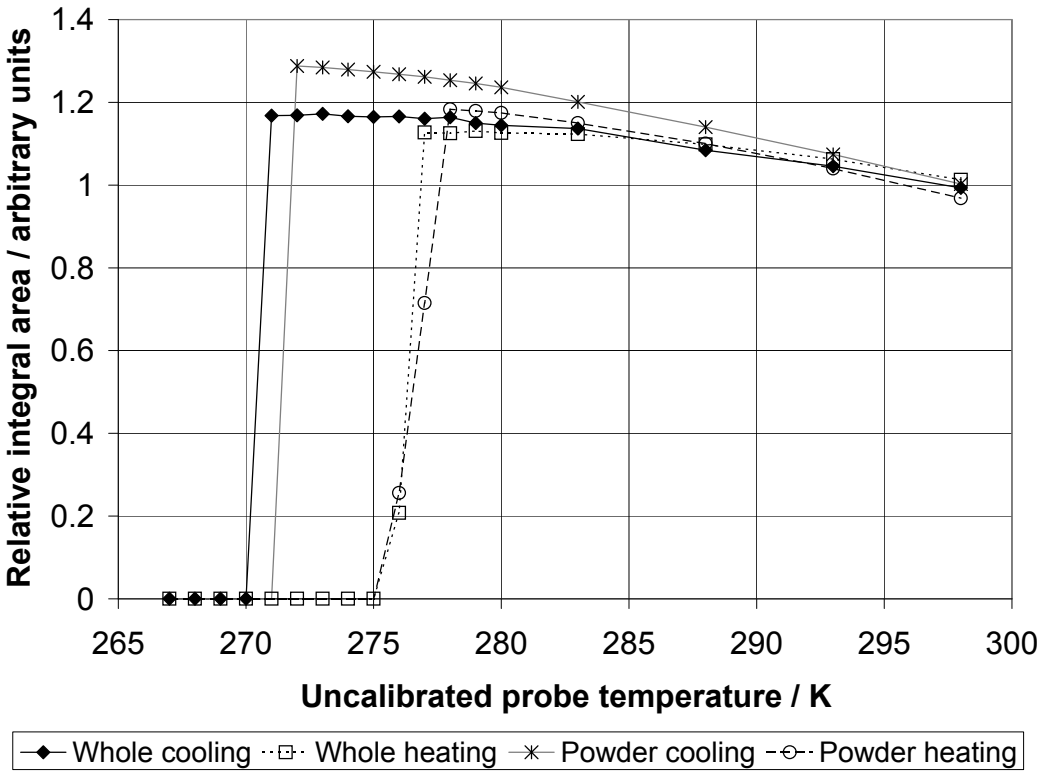

Figure 2.14: Whole and powdered c30 pellet freeze-thaw hysteresis at 12 minutes equilibration time

2.3.4 Comparison to mercury porosimetry data

Figure 2.15 shows mercury intrusion and extrusion data for whole pellet and powder samples of c30. It can be seen in Figure 2.15 that for a whole pellet sample mercury first intrudes when the pressure is equivalent to a pore size of around 0.045 μm, but for the powdered sample the first intrusion is at an equivalent pore size of 0.056 μm. Since the pore sizes for both samples are the same, this effect must be due to a change in the arrangement of the pore structure in the powdered sample compared to the whole sample, and the shielding effect of small pores being removed. This is also shown when the pore size distribution for the two samples is plotted from the intrusion data, Figure 2.16a. The powder sample again shows a maximum volume of pores with a greater diameter than is seen from the whole pellet sample. The pore diameter distribution calculated from the incremental extrusion, Figure 2.16b shows the maximum pore to be the same for both samples, of 0.105 μm and a narrower pore size distribution for the whole sample. The characteristics of the extrusion of mercury from the whole and powdered samples also differ, Figure 2.15. More mercury is left entrapped within the whole pellet sample, 55%, compared to the powdered samples, 30%, this again suggests a shielding effect of narrow pore necks with larger pores contained

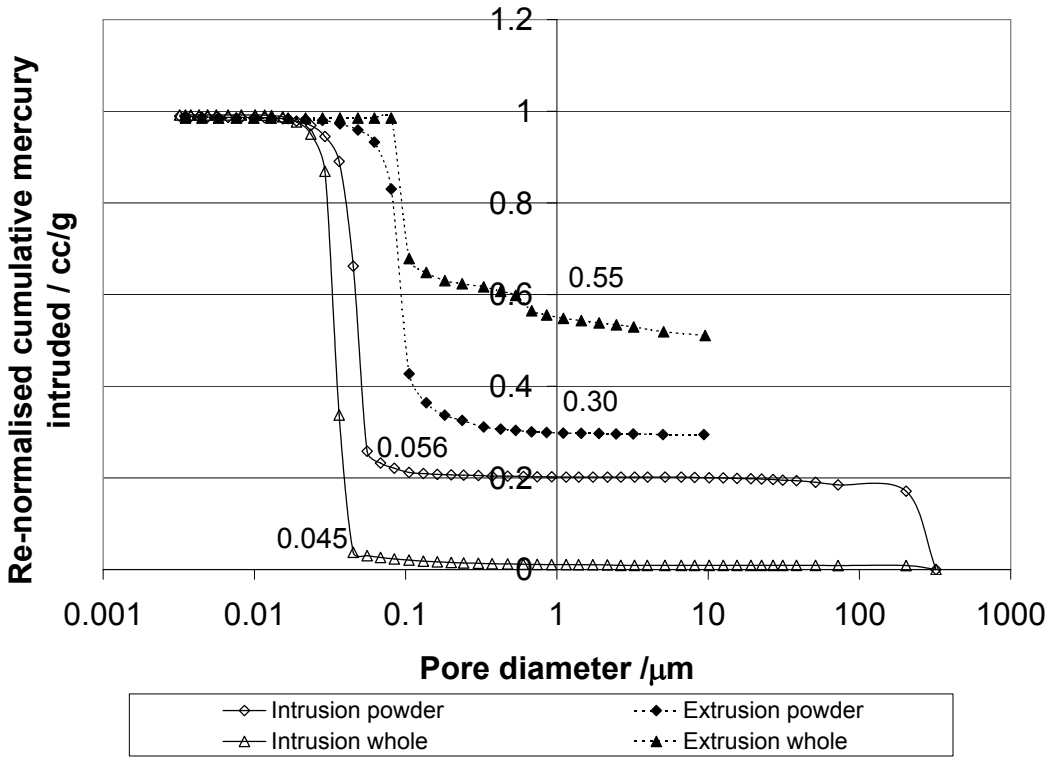

Figure 2.15: Whole and powdered c30 pellet mercury porosimetry intrusion extrusion hysteresis

in the inner structure. As this arrangement is disrupted more mercury is able to extrude from the sample. The step within the extrusion curve for the whole pellet suggests some discontinuity in the extrusion of the mercury, which is not present for the powdered sample.

Comparison of the freeze-thaw hysteresis is made with the intrusion-extrusion of mercury for c30. As previously described in Section 2.3.3, there is a difference in the freezing temperature for whole and powdered sample imbibed liquid. The liquid imbibed in the whole pellet sample freezes at a lower temperature suggesting a smaller pore size, in a similar manner to the shift seen for mercury intrusion for whole and powder samples. Like mercury extrusion, no change is seen in the melting characteristics between whole and powder samples. The pore size distribution of the whole and powdered pellet samples being the same, this reinforces the suggestion of a shielding effect being seen in the freezing process, like that seen for mercury intrusion.

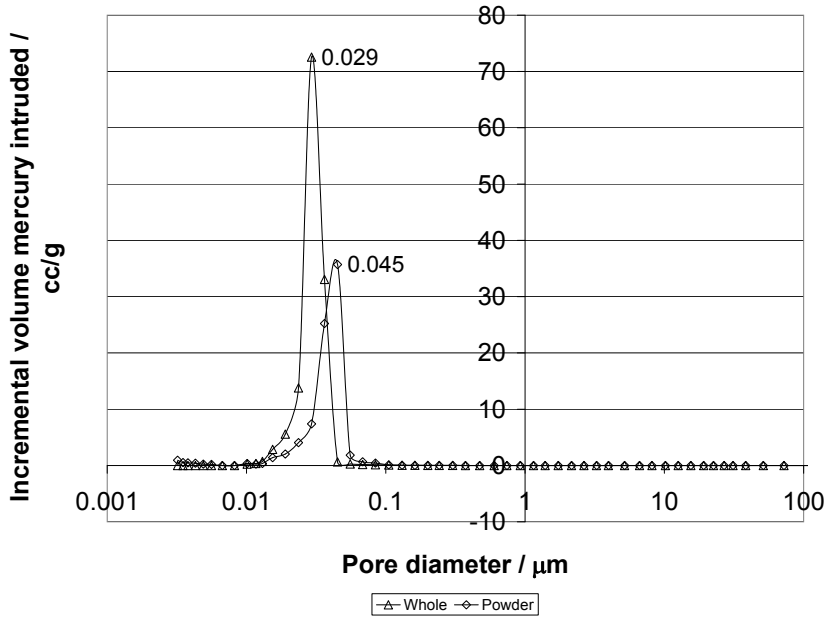

(a) Intrusion diameter

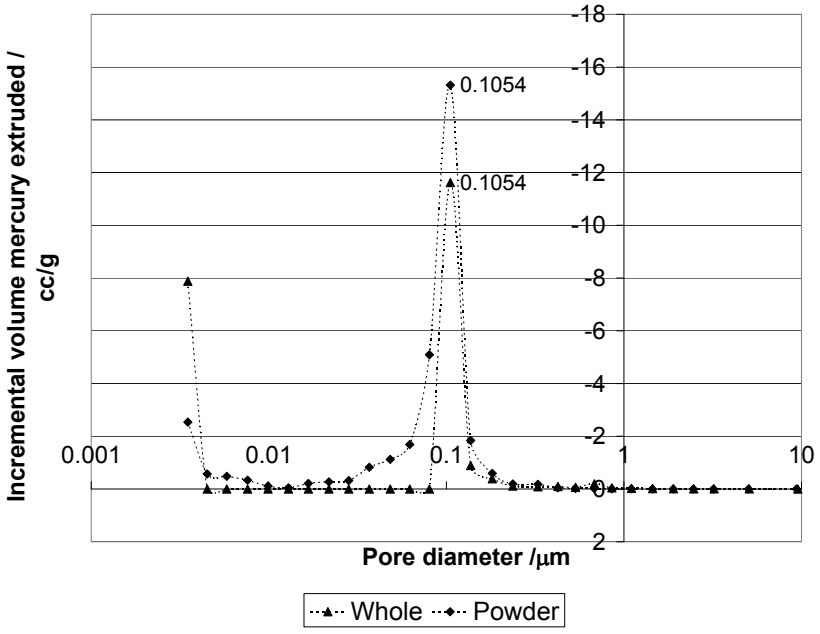

(b) Extrusion diameter

Figure 2.16: Whole and powdered c30 pellet pore size distribution determined from mercury intrusion and extrusion

2.4 Conclusions

This work has established an improved cryoporometry method that provides accurate temperature measurements and, therefore, a robust account of pore size distribution to be determined for model systems. The temperature profile within the sample has been reduced to a level such that the experimental error in pore size determination is within acceptable limits. The pore size distribution may then be compared to that found by alternative methods such as gas sorption and mercury porosimetry, the comparison of which may be used to estimate the Gibbs-Thomson parameter. In this chapter it has been shown that it is possible to compare the overall trend of cryoporometry results with mercury intrusion and extrusion data to form a better understanding of the freezing mechanism involved. Heterogeneous nucleation by means of a freezing front that progresses in toward the centre of the pellet has been suggested as a potential contributory freezing mechanism and one of the causes of the freeze-thaw hysteresis. Further work has been carried out on silica materials to reinforce and consolidate these findings, see Chapter 3. From this further work, a better understanding of the freezing mechanism will be established to enrich the interpretation of cryoporometry data. The spectra collected from a combination of NMR techniques, cryoporometry and pulsed field gradient diffusometry will be used to investigate drug delivery mechanisms from polymer microspheres. This is discussed later in Chapters 5 and 6.

References

N. K. Adam. *Nature*, 180:809, 1957.

J. M. Coulson and J. F. Richardson. *Coulson and Richardson's Chemical Engineering Volume 1 Fluid Flow, Heat Transfer and Mass Transfer*. Butterworth Heinemann, fifth edition, 1999.

G. Dosseh, Y. Xia, and C. Alba-Simionesco. Cyclohexane and benzene confined in mcm-41 and sba: Confinement effects o freezing and melting. *Journal of Physical Chemistry B*, 107(6445-6453), 2003.

A. Dupré. *Théorie méchanique de la chaleur,*. Paris, 1869.

A. V. Filippov and V. D. Skirda. An investigation of the structure of a porous substance by nmr cryodiffusometry. *Colloid Journal*, 62(6):759–764, 2000.

P. Fritsch. Bruker edte: Vtu software user manual edte version 002. 2000.

P. A. C. Gane, C. J. Ridgway, E. Lehtinen, R. Valiullin, I. Furo, J. Schoelkopf, H. Paulapuro, and J. Daicic. Comparison of nmr cryoporometry, mercury intrusion porosimetry, and dsc thermoporosimetry in characterizing pore size distributions of compressed finely ground calcium carbonate structures. *Industrial & Engineering Chemistry Research*, 43(24): 7920–7927, 2004.

A. L. V. Geet. Calibration of methanol nuclear magnetic resonance thermometer at low temperature. *Analytical Chemistry*, 42(6):679–680, 1970.

J. W. Gibbs. *Collected Works, 2 vols.* New York, 1928.

E. W. Hansen, R. Schmidt, and M. Stocker. Pore structure characterization of porous silica by h nmr using water, benzene and cyclohexane as probe molecules. *Journal of Physical Chemistry*, 100:11396–11401, 1996.

E. W. Hansen, G. Fonnum, and E. Weng. Pore morphology of porous polymer particles probed by nmr relaxometry and nmr cryoporometry. *Journal of Physical Chemistry B*, 109:24295–24303, 2005.

M. Iza, S. Woerly, C. Danumah, S. Kaliaguine, and M. Bousmina. Determination of pore size distribution for mesoporous materials and polymeric gels by means of dsc measurements: thermoporometry. *Polymer*, 41(15):5885–5893, 2000.

C. L. Jackson and G. B. McKenna. The melting behavior of organic materials confined in porous solids. *Journal of Chemical Physics*, 93(12):9002–9011, 1990.

A. H. Janssen, H. Talsma, M. J. van Steenbergen, and K. P. de Jong. Homogeneous nucleation of water in mesoporous zeolite cavities. *Langmuir*, 20(1):41–45, 2004.

L. B. Lane. Freezing points of glycerol and its aqueous solutions. *Industrial and Engineering Chemistry*, 17(9):924, 1925.

L. I. Mikhalovska, V. M. Gun'ko, V. V. Turov, V. I. Zarko, S. L. James, P. Vadgama, P. E. Tomlins, and S. V. Mikhalovsky. Characterisation of the nanoporous structure of collagen-glycosaminoglycan hydrogels by freezing-out of bulk and bound water. *Biomaterials*, 2006.

J. Mitchell, S. C. Stark, and J. H. Strange. Probing surface interactions by combining nmr cryoporometry and nmr relaxometry. *Journal of Physics D-Applied Physics*, 38: 1950–1958, 2005.

J. Mitchell, J. B. W. Webber, and J. Strange. Nuclear magnetic resonance cryoporometry. *Physics Reports*, 2008.

O. Petrov and I. Furo. Curvature-dependent metastability of the solid phase and the freezing-melting hysteresis in pores. *Physical Review E*, 73(1), 2006. Part 1.

O. Petrov, I. Furo, M. Schuleit, R. Domanig, M. Plunkett, and J. Daicic. Pore size distributions of biodegradable polymer microparticles in aqueous environments measured by nmr cryoporometry. *International Journal of Pharmaceutics*, 309(1-2):157–162, 2006a.

A. Quinson, JF. Determination of surface-areas by thermoporometry. *Applied catalysis. A, General*, 30(1):123–130, 1987.

J. F. Quinson and M. Brun. Progress in thermoporometry. *Characterization of Porous Solids*, pages 307–315, 1988.

J. F. Quinson, J. Dumas, and J. Serughetti. Alkoxide silica-gel - porous structure by thermoporometry. *Journal of Non-Crystalline Solids*, 79(3):397–404, 1986.

S. P. Rigby, P. I. Chigada, E. L. Perkins, M. J. Watt-Smith, J. P. Lowe, and K. J. Edler. Fundamental studies of gas sorption within mesopores situated amidst an inter-connected, irregular network. *Adsorption-Journal of the International Adsorption Society*, 14(2-3): 289–307, 2008.

R. Schmidt, E. W. Hansen, M. Stocker, D. Akporiaye, and O. H. Ellestad. Pore-size determination of mcm-41 mesoporous materials by means of h-1-nmr spectroscopy, n-2 adsorption, and hrem - a preliminary-study. *Journal of the American Chemical Society*, 117(14):4049–4056, 1995.

A. Schreiber, I. Ketelsen, and G. H. Findenegg. Melting and freezing of water in ordered mesoporous silica materials. *Physical Chemistry Chemical Physics*, 3:1185–1195, 2001.

M. Sliwinska-Bartowiak, G. Dudziak, R. Sikorski, R. Gras, R. Radharakrishnan, and K. E. Gubbins. Melting/freezing behaviour of a fluid confined in porous glasses and mcm-41: Dielectric spectroscopiy and molecular simulation. *Journal of Chemical Physics*, 114(2): 950–962, 2001.

J. H. Strange, M. Rahman, and E. G. Smith. Characterization of porous solids by nmr. *Physical Review Letters*, 71(21):3589–3591, 1993.

J. H. Strange, J. Mitchell, and J. B. W. Webber. Pore surface exploration by nmr. *Magnetic Resonance Imaging*, 21(3-4):221–226, 2003.

J. J. Thomson. *Applications of Dynamics*. PhD thesis, London, 1888.

W. T. Thomson. *London, Edinburgh and Dublin Philosophical Magazine and Journal of Science*, 42(4):448, 1871.

D. Topgaard and O. Soderman. Self-diffusion of nonfreezing water in porous carbohydrate polymer systems studied with nuclear magnetic resonance. *Biophysical Journal*, 83(6): 3596–3606, 2002.

R. Valckenborg, L. Pel, and K. Kopinga. Cryoporometry and relaxometry of water in silica-gels. *Magnetic Resonance Imaging*, 19(3-4):489–491, 2001.

R. M. E. Valckenborg, L. Pel, and K. Kopinga. Combined nmr cryoporometry and relaxometry. *Journal of Physics D-Applied Physics*, 35:249–256, 2002.

R. Valiullin and I. Furo. Low-temperature phase separation of a binary liquid mixture in porous materials studied by cryoporometry and pulsed-field-gradient nmr. *Physical Review E*, 66(3), 2002. Part 1.

R. Valiullin and I. Furo. The morphology of coexisting liquid and frozen phases in porous materials as revealed by exchange of nuclear spin magnetization followed by h-1 nuclear magnetic resonance. *Journal of Chemical Physics*, 117(5):2307–2316, 2002a.

E. W. Washburn. The dynamics of capillary flow. *The Physical Review*, 17(3):273–283, 1921.

J. B. W. Webber. *Characterising porous media*. PhD thesis, University of Kent, Canterbury, 2000.

J. B. W. Webber, J. H. Strange, and J. C. Dore. An evaluation of nmr cryoporometry, density measurement and neutron scattering methods of pore characterisation. *Magnetic Resonance Imaging*, 19(3-4):395–399, 2001.

Chapter 3

Application of the cryodiffusometry experimental method to sol-gel silica materials

3.1 Introduction

The work described in this chapter uses the cryoporometry method developed in Chapter 2 to further the understanding of the freezing process of an imbibed liquid within a porous material. By comparing cryoporometry freeze-thaw hysteresis with better know porosimetry methods, such as mercury porosimetry and gas sorption it hoped that the causes of the freeze-thaw hysteresis may be identified. The material used for this work is a commercially available sol-gel silica pellet which has been previously studied within the group (Rigby et al., 2008a). It is known to have an 'ink bottle' pore structure, where larger pores are only accessible to the surface or surrounding pore network by narrow pores thus simulating the body and neck of an ink bottle. Using this model structure allows further interpretation of the freeze-thaw hysteresis. The difference in freezing and melting mechanism is investigated using whole pellet and ground-up powder samples. A direct comparison with mercury intrusion-extrusion hysteresis and nitrogen adsorption-desorption hysteresis has shown that the freezing curve can provide additional complimentary information to the melting curve during the investigation of pore network characteristics by cryoporometry.

3.2 Background and Theory

Silica materials are currently of interest for use as a drug delivery system (Rigby et al., 2008b). The development of mesoporous silica materials has enabled the tailoring of pore sizes, pore arrangements, surface chemistry and accessibility to the pore network via responsive gates (Mal et al., 2003). Thus silica material design has clear advantages over polymeric systems, in terms of structure and surface property control. Recent studies have considered a variety of silica materials for drug delivery, such as mesoporous templated silica (Vallet-Regi et al., 2006), sol-gel silicas (Veith et al., 2004), mesoporous microspheres (Wang and Caruso, 2005; Zhu et al., 2005) and a combination polymer-silica xerogel (Xue et al., 2006). Whilst polymer devices have the advantage of proven biocompatability, the inorganic silica material structure design is better understood and able to host protein and enzymes with little effect on their characteristic functionality (Hartmann, 2005).

Cryoporometry has previously been compared with other porosimetry techniques such gas sorption, neutron scattering and liquid intrusion (Gane et al., 2004; Denoyel et al., 2004; Webber et al., 2001). However, the focus of much of this work has been on the melting characteristics of the imbibed fluid. Some hysteresis comparisons have been made by Denoyel et al. (2004), who concludes that the hystereses of gas adsorption-desorption and freeze-thaw cycles are very comparable, but they do not explain why this is. It has only been very recently that interest has grown to include the significance of the freezing curve (Petrov and Furo, 2006; Khokhlov et al., 2007; Vargas-Florencia et al., 2008).

3.2.1 Further Cryoporometry Theory

The fundamental principles of cryoporometry theory were introduced in Chapter 2, this section describes further ideas that add detail to the complex nature of the freezing mechanism and the freeze-thaw hysteresis. The combination of cryoporometry with NMR diffusion studies, known as cryodiffusometry, is also explained. Combining these NMR techniques it is hoped that a more detailed understanding of pore structure for complex materials may be explored.

Traditionally in thermoporosimetry and early cryoporometry experiments pore size distributions were determined from the melting behaviour of the imbibed liquid. Typically a sample was cooled until all the liquid contained was frozen and then gradually heated until all the liquid had melted again. The melting characteristics were chosen as they were not subject to the super cooling effects seen during freezing (Strange et al., 1993) and the mechanism of melting was better understood, as described previously in Section 2.1. The mechanism for freezing of an imbibed liquid and, therefore, the causes of the freeze-thaw

hysteresis have been more recently discussed (Petrov and Furo, 2006; Khokhlov et al., 2007; Vargas-Florencia et al., 2008). It is with a better understanding of the freezing mechanism that there is the opportunity to gain additional structural information from the characteristic freezing curve.

Within the literature there are three common theories for the cause of the freeze-thaw hysteresis, as described by Petrov and Furo (2006):

i An uncontrollable delay by homogeneous nucleation on cooling, like that seen in bulk liquids. In the absence of nucleation sites such as foreign particles in a bulk liquid, it is possible to cool the liquid below its freezing point and for it to remain liquid. When the liquid is further cooled homogeneous nucleation can occur and the liquid freezes, this phenomena is known as super-cooling. This effect can be seen on a series of independent experiments, however, the temperature at which super-cooling occurs is not consistent for any given sample.

ii Pore-blocking effects on penetration of a solid front moving from the outside that causes an apparent delay in the freezing of the internal pores. For an imbibed liquid, external pores are in contact with the bulk liquid, which will freeze first, once frozen the bulk liquid provides a nucleation site for liquid in contact with it. However, for this liquid to freeze the temperature must reach the value appropriate for the pore size it is contained within. If a larger inner pore is shielded from the bulk by a smaller pore, the inner pore can only freeze when the temperature is low enough to freeze the smaller pore, as predicted by the Gibbs-Thomson equation 2.1, thus shifting the freezing curve to smaller apparent pore sizes.

iii The shape of the pore determines the shape of the meniscus between liquid and solid state during melting and freezing. Whilst the propagation of freezing within the pore occurs along the axis of the pore, it is thought that the melting front of the pore propagates from the pore wall radially toward the pore center. Thus, the hysteresis is due to some shape factor that accounts for the difference in the propagation of these two fronts.

In addition there is support within the literature for the idea that the freezing mechanism may be a combination of two or more of the above mechanisms acting together:

- Janssen et al. (2004) suggest that the freezing mechanism within a porous solid is a combination of heterogeneous and homogeneous nucleation. Ice forms at the open ends of the pores and then gains access to the pore network, such that freezing

progresses inward by heterogeneous nucleation. In addition, some homogeneous nucleation occurs within the pores that are connected to the surrounding network by micropores, and supercooling occurs before the freezing front gains access. The influence of the delayed nucleation affects the calculated pore size determined from the freezing behaviour, therefore, the melting curve is more reproducible and most often used for pore diameter calculations.

- Petrov and Furo (2006) describe hysteresis in terms of a free-energy barrier between metastable state and stable states, describing melting as a function of curvature of the pore surface, whilst freezing is a function of surface to volume ratio of the pore. The model derived in this work for a single pore hysteresis gives the relationship between freezing and melting point depression, equation 3.1, where κ is the integral mean surface curvature and $\frac{V}{S}$ is the volume to surface area ratio of the pore, such that $\frac{2\kappa V}{S}$ is $\frac{1}{2}$ for open ended cylindrical pores, and $\frac{2}{3}$ for spherical pores.

$$\Delta T_m = \Delta T_f \frac{2\kappa V}{S} \tag{3.1}$$

- Khokhlov et al. (2007) use mesoporous etched silicon materials to experimentally determine the freezing process. The known size, geometry and arrangement of pores lead them to conclude that the freezing mechanism within pores is a combination of both pore blocking effects of the freezing front penetrating the pore network, and homogeneous nucleation of pores that are sufficiently shielded within the pore network, where spontaneous nucleation can occur before the ice front reaches the pore.

It is widely considered within the literature that a pore containing a frozen liquid has a non-frozen layer between the solid frozen core and the pore walls (Quinson and Brun, 1988; Schmidt et al., 1995; Hansen et al., 1996; Iza et al., 2000; Schreiber et al., 2001; Janssen et al., 2004; Khokhlov et al., 2007). This has lead to a modified Gibb-Thomson equation, as expressed in Schreiber et al. (2001), equation 3.2,

$$\Delta T_m = \frac{k_{GT}}{2(r_p - t)} \tag{3.2}$$

where k_{GT} is the Gibbs-Thomson constant, r_p is the pore radius and t is the thickness of

the non-freezing surface layer. Typical values of k_{GT} and t for water are 25–57.3 nmK and 0.35–0.38 nm respectively (Schmidt et al., 1995; Schreiber et al., 2001; Webber et al., 2001; Vargas-Florencia et al., 2007).

It is not always possible to gain an a priori value for the Gibbs-Thomson constant for any given system, therefore, it is necessary to calibrate this parameter with another porosimetry technique such as mercury porosimetry, as will be shown in Section 3.4.6.

In common with other porosimetry techniques, cryoporometry data requires some manipulation to calculate a pore size distribution, $p(d)$. The measured parameters of melting point depression, ΔT_m, and signal intensity, I, are inversely proportional to pore size, x, and directly proportional to volume of liquid, v , respectively. Thus, the pore size distribution is determined from the change in NMR signal intensity during melting or freezing (Strange et al., 1993).

The cumulative pore volume, v, is a function of pore diameter. Therefore, the volume of pores with a diameter between x and $x + \Delta x$ is $\frac{dv}{dx}\Delta x$. As the NMR signal intensity, I, is directly proportional to molten pore volume, then $\frac{dI}{dx}\Delta x = \frac{dv}{dx}\Delta x$ holds true. The pore size distribution as a function of the change of signal intensity, is derived using the chain rule as shown in equation 3.3.

$$\frac{dI}{dx} = \frac{dI}{dT_m(x)}\frac{dT_m(x)}{dx} \tag{3.3}$$

From the simplified Gibbs-Thomson equation, equation 2.5, $\frac{dT_m(x)}{dx} = \frac{k}{x^2}$. Substituting into equation 3.3 gives the pore size distribution equation in terms of NMR signal intensity, melting point depression and k_{GT}, equation 3.4 (Strange et al., 1993).

$$p(d) = \frac{dI}{dx} = \frac{dI}{dT_m(x)}\frac{k_{GT}}{x^2} \tag{3.4}$$

3.2.2 Cryodiffusometry

Cryodiffusometry is the combination of cryoporometry with NMR pulsed field gradient (PFG) diffusion studies. The study of diffusion by NMR began it's development in the 1950s with the works of Hahn (1950) and Carr and Purcell (1954). Further developments included the use of spin echoes (Stejskal and Tanner, 1965) and stimulated spin echo (Tanner, 1970) sequences for studying diffusion coefficients. Most modern diffusion sequences are

derivatives of these two sequences (Kerssebaum, 2002). A comparison of some of the most popular sequences for use in Diffusion Ordered Spectroscopy (DOSY) has been published by Avram and Cohen (2005), including the Pulsed Gradient Spin Echo, (PGSE), the Pulsed Gradient Stimulated Echo (PGSTE), the Longitudinal eddy current delay (LED) and the Bipolar gradient with Longitudinal Eddy Current Delay (BPLED) sequences. Avram and Cohen (2005) discuss the type of pulse sequence used and its effect on water signal decay, including how the exponential behaviour observed may be different with the introduction of the longitudinal eddy delay if that delay is greater than around 4 ms, such that a second slower component diffusion may be seen that is not observed without the eddy delay. Such an effect was not observed in this work where the eddy delay was 5 ms, and in some cases mono exponential decays were observed, therefore, deviation from mono exponential behaviour observed are not attributed to this effect.

The acquired data from PFG experiments shows an attenuation in signal amplitude for the required nucleus as a result of diffusion of the nuclei within the observed diffusion time. The attenuation of the signal intensity follows an exponential curve, equation 3.5, where signal intensity, I, is a function of I_0, the reference intensity, D, the diffusion coefficient, γ, the gyromagnetic ratio of the observed nucleus, g, the gradient strength, δ the length of the gradient, Δ the diffusion time and τ the correction time for the phasing and dephasing between bipolar gradients *.

$$I = I_0 \exp\left(-D\gamma^2 g^2 \delta^2 (\Delta - \delta/3 - \tau/2)\right) \tag{3.5}$$

This equation can be used to calculate the diffusion coefficient of the observed nucleus in a homogeneous system, where the desired nucleus is effectively in one phase and the log attenuation plot, $Ln(I/I_0)$ against $\zeta = \gamma^2 g^2 \delta^2 (\Delta - \delta/3 - \tau/2)$, is linear.

Combining cryoporometry and diffusometry provides the ability to assess the diffusion characteristics of a part molten, part frozen sample, this can provide additional pore structure information, and the arrangement of ice within that structure. PFG experiments carried out at equal signal intensities on the freezing curve for whole and powder samples should indicate if there is a difference in the distribution of ice during the freezing process for these two samples. The effective diffusion coefficient, D_e, is a measure of how the water is diffusing within the porous network. The tortuosity of the pore network, τ_p, is a measure of the potential deviation from a linear path that a diffusing molecule may experience. The greater value of tortuosity, the more complex the path of the diffusing molecule, implying a more complex network. The relationship between effective diffusion coefficient and

*As expressed in (Kerssebaum, 2002)

tortuosity is given by equation 3.6[†],

$$D_e = D_B \frac{\epsilon_p}{\tau_p} \tag{3.6}$$

where D_B is the bulk diffusion coefficient at the experimental temperature and ϵ_p is the voidage or porosity of the material.

The diffusion coefficient calculated from NMR PFG studies, D_{PFG}, contains a contribution from the spin density which is directly related to the voidage (Hollewand and Gladden, 1995), and is related to the effective diffusion coefficient by equation 3.7.

$$D_e = \epsilon_p D_{PFG} \tag{3.7}$$

The combination of equations 3.6 and 3.7 allow the determination of tortuosity from the bulk diffusion coefficient and the measured diffusion coefficient by equation 3.8.

$$\tau_p = \frac{D_B}{D_{PFG}} \tag{3.8}$$

The bulk diffusion coefficient of water can be estimated for a given temperature using measured values found in literature (Mills, 1973; Holz et al., 2000). To estimate the value of bulk diffusion at sub-cooled temperatures an extrapolation of the line of best fit for literature data is made. It is not possible to measure the bulk diffusion coefficient at sub-cooled temperatures used for these experiments, as bulk water will freeze. Validity of the application of this method is discussed later in Section 3.4, but the estimation of the bulk diffusion coefficient allows a quantitative analysis of tortuosity to be made. If a significant difference is seen in the tortuosity between freezing of whole and powder sample, this implies a difference in the arrangement of the ice and thus, a difference in the dominant freezing mechanism.

The calculated root mean square (rms) displacement, r_{rms}, of a molecule for the diffusion time studied, according to the Stokes-Einstein equation 3.9[‡] is approximately 10–20 μm. Therefore, it is expected that within the whole pellet sample, pellet diameter of ap-

[†]As expressed in (Hollewand and Gladden, 1995)

[‡]For spherical pores described by Hollewand and Gladden (1995)

proximately 2–3 mm, a statistically insignificant number of molecules will encounter the boundary layer of ice around the pellet during the diffusion time. However, if the pellet size was of the order of 1–2 times the rms displacement distance it is possible that a significant number of molecules will encounter and interact with the boundary layer ice. To compensate for this effect, the unrestricted intra-particle diffusion shall be estimated using the short time diffusion model for porous media derived by Mitra et al. (1993). According to equation 3.10, a plot of the measured diffusion coefficient, D_{PFG}, against the square root of the diffusion time, $\Delta^{\frac{1}{2}}$, gives an intercept value equivalent to the intra-particle diffusion coefficient, D_0,

$$r_{rms} = (6D\Delta)^{0.5} \tag{3.9}$$

$$D_{PFG} = D_0 - \frac{4D_0^{\frac{3}{2}}S}{9\pi^{\frac{1}{2}}V}\Delta^{\frac{1}{2}} \tag{3.10}$$

where $\frac{S}{V}$ is the surface to volume ratio of the boundary surface, ie. the pore walls and ice walls.

3.2.3 Gas adsorption

Gas adsorption relies on the physical and chemical attraction between a solid surface, the adsorbent, and gas molecules, the adsorbate, at some defined pressure. Considering the physical attractive forces, or van der Waals' forces, the amount of gas adsorbed to the surface of the solid is a function of pressure, temperature and the properties of the solid and gas (Gregg and Sing, 1982). The amount of gas adsorbed on the solid surface can be measured in terms of a reduction in pressure within the system, or an increase in weight of the solid sample. The gas will adsorb first to the solid surface as a monolayer, i.e. a layer that is one molecule thick, then additional layers of gas build onto the monolayer to form a multilayer [§]. Within a porous material the gas layers continue to fill the pore until the pressure is sufficient that the gas condenses into a 'liquid-like phase'. The pressure at which the gas condenses can be related to the pore size according to the Kelvin equation, 3.11,

$$ln\frac{p}{p_0} = -\frac{2\gamma_l V_m}{r_p RT}\cos\phi \tag{3.11}$$

where p is the pressure, p_0 is the saturation pressure of the gas at the given temperature,

[§]Adsorption model of Brunauer, Emmett and Teller as described in Gregg and Sing (1982)

($\frac{p}{p_0}$ is termed the relative pressure,) γ_l is the surface tension of the adsorbate in liquid form, V_m is the molar volume of the adsorbate in liquid form, r_p is the pore radius, R is the universal gas constant, T is the temperature and ϕ is the contact angle between the liquid and the wall of the pore. The contact angle, ϕ, is often given an assumed value of 0, i.e. that the liquid wets the pore wall, in reality the contact angle changes (Gregg and Sing, 1982) as the pore fills and the pore shape varies, it is, therefore, difficult to determine directly within the small porous networks being studied.

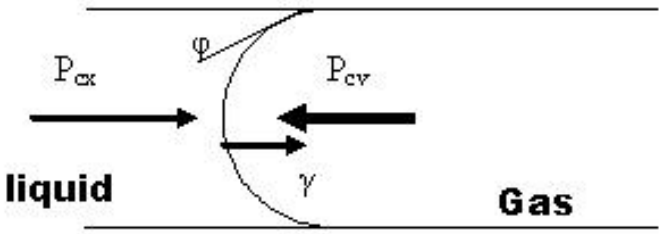

Figure 3.1: Diagram of forces on a curved meniscus

In common with cryoporometry freeze-thaw hysteresis, there is a hysteresis between the adsorption and desorption isotherms within a mesoporous material, due to the different mechanisms involved in the two processes. Adsorption begins at the wall of the pore and progresses toward the centre of the pore, and is generally assumed independent of the pore network. When the adsorbed gas layer is sufficiently thick that the gap between opposing layers is small enough, capillary condensation occurs within the pore. The gas adsorption within a pore can, therefore, be considered as starting at the pore wall and progressing radially into the core of the pore. In capillary condensation the gas-liquid meniscus travels along the axis of the pore to the pore surface where it eventually flattens with increasing pressure and the bulk gas becomes saturated. For desorption to occur a curved meniscus must re-form between the condensed liquid in the pore and the gas phase of the bulk, this requires a reduction in the bulk pressure. For a curved meniscus in equilibrium, the forces on either side must balance, as shown in Figure 3.1. The sum of pressure on the concave side of the meniscus, P_{cv}, is equal to the sum of the pressure on the convex side of the meniscus, P_{cx}, and the surface tension, therefore, $P_{cx} \leq P_{cv}$. This effect is greatest for a hemispherical meniscus, therefore, during desorption the pressure is reduced and the meniscus at the surface of the pore begins to curve until it reaches a hemispherical dome

protruding into the pore. The surface tension enables the pore to remain filled with liquid which is in equilibrium with the gas at pressures below it saturation pressure. After forming the meniscus, further decreases in pressure cause the adsorbent to evaporate according to the size of pore in which it is contained. This is similar to the freezing front penetrating the pore within cryoporometry. The pressure difference required to create the meniscus is also inversely proportional to the radius of the pore, according to equation 3.11. For ink-bottle style pores exposed to the bulk via smaller pores, the relative pressure required to form the meniscus is dominated by the outer pore, the adsorbed gas can only begin to evaporate when the pressure is sufficient to form a meniscus within the smaller outer pore, at which point the whole pore will empty. The desorption isotherm is, therefore, shifted toward the smaller pore sizes and subject to pore shielding effects (Rigby and Fletcher, 2004).

The surface area of the material may be determined by gas adsorption using the Brunauer, Emmett and Teller (BET) equation 3.12. The BET equation is applied to the start of the adsorption branch for relative pressure values typically between 0.05 and 0.35, when it is assumed that the adsorption of gas is building as a multilayer on the surface of the solid (Gregg and Sing, 1982).

$$\frac{p}{x(p_0 - p)} = \frac{1}{x_m c} + \frac{c-1}{x_m c}\frac{p}{p_0} \tag{3.12}$$

where x_m is the monolayer capacity and c is BET constant. x_m and c can be determined from the straight line plot of $\frac{p}{x(p_0-p)}$ against $\frac{p}{p_0}$, with slope, s and intercept, i , according to the simultaneous equations 3.13 and 3.14,

$$x_m = \frac{1}{s+i} \tag{3.13}$$

$$c = \frac{s}{i} + 1 \tag{3.14}$$

The monolayer capacity can be used to determine the specific surface area, S_a, according to the equation 3.15¶,

$$S_a = \frac{x_m}{22414} N_A A_m \times 10^{-20} \tag{3.15}$$

¶As expressed in Gregg and Sing (1982)

where S_a is the specific surface area of the solid in m^2g^{-1}, x_m is the monolayer capacity in cm^3 of adsorbate per gram of solid, N_A is Avagadro's constant (6.02×10^{23}), 22414 is the volume in cm^3 of 1 mole of gas at standard temperature and pressure (273.15K and 1 atm) and A_m is the molecular cross-sectional area of the adsorbate in Å ^{2}, which for nitrogen at 77 K is given as 16.2 Å^2 (Gregg and Sing, 1982).

3.2.4 Mercury porosimetry

Further to the theory explained in Chapter 2, a more in depth discussion of mercury porosimetry follows. Recent work (Rigby and Edler, 2002) has advocated the use of more refined equations relating pore size to applied pressure for mercury intrusion, equation 3.16 and extrusion, equation 3.17 in silica materials. Equations 3.16 and 3.17 are empirically derived from the Washburn equation, 2.6 (Rigby and Edler, 2002) and account for changes in contact angle and surface tension relative to pore radius, thus removing their contribution to the hysteresis (Rigby and Fletcher, 2004). The validity of pore radii for equations 3.16 and 3.17 are 6–99.75 nm and 4–68.5 nm respectively,

$$r_p = \frac{302.533 + \sqrt{91526.216 + 1.478p}}{p} \tag{3.16}$$

$$r_p = \frac{68.366 + \sqrt{4673.91 + 471.122p}}{p} \tag{3.17}$$

where r_p is the pore radius in nm and p is the pressure in MPa.

The causes of hysteresis between mercury intrusion and extrusion are relatively well understood (Rigby et al., 2002; Rigby and Edler, 2002; Rigby and Fletcher, 2004) it has been shown that hysteresis is dependent upon contact angle, surface tension and network structure (Rigby et al., 2002). Using equations 3.16 and 3.17 to remove contact angle and surface tension hysteresis, the resultant observed hysteresis is due to structural effects. One such effect is pore shielding, this occurs when larger internal pores are connected to the network or bulk by smaller pores, ie. pores so called 'ink-bottles'. For mercury to intrude into larger internal pores via connecting small pores, a greater applied pressure is required, therefore, the apparent volume of small pores is increased. During extrusion the applied pressure decreases and mercury extrudes from small external pores, however, pressure is not sufficiently low to allow extrusion from larger internal pores, the mercury

ganglion 'snaps' and mercury is retained within the larger pores. The mercury remains permanently entrapped within these pores. If the network structure is sufficiently disrupted by grinding the solid into a powder where the pieces are small enough that all of the larger pores are directly exposed to the outside surface, it is possible to remove these shielding effects (Rigby et al., 2002, 2008a). For the silica materials used here, pieces smaller than 30-40 μm are sufficient to remove these shielding effects.

3.2.5 Percolation theory

Percolation theory has previously been used to determine pore connectivity and study pore blocking effects seen in nitrogen sorption and mercury intrusion hysteresis of porous materials (Seaton, 1991; Murray et al., 1999). In this work the percolation theory described by Seaton (1991) has been adapted for use with the freezing curve data from cryoporometry experiments. If the pore network is considered as a lattice model of bonds and nodes, such that the pores are identified as bonds and the connections between pores as nodes, any porous network can be modelled as a lattice with a given number of bonds and nodes, see Figure 3.2.

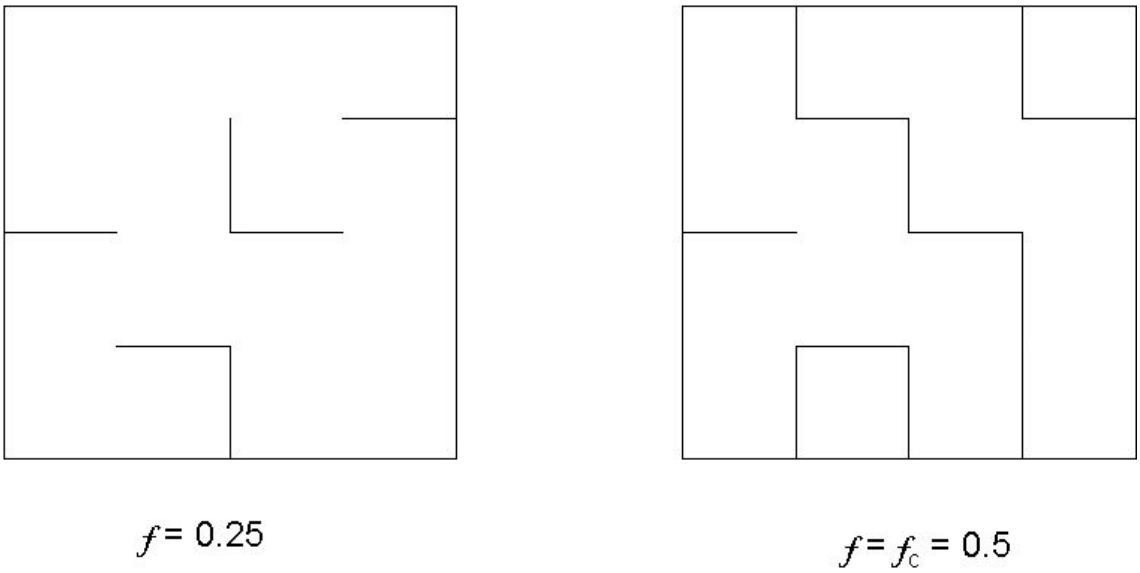

Figure 3.2: Diagram of lattice models

A lattice is described in terms of, L, an average linear dimension of the bond and, Z, the coordination number, i.e. the number of bonds that connect to one node. A percolation cluster is the term used to describe a network of bonds that provide a pathway for mass or energy to traverse from one side of the lattice to the other.

When describing percolation in a network, a bond may be described in three ways, unoccupied, occupied but not in the percolation cluster, and occupied within the percolation cluster. To describe the thermodynamic mechanism of freezing within a porous network, the three bond types are defined in terms of pore content as:

- An unoccupied pore contains liquid above it's freezing temperature, therefore, no progress of the freezing front is possible
- An occupied pore contains liquid below it's freezing temperature, therefore, the freezing front could progress along this bond, but it is not part of the percolation cluster and not in contact with the freezing front, the liquid contained cannot freeze
- An occupied bond within the percolation cluster is a pore containing solid (ice), the liquid is below its freezing point and in contact with the freezing front, thus, the contained liquid has frozen

Percolation theory states there is a critical value of occupied bonds that must exist for a percolation cluster to be formed, i.e. the fraction of occupied bonds, f, reaches a critical value, f_c, see Figure 3.2. The fraction of occupied bonds is equal to the probability of a bond being occupied. The probability, F, of a bond being part of the percolation cluster is related to the probability of a bond being occupied, f, as shown in equation 3.18,

$$L^{\frac{\beta}{\nu}} ZF = h[(Zf - \frac{3}{2})L^{\frac{1}{\nu}}] \tag{3.18}$$

where the critical exponents of β and ν are 0.41 and 0.88 respectively[‖].

In order to show that there is a penetrating freezing front which moves into and through the porous network from the bulk outside the freezing mechanism is modeled by percolation theory. To model the freezing of water in the pore network, it must be said that the liquid contained in a pore will only freeze if it is below it's freezing temperature and is in contact with the freezing front, i.e. it is an occupied bond that is part of the percolation cluster. The probability of a bond being occupied, f, is the ratio of number of occupied bonds to total number of bonds, equation 3.19. The probability of a bond being in the percolation cluster, F, is the ratio of the number of occupied bonds in the percolation cluster (pores containing ice) to the total number of bonds, equation 3.20,

$$f = \frac{N_b}{N_T} \tag{3.19}$$

[‖] As expressed in Seaton (1991)

$$F = \frac{N_f}{N_T} \tag{3.20}$$

where N_b is the number of pores below freezing point, N_T is the total number of pores and N_f is the number of pores frozen.

From cryoporometry freezing data for the powder sample of the macroscopically heterogeneous material, it is possible to calculate the probability of a bond being occupied, f, as shielding has been physically removed, freezing is determined by pore size. The powder melting curve, if adjusted for shape factor hysteresis assuming a cylindrical geometry (Petrov and Furo, 2006) may also be used to determine, f. The cryoporometry signal intensity, I, is directly proportional to the volume, V_i, of liquid contained in the pores, therefore, the number of molten pores, n_i, of a given diameter, d_i, can be determined according to equation 3.21,

$$n_i = \frac{V_i}{\frac{\pi}{4} d_i^2 l_i} \tag{3.21}$$

where l_i is the average pore length.

If l_i is assumed to be constant and independent of the pore diameter, it can be cancelled from numerator and denominator when calculating f and F. Once f and F have been calculated it is possible to estimate values of L and Z, using equation 3.18. If L is large and Z small, then a greater hysteresis can be seen than if L is small and Z is large.

3.3 Experimental

3.3.1 Materials

The silica pellets are commercially available sol-gel silicas, *s980a***, the pellets have pore sizes in the 5–10 nm range, with heterogeneous pore networks that include ink-bottle style pores (Rigby and Edler, 2002). As described earlier in Section 3.2.4 it is possible to break the pore network within the pellet and remove any shielding effects by breaking up the pellets into pieces smaller than 30–40 μm.

**Produced by Shell

3.3.2 Cryoporometry

The objective was to obtain freeze-thaw characteristics for whole and powdered samples of the model silica pellet with ink bottle geometry. Furthermore, a comparison of the whole and powder sample freeze-thaw cycles with nitrogen sorption and mercury porosimetry data was made. The experimental procedure for the cryoporometry method was improved from that already used within the literature, as described earlier in Chapter 2. The developments included an increased accuracy of sample temperature measurement and a reduction in the temperature gradient along the sample length.

The silica pellets used have a bimodal pore distribution with modal pore diameters of around 5 nm and 10 nm. For experiments on whole pellets, pellets were immersed in ultrapure water for at least 24 hours. Ultrapure water, of resistivity of 18 mΩ at 25 °C, was obtained from a millipore water purification system. After immersion, two pellets were removed and placed between two susceptibility plugs within a 5 mm outer diameter thin-walled NMR tube. The upper susceptibility plug had a coaxial hole of 1.1 mm diameter through which the thermocouple could be placed in direct contact with the top silica pellet.

Powdered samples were produced using 20–30 pellets which were ground by hand with a mortar and pestle. Powder grains were examined by light microscopy to determine their approximate size to be less than 30 μm, at which size, the pore network is sufficiently disrupted and all pores are exposed to the external surface (Rigby and Edler, 2002). This grinding procedure ensures that any shielding effects seen in whole pellet is removed from the powder sample. Powder samples were immersed for at least 24 hours in ultrapure water and dabbed gently on damp tissue to remove some excess bulk water. This was carried out to prevent the NMR tube from cracking during the freezing expansion of bulk water, however, a sufficient amount of bulk water remained as a nucleation point for freezing. A small plug of wet powder approximately 2 mm high was placed between two susceptibility plugs, within the NMR tube. The thermocouple was placed in contact with the top of the silica powder through the hole in the top susceptibility plug, and the top of the thermocouple was secured at the top of the NMR tube using blu-tak. The thermocouple temperature was recorded at 10 s intervals, by connecting it to a second temperature control unit and computer.

All NMR experiments were carried out on a Bruker Avance 400 MHz spectrometer with a static field strength of 9.4 T, yielding a resonance frequency of 400.13 MHz for ^1H nucleus. The BVT3200 temperature control unit within the NMR probe utilises a controlled flow of cool nitrogen gas evolved from liquid nitrogen in combination with a heating element below the sample in the gas flow stream. This system is able to adjust and maintain a temperature with $\pm$ 0.1 K accuracy in the range of 123–423 K. Preliminary experiments similar to those

described in Chapter 2 were carried out to determine appropriate experimental parameters: Temperature set point range of 271–265 K for freezing and 269–273 K for thawing and equilibration time of 20 minutes. A simple spin echo sequence is used in preference to the basic pulse-acquire sequence as it accounts for small magnetic field inhomogeneities that are present within the sample, therefore enhancing the quality of the signal obtained. An echo time of 10 ms, was used.

The temperature was step changed through a series of three freeze-thaw cycles. After each temperature change, the sample was allowed to equilibrate for 20 minutes before the acquisition was taken. Initially, samples were fast cooled until all the sample was frozen, then slowly warmed in steps, 0.5–2 K, until all of the pore water was molten, demonstrated by a plateau in signal intensity below the bulk freezing temperature. The sample was then slowly cooled and warmed twice more, before complete thawing on the last warming series. At each step change the signal intensity and sample temperature were recorded.

3.3.3 Cryodiffusometry experiments

Pulsed field gradient (PFG) experiments were conducted at points of equal signal intensity on the freezing curve for both whole and powder samples. By modification of the multiple temperature automated program to include a series of three PFG experiments at different temperatures during the freezing process it was possible to acquire data at equal signal intensities for both samples. At the pre-chosen temperatures PFG experiments were conducted after the spin echo acquisition. The pulse sequence used for PFG experiments was a pulsed field bipolar gradient stimulated echo with longitudinal eddy delay (PGSTE-BPLED), as discussed in Section 3.2.2. The experimental parameters used were diffusion time, Δ, of 0.15 s, gradient length, δ, of 0.002 s, a bipolar correction delay, τ, of 0.0001 s and a gradient field strength, g, of 0.674 to 32.030 G/cm. Each experiment had 8 data points collected, of 16 scans each. Signal attenuation was used to calculate the diffusion coefficient and comparative tortuosities of the molten water, as described in Section 3.2.2.

3.3.4 Nitrogen adsorption and mercury porosimetry

Nitrogen adsorption and mercury porosimetry data had previously been collected within the group using the following experimental procedure: Nitrogen adsorption measurements were taken using a Micromeritics ASAP 2400 apparatus, the sample was evacuated at 250 °C for 24 hours before adsorption and desorption isotherms were measured at 77 K. The sample was then allowed to reach room temperature, 298.9 K, before being transferred to the mercury porosimeter under a nitrogen atmosphere. Mercury porosimetry measurements

were taken using a Micromeritics Autopore IV 9420. The sample was evacuated to 6.7 Pa to remove physisorbed gases before measurements were taken. At each pressure change, equilibration times of 15 and 100 seconds were used, no significant differences of intruded volume were found between these times. Blank corrections to account for compressibility effects of the penetrometer were made as suggested by the manufacturer of the porosimeter. The materials retained structural integrity during these experiments.

3.4 Results and Discussion

3.4.1 Comparing hysteresis from different techniques

Method	**Sample**	**Hysteresis**	**Single pore**	**Pore shielding**	**Data**	**Percolation theory applicable**
N_2	whole	Yes	Yes	Yes	$V - P_r$	Yes
N_2	powder	Yes	Yes	No*	$V - P_r$	No
Hg	whole	Yes	No**	Yes	$V - P_a$	Yes
Hg	powder	No	No**	No*	$V - P_a$	Yes
Cryo	whole	Yes	Yes***	Yes	$I - T$	Yes
Cryo	powder	Yes	Yes***	No*	$I - T$	No

* Pore shielding effects are removed by breaking the whole pellet sample into a powder.
** Single pore hysteresis is present in mercury porosimetry in the form of contact angle and surface tension hysteresis, these effects are removed by applying equations 3.16 and 3.17.
*** Single pore hysteresis can be removed from cryoporometry data according to theory of Petrov and Furo (2006).

Key

N_2= Nitrogen adsorption desorption
Hg= Mercury intrusion and extrusion
Cryo= Cryoporometry freeze-thaw
V= Volume gas adsorbed or mercury intruded
P_r= Relative pressure
P_a= Pressure applied
I= NMR Signal intensity
T= Temperature

Table 3.1: Causes of hysteresis in porosimetry

In order to understand the causes of hysteresis in the cryoporometry freeze-thaw process, it is important to understand the mechanisms of hysteresis in the other techniques that are used for comparison. Table 3.1 provides a summary of the causes of hysteresis in the techniques used in this chapter, the experimental evidence of which is described in this section.

3.4.2 Cryoporometry Results

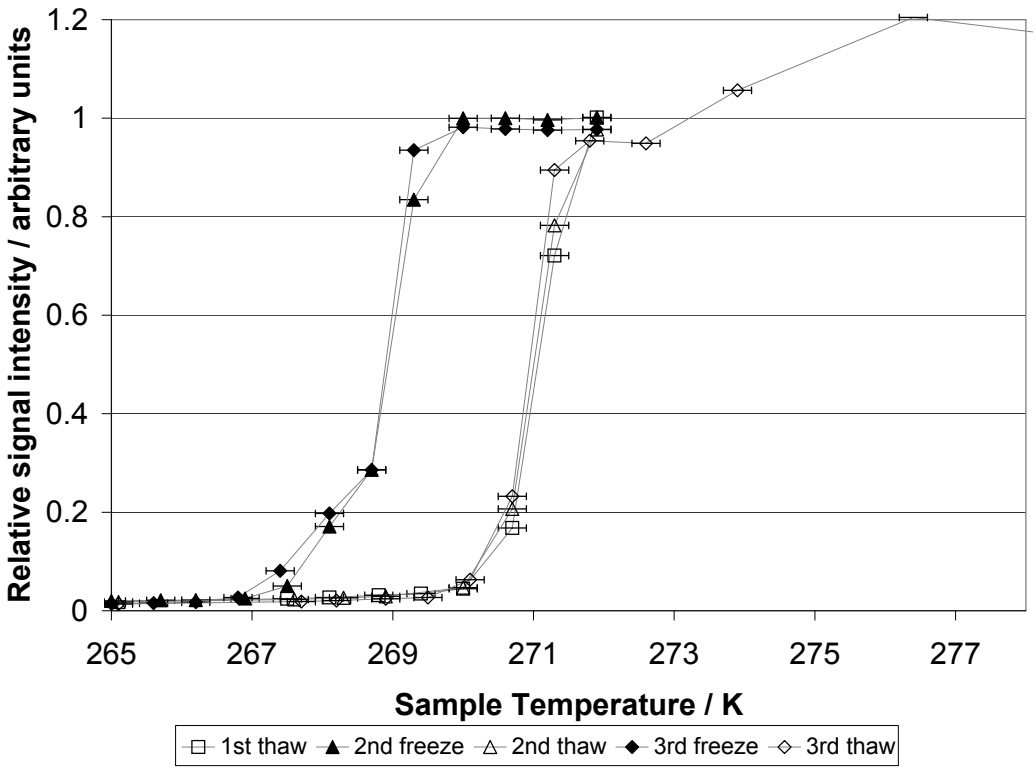

Figure 3.3: Two serial freeze-thaw cycles for whole silica pellet sample

Figure 3.3 shows two serial freeze-thaw cycles of a whole silica pellet sample, signal intensity is proportional to the volume of pores in the liquid phase at a given temperature. The lines connecting the data points in Figure 3.3 are included only as a guide. To remove the effect of the presence of bulk water, the signal intensity has been normalised to account for pore contained water only, a relative signal intensity of unity implies all pore water is in the liquid phase, and a relative signal intensity of zero, all pore water is in the solid phase. A relative signal intensity greater than one implies that bulk water is also in the liquid state.

On first cooling the sample from room temperature, super-cooling of the bulk water is seen, therefore the sample is frozen quickly in just three steps. The temperature at which

the super-cooled freezing of the bulk water occurs is sufficiently low that the imbibed water also freezes simultaneously with the bulk. As the sample is warmed the imbibed water begins to melt and the signal intensity observed increases, the signal intensity plateau below the bulk melting temperature is indicative that all imbibed water has melted and only the bulk water remains frozen. From this point the sample is cooled again to re-freeze the pore water, providing information on the freezing characteristics of the imbibed water, without the effect of supercooling in the bulk. The freeze-thaw hysteresis is observed, and the cycle repeated. On the third warming the sample is thawed completely. The second and third cycles overlay each other, within experimental uncertainty, therefore, it is observed that the freeze-thaw process does not destroy the pore structure and the cycle is repeatable.

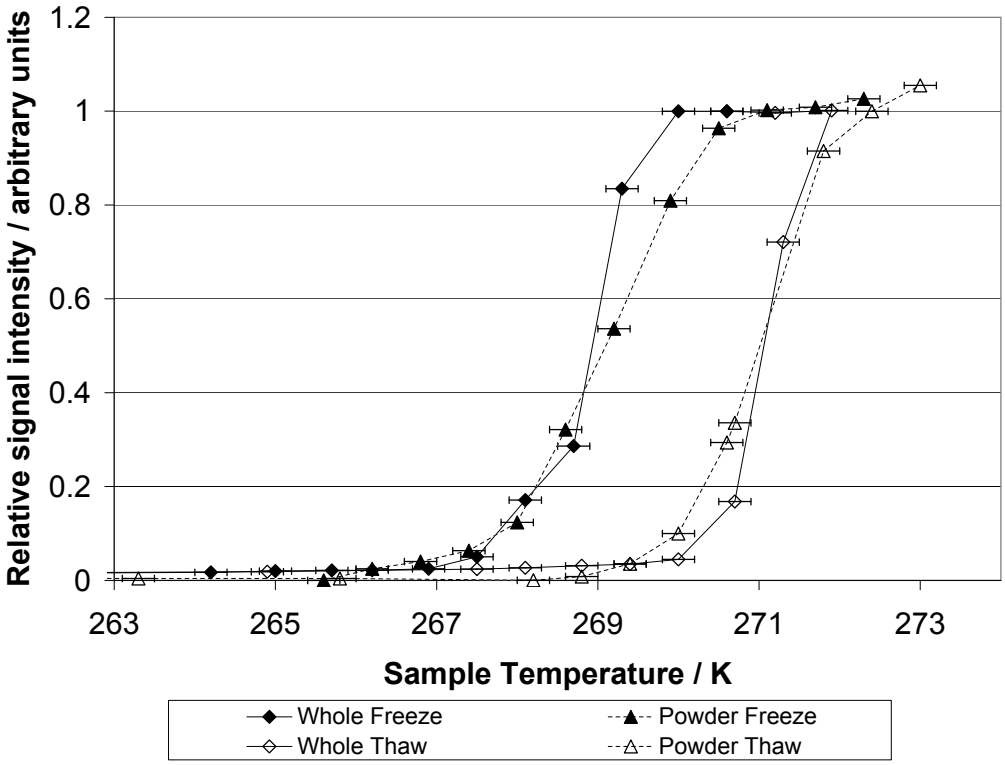

Figure 3.4: Freeze-thaw hysteresis for whole pellet and powdered silica sample A

Figures 3.4 and 3.5 shows the freeze-thaw hysteresis for both whole and powdered silica pellet for two independent samples, A and B. There are two key features to note from these results. Firstly there is no change, within experimental error, to the melting curve of the whole and powdered samples. Secondly, the freezing curve for the whole pellet sample shows an overestimation of the volume of the smaller pores than is shown by the powder sample, i.e. the upper section of the freezing curve for the whole pellet sample is shifted toward lower temperatures.

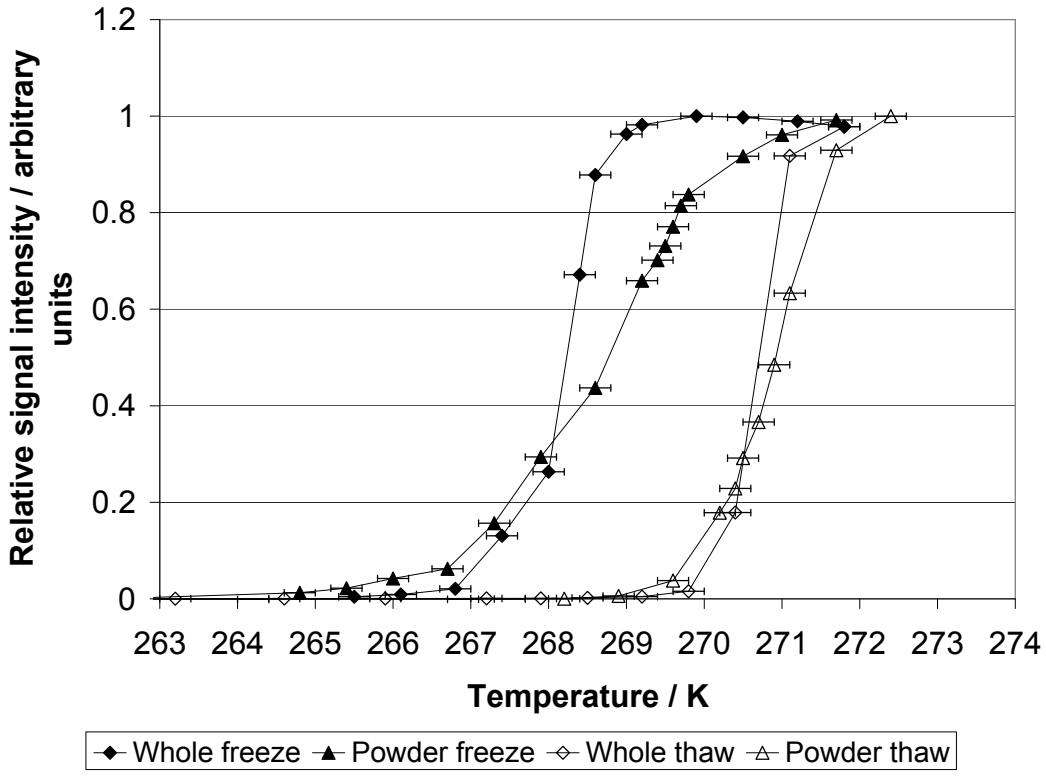

Figure 3.5: Freeze-thaw hysteresis for whole pellet and powdered silica sample B

If freeze-thaw hysteresis were due only to single pore hysteresis, then by applying the theory of Petrov and Furo (2006) described in Section 3.2.1, it should be possible to predict the freezing curve from the melting curve. The melting curve of either powder or whole pellet sample could, therefore, be used to predict the freezing curve that can be expected due to single pore hysteresis according to equation 3.1. If a cylindrical pore shape is assumed and the melting curve of the whole pellet sample is used to determine the expected freezing curve, the results can be seen in Figure 3.6. The estimated freezing curve for the whole pellet sample is in good agreement with the actual freezing curve of the powder sample, and showing some difference to the whole pellet freezing curve at larger pore sizes. This suggests that the freeze-thaw hysteresis for the whole pellet sample has more than one contributory factor. Close agreement between the estimated freezing curve and the actual powder freezing curve suggests that single pore effects alone, cause the hysteresis within the powder sample. The changes caused to the pore network arrangement within the powder sample have been shown previously to remove the shielding effects seen in gas adsorption and mercury porosimetry (Rigby et al., 2008a). By direct comparison to mercury porosimetry data the second cause of the freeze thaw hysteresis may be identified as predominantly pore shielding effects , it is, therefore, proposed that the freeze-thaw hysteresis for the whole

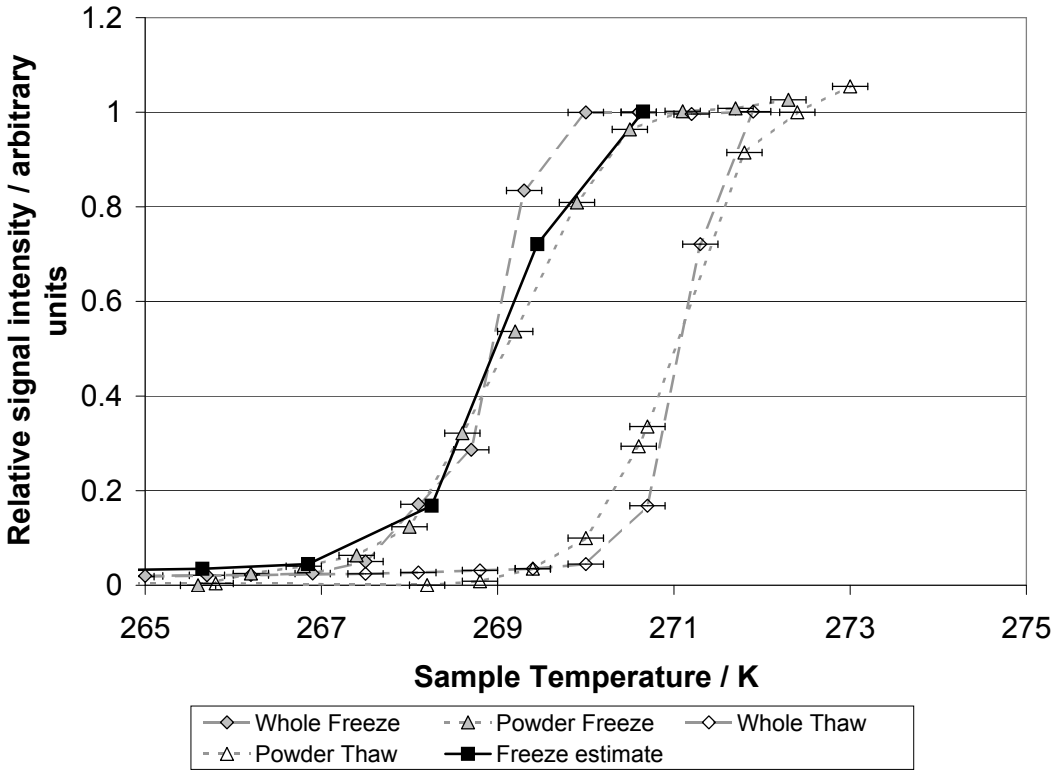

Figure 3.6: Estimated freezing curve due to single pore hysteresis for whole silica pellet sample

pellet sample is subject to both pore shielding effects on the propagation of a freezing front into the pore network and is a function of the single pore hysteresis as proposed by Petrov and Furo (2006).

3.4.3 Cryodiffusometry Results

PFG experiment results for whole pellet and powder silica samples were collected at similar relative signal intensities where a significant difference is seen in the freezing curve position for the two samples. The diffusion coefficient of the molten component of each sample was calculated from the gradient of the log attenuation plot, as described in Section 3.2.2. Figures 3.7 shows the log attenuation plot for a whole pellet sample, the diffusion coefficient for the molten fraction is given by the negative value of the gradient. The root mean square (rms) displacement of a molecule during the diffusion time for the whole pellet sample is around 20 μm, therefore, the fraction of molecules that may interact with the bulk ice at the surface of the 2-3 mm pellet is considered negligible.

PFG experiments on powder sample were conducted at two different diffusion times, 0.05 s and 0.15 s with rms displacements of around 9 and 12 μm respectively. The particle

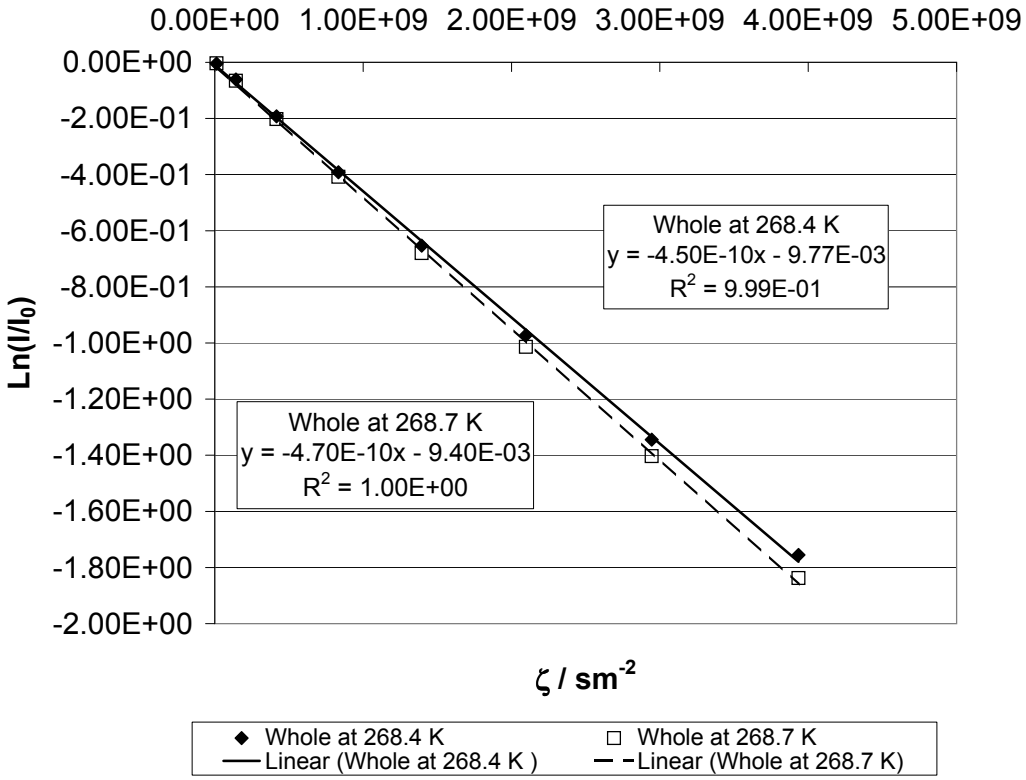

Figure 3.7: Log attenuation plot to estimate diffusion coefficient in part frozen whole silica pellet sample

size of the powder samples is of the order of 20 μm, therefore, the fraction of molecules that likely to interact with the bulk ice at the surface of the particles is significant and will affect the value of the diffusion coefficient observed. The log attenuation plots for these two experiments are given in Figures 3.8 and 3.9. The observed diffusion coefficients determined from these experiments are plotted against the square root of the diffusion time, as shown in Figure 3.10, to estimate the diffusion coefficient at zero observation time, the intra-particle diffusion coefficient, from the intercept in accordance with the theory of Mitra et al. (1993) described previously in Section 3.2.2.

The diffusion coefficients estimated for the whole and powder samples can then be used to determine tortuosity for each system. Any difference in the distribution of the ice pockets within the samples at equal relative signal intensities should be seen as a change in tortuosity between whole and powder samples. If ice pockets within the samples are distributed differently, the freezing mechanism of the two samples is different.

To calculate the tortuosity, the free diffusion coefficient at different temperatures must be known. The relationship between temperature and free diffusion coefficient for water above the bulk melting temperature can be found in the literature (Holz et al., 2000; Mills,

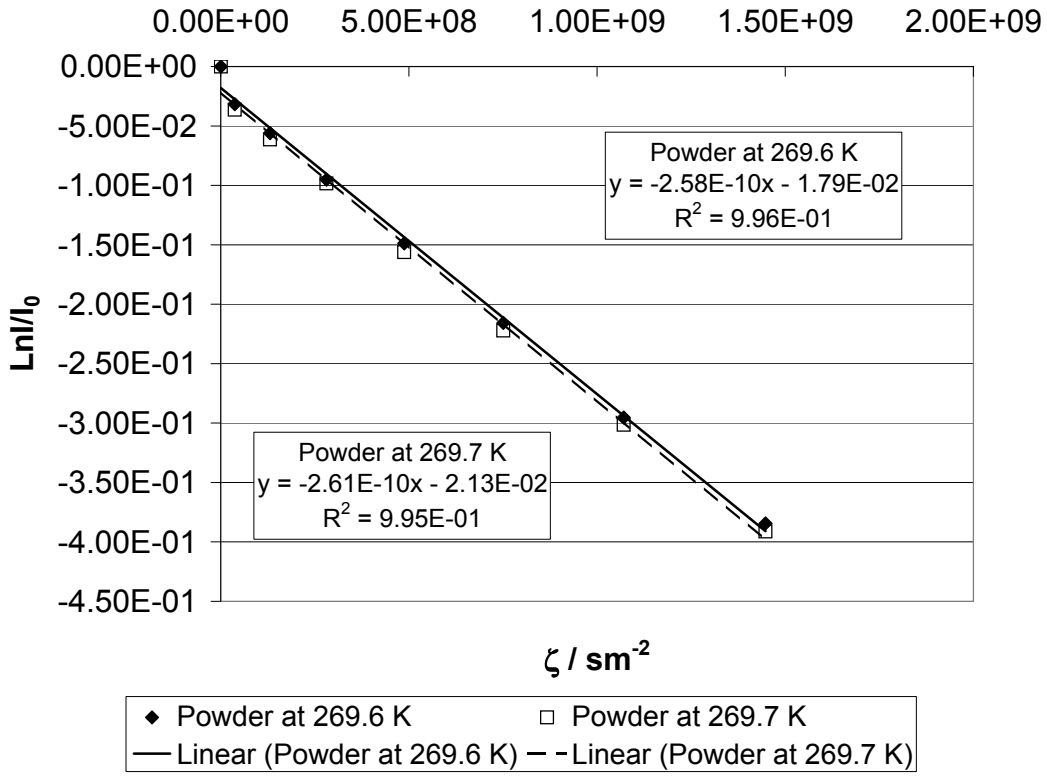

Figure 3.8: Log attenuation plot to estimate diffusion coefficient in part frozen powder silica pellet sample, diffusion time, Δ, 0.05 s

1973). To estimate the value of the free diffusion coefficient for water at temperatures below the bulk melting point, a model of diffusion coefficient as a function of temperature was found using literature data and extrapolated back to the temperatures of interest, as shown in Figure 3.11. The extrapolation extended 24 K below the lowest known value of diffusion coefficient, therefore, to estimate the level of expected error from the extrapolation a similar model was fitted to data that was 24 K above the lowest known value, this model was used to estimate diffusion coefficients of known values at lower temperature. The greatest error in this model, at lowest diffusion coefficient was found to be less than 3 %, providing confidence in the low temperature extrapolation of the model. A third order polynomial fit to all the data points in the literature, given by equation 3.22, was chosen as the low temperature model. This model showed good agreement with the ambient temperature model developed by Holz et al. (2000) to estimate the free diffusion coefficient based on temperature for the range 0–100 °C.

$$D_B = 6.98 \times 10^{-17} T^3 + 3.03 \times 10^{-13} T^2 - 1.42 \times 10^{-10} T + 1.59 \times 10^{-8} \qquad (3.22)$$

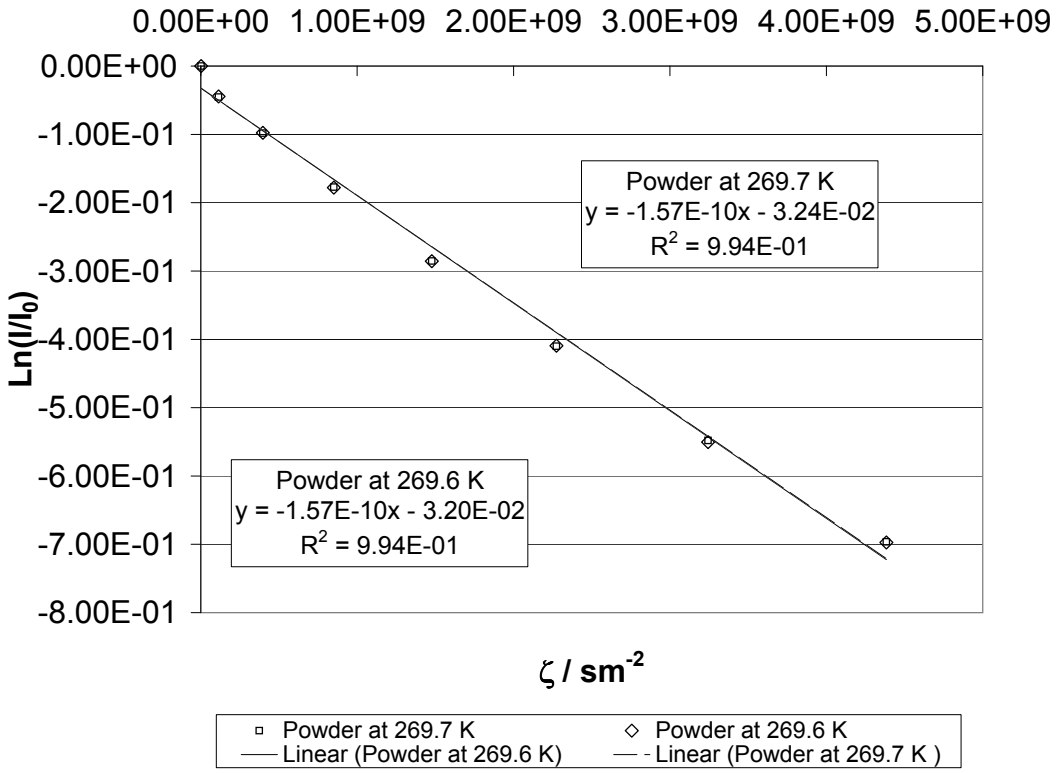

Figure 3.9: Log attenuation plot to estimate diffusion coefficient in part frozen powder silica pellet sample, diffusion time, Δ, 0.15 s

where D_B is the estimated bulk diffusion coefficient at a given temperature, T, K. The tortuosity values for whole and powder samples were calculated, according to equation 3.8, from the measured diffusion coefficients and the estimated free diffusion coefficient. A summary of calculated diffusion coefficients and tortuosities for whole and powder samples is presented in Table 3.2.

By linear interpolation of the diffusion coefficient for the whole pellet sample, between relative signal intensities of 0.67 and 0.88 the intra-particle tortuosity at a relative signal intensity of 0.75 is determined to be 2.10. This can be compared to that for the powder sample at a relative signal intensity of 0.75, which is 2.51. This suggests a difference in the spatial distribution of the molten liquid and frozen pockets of ice within the two samples.

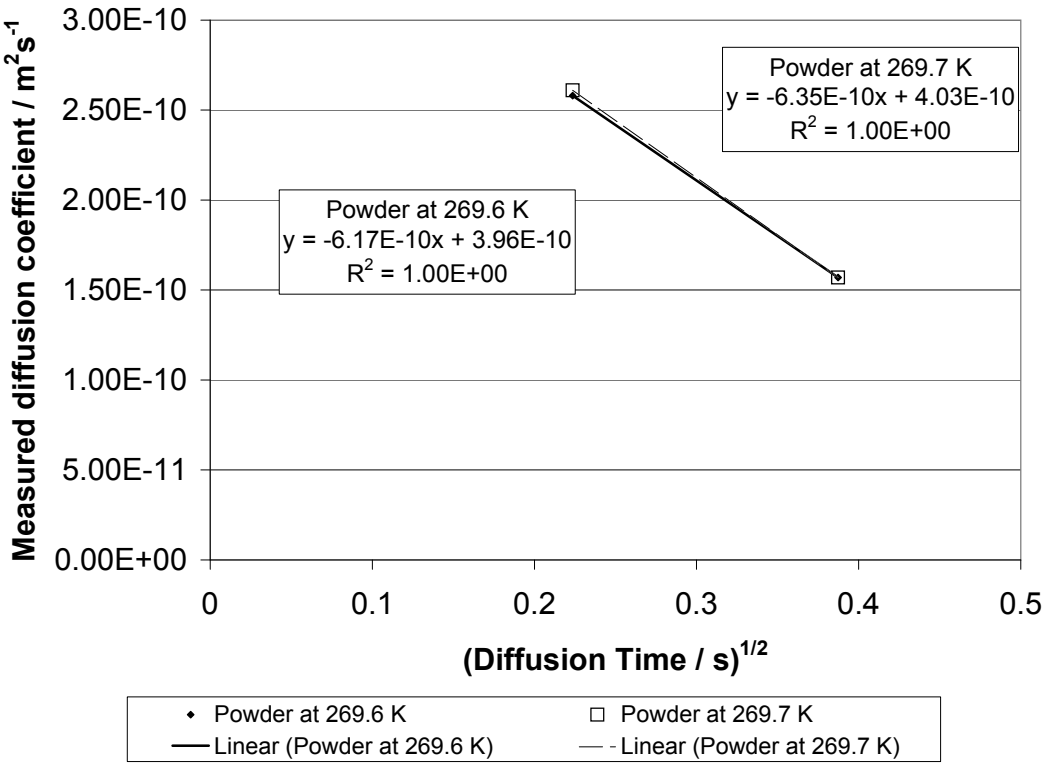

Figure 3.10: Plot of observed diffusion coefficient against square root of diffusion time used to calculate unrestricted intra-particle diffusion coefficient

Sample	T (K)	D_B	Δ (s)	Signal Intensity	D_{PFG}	rms displacement (μm)	Observed particle tortuosity τ_p	Intra-particle tortuosity τ_0
		$\times 10^{10} m^2 s^{-1}$			$\times 10^{10} m^2 s^{-1}$			
Whole	268.4	9.64	0.15	0.67	4.50	20.1	2.14	2.14
Whole	268.7	9.75	0.15	0.88	4.70	20.6	2.07	2.07
Powder	269.6	10.1	0.05	0.71	2.58	8.8	3.91	2.55
Powder	269.6	10.1	0.15	0.71	1.57	11.9	6.42	2.55
Powder	269.7	10.1	0.05	0.75	2.61	8.8	3.88	2.51
Powder	269.7	10.1	0.15	0.75	1.57	11.9	6.44	2.51

Table 3.2: Summary of calculated diffusion and tortuosity data for whole and powder silica pellet samples

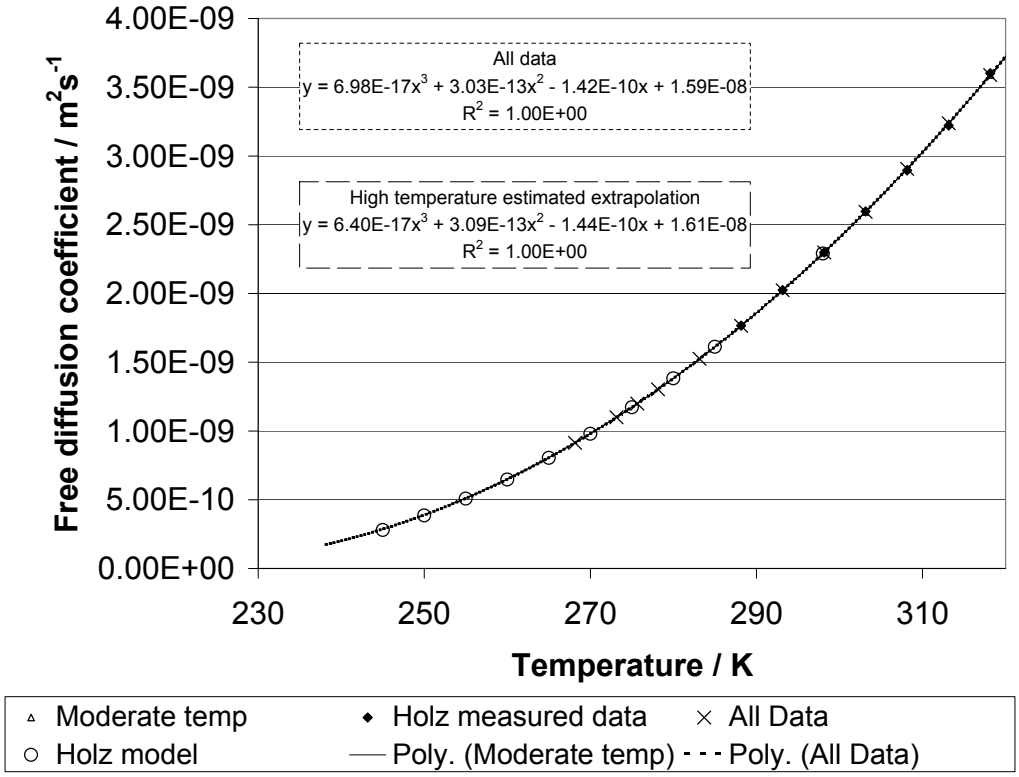

Figure 3.11: Diffusion coefficient as a function of temperature

3.4.4 Comparison with nitrogen adsorption-desorption

Nitrogen adsorption-desorption results previously collected within the group for whole and powdered silica pellets are shown in Figure 3.12 (Rigby et al., 2008b), the data is presented as the volume of gas adsorbed against the relative pressure. The relative pressure is related to the pore size according to the Kelvin equation 3.11. As described earlier in Section 3.2.3 the desorption isotherm is susceptible to pore shielding effects and, therefore, thought to be comparable to the freezing curve of cryoporometry. The powder sample desorption and freezing curves in Figures 3.12 and 3.4 show a similar shift toward higher temperature, or relative pressure, than the curves for the whole sample. The desorption curve for the powder sample has not only shifted, but the angle of the desorption knee has been smoothed, this shows desorption commencing at higher relative pressures which equates to larger pore sizes, and a broader pore size distribution. Both of these features are also seen in the freezing curve of the powder sample when compared to the whole pellet sample.

The hysteresis gap between adsorption and desorption for the powder sample has also become narrower, a feature synonymous with mercury porosimetry results when pore shielding factors have been removed. The remaining cause of hysteresis for the powder sample

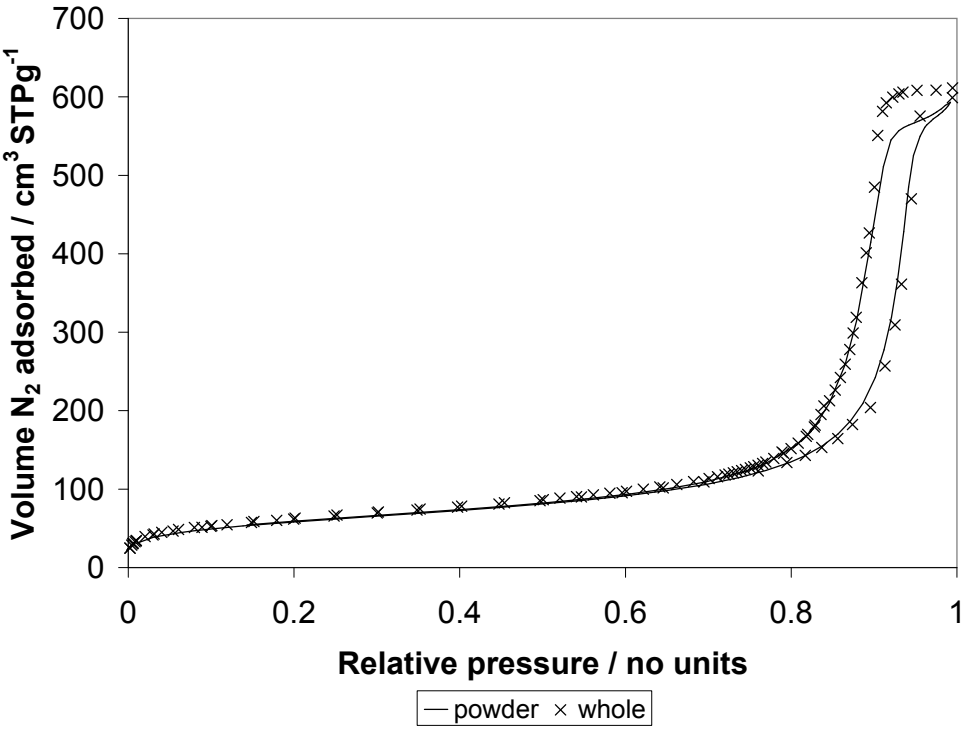

Figure 3.12: Nitrogen adsorption and desorption curves for whole and powder silica pellet samples

has been suggested to be single pore hysteresis (Rigby et al., 2008a), similar in nature to that in cryoporometry described by Petrov and Furo (2006). For gas sorption the single pore hysteresis can be described in terms of the difference in the mechanisms for adsorption and desorption. During the adsorption of gas the layers build from the pore wall toward the centre and condensation occurs, whereas during desorption the gas-liquid meniscus must form at the end of the pore and travel axially along the pore for evaporation to occur.

Adsorption of the monolayer and initial multilayers of gas are insensitive to spatial arrangement within the pore network, therefore, comparison of these regions for powder and whole pellet samples should show any changes to the pore network structure that may be the result of the grinding process. No significant difference was seen in the BET surface area for whole and powder samples, or in the multilayer adsorption region between 0.03 and 0.70 on the relative pressure scale, thus showing there was no significant change seen in the pore network as a result of the whole pellet being ground up.

3.4.5 Mercury porosimetry results

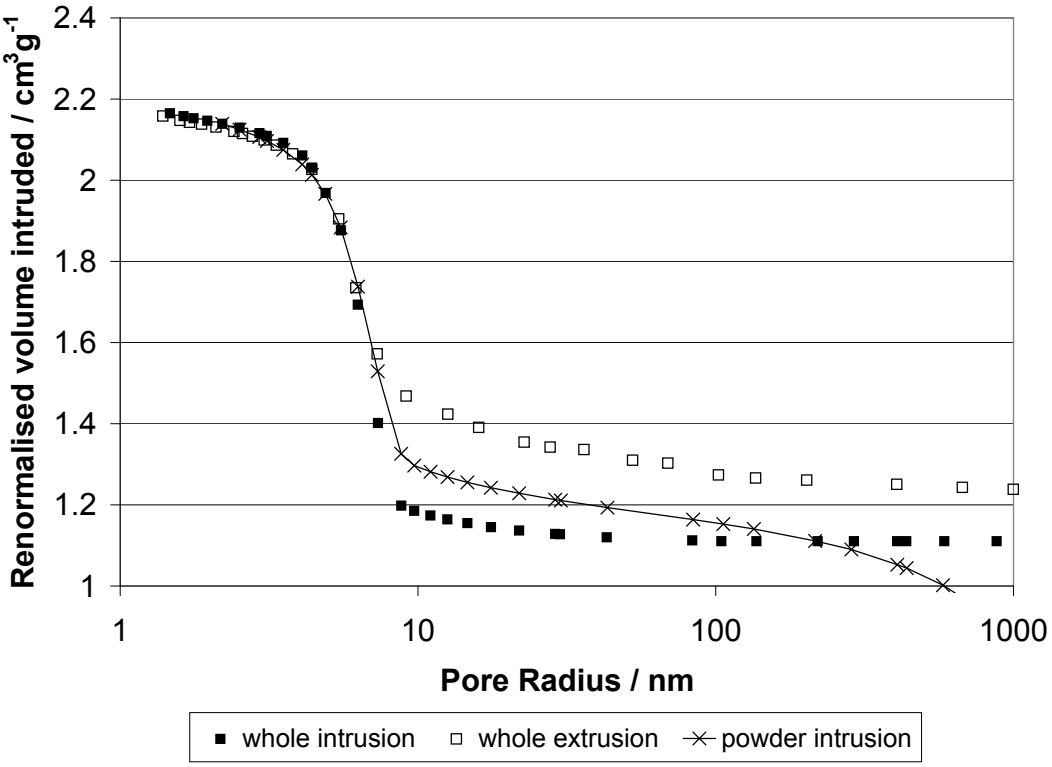

Figure 3.13: Mercury intrusion and extrusion curves for whole pellet silica and intrusion curve for and powdered silica

Mercury porosimetry data for whole and powder silica pellet samples had previously been collected within the group (Rigby and Edler, 2002) and is now compared with cryoporometry results collected in this work. Mercury porosimetry gives the volume of intruded mercury against the applied pressure, for both intrusion and extrusion curves. The applied pressure can be converted to an equivalent pore radius using equations 3.16 and 3.17. The volume intruded for the whole pellet sample was renormalised to account for intra-particle intrusion within the powder sample, to enable a direct comparison of the whole and powder sample results. Figure 3.13 shows the whole intrusion and extrusion curves and powder intrusion curve as a function of pore radius. Renormalized intrusion and extrusion volumes for the powder sample are shown in Figure 3.14. The powder intrusion and extrusion curves are in good agreement with each other, showing no hysteresis. The hysteresis seen for the whole pellet intrusion-extrusion is not conserved within the powder sample data, therefore, it is suggested that the hysteresis seen in the whole pellet sample is a consequence of pore shielding, and is removed by breaking up the pore network and opening all pores to the surface of the material. Contact angle and surface tension hysteresis often seen in mercury

porosimetry have been accurately discounted by the application of equations 3.16 and 3.17.

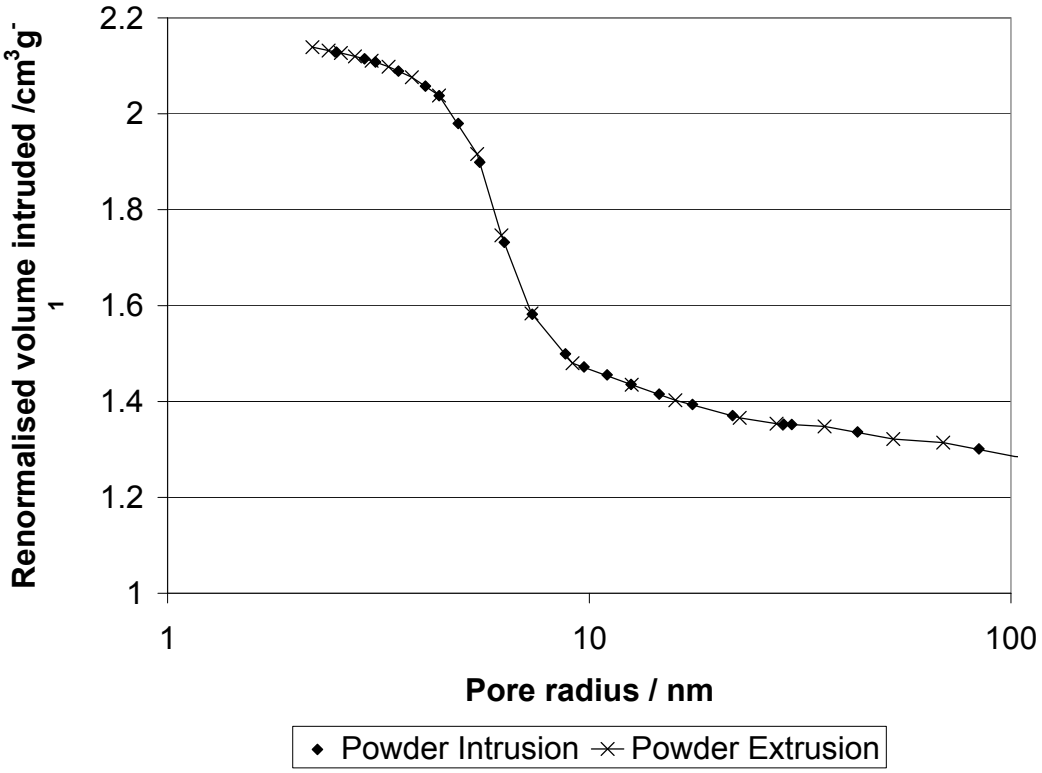

Figure 3.14: Mercury intrusion and extrusion curves for powdered silica

3.4.6 Prediction of Gibbs-Thomson parameter using powder mercury intrusion and freezing curves

To calibrate the Gibbs-Thomson parameter for this system, the powder sample intrusion curve and powder freezing curve are compared, the powder curves provide data that is not influenced by pore shielding effects. To compare the two data sets they are plotted on the same axes, renormalised volume intruded or frozen against pore radius. From mercury intrusion data, the pore radius can be calculated from equation 3.16 and renormalised volume, V_N is calculated in terms of the total volume intruded, V_0, according to equation 3.23, where V is the volume of mercury intruded at a given pore size.

$$V_N = 1 - \frac{V}{V_0} \tag{3.23}$$

From the cryoporometry freezing curve the renormalised volume V_N can be calculated as a function of relative signal intensity I and the total signal intensity I_0, equation 3.24.

$$V_N = \frac{I}{I_0} \tag{3.24}$$

The freezing point depression is related to melting point depression according to equation 3.1 where $\frac{2\kappa V}{S}$ is $\frac{1}{2}$ for open-ended cylindrical pores (Petrov and Furo, 2006). At each temperature point of the cryoporometry freezing curve, an equivalent melting point depression is calculated, the melting point depression is then related to the pore radius according to equation 3.2, which rearranged, gives 3.25.

$$r_p = \frac{k_{GT}}{2\Delta T_m} + t \tag{3.25}$$

By changing the values of k_{GT} and t in equation 3.25 it is possible to fit the cryoporometry freezing data directly onto the mercury intrusion data for the powder silica sample, as shown in Figure 3.15. The values of k_{GT} and t are found to be 24 nmK and 0.4 nm respectively, in agreement with values found in the literature (Schmidt et al., 1995; Vargas-Florencia et al., 2007).

The sensitivity of the fit to the estimated values of k_{GT} and t can be seen in Figure 3.16. The fit of the model to the data is most sensitive to k_{GT}.

The pore size distribution for freezing and thawing curves can now be estimated by substituting the Gibbs-Thomson parameters into equation 3.4. The pore size distribution estimates from the freezing and thawing curves for whole and powder samples are shown in Figure 3.17. Also shown in Figure 3.17 are the adjusted freezing pore size distribution, with single pore hysteresis effect removed (Petrov and Furo, 2006). The modal pore size for the freezing curve is smaller than that for the thawing curve, and the width of the pore size distribution is also narrower for the freezing curve estimates. If single pore hysteresis effects are removed, the adjusted freezing pore size distributions for the powder sample has the same range as the thawing curve, 18.5–5.9 nm, but a bimodal distribution with peaks at 12.9 nm and 8.9 nm, compared to a unimodal distribution peaking at 11.6 nm for actual thawing. For the whole pellet sample, the adjusted freezing pore size distribution has a smaller range than the thawing curve, 15.6–7.3 nm compared to 18.1–8.3 nm and also shows a bimodal distribution with peaks at 11.2 nm and 8.9 nm compared to the unimodal

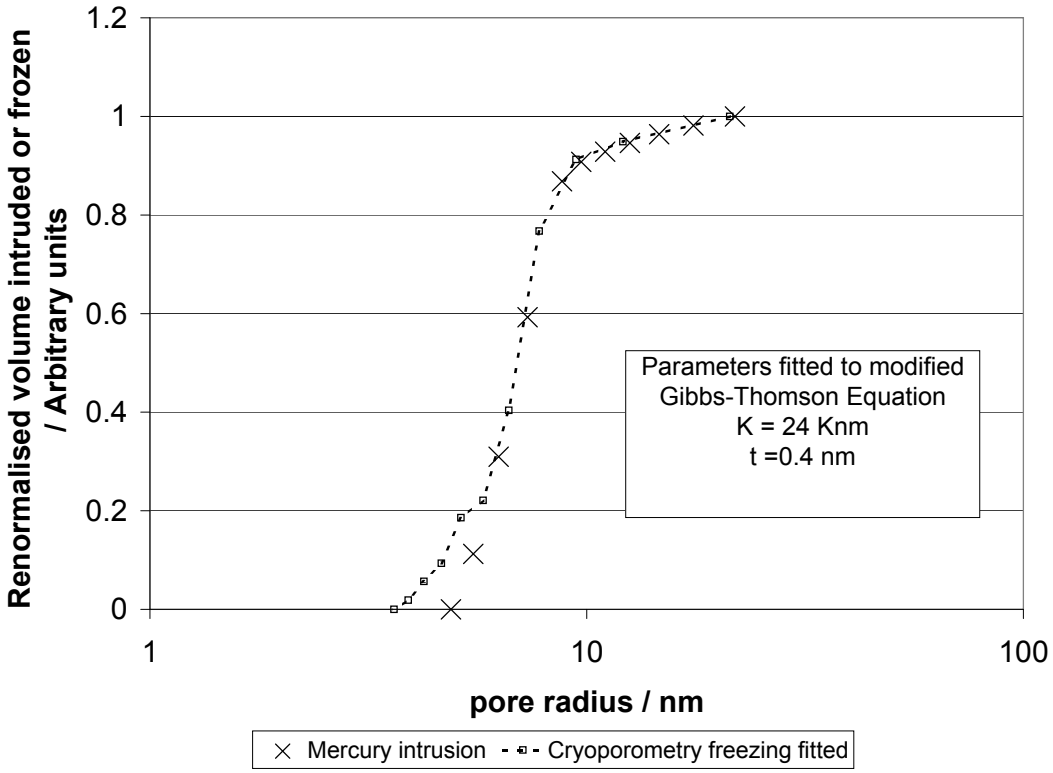

Figure 3.15: Mercury intrusion and fitted freezing curve for powdered silica

thawing curve peak at 13.4 nm, which is still significantly larger than those of the freezing curve.

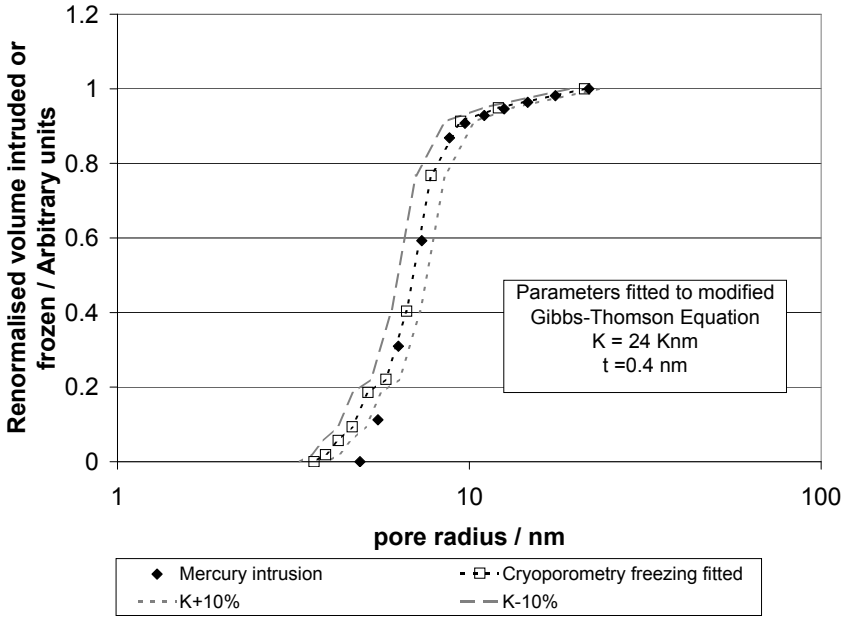

(a) Sensitivity to k_{GT}

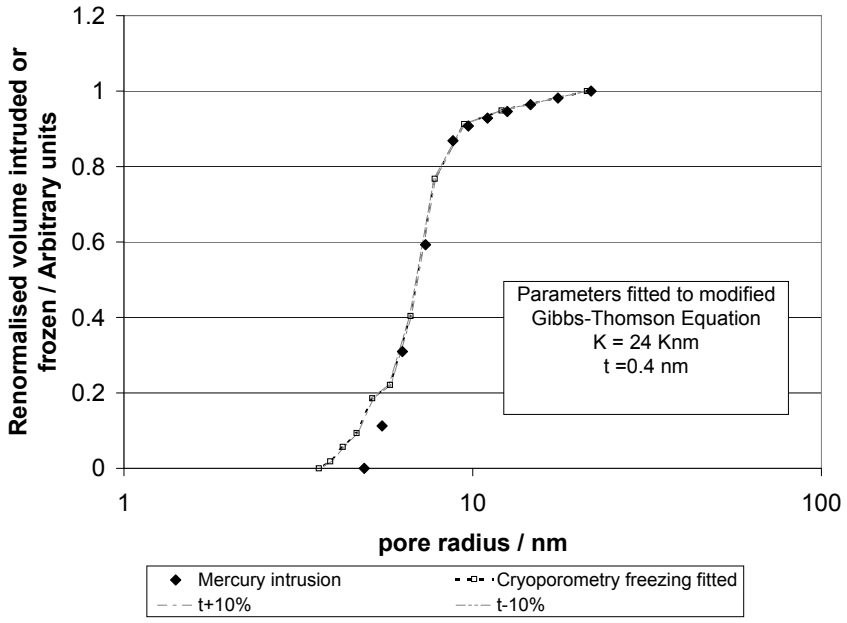

(b) Sensitivity to t

Figure 3.16: Mercury intrusion and fitted freezing curve sensitivity of k_{GT} and t values

3.4.7 Prediction of whole pellet freezing curve from whole pellet mercury intrusion data

From the hysteresis relationships shown in Table 3.1, it is possible to predict the cryoporometry freezing curve for the whole pellet sample, using mercury intrusion data, for

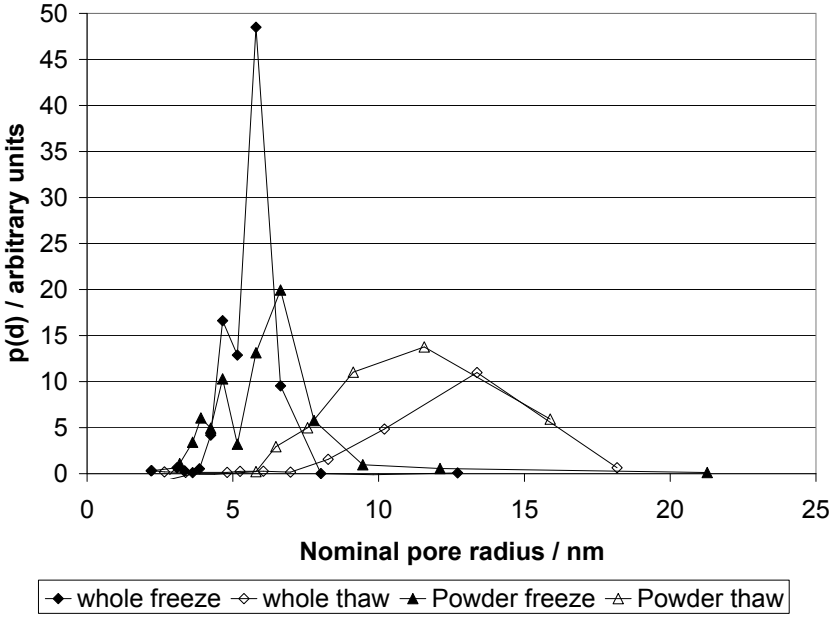

(a) Freeze-thaw data

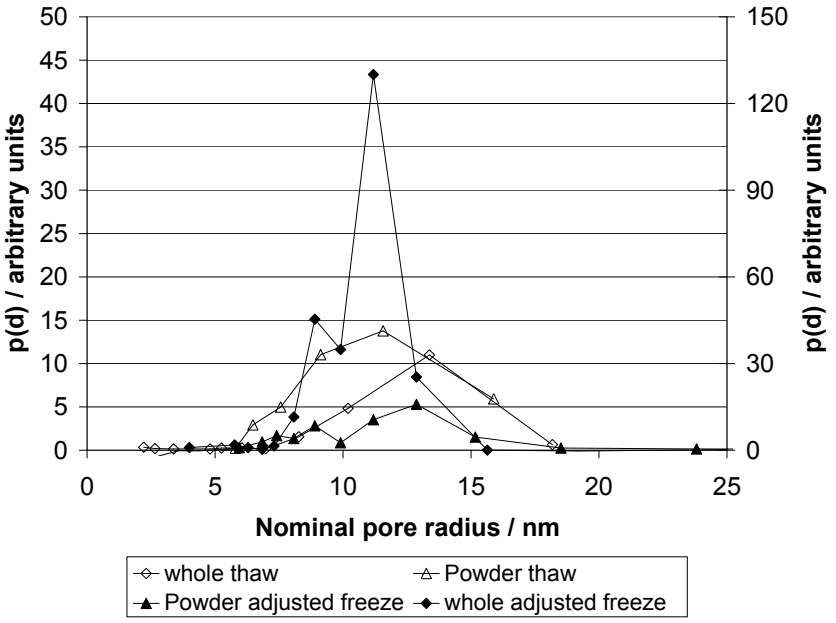

(b) Adjusted freeze-thaw data

Figure 3.17: Pore size distributions determined from freezing and thawing curve data for whole pellet and powder samples

both powder and whole samples and the cryoporometry freezing data for the powder sample. A comparison of the powder freezing curve and powder intrusion curve can be used to account for the single pore hysteresis seen in cryoporometry and not seen in the analysed mercury intrusion data. The whole pellet mercury intrusion data, affected by pore shielding

hysteresis, can then be used to estimate the additional hysteresis caused by pore shielding that is seen in the whole pellet freezing curve and not in the powder. The following steps are used to estimate the whole pellet freezing curve:

i Powder freezing curve data is modelled to define the freezing point depression as a function of the signal intensity, $\Delta T_f = f(I)$, equation 3.26. The shielding effects have been removed from powder data, but single pore hysteresis is still present. This model relationship, therefore, accounts for single pore hysteresis effects when calculating ΔT_f from I,

$$\Delta T_f = \frac{A(1-I)}{1+B(1-I)} + C \tag{3.26}$$

where A, B and C are fitting parameters.

ii Powder intrusion curve data is modelled to define the signal intensity (or volume intruded) as a function of the pore radius, $I = f(r)$, equation 3.27. Mercury intrusion data for the powdered sample shows no hysteresis, therefore, the relationship is required only to estimate the expected signal intensity in a cryoporometry freezing curve as a function of pore radius from the mercury intrusion data,

$$I = \frac{D(r+G)}{1+E(r+G)} + F(r+G) \tag{3.27}$$

where D, E, F and G are fitting parameters.

Together these two relationships are used to estimate the cryoporometry freezing point depressions expected at a given pore radius from mercury intrusion data, where single pore hysteresis effects apply in cryoporometry freezing mechanism, but not in mercury intrusion.

iii The whole pellet sample suffers from shielding effect hysteresis, this is true in both mercury intrusion and cryoporometry freezing data. The whole pellet mercury intrusion data is, therefore, used to predict the freezing curve for the whole pellet. Using the relationships $\Delta T_f = f(I)$ and $I = f(r)$ described above, mercury intrusion data with no single pore hysteresis can be converted into cryoporometry data that is subject to single pore hysteresis. Mercury intrusion data for the whole pellet sample inherently includes pore shielding hysteresis, which is carried through to the estimate of the whole pellet freezing curve.

Parameter	Value
A	29.2947
B	9.1217
C	1.1393
D	3.2541
E	3.6564
F	7.7914×10^{-4}
G	-6.7775

Table 3.3: Model parameter values for predicting cryoporometry freezing curve

The fitting parameters used in equations 3.26 and 3.27 are given in Table 3.3, and the predicted whole pellet freezing curve is shown on Figure 3.18. Actual freezing curves for whole and powdered samples are also shown with the predicted freezing curve for the whole pellet sample lying between the actual freezing curves of the powder and whole pellet samples.

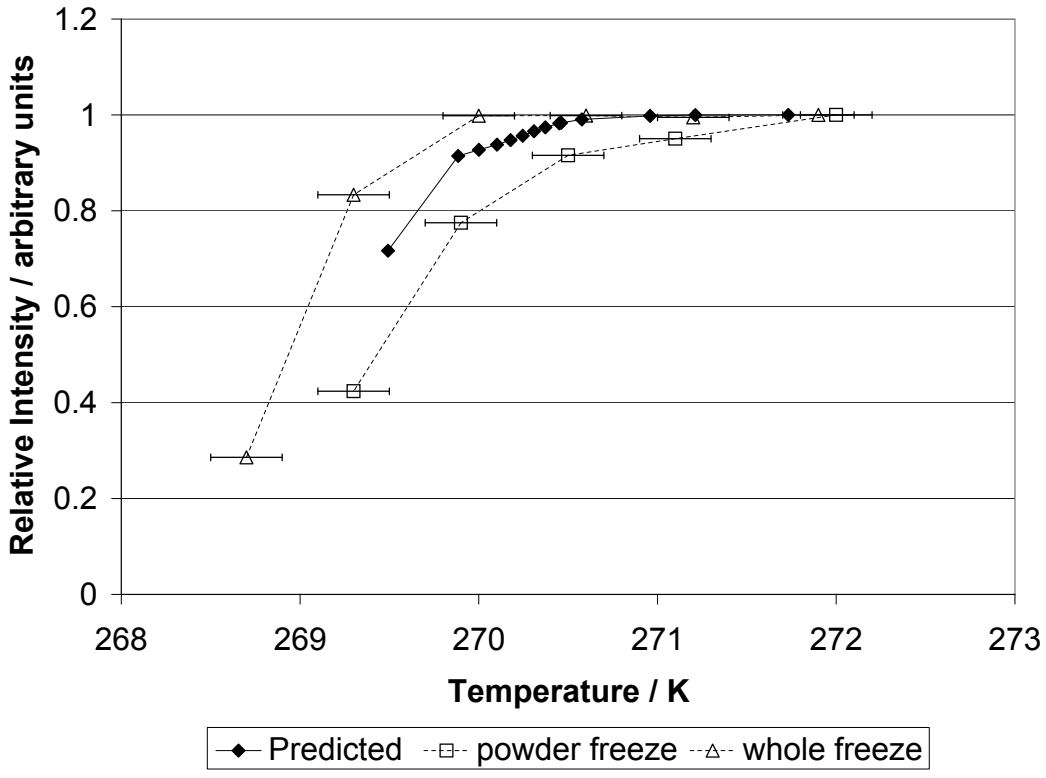

Figure 3.18: Whole pellet freezing curve predicted from mercury intrusion model

3.4.8 Percolation Analysis

The freezing mechanism for imbibed liquid within porous material has now been shown to suffer from shielding effects as seen for mercury porosimetry and nitrogen adsorption. Percolation theory may, therefore, be applied to the propagation of the freezing front in cryoporometry synonymously with the intrusion of mercury and desorption of nitrogen (Murray et al., 1999). The theory outlined in Section 3.2.5 is applied to cryoporometry data, to determine the percolation parameters L and Z, the characteristic length of a bond and the co-ordination number. Firstly, the powder freezing curve was used to determine the probability of a bond being occupied (pore containing water below its freezing point) at any given temperature using the modified Gibbs-Thomson equation 3.2. Accordingly, a layer of water at the pore wall does not freeze, and integral intensities are indicative of the core radius, r_c. For each point on the freezing curve, an equivalent core radius can be determined by equation 3.28, the pore radius, r_p, can then be calculated using the core radius and thickness of the unfrozen layer, t, equation 3.29,

$$r_c = \frac{k_{GT}}{\Delta T_m} \tag{3.28}$$

$$r_p = r_c + t \tag{3.29}$$

The change in integral signal intensity, dI is proportional to the volume of 'cores' that have frozen, V_c, therefore, to calculate the pore volume frozen, V_p, at each temperature an adjustment factor is required, equation 3.30,

$$dV_p = dI \frac{(r_p^U + r_p^L)^2}{(r_c^U + r_c^L)^2} \tag{3.30}$$

where the superscripts U and L represent the upper and lower estimate of radius for the change in temperature that induces a change in signal intensity, subscripts p and c represent pore and core attributes respectively.

To convert the volume change of frozen pores into a change in the number of frozen pores, N_p, an average pore radius, $r_{p,ave}$, for each increment is calculated using equation 3.31.

$$r_{p,ave} = \frac{r_p^U + r_p^L}{2} \tag{3.31}$$

The number of pores that have frozen in the powder sample is equivalent to the number of pores containing water below its freezing point at a given temperature for the whole pellet sample, N_b, and is determined using equation 3.32

$$N_p = \frac{dVp}{(r_{p,ave})^2} = N_b \tag{3.32}$$

The cumulative values of the number of pores below their freezing point at decreasing temperature is equivalent to the probability, f, of a bond being occupied at a given temperature T. From the definition of f and F in equations 3.19 and 3.20, it follows that the ratio of $\frac{F}{f}$ can be determined in terms of the difference in signal intensity at a given temperature between the whole, I_w, and powdered sample, I_p, as given in equation 3.33,

$$\frac{F}{f} = \frac{N_f}{N_b} = \frac{1 - I_w}{1 - I_p} \tag{3.33}$$

The probability, F, that a pore has frozen, i.e. is below its freezing point and in the percolation cluster can be determined by equation 3.34,

$$F = \frac{F}{f} \times f \tag{3.34}$$

A plot of F against f is shown in Figure 3.19, if no percolation effect were present F would be equal to f for all values of F, as indicated by the solid line. However, the data points plotted show, in accordance with theory, that below a certain value of f, f_c, then f is less than F, and above f_c, the percolation threshold, then f is equal to F. From Figure 3.19, f_c is approximately 0.3.

A plot of $L^{\frac{\beta}{\nu}}ZF$ against $(Zf - \frac{3}{2})L^{\frac{1}{\nu}}$ is fitted to the generalised function given by Seaton (1991) and is shown in Figure 3.20. The values of L and Z estimated by this fit are 9 and 3.8 respectively.

It has previously been show that the application of percolation theory is appropriate to nitrogen desorption and mercury intrusion for sol-gel silica materials, and the mechanisms for these processes are controlled by pore blocking (Rigby and Fletcher, 2004,a). Here, a comparison of whole pellet and powdered pellet sample freezing curves are used as a means to determine the type of nucleation that dominates the freezing mechanism. No difference in the freezing curve of the whole and powdered samples would be indicative of purely homogeneous nucleation, this type of nucleation is independent of the arrangement of pores

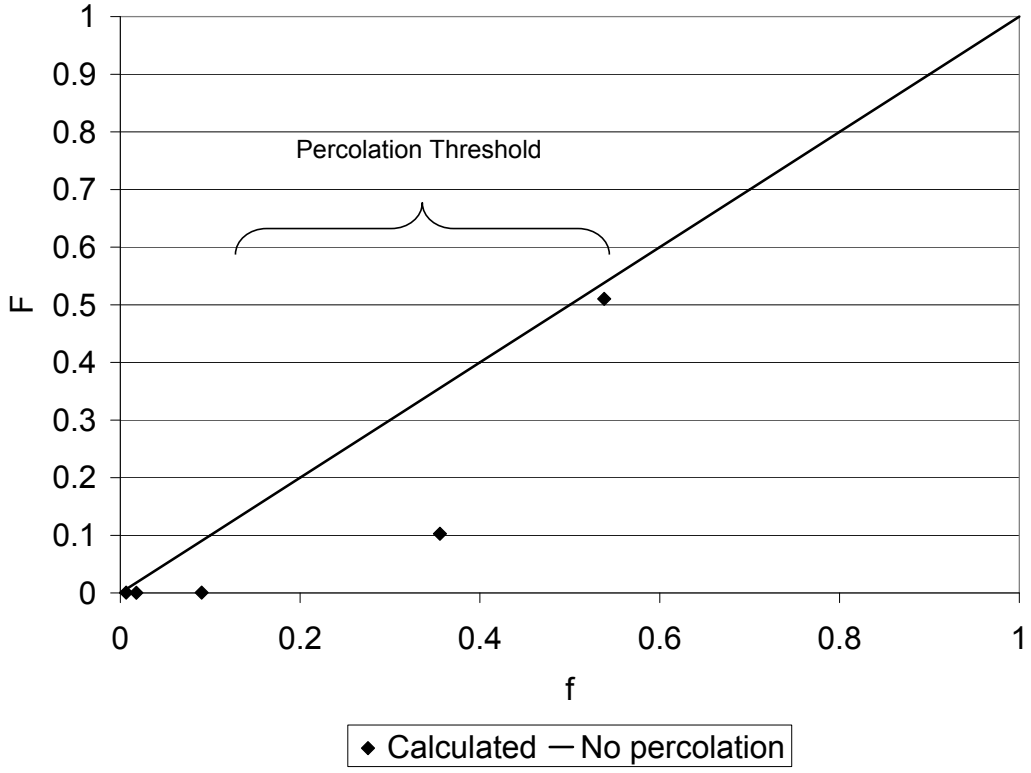

Figure 3.19: Probability of a pore being frozen and in the percolation cluster against the probability that a pore being frozen

within the network. A combination of homogeneous and heterogeneous nucleation would give a freeze-thaw hysteresis that was significantly more narrow than that observed for the mercury intrusion-extrusion of a whole pellet sample, where the hysteresis is dominated by pore blocking effects. As neither of these conditions apply here, this suggests the freezing mechanism in the sol-gel silica material is dominated by heterogeneous nucleation. Percolation theory may, therefore, be justly applied to the freezing mechanism of the imbibed liquid within this material.

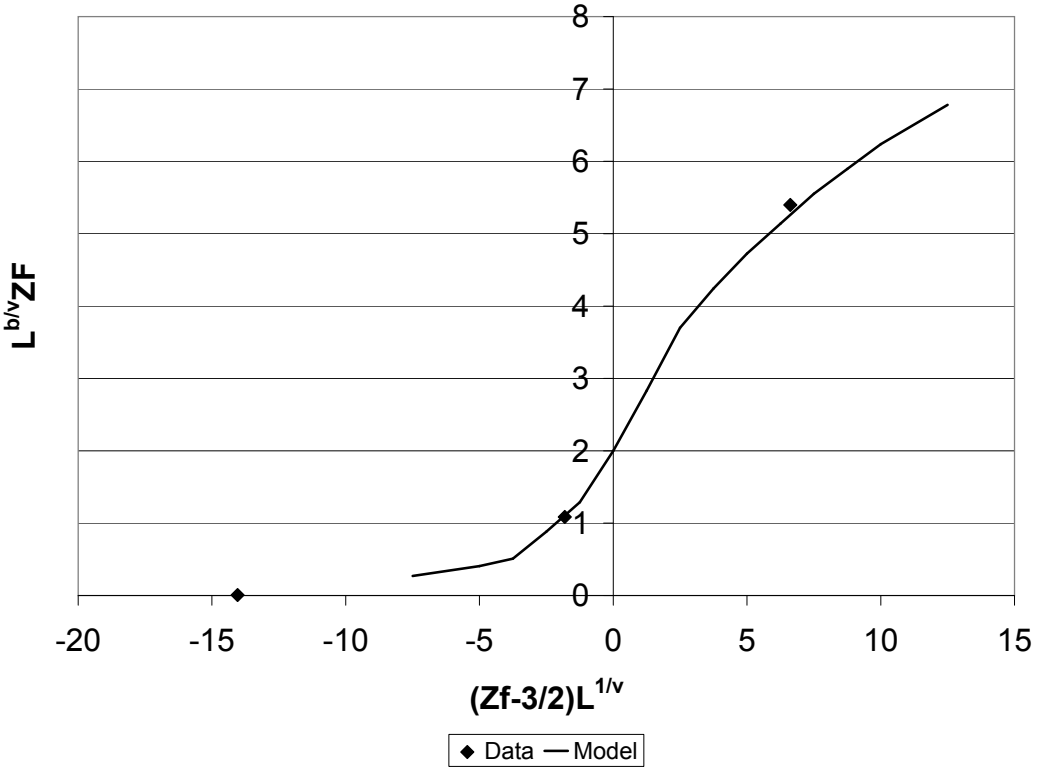

Figure 3.20: Percolation model fit to experimentally derived data

3.5 Conclusions

The robust cryoporometry experimental method developed in Chapter 2 has been used to show that a freeze-thaw hysteresis exists between the freezing and thawing process of an imbibed liquid in a porous silica material. This hysteresis is reproducible once supercooling effects have been removed, this is achieved by ensuring the bulk solution remains frozen during the cycle of freezing and thawing of the imbibed liquid. The repeatability of the freezing and thawing curves prove that the material is not damaged or altered by the freeze-thaw process and provides an opportunity to use the freezing data to gain additional pore characteristic information.

Cryodiffusometry results for part frozen powder and whole pellet samples have shown a change in the tortuosity at equivalent fractions of imbibed ice and molten water, therefore, suggesting a difference in the distribution of molten and solid water regions for the two samples. This provides evidence that the mechanism by which the imbibed water freezes is different in the powder and whole pellet sample, where the pore shielding effects have been removed in the powder sample. The causes of the freeze-thaw hysteresis are, therefore, different for the shielded and unshielded pore network.

Comparison with mercury porosimetry data has shown cryoporometry freeze-thaw hysteresis to be the result of both single pore hysteresis and pore shielding effects. With analysis of whole pellet and ground powder samples of the silica material it has been possible to remove the pore shielding contribution of the hysteresis in both mercury porosimetry and cryoporometry enabling the confirmation of the cylindrical single pore hysteresis model for the freezing mechanism as suitable to be applied to this material (Petrov and Furo, 2006). The Gibbs-Thomson parameter has been estimated for this system and is in agreement with values in the literature for similar systems.

The mechanism for freezing of imbibed liquid has been shown to be affected by pore shielding in a similar way to that of gas desorption and mercury intrusion, it is, therefore, suggested that the freezing of the imbibed liquid occurs as a freezing front that penetrates the pore network from outside of the material. Using mercury intrusion data an estimated freezing curve for the whole pellet sample has been derived. This predicted curve is found to lie between the actual freezing curve for powder and whole pellet samples. The pore shielding effects seen for whole pellet samples suggest that the freezing curve is, therefore, indicative of the size of the pore entrances, or necks, whilst the melting curve is indicative of the actual pore body size.

It has also been shown that it is possible to apply percolation theory to the penetration of the freezing front into the whole pellet sample and to calculate the percolation threshold and the characteristic parameters for the pore network.

References

L. Avram and Y. Cohen. Diffusion measurements for molecular capsules: Pulse sequences effect on water signal decay. *Journal of the American Chemical Society*, 127(15):5714–5719, 2005.

H. Y. Carr and E. M. Purcell. Effects of diffusion precession in nuclear magnetic resonance experiments. *Physical Review*, 94(3):630–638, 1954.

R. Denoyel, P. Llewellyn, I. Beurroies, J. Rouquerol, F. Rouquerol, and L. Luciani. Comparing the basic phenomena involved in three methods of pore-size characterization: Gas adsorption, liquid intrusion and thermoporometry. *Part. Part. Syst. Charact.*, 21:128–137, 2004.

P. A. C. Gane, C. J. Ridgway, E. Lehtinen, R. Valiullin, I. Furo, J. Schoelkopf, H. Paulapuro, and J. Daicic. Comparison of nmr cryoporometry, mercury intrusion porosimetry, and dsc thermoporosimetry in characterizing pore size distributions of compressed finely ground calcium carbonate structures. *Industrial & Engineering Chemistry Research*, 43(24): 7920–7927, 2004.

S. Gregg and K. Sing. *Adsorption, Surface Area and Porosity*. Academic Press, 2nd edition, 1982. Chap 3: Physical adsorption of gases by mesoporous Solids- Type IV Isotherm Chap6: The Use of Gas Adsorption for the determination of surface area and pore size distribution.

E. L. Hahn. Spin echoes. *Physical Review*, 80(4):580–594, 1950.

E. W. Hansen, R. Schmidt, and M. Stocker. Pore structure characterization of porous silica by h nmr using water, benzene and cyclohexane as probe molecules. *Journal of Physical Chemistry*, 100:11396–11401, 1996.

M. Hartmann. Ordered mesoporous materials for bioadsorption and biocatalysis. *Chem. Mater.*, 17:4577–4593, 2005.

M. P. Hollewand and L. F. Gladden. Transport heterogeneity in porous pellets .1. pgse nmr-studies. *Chemical Engineering Science*, 50(2):309–326, 1995.

M. Holz, S. R. Heil, and A. Sacco. Temperature-dependent self-diffusion coefficients of water and six selected molecular liquids for calibration in accurate h-1 nmr pfg measurements. *Physical Chemistry Chemical Physics*, 2(20):4740–4742, 2000.

M. Iza, S. Woerly, C. Danumah, S. Kaliaguine, and M. Bousmina. Determination of pore size distribution for mesoporous materials and polymeric gels by means of dsc measurements: thermoporometry. *Polymer*, 41(15):5885–5893, 2000.

A. H. Janssen, H. Talsma, M. J. van Steenbergen, and K. P. de Jong. Homogeneous nucleation of water in mesoporous zeolite cavities. *Langmuir*, 20(1):41–45, 2004.

R. Kerssebaum. Dosy and diffusion manual users guide for xwinnmr 3.1/3.5 version 1.0. 2002.

A. Khokhlov, R. Valiullin, J. Karger, F. Steinbach, and A. Feldhoff. Freezing and melting transitions of liquids in mesopores with ink-bottle geometry. *New Journal of Physics*, 9, 2007. Khokhlov, Alexey Valiullin, Rustem Kaerger, Joerg Steinbach, Frank Feldhoff, Armin.

N. K. Mal, M. Fujiwara, and Y. Tanaka. Photocontrolled reversible release of guest molecules from coumarin-modified mesoporous silica. *Nature*, 42:350–353, 2003.

R. Mills. Self- diffusion in normal and heavy water in the range 1-45'. *The Journal of Physical Chemistry*, 77(5):685–688, 1973.

P. P. Mitra, P. N. Sen, and L. M. Schwartz. Short-time behavior of the diffusion-coefficient as a geometrical probe of porous-media. *Physical Review B*, 47(14):8565–8574, 1993.

K. L. Murray, N. A. Seaton, and M. A. Day. Use of mercury intrusion data, combined with nitrogen adsorption measurements, as a probe of pore network connectivity. *Langmuir*, 15(8155-8160), 1999.

O. Petrov and I. Furo. Curvature-dependent metastability of the solid phase and the freezing-melting hysteresis in pores. *Physical Review E*, 73(1), 2006. Part 1.

J. F. Quinson and M. Brun. Progress in thermoporometry. *Characterization of Porous Solids*, pages 307–315, 1988.

S. P. Rigby and K. J. Edler. The influence of mercury contact angle, surface tension, and retraction mechanism on the interpretation of mercury porosimetry data. *Journal of Colloid and Interface Science*, 250(1):175–190, 2002.

S. P. Rigby and R. S. Fletcher. Experimental evidence for pore blocking as the mechanism for nitrogen sorption hysteresis in a mesoporous material. *Journal of Physical Chemistry B*, 108:4690–4695, 2004.

S. P. Rigby and R. S. Fletcher. Interfacing mercury porosimetry with nitrogen sorption. *Particle & Particle Systems Characterization*, 21(2):138–148, 2004a.

S. P. Rigby, D. Barwick, R. S. Fletcher, and S. N. Riley. Interpreting mercury porosimetry data for catalyst supports using semi-empirical alternatives to the washburn equation. *Applied Catalysis A: General*, 6186:1–16, 2002.

S. P. Rigby, P. I. Chigada, E. L. Perkins, M. J. Watt-Smith, J. P. Lowe, and K. J. Edler. Fundamental studies of gas sorption within mesopores situated amidst an inter-connected, irregular network. *Adsorption-Journal of the International Adsorption Society*, 14(2-3): 289–307, 2008a.

S. P. Rigby, M. Fairhead, and C. F. van der Walle. Engineering silica particles as oral drug delivery vehicles. *Current Pharmaceutical Design*, 14(18):1821–1831, 2008b.

R. Schmidt, E. W. Hansen, M. Stocker, D. Akporiaye, and O. H. Ellestad. Pore-size determination of mcm-41 mesoporous materials by means of h-1-nmr spectroscopy, n-2 adsorption, and hrem - a preliminary-study. *Journal of the American Chemical Society*, 117(14):4049–4056, 1995.

A. Schreiber, I. Ketelsen, and G. H. Findenegg. Melting and freezing of water in ordered mesoporous silica materials. *Physical Chemistry Chemical Physics*, 3:1185–1195, 2001.

N. A. Seaton. Determination of the connectivity of porous solids from nitrogen sorption measurements. *Chemical Engineering Science*, 46(8):1895–1909, 1991.

E. O. Stejskal and J. E. Tanner. Spin diffusion measurements: spin echoes in the presence of a time dependent field gradient. *Journal of Chemical Physics*, 42(288-292), 1965.

J. H. Strange, M. Rahman, and E. G. Smith. Characterization of porous solids by nmr. *Physical Review Letters*, 71(21):3589–3591, 1993.

J. E. Tanner. Use of stimulated echo in nmr diffusion studies. *Journal of Chemical Physics*, 52:2523–2526, 1970.

M. Vallet-Regi, L. Ruiz-Gonzalez, I. Izquierdo-Barba, and J. M. Gonzalez-Calbert. Revisiting silica based ordered mesoporous materials: medical applications. *Journal of Materials Chemistry*, 16:26–31, 2006.

D. Vargas-Florencia, T. Edvinsson, A. Hagfeldt, and I. Furo. Pores in nanostructured tio2 films. size distribution and pore permeability. *Journal of Physical Chemistry C*, 111(21): 7605–7611, 2007.

D. Vargas-Florencia, I. Furo, and R. W. Corkery. Pore morphology and interconnectivity in a mesoporous/macroporous polyhedral silica foam material. *Langmuir*, 24(9):4827–4832, 2008. Vargas-Florencia, Dulce Furo, Istvan Corkery, Robert W.

S. R. Veith, E. Hughes, and S. E. Pratsinis. Restricted diffusion and release of aroma molecules from sol-gel-made porous silica particles. *Journal of Controlled Release*, 99: 315–327, 2004.

Y. J. Wang and F. Caruso. Mesoporous silica spheres as supports for enzyme immobilization and encapsulation. *Chemistry of Materials*, 17(5):953–961, 2005.

J. B. W. Webber, J. H. Strange, and J. C. Dore. An evaluation of nmr cryoporometry, density measurement and neutron scattering methods of pore characterisation. *Magnetic Resonance Imaging*, 19(3-4):395–399, 2001.

J. M. Xue, C. H. Tan, and D. Lukito. Biodegradable polymer-silica xerogel composite microspheres for controlled release of gentamicin. *Journal of Biomedical Materials Research Part B-Applied Biomaterials*, 78B(2):417–422, 2006.

Y.-f. Zhu, J.-l. Shi, Y.-s. Li, H.-r. Chen, W.-h. Shen, and X.-p. Dong. Storage and release of ibuprofen drug molecules in hollow mesoporous silica spheres with modified pore surface. *Microporous and mesoporous Materials*, 85:75–81, 2005.

Chapter 4

Preparation and characterisation of Poly-(lactic-co-glycolic acid) (PLGA) microspheres for drug delivery

4.1 Introduction

This chapter introduces PLGA microspheres as a drug release system and describes some of the preparation methods and characterisation techniques used to study these microspheres. The aims of these studies were to compare physical changes to the microsphere structure at the micrometer scale when slight variations were made to the preparation technique and to establish a robust preparation method. This knowledge will be used to aid interpretation of further Nuclear Magnetic Resonance (NMR) experiments described in Chapter 6. Microspheres were made by double emulsion solvent evaporation technique and characterised by Scanning Electron Microscopy (SEM), and Pulsed Field Gradient (PFG) NMR.

4.2 Background and Theory

4.2.1 PLGA microspheres

Polymer microspheres are spherical structures made from one or more polymers, they range in size from a few micrometres to several hundred micrometres. The internal structure of the microspheres is dependent on the preparation technique, but may be hollow, contain micron scale spherical 'bubble-shaped' pores, or be solid polymer matrix. During the preparation of microspheres it is possible to encapsulate molecules that will be released as the microspheres

react to a change of environment, and eventually degrade. The actual structure and size distribution of any given batch of microspheres will be dependent on many factors including the number and type of polymers used, the preparation technique, and the encapsulated molecule, if one is used.

Polymer microspheres have been of interest for their potential use as controlled drug release device for many years. The idea to use biodegradable polymers for controlled drug delivery was first suggested in the 1960s, where the choice of polymer was determined by biocompatibility (Freiberg and Zhu, 2004). PLGA has been a popular candidate for developing a controlled Drug Delivery System (DDS) for many research groups because of its proven history within medical applications as, for example, a degradable suture material (Benoit et al., 2000). This experience and previous approval for internal medicinal use reduces the effort required on the legislative development of this material as a DDS. One advantage of polymers, like PLGA, is the ability to manipulate the time it takes for the polymer to biodegrade by varying its composition. An understanding of the degradation mechanism and its role in the release of an encapsulated molecule is key to the ability to tailor a given polymer for different applications. Another advantage of biodegradable polymers as a DDS is that the device will not require removal from the patient after the drug has been released (Noorsal et al., 2005). The degradation products are non-toxic and metabolised to carbon dioxide and water, or excreted from the body via the kidneys (Liu et al., 2003).

Other potential applications for microsphere based DDS include implanting microspheres within the scaffolding matrix used for in vitro tissue growth (Ungaro et al., 2006). Within a complex three dimensional structure good cell growth relies on a controlled release of growth hormone and nutrients to simulate in-vivo conditions. The distribution of these molecules is often restricted by poor mass transport in conventional tissue engineering systems, or bioreactors, particularly in bone tissue engineering where the support structures required for growth are often large and complex. The potential to implant microspheres loaded with hormones and nutrients throughout the scaffold used to support and grow the tissue cells has been suggested as a viable option to improve in-vitro tissue growth (Kempen et al., 2006). PLGA DDS have also been suggested as an improved method for the treatment of neuro-oncology, and degenerative disorders such as Parkinson's disease, Alzheimer's disease and Huntington's disease (Benoit et al., 2000). Direct injection of the DDS into the brain tissue eliminates the need for a drug to cross the blood-brain barrier, which can be difficult for many drug molecules and impossible for proteins. The design of bioadhesive polymers that bind to specific sites such as mucus, mucoadhesion (Lehr, 2000) are also of interest for targeted drug delivery (Peppas and Sahlin, 1996; Vasir et al., 2003). More recently,

another alternative application for controlled drug delivery has been investigated, to design device that would increase its retention time within the stomach by floating on the surface of the stomach fluids (Arora et al., 2005).

The chemical structures of poly(lactic acid) and poly(glycolic acid) are shown in Figure 4.1. PLGA is a co-polymer derived from a combination of these two monomers. The monomer ratio, lactic acid to glycolic acid, can be manipulated during the synthesis of the co-polymer and subsequently changes the properties of the polymer. The mechanism for PLGA degradation occurs by the succession of water uptake into the polymer matrix, carboxylic acids are then produced from chain scission which can then go on to catalyse the ester bonds (Li et al., 2008). The reaction schemes for the hydrolytic degradation and the autocatalytic degradation of PLGA are shown in Figure* 4.2. The mass transport of water and the carboxylic acid groups within the polymer matrix are, therefore, fundamental to the progress of the polymer degradation.

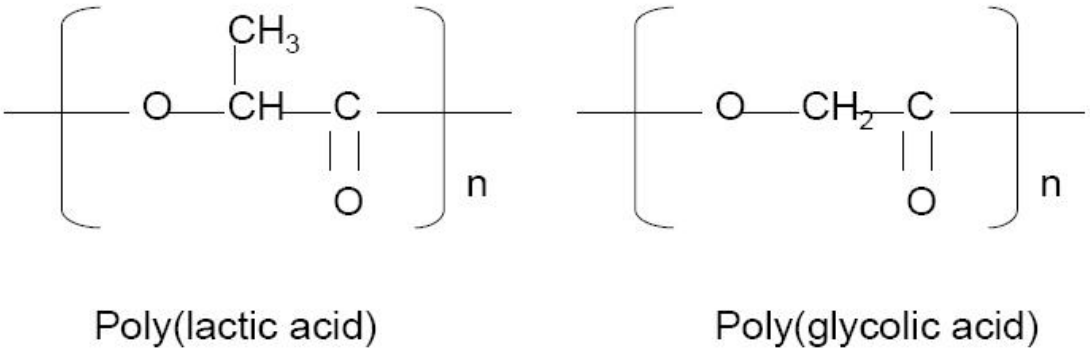

Figure 4.1: Chemical structures of poly(lactic acid) and poly(glycolic acid)

Characteristics of microspheres such as porosity, pore size and microsphere diameter are closely related to the preparation method used and can have significant effects on the subsequent drug release profile. For example, microspheres made by double emulsion show that increasing the polymer concentration in the organic phase decreases the pore size and porosity, but increases the mean diameter of the microspheres (Mao et al., 2007). Also, decreasing the volume of aqueous phase in the primary emulsion decreases the porosity of the microspheres but has negligible effect on the pore size (Mao et al., 2007). Pore size distribution can be affected by homogeniser speed during the formation of the primary emulsion, at faster homogeniser speeds the modal pore size decreases and the width of the pore size distribution is reduced, but there is little change in the porosity (Ehtezazi et al.,

*Based on Vey et al. (2008)

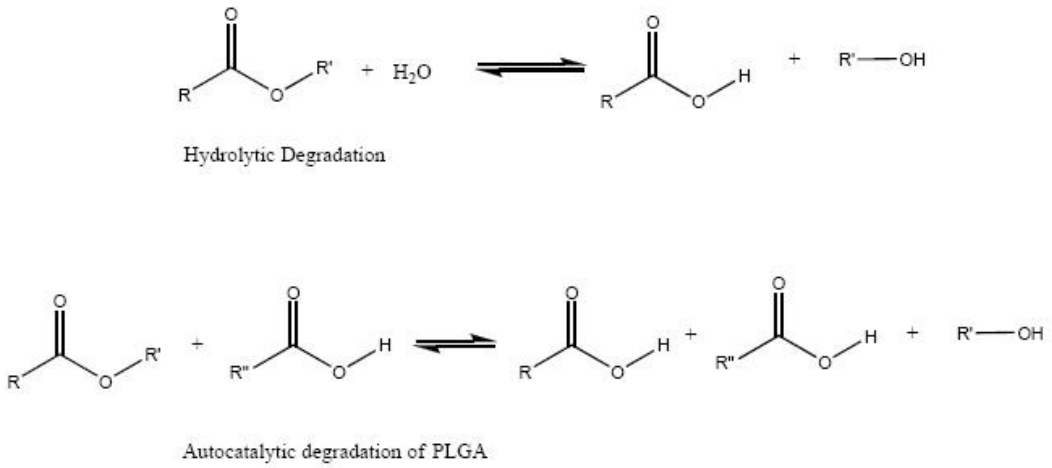

Figure 4.2: Reaction scheme for hydrolytic and autocatalytic degradation of PLGA

1999). Preparation temperature affects the size of the microspheres produced as the solvent evaporation speed changes (Yang et al., 2000; Messaritaki et al., 2005; Allison, 2008). For polymer nanospheres, it has also been shown that the choice of solvent for the organic phase containing the polymer can affect the size of the sphere produced, with the addition of acetone to Dichloromethane (DCM) a decrease in the size of spheres produced was observed (Niwa et al., 1993). The interfacial tension between organic phase and aqueous medium decreased with increasing addition of acetone, improving drug encapsulation of 5-Fluorouracil (Niwa et al., 1993). Siepmann et al. (2004) have observed an increase in drug release rate with an increase in microsphere diameter, relating to the increase in porosity of larger spheres which overcomes the increase in the diffusion pathway that is associated with larger spheres. Cohen et al. (1991) have categorised the different microspheres based on the time over which they release encapsulated drug and equated this to the microsphere porosity (Yang et al., 2000).

Microspheres can be made by various preparation techniques, according to Freiberg and Zhu (2004) the methods of microsphere synthesis can be divided into two categories:

1. Polymerisation of monomers, known as an emulsion suspension or dispersion technique.

2. Synthesis from linear polymers, known as a solvent evaporation or double emulsion technique, also spray drying.

There are several papers that specifically discuss the preparation methods and techniques for polymer microsphere preparations, these include: Weert et al. (2000); Yang et al. (2000); Ruan and Feng (2003); Freiberg and Zhu (2004); Wang et al. (2004); Freitas et al.

(2005); Mao et al. (2007). The most popular method for experimental scale preparation of microspheres is the double emulsion, water/oil/water, technique. The first emulsion is water in oil, the second emulsion uses the first emulsion in another water phase. The double emulsion technique typically produces microspheres with microporosity within the polymer matrix, which provides an additional access network for the external media to penetrate the microspheres, and for drug molecules to be released.

Composite double-wall microsphere preparations have also been described in the literature by Eng et al. (2005); Lee et al. (2002); Leach and Mathiowitz (1998). The properties of such systems are more complex due to the range of combinations of polymers that may be chosen for their fabrication. Long term considerations should be made for the scale up of the preparation technique used if microspheres are to be produced on a commercial scale. A review of technologies for large scale production by extraction-evaporation techniques and the effects of different parameters on the microspheres has been considered by Freitas et al. (2005). They concluded that simple design, ease to sterilise and a straight forward scale-up make micromixers a strong candidate for large scale aseptic microsphere manufacture by solvent evaporation.

4.2.2 Drug release mechanism

Typical delivery devices, currently discussed in the literature, are matrix tablets, polymer microspheres, coated tablets or microspheres, nanospheres and larger implant devices. Drug release studies have commonly identified three stages of drug release, initial burst, sustained release, and a reduced level of release. The theories behind the mechanisms responsible for the release of a drug from within a polymeric based delivery device include diffusion controlled release, polymer matrix degradation controlled release, or a combination of the two. The three stages of the release profile are described in terms of the suggested release mechanisms:

1. *Initial burst release.*
   The release of molecules either loosely attached to the surface of the microspheres or released from the pores open to the surface of the microsphere. The initial swelling of the microspheres when placed in an aqueous environment can open and close the pores within the microsphere, including those on the surface, controlling the initial drug release. A large fraction of the contained drug can be released at this stage. This stage is thought to be controlled by the drug mobility within the medium.

2. *Sustained period of slow release.*
   Molecules within the inner pores and just inside the matrix of the polymer are released

as the polymer continues to swell and begins to degrade. This stage is thought to be controlled by the drug mobility within the polymer matrix.

3. *Reduced level of release.*
   Small amounts of molecules that are tightly bound within the inner matrix structure of the polymer are eventually released in the final stages of the polymer degradation. This stage is thought to be controlled by the polymer degradation.

Whilst there is agreement within the literature that these three stages exist, it is believed that the presence of, or length of any of these stages is characteristic of the microsphere system being studied. A recent study suggests that the three stages of the release profile identified are solely controlled by the evolution of the polymer matrix (Allison, 2008), therefore, an understanding of the matrix structure and its evolution with time is key to determining the release mechanism. Once the matrix evolution is understood, greater control of the release profile may be considered at the design stage for a particular system or application.

Factors that affect the release rate can be drug related, polymer related, or as mentioned previously, related to the physical characteristic determined by the microspheres preparation. The polymer and drug related factors are listed in Table 4.1. Although much work has been done to understand the release kinetics of drug molecules (Peppas, 1983; Ritger and Peppas, 1987; Batycky et al., 1997) and latterly protein molecules (Sandor et al., 2001; Koennings et al., 2007) from controlled delivery devices, far less has been done to understand the mechanisms that determine the release profile.

Polymer Related	Drug Related
Type of polymer	
Molecular weight	
Single or multiple co-block polymer	
Type of polymer crosslinker	
Use of coating	
Storage history	
	Drug binding characteristics
	Drug hydrophobicity
	Drug molecular size and diffusivity
	Presence of nucleophilic groups
Polymer-drug interactions	Polymer-drug interactions

Table 4.1: Factors that affect release rate

The importance of the initial burst release has been recognised (Huang and Brazel, 2001) but the actual mechanisms involved are still poorly understood. More recent work has

attempted to address this gap in knowledge by investigating the burst release (Messaritaki et al., 2005; Luan et al., 2006; Jaraswekin et al., 2007; Koennings et al., 2007; Kang and Schwendeman, 2007). The burst release can be considered either an advantage or disadvantage of this type of drug delivery system. For some drugs a high initial dose is required to initiate treatment, therefore, a controlled burst release could start such a regimen. Conversely, for other drugs a large dose may have toxic effects on the surrounding tissue, or the body as a whole, therefore, a burst release would be undesirable and could potentially be dangerous for the patient. Either scenario requires a thorough understanding of the cause of the initial burst release to ensure its effect is controlled.

4.2.3 Scanning electron microscopy (SEM) basic theory

Electron microscopy is a common method used to study the structure of polymer microspheres. Microscopy is the science of forming an image from an object, that image is often magnified. Optical microscopes using light date back to the seventeenth century. They require a system of lenses to focus and magnify the image of an object. Electron microscopy uses a beam of high velocity electrons, generated from an electron gun and focused by electromagnetic fields. Electrons interact with the object and can be scattered by the object, or enter the object and cause the release of secondary electrons or x-ray energy. Secondary electrons and scattered electrons are detected by a photomultiplier, the signal from which is used to build the image displayed on a cathode ray tube, or more recently, via software on a computer screen. The advantages of electron microscopy over light microscopy are that electrons have a much shorter wavelength than light, therefore, resolution and depth of field are increased. Scanning of an object is possible with electrons since the beam of charged electrons can easily be directed by the manipulation of electromagnetic fields. SEM can produce images of the surface structure of a material with a theoretical resolution of 5 nm (Goodhew and Humphreys, 1988).

4.2.4 NMR PFG theory

Nuclear magnetic resonance pulsed field gradient studies have previously been used to study the behaviour of water within a materials as diverse as wheat germ tissue (Callaghan et al., 1979) and sandstone (Fordham et al., 1994). From these studies structural information about average pore size and shape can be assessed by the type of diffusion observed. This techniques has been used with PLGA microspheres to estimate the average size of the 'bubble' pores observed during the swelling stage that occurs after immersion in an aqueous medium (Messaritaki et al., 2005). If there is restricted diffusion of water within

the 'bubble' pores, the estimation of the cavity size is representative of average 'bubble' pore size, see section below on restricted diffusion.

The origins and use of NMR PFG have been discussed in Chapter 3, further discussion on the interpretation of diffusion studies for non-linear log attenuation plots is discussed in this chapter. The work of Callaghan (1991) has greatly contributed to the development of diffusion models when the motion of the diffusing molecule is restricted (Callaghan et al., 1979) or constrained within one or two dimensions (Callaghan et al., 1983) and the influence of gradient field strength on diffusion within porous media (Callaghan et al., 1991a). Hollewand and Gladden (1995) have also developed models for diffusion in porous media, where the signal attenuation is affected by the porous media in which the diffusing liquid is contained and the observed diffusion behaviour is interpreted as contributions from different components, or phases of the investigated molecule which have different diffusion coefficients. One such study of the changes in diffusion behaviour in bicontinuous polymer emulsions defined two components as free water and water associated with the surfactant molecule at different water content values (Challa et al., 2003).

Relaxation effects

For a system where the diffusion is slow compared to the relaxation behaviour of the molecule, it is possible to measure the diffusion coefficient using the stimulated echo sequence rather than the spin echo. The stimulated echo has two 90 °pulses in place of the 180 °pulse in the spin echo sequence, the first 90 °pulse stores the magnetisation and phase shift along the z-axis before the second 90 °pulse, after which the stimulated echo occurs (Hollewand and Gladden, 1995).

Multi-component fit

A linear log attenuation plot suggests diffusion of a single component in a homogeneous environment, the relationship between signal attenuation and the diffusion coefficient is discussed in Chapter 3, equation 3.5. The deviation from linearity of the log attenuation plot for liquid within a porous structure was investigated by Hollewand and Gladden (1995). Diffusion measurements were shown to be sensitive to the structure of the porous material in which the liquid is contained, where the root mean square (rms) displacement of the molecule during the experiment is comparable to the pore size. This suggests that one of the causes of heterogeneity in the diffusion coefficient is an effect of the structure of the porous medium. A discrete multicomponent model was derived by Hollewand and Gladden (1995), equation 4.1, where the heterogeneity in the apparent diffusion coefficient is attributed to i

components, each containing the fraction, p_i, of observed nuclei, with the actual diffusion coefficient, D_i. ζ is characteristic of the experimental parameters, as defined for equation 3.5.

$$I = I_0 \Sigma p_i \exp(-D_i \zeta) \tag{4.1}$$

Restricted diffusion

Non-linearity of the log attenuation data for the diffusion of fat and water in cheese was attributed to the diffusion being restricted (Callaghan et al., 1983). Restricted diffusion was suggested to be the cause of the deviation from linearity seen at longer diffusion times, where the rms displacement is of the same order or greater than the dimension of the restricting structure. For a spherical pore, the typical cavity radius, in which the diffusion has been restricted, can be calculated based on the diffusion time, Δ, and the length of the gradient pulse the nucleus is exposed to, δ (Callaghan et al., 1983) equation 4.2 [†], where r_{cavity} is the cavity radius in meters, both Δ and δ have the units of seconds.

$$r_{cavity} = (5D(\Delta - \delta/3))^{0.5} \tag{4.2}$$

For the pulse sequence used in this work, the value of half the bipolar correction time, $\frac{\tau}{2}$ should strictly be included in equation 4.2, but is very small compared to the diffusion time and gradient length, therefore, it is not considered significant in the estimate of the cavity size.

Choice of diffusion time

For the relationship in equation 4.2 to hold, Δ must be sufficiently large for the diffusion of all molecules to be restricted. The effective diffusion coefficient calculated from a one component fit, equation 3.5 will be characteristic of the average motion of all molecules and, therefore, will be a combination of free diffusion and restricted diffusion. With a very small value of Δ, i.e. a short diffusion time, none of the molecules will be restricted as none of the molecules will have sufficient time to reach the walls of the pores. The effective diffusion coefficient measured is that of a molecule in free solution. Conversely, if Δ is sufficiently large all the molecules contained within the pores will contact the pore walls and thus undergo restricted diffusion. The effective diffusion coefficient measured is that of molecules trapped inside the pores and can be used to calculate the pore size as in equation 4.2. At any value of Δ between these extremes, the effective diffusion coefficient is a

[†]As expressed by Messaritaki et al. (2005)

representative combination of free and trapped molecules. The choice of Δ is, therefore, critical if pore size is to be calculated from the effective diffusion coefficient determined by a one component fit model, equation 3.5. The relationship between the effective diffusion coefficient and the diffusion time for a given batch of microspheres is shown in Figure 4.3. For this microsphere batch it can be seen that even at very small diffusion times, 0.01 s, the effective diffusion coefficient is significantly affected by the microsphere pore structure, the free diffusion coefficient for this system is expected to be $1.88 \times 10^{-9}\ m^2 s^{-1}$. The gradual slope behaviour of the effective diffusion coefficient with the diffusion time shown in Figure 4.3 suggests that there is a broad range of pore sizes observable in this batch of microspheres, from approximately 9 μm, and that a plateau of totally restricted diffusion occurring at long diffusion times ≥ 0.09 s is at around $0.6 \times 10^{-9}\ m^2 s^{-1}$, which coincides with a cavity size of approximately 16 μm.

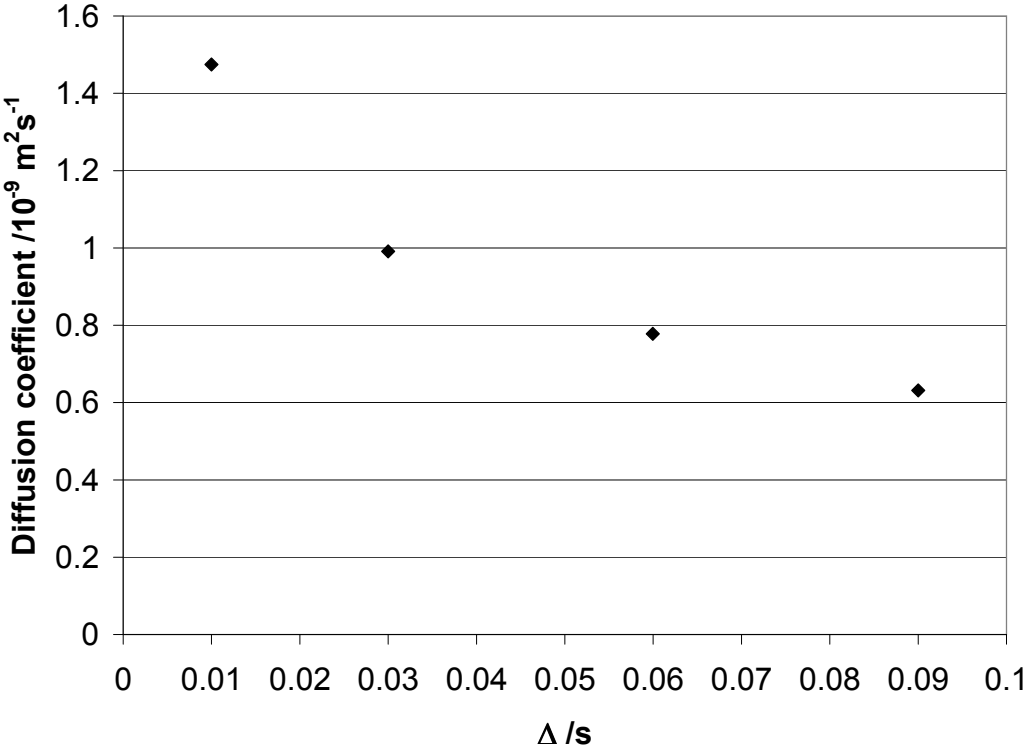

Figure 4.3: Graph to show the change in calculated effective diffusion coefficient for a range of values of diffusion times, Δ.

The effect of diffusion time on the observed diffusion coefficient is considered when determining the appropriate model for interpreting the NMR PFG data, as described in the experimental Section 4.3.4. The experimental Section 4.3.1 describes the preparation methods for the PLGA microspheres and the considerations that are made with respect to

ensuring the number of variables changed between each batch is limited.

4.3 Experimental

PLGA of two different inherent viscosities, one with a high average molecular weight of approximately 135000 D and the other with a low average molecular weight of approximately 14000 D were obtained from Lakeshore Biomaterials. Both batches had a 50:50 monomer ratio of lactic to glycolic acid. The model drugs 5-Fluorouracil (5-FU) and 5-Fluoro-5'Deoxyuridine (5-FD) were obtained from Sigma Aldrich, and 4-(trifluoromethyl)umbelliferone (TFMU) was obtained from Fluka. Dichloromethane (DCM) and acetone were obtained from Fisher and PVA from MP Biomedicals. Ultra pure water (resistivity 18 MΩ) was generated from a Milli-Q water purification unit. The homogeniser used was an Ultra Turrax IKA T18 basic homogeniser.

4.3.1 Double emulsion preparation method

The chosen method for microsphere preparation is a double emulsion water-oil-water (w/o/w) solvent extraction evaporation method, as described in Messaritaki et al. (2005). The microsphere preparation steps were as follows:

1. 300–600 mg of PLGA was dissolved in a DCM and acetone mixture consisting of 2.4 ml and 0.6 ml respectively, to make a 10-20 % w/v solution; this was the oil phase.

2. Approximately 30 mg of model drug (5-FU, 5-FD or TMFU) was dissolved in 0.6 ml 1N ammonium hydroxide for 5-FU or 0.6 ml water for 5-FD or TFMU. To this 10 μl of 0.4 % w/v polyvinylalcohol (PVA) was added as a surfactant; this was the internal water phase.

3. These two phases were emulsified by homogenization for 60 s at 13500 pm.

4. This emulsion was immediately transferred into the external aqueous phase at room temperature, 180 ml of 2 or 4 % w/v PVA and stirred by a basic lab stirrer for between 3 and 18 hours to allow for the complete evaporation of DCM and acetone.

5. The microspheres formed were then filtered and washed 3 times with distilled water to remove PVA residues and any non-encapsulated drug.

6. The microspheres were then air dried within a fumehood for at least 48 hours.

As discussed previously in Section 4.2, there are many preparation parameters that are thought to have an effect on the physical characteristics of the microspheres produced and subsequently alter the drug release profile. During the preparation of a given batch of microspheres considerations for these effects were made:

- *Preparation temperature*
  Primarily the temperature of the hardening bath, is thought to affect the size of the microspheres as it changes the rate of evaporation of the solvent. Unless otherwise stated, all preparations were carried out using PVA solution that had equilibrated to lab temperature (25 ± 1°C.)

- *Polymer molecular weight*
  This affects the viscosity of the organic phase which will change the behaviour of the emulsion characteristics. Two batches of PLGA were purchased with different inherent viscosities that equate to molecular weight averages of 135000 D and 14000 D, denoted as high molecular weight and low molecular weight respectively.

- *Polymer ratio*
  Affects the structure of the polymer and, therefore affect its properties such as degradation mechanism. Both polymers purchased were of a 50:50 monomer ratio of lactic acid and glycolic acid.

- *Polymer degradation*
  Degradation is dependent on molecular weight and storage conditions. The molecular weights were as described above. Both batches of polymer were stored in the same conditions, a sealed container stored in a freezer (-18 °C). After preparation, microspheres were stored in sealed containers in a refrigerator (2–5 °C).

- *Homogeniser speed and duration*
  These affect the first emulsion characteristics and, therefore, the porosity of the microspheres. The same speed setting and time for homogenising was used for each sample unless otherwise stated.

- *The choice of surfactant for primary or secondary emulsion and their concentration*
  The surfactant affects the formation of the macropores in the primary emulsion and the microspheres in the secondary emulsion. The primary emulsion surfactant and concentration was unchanged. For the secondary emulsion, the choice of surfactant was kept constant as PVA, but the concentration was adjusted for some samples from 4 % w/v to 2 % w/v, as stated.

- *The choice of solvent for organic phase containing polymer*
  The volatility of the organic solvent affects the speed of the formation of the microspheres and subsequently can change the size of the microspheres produced. Acetone was added to DCM at the same ratio for each batch unless otherwise stated. For two batches ethyl acetate was used as the solvent, instead of DCM with acetone.

- *Encapsulated drug characteristics*
  Different drug molecules interact with the polymer and the solvents used in the preparation in different ways. Microspheres were made with two types of model drug, 5-Fluorouracil (5FU) and 5-Fluoro-5'Deoxyurridine (5-FD) and a fluorescent molecule, 4-(trifluoromethyl)umbelliferone (TFMU). Some batches of microspheres were made without any drug encapsulation, for this the inner water phase was 0.6 ml water and 10 μl of 0.4 % w/v PVA.

4.3.2 Preparation of Double wall microspheres

Two batches were also made by a different method, in which a series of organic phases were added to the internal water phase, this emulsion was then added to final water phase to make double walled microspheres. It was possible to make blank microspheres by this method, but microspheres would not form when trying to encapsulate 5-FU, see Section 4.4. The steps for this preparation were as follows:

1. Three organic phases were prepared:
   (a) 50 mg high molecular weight PLGA in 1 ml DCM
   (b) 200 mg high molecular weight PLGA in 1 ml DCM
   (c) 200 mg low molecular weight PLGA in 1 ml DCM
2. Two aqueous phases were prepared:
   (a) 100 μl internal phase of 10 μl 0.4 % w/v PVA and 90 μl water
   (b) Second aqueous phase 160 ml of 2.5 % w/v PVA
3. The first organic phase and the internal water phase were homogenised at 6500 pm for 60s
4. The second organic phase was added and further homogenised at 9500 pm for 60s
5. The third organic phase was added and further homogenised at 9500 pm for 60s

6. This emulsion was then added to the second aqueous phase and stirred for approximately 3 hours.

7. The microsphere were then filtered, washed 3 times with distilled water and air dried as for the standard double emulsion technique described previously.

4.3.3 SEM methods

Two methods were used for taking SEM images of the polymer microsphere internal and external structure. In the first method images were taken using the cryogenic stage facility of the JEOL JSM6310 microscope. A hydrated sample of microspheres was placed between two sample plates and fast frozen by immersion in liquid nitrogen. Once frozen and placed within a cryogenic chamber of the SEM the top sample plate was ripped off in an attempt to fracture some of the microspheres. The sample was then sputter coated with gold to complete the electric circuit required for electron transfer. For some batches it was not possible to fracture the microspheres in this way, therefore an alternative method was used. This alternative method used the JSM6480LV SEM, without cryogenic stage facility. A sample of dry microspheres were mounted within the surface of an adhesive drop on the top of a small resin block. The top of the resin block was then cut to an approximate 1 mm square tip using a razor blade. Fine slices, less than a micron in thickness, were then cut from the top of the resin block using a microtome. The slices of adhesive containing microspheres were mounted onto an aluminium dish and sputter coated for 4-5 minutes before being imaged on the microscope.

4.3.4 PFG at room temperature

A generous amount, ≥ 50 mg, of a given batch of microspheres was placed in a 5 mm thin-walled NMR tube, to which a 1 % H_2O in D_2O (Aldrich $\geq 99.9\%$) was added until there was sufficient volume to cover the region of the receiver coil, approximately 3 cm height. The D_2O is both a reference for the NMR spectrometer and a diluent of the H_2O signal. Due to the initial floating nature of many of the microspheres it was necessary to use a susceptibility plug to force the microspheres below the surface of the solution and within the area of the receiver coil, see Figure 4.4. The sample was placed into the spectrometer and PFG experiments were carried out at varying time intervals after the initial immersion of microspheres into aqueous media. The PGSTE-BPLED pulse sequence was used for this experiment, the same as was used previously for silica cryodiffusometry, see Chapter 3. A series of eight spectra were taken at increasing gradient strengths between 0.674 to 32.030

G/cm and a diffusion time of 0.05 s, gradient length and bipolar correction time of 0.002 s and 0.0001 s, respectively. The number of scans for each spectrum was 16, with 16 dummy scans used at the beginning of each experiment. It is assumed that the magnetic field is uniform (Brand et al., 2006) and there is no cross-relaxation with the polymer (Peschier et al., 1996).

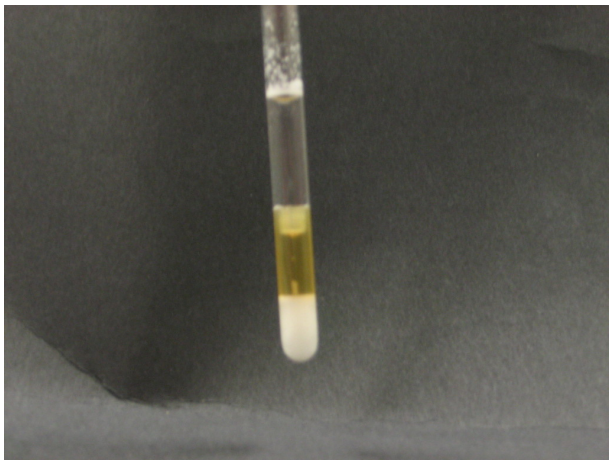

Figure 4.4: Photograph showing microspheres held in aqueous environment by susceptibility plug within the NMR tube

As the structure of the microspheres evolve with time immersed in an aqueous media, the measured diffusion coefficient is sensitive to time, in addition to temperature. Due to the time required to collect the data a compromise between the number and the quality of the data points must be made. It takes longer to collect more scans which would increase the quality of each data point, during which time changes in the polymer microspheres may have occurred and the diffusion coefficient will also have changed. Increasing the number of data points would also increase the experiment time with similar consequences. The temperature of the sample may rise significantly with a large number of scans and this too would affect the observed diffusion coefficient. The final parameters chosen were to collect 8 data points of 16 scans each. The collection of this data takes approximately 18 minutes; a short enough time period not to show significant changes in the diffusion coefficient, due to structural changes of the microsphere, which are observable on the scale of hours. Heating effects on the sample from application of repeated radio frequency pulses had little effect on the signal attenuation observed, as described later in Section 4.4.3.

4.4 Results and Discussion

4.4.1 SEM images

A series of SEM images were taken of different batches of microspheres, each batch made with one variation in the preparation method, e.g. With and without encapsulated drug (blank). As discussed in Section 4.2, there are many variables in the preparation technique that can affect the final structure of the resulting microspheres. A summary of some of the batches of microspheres produced and their resulting structures are given in Table 4.2. The SEM images shown in this section are typical representative examples of the images taken for the batch of microspheres being described.

Batch	Molecular weight	Drug	Solvent	Sphere diameter from SEM/μm	Pore diameter from SEM/μm	Method
MS006	High	None	DCM	10-100	1-10+	DE, 2 % PVA
MS011	High& Low	None	DCM	c. 50	2-3	DW
MS018	High	5-FU	Ethyl acetate	10-500+	external upto 5	DE, 2 % PVA
MS023	High	TFMU	DCM & acetone	50-500	external 1-2	DE, 2 % PVA
MS035	High	5-FU	DCM & acetone	25-200	1-25	DE, 4 % PVA
MS036	High	None	DCM & acetone	20-150	10-20	DE, 4 % PVA
MS041	Low	None	DCM & acetone	20-100+	1-10	DE, 4 % PVA
MS042	Low	5-FD	DCM & acetone	30-100	5-10	DE, 4 % PVA
MS043	High	5-FD	DCM & acetone	50-200	5-20	DE, 4 % PVA
MS045	Low	5-FD	DCM & acetone	10-100	5-10	DE, 4 % PVA

Key DE = Double Emulsion, DW = Double Wall

Table 4.2: Summary of some PLGA microsphere characteristics

Figure 4.5 is an SEM image of microspheres made from high molecular weight polymer with the model drug 5-FU encapsulated, the image shows the spherical nature of the microspheres with varying sizes of approximately 10–150 μm diameter. Some microspheres have been cross-sectioned and it is possible to see the 'bubble' pores created within the polymer matrix. These 'bubble' pores vary in size and spatial distribution within the polymer matrix, and show inter-batch variability. These characteristics are typical of most microsphere batches made by the double emulsion technique in this work.

In comparison, Figure 4.6 shows an example double-walled microsphere with a much higher porosity than those made by the double emulsion technique. The internal structure of

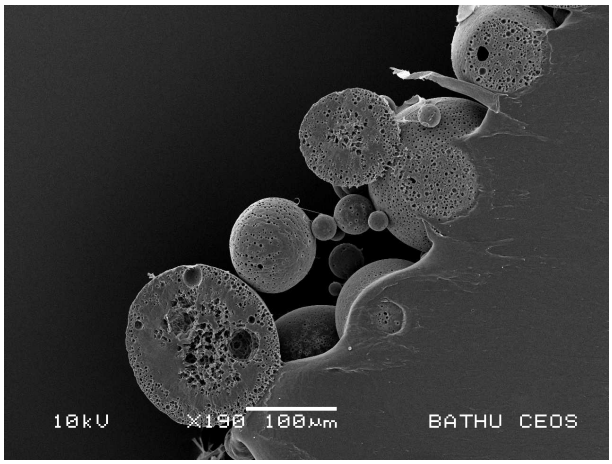

Figure 4.5: SEM image of high molecular weight microspheres with 5-FU model drug encapsulated, batch MS035

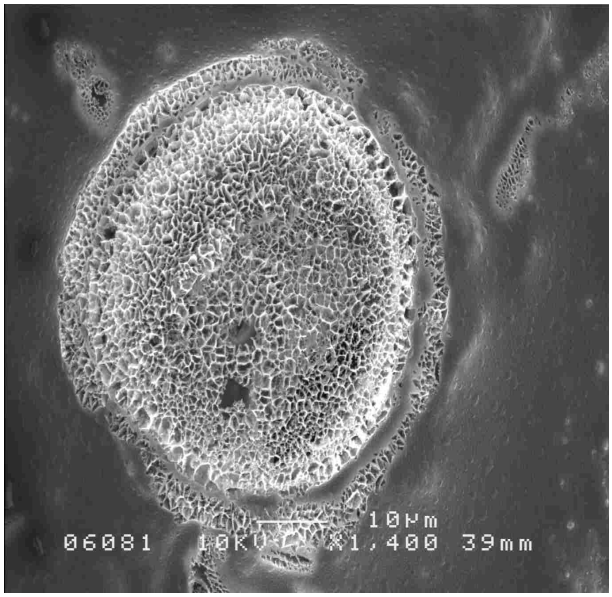

Figure 4.6: SEM image of double-walled microspheres without drug encapsulated, batch MS011

the double walled microspheres shows a more homogeneous distribution of pores separated by much thinner walls of polymer matrix than other batches. The pores are less spherical and more angular than those produced by the double emulsion technique. Near the external surface a boundary layer can be seen between the internal structure and that of a porous surface layer. The surface layer has a porous structure similar to that of the central region of the microsphere.

(a) With 5-FU encapsulated batch MS035

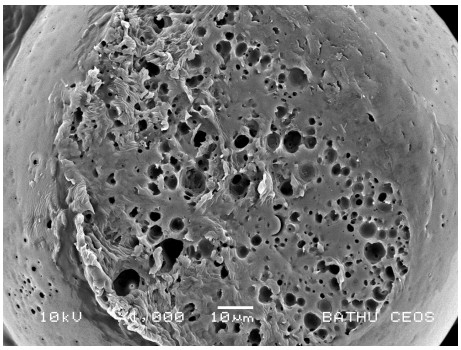

(b) With 5-FU encapsulated batch MS035

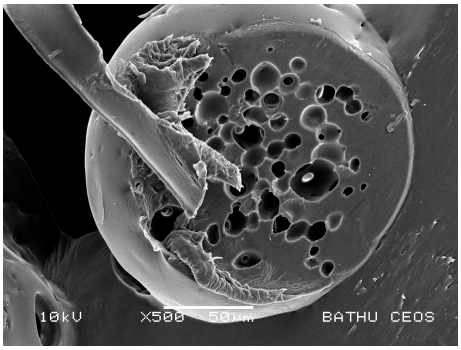

(c) No drug encapsulated batch MS036

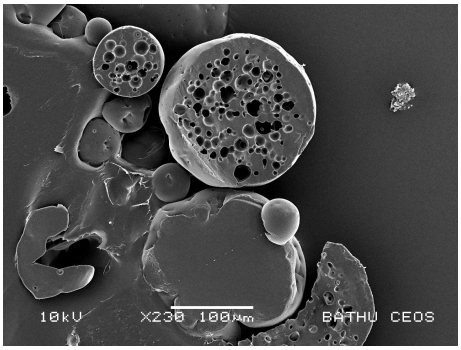

(d) No drug encapsulated batch MS036

Figure 4.7: SEM images of a high molecular weight microspheres with and without encapsulated drug

Comparison of drug encapsulated and blank microspheres made with high molecular weight polymer

Figures 4.7a, 4.7b, 4.7c and 4.7d show SEM images of high molecular weight microspheres made with encapsulated 5-FU, batch MS035, and without encapsulated drug, batch MS036, respectively. The internal aqueous phase for encapsulated 5-FU contains 1 N NH_4OH with 0.4 % PVA and for the blank microsphere this phase was water with 0.4 % PVA. Whilst the overall size of these example microspheres show similar diameters (80–100 μm), the 'bubble' pores within the microspheres show a significant difference with the introduction of encapsulating 5-FU. The microspheres with encapsulated drug show a greater number of smaller 'bubble' pores, these pores are distributed closer to the surface of the microsphere than for the blank microsphere. The drug encapsulated microsphere has many 'bubble' pores close to the surface causing a surface porosity, this provides an access route into and out of the microsphere for the external medium and encapsulated drug. Connections between the pores are also visible, providing pathways within the porous network of the microsphere. In contrast, the blank microspheres show little, or no, surface porosity and a thick matrix wall between the surface and the internal bubble pores. Connections between

the 'bubble' pores can be seen, providing pathways within the porous network. Whilst all the images of drug encapsulating microspheres show the same trend in porosity, it is observed that for some of the blank microspheres there is little or no porosity at the micrometer scale, as shown in Figure 4.7d.

Comparison of low molecular weight microspheres with high molecular weight microspheres, both with 5-FD encapsulated

Samples of microsphere batches MS043 and MS045 made from high and low molecular weight respectively, both encapsulated with the model drug 5-FD, were imaged by SEM, typical images are shown in Figures 4.8a, 4.8b, 4.8c and 4.8d. From the SEM images it can be seen that both high and low molecular weight batches show varying 'bubble' pore sizes with connecting spaces between pores that form networks of 'bubble' pores. The thickness of the matrix walls between the 'bubble' pores are, on average, slightly thicker for the low molecular weight microspheres, and the 'bubble' pores are smaller.

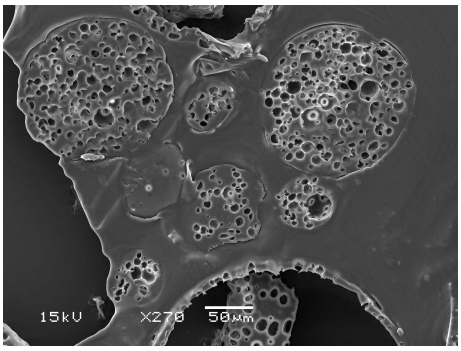

(a) High molecular weight microspheres batch MS043

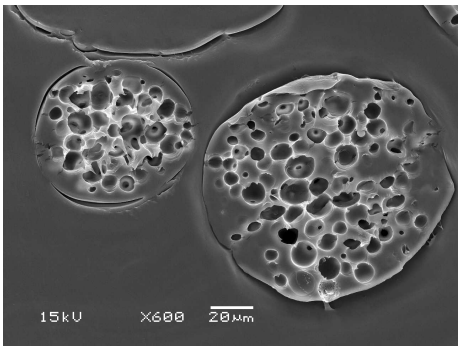

(b) High molecular weight microspheres batch MS043

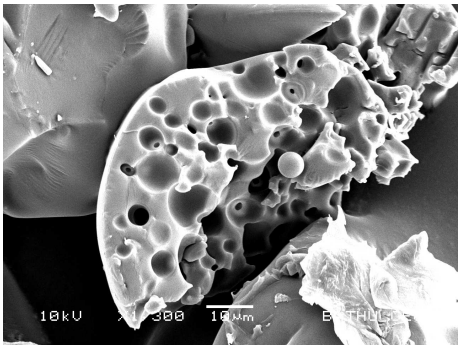

(c) Low molecular weight microspheres batch MS045

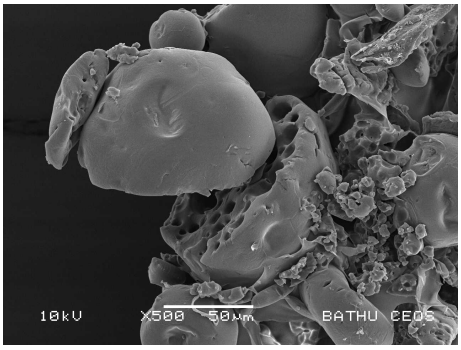

(d) Low molecular weight microspheres batch MS045

Figure 4.8: SEM images of a high and low molecular weight microspheres with 5-FD as encapsulated drug

Comparison of low molecular weight microspheres with and without encapsulated drug 5-FD

Figures 4.9a and 4.9b are typical SEM images of blank microspheres made with low molecular weight polymer, showing narrower pore walls and more connections between 'bubble' pores than the 5-FD encapsulated low molecular weight microspheres, shown in Figures 4.9c and 4.9d. The blank microspheres show a high level of porosity with bubble pores in the order of ≤ 10 μm, with comparatively narrow walls between the 'bubble' pores.

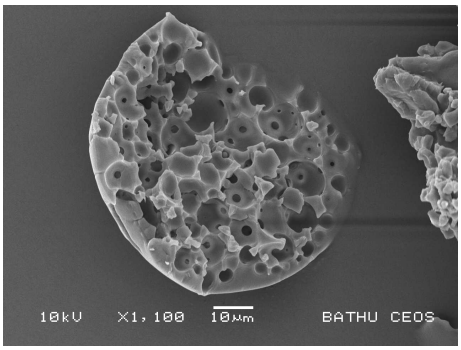

(a) Drug encapsulated microspheres batch MS041

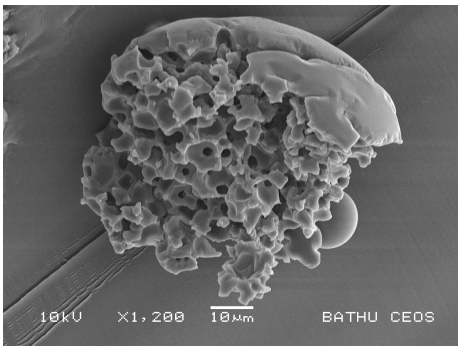

(b) Drug encapsulated microspheres batch MS041

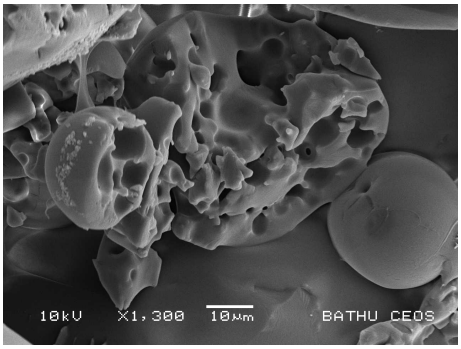

(c) Blank microspheres batch MS045

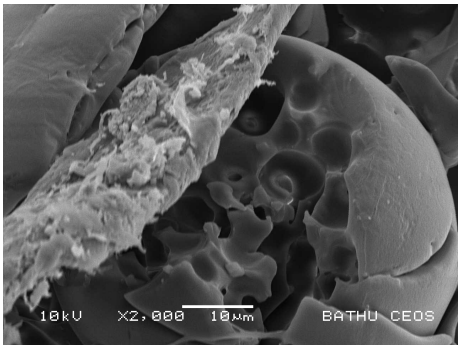

(d) Blank microspheres batch MS045

Figure 4.9: SEM images of low molecular weight microspheres with and without 5-FD as encapsulated drug

4.4.2 Fluorine detection

Both model drugs used for encapsulation, 5-FU and 5-FD, contain fluorine which can be detected using NMR of fluorine-19 nucleus. A spectrum was taken of each drug molecule dissolved in water in order to locate the chemical shift of the fluorine for each drug molecule. The peak of fluorine was at -169.3 ppm for 5-FU and at -165.99 ppm for 5-FD with reference to trichlorofluoromethane. Experiments with a batch of 5-FU encapsulated microspheres has shown that when microsphere are first immersed in water there is no free moving drug

in solution. After 16 days, free moving 5-FU is found to be present. Experiments on the water soluble 5-FD molecule does not show the presence of 5-FD after immersion in aqueous media after 30 days. This suggests that 5-FD has either not been released in this period, or it may not be encapsulated into the polymer microspheres. It is possible that the higher solubility of 5-FD in water caused it to be washed out of the polymer during the hardening phase of the preparation, whereas 5-FU, being less soluble in water remained entrapped within the microspheres. The drug 5-FD contains nitrogen and should be detectable by elemental analysis of carbon, hydrogen and nitrogen. Two batches of microspheres, one containing 5-FD and one blank, were analysed by this method and no difference was seen in the nitrogen content for the two batches, suggesting that encapsulation is too low to detect, or 5-FD is not present in the microspheres. However, as can be seen from the SEM images, the presence of 5-FD in the preparation of the microspheres does appear to affect the internal structure of the microspheres produced.

4.4.3 NMR PFG studies at room temperature, measuring the average cavity size and comparing to SEM

Temperature effects

Each set of data is collected in order of increasing gradient strength and as the experiment progresses, the sample is subjected to an increasing number of radio frequency pulses. The cumulative effect of these pulses can cause the sample temperature to increase, thus affecting the measured signal attenuation. To identify if any temperature effects are seen during the experiment time, a set of data points were collected manually in random order of changing gradient strength, as suggested by Hollewand and Gladden (1995). Figure 4.10 shows the results of collecting the data points in order of increasing gradient strength and random order of gradient strength.

It can be seen in Figure 4.10 that there is very little difference in the two sets of collected data. The values for randomly ordered individual data points vary from sequential data points by at most $+4$ %, but many of the values lie with $+1$ %, the average error being $+2$ %. The increasing temperature effect is seen as a reduction in the signal intensity seen, which increases the calculated diffusion coefficient. An error in the measured signal intensity of 2 % equates to an error of around 2–2.5 % in the diffusion coefficient for a one component model. This error is smaller than the experimental error expected for diffusion coefficient calculated using a one component model fit of data. Therefore, the effect of temperature is not considered significant for these experiments.

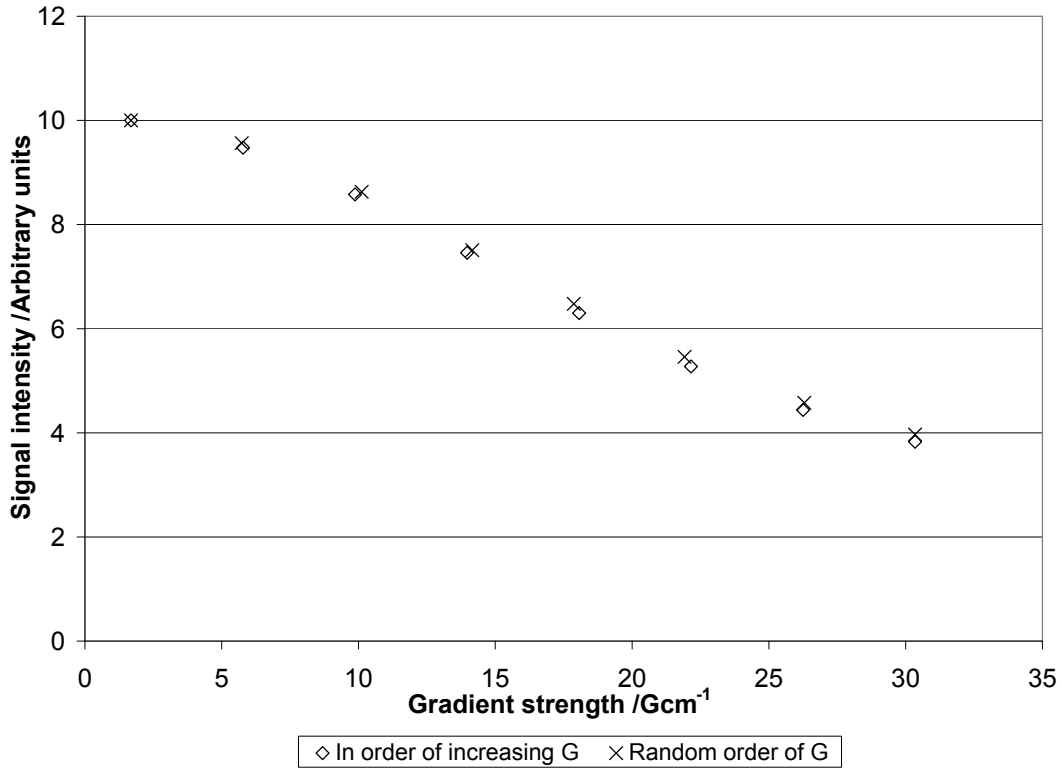

Figure 4.10: Comparison of data collection for increasing gradient strength and random order

Choice of diffusion model

The signal attenuation measured gave non-linear log attenuation plots, with systematic deviation from linearity, as can be seen in the example plots shown in Figure 4.11. Figure 4.11 shows the log attenuation plots for two batches of high molecular weight microspheres, drug encapsulated (MS029) and blank (MS030) at time zero and at around four and a half hours after immersion in an aqueous medium. The non-linearity shown in the data suggests either restricted diffusion, a multi-component system, or, a combination of the two systems. A multi component system is proposed here, as water is contained within three environments, the bulk, the 'bubble' pores and the polymer matrix. Assuming that the diffusion coefficient of the water contained in the matrix is several orders of magnitude smaller compared to that in the bulk and the 'bubble' pores and the proportion of water contained within the matrix is small ($\ll 2\%$), the signal attenuation will be dominated by the bulk and 'bubble' pore components. The multi-component model is, therefore, reduced to a two component fit, free water and water trapped within the 'bubble' pores of the microspheres, equation 4.3[‡], where D_1 and D_2 are the diffusion coefficients of water in free

[‡]As described by Messaritaki et al. (2005), using the notation of ζ

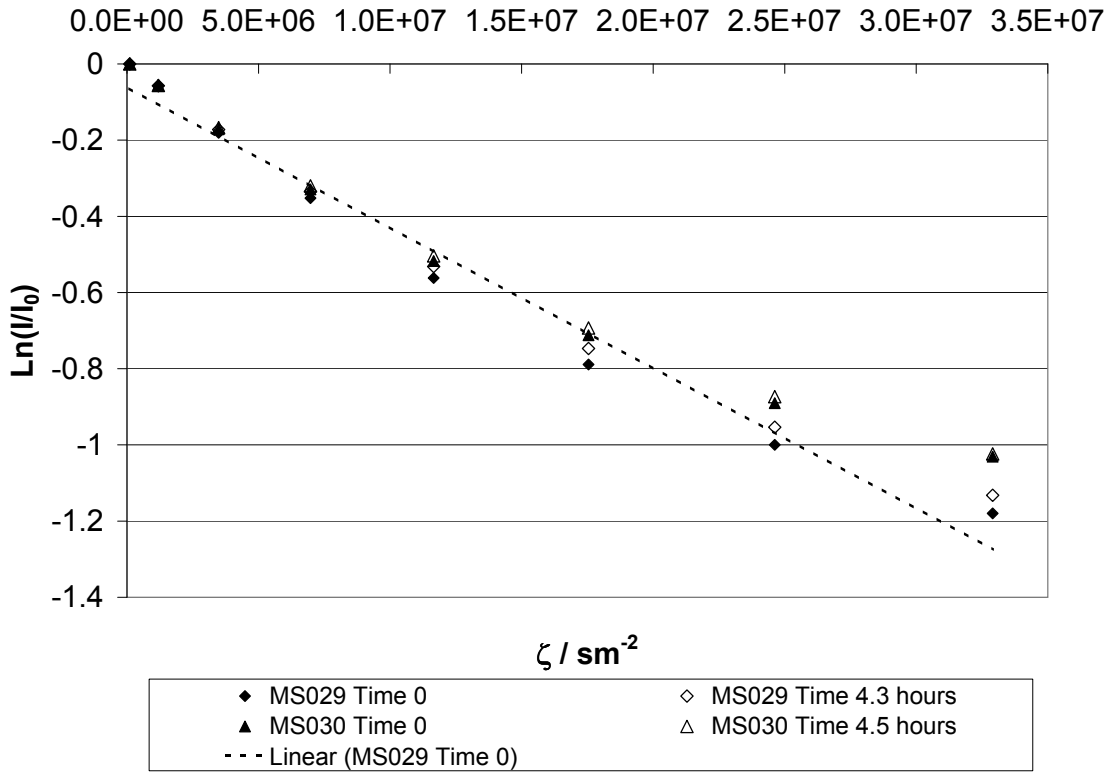

Figure 4.11: Log attenuation plots for drug encapsulated (MS029) and blank (MS030) microspheres immediately and around 4.5 hours after immersion

solution and trapped water within the pores of the microspheres respectively. The fraction of water in the free solution phase is denoted as p, therefore, $(1-p)$ is the remainder fraction of water that is assumed to be in the second phase, trapped water within the microsphere pores.

$$I = I_0(p\exp(-D_1\zeta)+(1-p)\exp(-D_2\zeta)) \tag{4.3}$$

The chosen diffusion time is such that both unrestricted diffusion in the bulk and restricted diffusion in the 'bubble' pore phase is possible, as discussed in Section 4.2.4. For the diffusion time studied, the *rms* displacement of water in the bulk is 24 μm and within the 'bubble' pores is of the order of 9.3–10.0 μm for drug encapsulated microspheres and 7.6–8.9 μm for blank microsphere. From SEM images of identically prepared batches studied with NMR PFG the 'bubble' pores diameter is 1–25 μm for drug encapsulated microspheres and 10–20 μm for blank microspheres . The average cavity radii determined from PFG, calculated by equation 4.2 for the microspheres immediately after immersion equates to average diameters of 17 μm for drug encapsulated microspheres and 14 μm for blank

microspheres, which agrees with the upper limit of the 'bubble' pore diameter seen by SEM. One explanation for the difference seen between SEM and PFG determined diameter is that the SEM images are of dry microspheres whilst the PFG experiments are carried out on wet microspheres.

Calibration of the bulk diffusion coefficient for water in a water and deuterium oxide mixture

To reduce the number of free parameters within the two-component fit, the free diffusion coefficient of water may be estimated, thus, the number of variables is three, the entrapped water diffusion coefficient, D_2, the fraction of free water, p and the reference signal intensity, I_0. The value of the free water diffusion coefficient, D_1, for use in multicomponent modelling for PFG experiments can be determined both experimentally and theoretically as described below.

Experimental determination of bulk water diffusion coefficient

A sample of the $D_2O : H_2O$ solution used for the ambient temperature PFG experiments was placed in an NMR tube and the free diffusion coefficient of water was measured. The parameters used were the same as those used for ambient condition PFG experiments.

Theoretical determination

Values of the self-diffusion of both water and deuterated water at various ambient temperatures are given by Mills (1973). These values can be used to calculate the diffusion coefficient for each solvent at a given temperature. An overall diffusion coefficient for a mixture of the two solvents can be calculated using equation 4.4,

$$D_1 = f_w \times D_w + f_d \times D_d \tag{4.4}$$

where D_1 is the overall diffusion coefficient of the mixture at temperature T, D_w and D_d are the self-diffusion coefficient of pure water and deuterated water at a temperature T, and f_w, f_d are the fraction of water and deuterated water present in the mixture.

Both methods have been used to determine the bulk diffusion coefficient of water, D_1 for a 1 % H_2O in D_2O mixture. The measured value of $2.17 \times 10^{-9} m^2 s^{-1}$ was significantly higher that the calculated value of $1.88 \times 10^{-9} m^2 s^{-1}$, a difference of 15 %. Possible causes for this discrepancy could be that the fraction of water in the D_2O is incorrect, or the temperature at which the diffusion coefficient was measured was greater than that used for the theoretical calculation. If the error was purely due to an incorrect value of f_w, then applying the measured diffusion coefficient to equation 4.4, the value of f_w would be around 0.7, much higher than the assumed value of 0.01, in order to compensate for the

difference found. If the error was purely due to temperature, then the difference equates to around $+4$ to 5 K. During the cryodiffusometry experiments described later in Chapter 6, a sample temperature increase of 3 to 4 K was found at a probe set temperature of 298 K. It is, therefore, suggested that the greatest contribution to the error between the theoretical value and the measured value of diffusion coefficient is temperature, with a possible smaller contribution from the error in the fraction of water in D_2O. In calculations, therefore, the measured value of diffusion coefficient is used as an estimate for the free water diffusion coefficient for the system. Under controlled temperature conditions, the diffusion coefficient for pure water was measured. It was found that the experimental value for D_w agreed with theoretical value to within $\pm 0.1 \times 10^{-9} m^2 s^{-1}$, giving an error of less than 5 %.

A sensitivity analysis was carried out to investigate the effects of changing D_1 on the predicted values of the diffusion coefficient of the entrapped water, D_2, the second component. It was found that a 10 % increase in D_1 can increase D_2 by an average of 25 %, and a 10 % decrease in D_1 can cause an average decrease in D_2 of 63 %, however, a 5 % decrease in D_1 causes an average decrease in D_2 of 37 %. The effect on the estimated cavity size caused by a change in the set value of D_1 can be seen in Table 4.3.

Batch	$D_1 \times 10^9 m^2 s^{-1}$	Calculated cavity size range over experiment time / μm
Drug encapsulated	2.1	8.5–9.1
Drug encapsulated	1.9	4.2–7.0
Blank	2.1	7.0–8.1
Blank	1.9	2.0–7.6

Table 4.3: Cavity radius determined from diffusion coefficient D_2 for changes in estimated value of the bulk diffusion coefficient D_1

Comparison of blank and 5-FU encapsulated high molecular weight microspheres studied by PFG at 298 K for 250 hours after immersion in aqueous media

For both the drug encapsulated and blank microspheres a significant increase in the diffusion coefficient of the 'bubble' pore contained water is seen in the first five to seven hours after immersion, see Figure 4.12. Significance was defined such that the difference between the calculated diffusion coefficient and the mean of the diffusion coefficient, between six and eighteen hours, was greater than five times the standard deviation. The absolute values for the diffusion coefficients are different for the two batches, however the magnitude of the change seen in this initial period is very similar, an increase of $0.08 \times 10^{-9} m^2 s^{-1}$. It has previously been suggested that these changes in the diffusion coefficient are indicative of the polymer swelling in the aqueous media and, therefore, the 'bubble' pores increasing in size (Messaritaki et al., 2005). For drug encapsulated microspheres the average 'bubble' pore

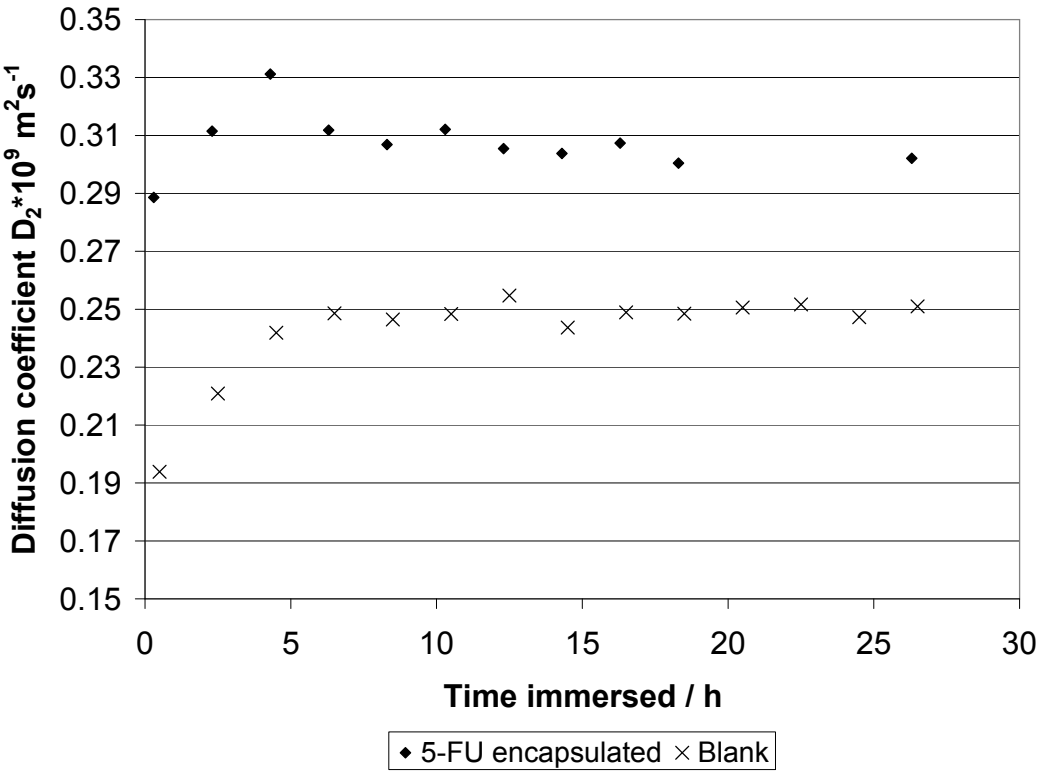

Figure 4.12: Diffusion coefficient of entrapped water for high molecular weight microspheres for the first 30 hours after immersion into aqueous media

radius increases from 8.5 to 9.1 μm in the first six hours and in the blank microsphere the average 'bubble' pore radius increases from 7.0 to 7.9 μm in the first six and a half hours. Following this initial period, the diffusion coefficient remains at a steady value, within five standard deviations from the mean, until around thirty hours after immersion, as shown in Figure 4.13.

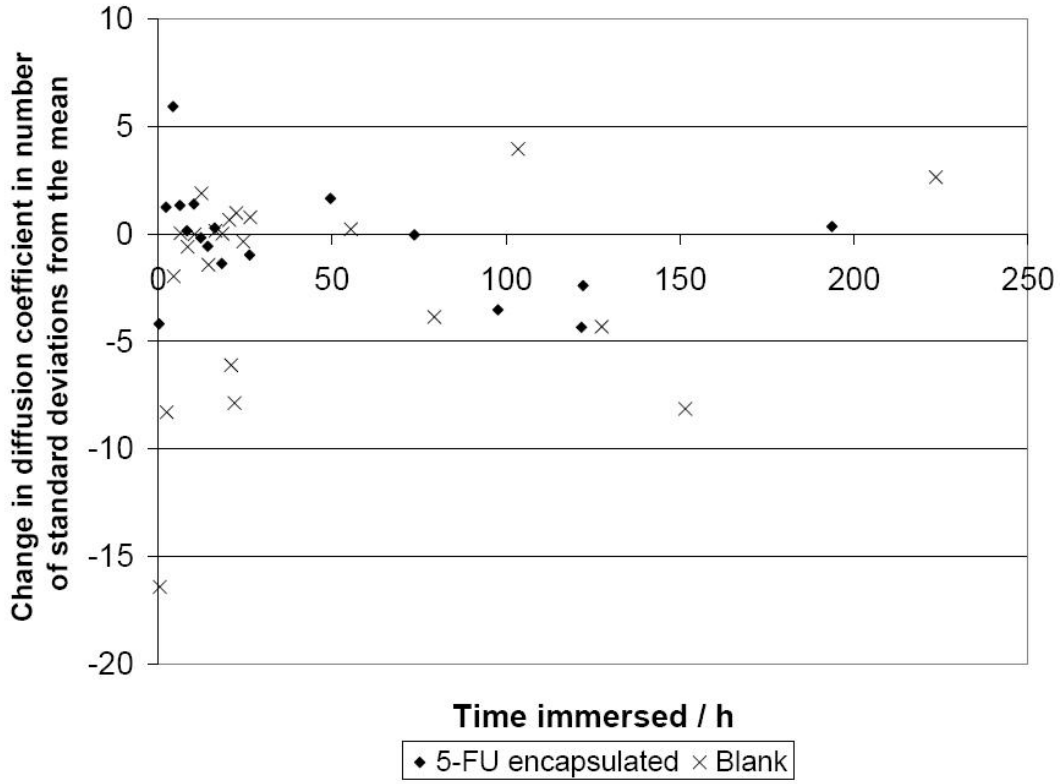

Figure 4.13: Change in diffusion coefficient of entrapped water in terms of the number of standard deviations from the mean, for high molecular weight microspheres for the first 250 hours after immersion into aqueous media

From Figure 4.14 it can be seen that, for the drug encapsulated microspheres, a further increase in diffusion coefficient occurs between thirty and fifty hours, followed by a decrease after a hundred hours. The blank microspheres show a steady diffusion coefficient until fifty hours and then less stability of diffusion coefficient after fifty hours, possibly indicating instability in the polymer structure at this time. It is possible that these changes are an early sign of polymer degradation affecting the structure of the polymer, although at this time, no degradation of the microspheres is noticeable to the eye.

The increase in diffusion coefficient within the 'bubble' pores of the polymer matrix suggests the average mass transport for water is improving with immersion time. As the mobility of water increases, drug molecule or polymer degradation product diffusivity within the network of 'bubble' pores within the microsphere should improve. Combining these findings with the additional experiments in Chapter 6, looking at water mobility within the polymer matrix structure, a better understanding of the polymer evolution and subsequent drug release should be possible.

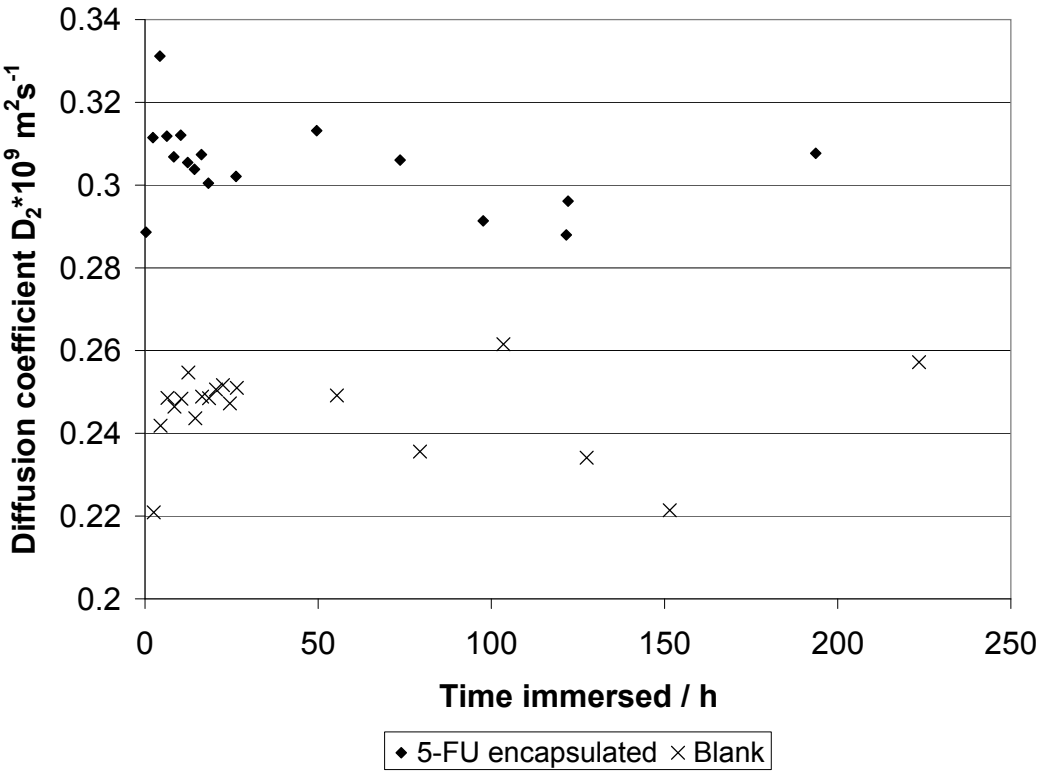

Figure 4.14: Diffusion coefficient of entrapped water for high molecular weight microspheres for the first 250 hours after immersion into aqueous media

4.5 Conclusions

The SEM images of the microsphere internal structure provide a source of comparison for the physical characteristics determined from the PFG experimental data. Agreement between observed 'bubble' pore sizes and estimated cavity sizes validate the appropriate use of the chosen PFG model and its interpretation. Confidence in the methods applied to the interpretation of PFG data is important for later cryodiffusometry experiments, where the length scale under investigation is beyond that of the resolution of SEM.

The selected preparation method of double emulsion technique has been used successfully to produce both blank and drug encapsulated microspheres with high molecular weight PLGA. Low molecular weight blank microspheres and 5-FD containing microspheres have also been achieved, although encapsulation of 5-FD is has not been confirmed. Double walled microspheres without encapsulated drug have also been successfully produced. The flexibility and success of using the double emulsion method, makes this the preparation method of choice for this work. Whilst some inter- and intra-batch variations are expected, microsphere sizes and shapes are within expected values. With microspheres ranging in di-

ameter from tens of micrometers to a few hundred micrometers. Pore sizes are of generally of the order of 20 μm and less with heterogeneous distribution. Pores show interconnections providing pathways for transport within the 'bubble' pore network.

Microspheres produced have successfully been imaged by SEM, and NMR PFG diffusion coefficients measured, from which the cavity radii calculated agree with those seen in SEM. Whilst it has been possible to encapsulate the model drug 5-FU into the microspheres of high molecular weight polymer, it has not been possible to produce microspheres of low molecular weight with 5-FU encapsulated. It has been noticed that there are affects on the pore and microsphere structure when a model drug is encapsulated, or is present in the preparation of the microsphere. The presence of 5-FD in the preparation has shown changes in the internal microsphere structure despite no evidence of encapsulation in the dried microspheres. Further investigations into the structural evolution of PLGA matrix at the nano-scale are required to form a better understanding of the mechanism behind the release of drug molecules from such systems.

References

S. D. Allison. Effect of structural relaxation on the preparation and drug release behavior of poly(lactic-co-glycolic) acid microparticle drug delivery systems. *Journal of Pharmaceutical Sciences*, 97(6):2024–2037, 2008.

S. Arora, J. Ali, A. Ahuja, R. K. Khar, and S. Baboota. Floating drug delivery systems: A review. *Aaps Pharmscitech*, 6(3), 2005.

R. P. Batycky, J. Hanes, R. Langer, and D. A. Edwards. A theoretical model of erosion and macromolecular drug release from biodegrading microspheres. *Journal of Pharmaceutical Sciences*, 86(12):1464–1477, 1997. PLGA 50:50, double emulsion, time evolved, change in molecular weight, erosion mechanism, theoretical model.

J.-P. Benoit, N. Faisant, M.-C. Venier-Julienne, and P. Menai. Development of microspheres for neurological disorders: From basics to clinical applications. *Journal of Controlled Release*, 65:285–296, 2000.

T. Brand, S. Richter, and S. Berger. Diffusion nmr as a new method for the determination of the gel point of gelatin. *Journal of Physical Chemistry B*, 110(32):15853–15857, 2006.

P. Callaghan, K. W. Jolley, and J. Lelievre. Diffusion of water in the endosperm tissue of wheat grains as studied by pulsed field gradient nuclear magnetic resonance. *Biophysical Journal*, 28:133–142, 1979.

P. Callaghan, D. Macgowan, K. J. Packer, and F. O. Zelaya. Influence of field gradient strength in nmr-studies of diffusion in porous-media. *Magnetic Resonance Imaging*, 9 (5):663–671, 1991a.

P. T. Callaghan. *Principles of Nuclear Magnetic Resonance Microscopy*. Oxford Science Publications, 1991.

P. T. Callaghan, K. W. Jolley, and R. S. Humphrey. Diffusion of fat and water in cheese as studied by pulsed field gradient nuclear magnetic-resonance. *Journal of Colloid and Interface Science*, 93(2):521–529, 1983.

V. Challa, K. Kuta, S. Lopina, H. A. Cheung, and E. von Meerwall. Microporosity of bicontinuous nanoporous polymeric materials, characterized with restricted diffusion. *Langmuir*, 19(10):4154–4161, 2003.

S. Cohen, T. Yoshioka, M. Lucarelli, L. H. Hwang, and R. Langer. Controlled delivery systems for proteins based on poly(lactic/glycolic acid) microspheres. *Pharmaceutical Research*, 8(6):713–720, 1991.

T. Ehtezazi, C. Washington, and C. Melia. Determination of the internal morphology of poly (d,l-lactide) microspheres using stereological methods. *Journal of Controlled Release*, 57: 301–314, 1999.

C. T. Eng, R.Lin, and C.-H. Wang. Fabrication of double-walled microspheres for the sustained release of doxorubicin. *Journal of Colloid and Interface Science*, 291(1):135–143, 2005.

E. J. Fordham, S. Gibbs, and L. Hall. Partially restricted diffusion in a permeable sandstone:observations by stimulated echo pfg nmr. *Magnetic Resonance Imaging*, 12(2): 279–284, 1994.

S. Freiberg and X. Zhu. Polymer microspheres for controlled drug release. *International Journal of Pharmaceutics*, 282:1–18, 2004.

S. Freitas, H. P. Merkle, and B. Gander. Microencapsulation by solvent extraction/evaporation: Reviewing the state of the art of microsphere preparation process technology. *Journal of Controlled Release*, 102:313–332, 2005.

P. J. Goodhew and F. J. Humphreys. *Electron Microscopy and Analysis*. Taylor & Francis, second edition, 1988.

M. P. Hollewand and L. F. Gladden. Transport heterogeneity in porous pellets .1. pgse nmr-studies. *Chemical Engineering Science*, 50(2):309–326, 1995.

X. Huang and C. S. Brazel. On the importance and mechanisms of burst release in matrix-controlled drug delivery systems. *Journal of Controlled Release*, 73(2-3):121–136, 2001.

S. Jaraswekin, S. Prakongpan, and R. Bodmeier. Effect of poly(lactide-co-glycolide) molecular weight on the release of dexamethasone sodium phosphate from microparticles. *Journal of Microencapsulation*, 24(2):117–128, 2007.

J. C. Kang and S. P. Schwendeman. Pore closing and opening in biodegradable polymers and their effect on the controlled release of proteins. *Molecular Pharmaceutics*, 4(1): 104–118, 2007.

D. H. R. Kempen, L. C. Lu, C. Kim, X. Zhu, W. J. A. Dhert, B. L. Currier, and M. J. Yaszemski. Controlled drug release from a novel injectable biodegradable micro sphere/scaffold composite based on poly(propylene fumarate). *Journal of Biomedical Materials Research Part A*, 77A(1):103–111, 2006.

S. Koennings, J. Tessmar, T. Blunk, and A. Gopferich. Confocal microscopy for the elucidation of mass transport mechanisms involved in protein release from lipid-based matrices. *Pharmaceutical Research*, 24(7):1325–1335, 2007. Koennings, Stephanie Tessmar, Joerg Blunk, Torsten Goepferich, Achim.

K. J. P. Leach and E. Mathiowitz. Degradation of double-walled polymer microspheres of plla and p(cpp:sa) 20:80. i. in vitro degradation. *Biomaterials*, 19:1973–1980, 1998.

T. H. Lee, J. J. Wang, and C. H. Wang. Double-walled microspheres for the sustained release of a highly water soluble drug: characterization and irradiation studies. *Journal of Controlled Release*, 83(3):437–452, 2002.

C. M. Lehr. Lectin-mediated drug delivery: The second generation of bioadhesives. *Journal of Controlled Release*, 65(1-2):19–29, 2000.

J. Li, G. Q. Jiang, and F. X. Ding. The effect of ph on the polymer degradation and drug release from plga-mpeg microparticles. *Journal of Applied Polymer Science*, 109 (1):475–482, 2008.

Y. Liu, L. K. Guo, L. Huang, and X. M. Deng. Preparation and properties of biodegradable polymer as a novel drug delivery system. *Journal of Applied Polymer Science*, 90:3150–3156, 2003.

X. S. Luan, M. Skupin, J. Siepmann, and R. Bodmeier. Key parameters affecting the initial release (burst) and encapsulation efficiency of peptide-containing poly(lactide-co-glycolide) microparticles. *International Journal of Pharmaceutics*, 324(2):168–175, 2006.

S. R. Mao, J. Xu, C. F. Cai, O. Germershaus, A. Schaper, and T. Kissel. Effect of wow process parameters on morphology and burst release of fitc-dextran loaded plga microspheres. *International Journal of Pharmaceutics*, 334(1-2):137–148, 2007.

A. Messaritaki, S. Black, C. F. v. d. Walle, and S. P. Rigby. Nmr and confocal microscopy studies of the mechanisms of burst drug release from plga microspheres. *Journal of Controlled Release*, 108(2-3):271–281, 2005.

R. Mills. Self- diffusion in normal and heavy water in the range 1-45'. *The Journal of Physical Chemistry*, 77(5):685–688, 1973.

T. Niwa, H. Takeuchi, T. Hino, N. Kunou, and Y. Kawashima. Preparations of biodegradable nanospheres of water-soluble and insoluble drugs with d,l-lactide glycolide copolymer by a novel spontaneous emulsification solvent diffusion method, and the drug release behavior. *Journal of Controlled Release*, 25(1-2):89–98, 1993.

K. Noorsal, M. Mantle, L. Gladden, and R. Cameron. Degradation and drug-release studies of a poly(glycolide-co-trimethylene carbonate) copolymer (maxon). *Journal of Applied Polymer Science*, 95:475–486, 2005.

N. A. Peppas. A model of dissolution-controlled solute release from porous drug delivery polymeric systems. *Journal of Biomedical Materials Research*, 17(6):1079–1087, 1983.

N. A. Peppas and J. J. Sahlin. Hydrogels as mucoadhesive and bioadhesive materials: A review. *Biomaterials*, 17(16):1553–1561, 1996.

L. J. C. Peschier, J. A. Bouwstra, J. d. Bleyser, H. E. Junginger, and J. C. Leyte. Cross-relaxation effects in pulsed-field-gradient stimulated-echo measurements on water in a macromolecular matrix. *Journal of Magnetic Resonance, Series B*, 110:150–157, 1996.

P. L. Ritger and N. A. Peppas. A simple equation for description of solute release i. fickian and non-fickian release from non-swellable devices in the form of slabs, spheres, cylinders or discs. *Journal of Controlled Release*, 5(1):23–36, 1987.

G. Ruan and S.-S. Feng. Preparation and characterization of poly(lactic acid)-poly(ethylene glycol)-poly(lactic acid) (pla-peg-pla) microspheres for controlled release of paclitaxel. *Biomaterials*, 24(27):5037–5044, 2003.

M. Sandor, D. Enscore, P. Weston, and E. Mathiowitz. Effect of protein molecular weight on release from micron-sized plga microspheres. *Journal of Controlled Release*, 76:297–311, 2001.

J. Siepmann, N. Faisant, J. Akiki, J. Richard, and J. P. Benoit. Effect of the size of biodegradable microparticles on drug release: experiment and theory. *Journal of Controlled Release*, 96(1):123–134, 2004.

F. Ungaro, M. Biondi, I. d'Angelo, L. Indolfi, F. Quaglia, P. A. Netti, and M. I. La Rotonda. Microsphere-integrated collagen scaffolds for tissue engineering: Effect of microsphere

formulation and scaffold properties on protein release kinetics. *Journal of Controlled Release*, 113(2):128–136, 2006.

J. K. Vasir, K. Tambwekar, and S. Garg. Bioadhesive microspheres as a controlled drug delivery system. *International Journal of Pharmaceutics*, 255(1-2):13–32, 2003.

E. Vey, C. Roger, L. Meehan, J. Booth, M. Claybourn, A. F. Miller, and A. Saiani. Degradation mechanism of poly(lactic-co-glycolic) acid block copolymer cast films in phosphate buffer solution. *Polymer Degradation and Stability*, 93:1869–1876, 2008.

L. Wang, C.-S. Chawa, Y.-Y. Yang, S. M. Moochhalab, B. Zhaob, S. Ng, and J. Heller. Preparation, characterization, and in vitro evaluation of physostigmine-loaded poly(ortho ester) and poly(ortho ester)/ poly(d,l-lactide-co-glycolide) blend microspheres fabricated by spraydrying. *Biomaterials*, 25:3275–3282, 2004.

M. v. d. Weert, R. v. t. Hof, J. v. d. Weerd, R. M. Heeren, G. Posthuma, W. E. Hennink, and D. J. Crommelin. Lysozyme distribution and conformation in a biodegradable polymer matrix as determined by ftir techniques. *Journal of Controlled Release*, 68:31–40, 2000.

Y. Y. Yang, H. H. Chia, and T. S. Chung. Effect of preparation temperature on the characteristics and release profiles of plga microspheres containing protein fabricated by double-emulsion solvent extraction/evaporation method. *Journal of Controlled Release*, 69(1):81–96, 2000.

Chapter 5

Cryoporometry studies of PLGA microspheres

5.1 Introduction

Cryoporometry is applied to the investigation of the structure of PLGA microspheres, for use as controlled drug delivery devices. Microsphere samples are immersed in an aqueous media and the water contained in the PLGA matrix is frozen and melted to study the pore size characteristics. Changes in the freezing point of the imbibed water show changes to the polymer matrix structure at increased immersion times. Three batches of microspheres are studied over a period of approximately one hundred days, batches are of high and low molecular weight polymer with encapsulated drug, and low molecular weight without encapsulated drug. Cryoporometry provides a means to study the nanoscale matrix structure of the polymer microspheres in terms of both the access channels, or pore necks, and pore body sizes.

5.2 Background and Theory

Cryoporometry has previously been used to study nanoporous materials such as silicas (Schreiber et al., 2001; Valckenborg et al., 2001), titania films (Vargas-Florencia et al., 2007) and some polymeric materials (Hansen et al., 2005; Petrov et al., 2006a) providing pore size information gathered from the melting characteristics of the imbibed liquid. Petrov et al. (2006a) used cryoporometry to study the polymer swelling over four days, investigating pore sizes of 30–70 nm (assuming a Gibbs-Thomson parameter of 50 nmK). The measured temperature was calibrated to the actual sample temperature using the bulk melting point

only, as discussed previously in Chapter 3 this is not as accurate as direct measurement of the sample temperature with a thermocouple.

Here, cryoporometry is applied to examine the structural changes in the polymer matrix of PLGA microspheres over longer time periods (≥ 90 days) in order to better understand the mechanism behind drug release behaviour from such a system. The complex structure of the polymer matrix will be described in terms of pore neck sizes determined from freezing characteristics and the pore body sizes determined from the melting characteristics, as described previously in Chapter 3. Changes in the pore sizes can be used in a qualitative assessment of the causes of the drug release mechanism from such materials. The neck size, or size of the access channels, restrict the motion of larger molecules into and out of the polymer matrix. The cavities between the polymer chains, in which a drug molecule may be encapsulated, can influence the pathway the molecule must travel through the matrix, before being released into the bulk medium. Polymer swelling and degradation are thought to dictate the release of an entrapped molecule as described in Chapter 4, however, with structural studies at the nanoscale level it is hoped that a greater understanding of the polymer matrix will aid design of new drug release systems.

On first freezing the microspheres, the bulk and 'bubble' pore contained water are supercooled and freeze together. The freezing front can progress from the bulk into the 'bubble' pore network through the micrometer scale connections between the 'bubble' pores. These connections are clearly visible in the SEM images discussed in Chapter 4. The second stage of the freezing of water contained in the polymer matrix, now progresses through a series of freezing fronts that originate from the external surface of the microsphere and the surface of the 'bubble' pore ice. The freezing fronts move through the matrix probing the necks, or access channels, that form a pathway into the matrix until all the matrix contained water is frozen, as described in Chapter 3. As the sample temperature is increased, the matrix contained water begins to melt in order of increasing pore size in which it is contained, see Figure 5.1. If the sample is only partially thawed, pockets of ice contained in the larger pore bodies within the matrix remain frozen, whilst the smallest pore body contained water is melted. From this point a reduction in temperature sees the freezing fronts progressing from these ice pockets within the matrix in addition to those from the external bulk and the 'bubble' pores. The observed neck size on re-freezing is larger than that seen during the first freezing process, suggesting that the smallest access channels have already been passed by the freezing front. Therefore, these smaller access channels lie between the bulk or 'bubble' pore and the internal matrix. When considering drug release, these smaller access channels are significant in controlling the progress of the drug molecule from the internal polymer matrix into the release medium. Where as the larger pore necks will control movement of

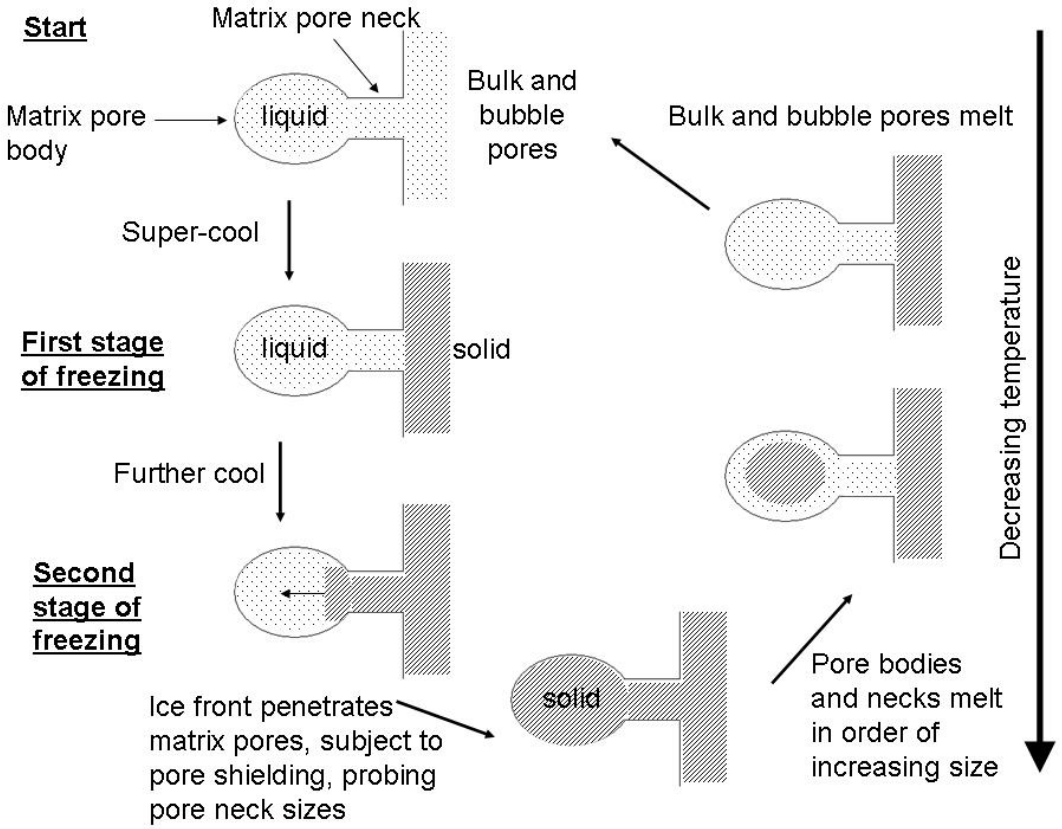

Figure 5.1: Diagram to show the freezing and thawing mechanism for water contained in polymer matrix

the drug molecule within the internal polymer matrix. Once within the release medium, the drug pathway out of the microsphere is determined by diffusion within the release medium through the micrometer scale 'bubble' pore network.

5.3 Experimental

Microspheres were prepared by double emulsion technique as described earlier in Chapter 4. From a given batch of microspheres approximately 10–20 mg were placed into a 100 μm pipette tip sealed at the lower end with parafilm. The pipette tip had been cut down in length such that its maximum diameter would fit into a 5 mm thin-walled NMR tube. The aqueous test medium was then added to the microspheres within the pipette tip and the top of the tip was sealed with parafilm. The sealed pipette tip was then placed between two susceptibility plugs within the NMR tube. The microspheres and aqueous media were placed into the pipette tip rather than directly into the NMR tube to protect the NMR tube from shattering when the aqueous medium froze and expanded.

The thermocouple was placed through the axial hole in the top susceptibility plug, piercing the parafilm seal over the top of the pipette tip, and was in direct contact with the aqueous solution containing the microspheres. In contrast to previous ambient temperature experiments, the aqueous media for cryodiffusometry did not contain any deuterium oxide. This increased the overall signal intensity seen for the partially frozen sample and removed any effects on cryoporometry results caused by the difference in melting point of deuterium oxide, 3.8 °C, and water, 0 °C. Differences in the freezing and melting mechanisms between water and deuterium oxide caused by the greater mass of deuterium was, therefore, removed.

Freeze-thaw cycles were carried out on the PLGA microsphere samples contained within the pipette tips. A simple spin echo pulse sequence, as described in the appendix Section A.7, was used with an echo time of 10 ms. The sample was cooled and warmed with step changes of 1 K in the region of interest. The sample was allowed to equilibrate for 9 minutes at each temperature before an acquisition was taken. This equilibration time had been determined by previous experiments as being sufficient for the microsphere sample to reach an equilibrium state.

On some cycles the sample was part thawed and refrozen to investigate possible shielding effects between the bulk or bubble pores and the internal matrix structure. Which was thought may affect the drug release profile in terms of the mass transport within the matrix and out of the matrix into the release media.

5.4 Results and Discussion

5.4.1 Change of aqueous medium

Initial cryoporometry curves of water imbibed microspheres showed supercooling of the bulk and 'bubble' pore contained water followed by the freezing of water within the polymer matrix. On warming the sample, very little melting was seen below the bulk melting temperature, therefore, very little information could be gained from the melting curve. An example of the freeze-thaw curves observed with water can be seen in Figure 5.2. To eliminate the possible insulating effects of ice on the temperature experienced in the polymer matrix, very long equilibration times of more than 3 hours were used on the thawing curves. No further melting was seen at these extended equilibration times before the bulk began to melt, therefore, very little of the melting curve for microspheres immersed in pure water could be seen. Water was replaced by a sodium chloride solution, the presence of salt in bulk water has the effect of lowering the freezing point temperature, for a 5 % w/v sodium chloride solution the bulk freezing temperature is 270 K (Najibi et al., 2006). By suppressing

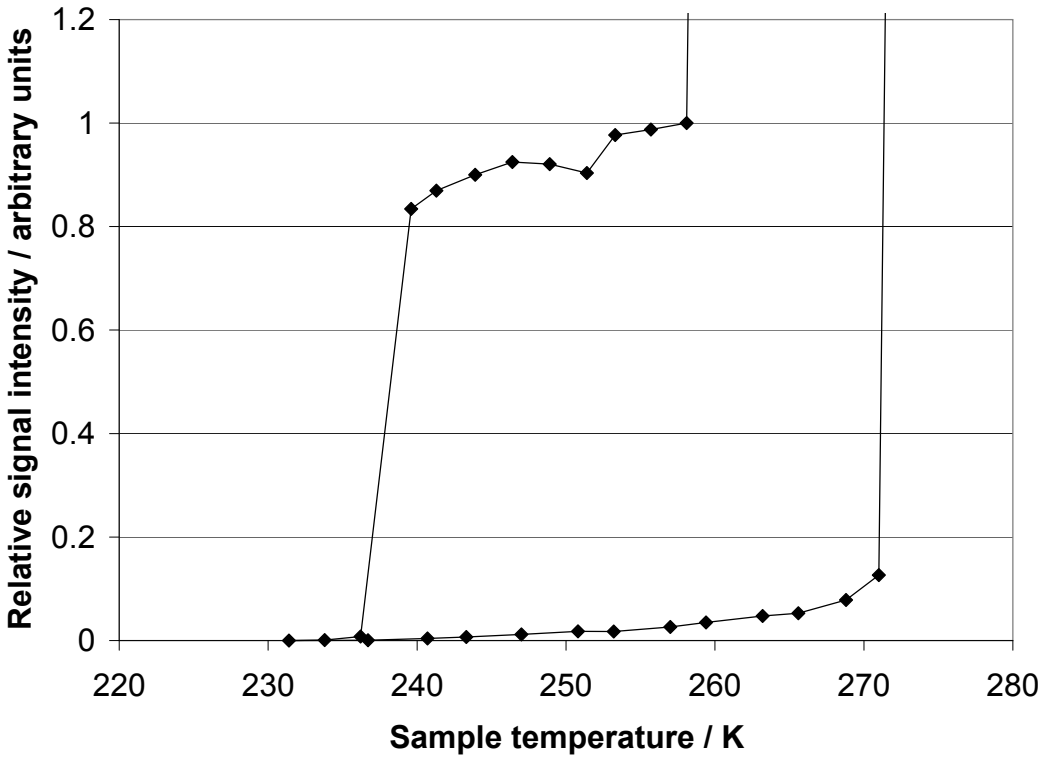

Figure 5.2: Freeze-thaw hysteresis curve observed for water imbibed in the polymer matrix of PLGA microspheres

the bulk melting point it is expected that the melting point depression for imbibed fluid will be increased and more of the melting curve may be observed. An experiment with the sol-gel silica material used in Chapter 3 showed the melting curve for the whole pellet sample was depressed by 2 K with 5 % w/v sodium chloride solution and maintained the same profile as water, see Figure 5.3.

The addition of salt requires further consideration with regards to its possible effects on the freezing mechanism and any interaction with the polymer. Salt exclusion can occur during freezing, where by, a compartment of water within the salt solution begins to freeze and the salt is forced to the non-freezing compartment of the solution, this compartment, therefore, becomes more concentrated and its freezing point is reduced further. On further decreasing the temperature, a second compartment of the water or weak saline begins to freeze and forces the salt into a yet more concentrated compartment. The effect of salt exclusion is to increase the temperature range over which the freezing of a solution occurs from a finite value to an extended range of freezing temperatures of many degrees (Najibi et al., 2006). On melting, the higher concentration solutions melt first, followed by those compartments of less concentrated solution, thus increasing the temperature range

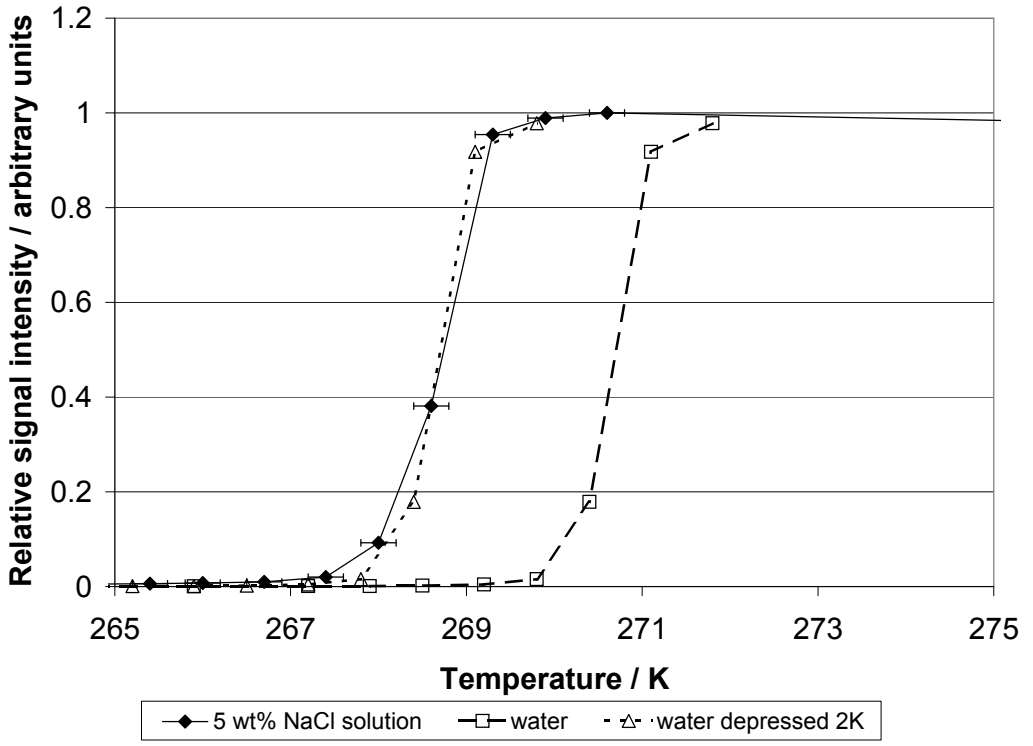

Figure 5.3: Melting curve for sol-gel silica whole pellet sample for water and 5 % sodium chloride solution

observed for melting. This effect will depend on the distribution of the salt ions within solution and would, therefore, change the freezing and melting curve observed for each repeated experiment. The effect of salt exclusion is not seen in the freezing of the salt solution within the silica pellets shown in Figure 5.3, as the shape of the freezing curve observed for salt solution is the same as that for water within experimental error. Any effect of salt exclusion would increase the range of the observed freezing behaviour.

It is also acknowledged that there may be some interaction between the salt and polymer. In these experiments looking at drug release systems it is considered that this effect may mimic any interactions of ions present within the blood or tissue, providing a better understanding of the behaviour of these systems in vivo. Therefore, salt solutions were used for the following studies of PLGA microsphere in this chapter and the cryodiffusometry studies in Chapter 6. In addition, changes in the salt concentration with time must also be considered. These changes may be the result of evaporation of water from the solution or salt interactions with the polymer and would cause a systematic decrease in the freezing and melting point of the bulk solution. Bulk freezing is subject to supercooling, and no such effect is seen in the bulk melting point.

5.4.2 Cryoporometry cycles

The cryoporometry results for three different batches of microspheres are presented and discussed, low molecular weight with 5-FD encapsulated, MS045, high molecular weight with 5-FD encapsulated, MS043, and low molecular weight without encapsulated drug, MS041. Whilst cryoporometry results provide structural information, diffusometry results provide mass transport information, and when combined the two techniques give a more complex interpretation of how the structure and mass transport are related within the PLGA microsphere systems. Cryodiffusometry results for these batches are discussed in Chapter 6. To this end, it is expected that a drug release profile may be better understood and the design of such drug delivery systems may be optimised.

Calculation of relative signal intensity

Absolute signal intensity, I_a, for a given experiment is calibrated to give the relative signal intensity, I_r, at a given temperature. The relative signal intensity is calculated in terms of the absolute signal intensity for the matrix contained water that remains unfrozen after bulk supercooling, I_m, and the minimum absolute signal intensity when all the water is frozen, I_{min}, as in equation 5.1. Thus, a relative signal intensity of 1 represents all the matrix contained water as molten and a relative signal intensity of 0, all water is frozen.

$$I_r = \frac{I_a - I_{min}}{I_m - I_{min}} \tag{5.1}$$

The NMR signal intensity is affected by temperature, a correction can be made based on the Curie Law (Mitchell et al., 2008). The signal intensity at a given temperature, I_T, can be calculated relative to the signal intensity at a reference temperature, 273 K, I_{273}, and the temperature, T, as expressed in equation 5.2*.

$$I_T = I_{273} \times \frac{273}{T} \tag{5.2}$$

According to this equation the signal intensity should increase with a decrease in temperature, for a totally molten sample, this effect is seen. However, this relationship does not account for the change in signal intensity due to portions of the sample freezing as temperature decreases. The absolute signal intensity measured, I_a, may be adjusted for temperature

*As expressed in Mitchell et al. (2008)

in a similar manner, I_{adj}, equation 5.3, where T_{ref} is the reference temperature.

$$I_{adj} = I_a \times \frac{T_{ref}}{T} \tag{5.3}$$

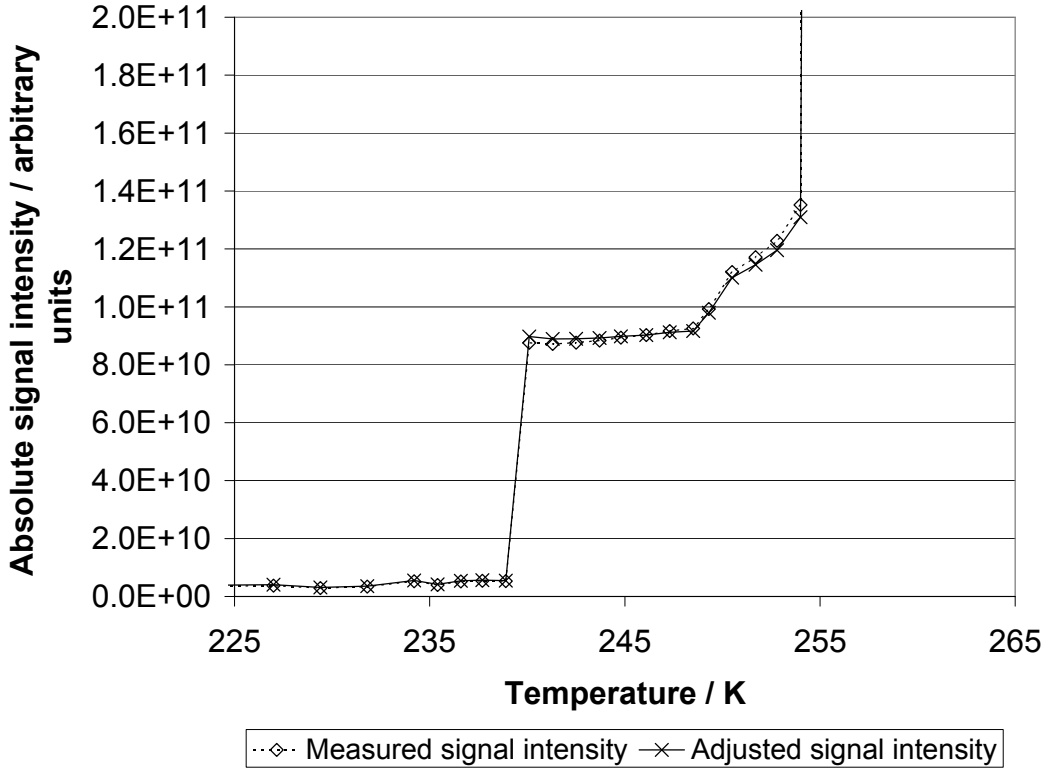

Figure 5.4: Absolute signal intensity against temperature for microsphere sample, raw data and corrected for temperature effects

The significance of this effect was investigated for the observed freezing curves for a microsphere sample, the raw data and corrected data curve can be seen in Figure 5.4, the reference temperature used was 246.1 K, a mid-value in the region of interest. It can be seen in Figure 5.4 that over the range of interest the effect of temperature on the signal intensity is small compared to the change in intensity due to sample freezing, and is less than experimental fluctuations. This effect has negligible impact on the pore size distribution obtained from cryoporometry data and is, therefore, not included in the calculations of relative signal intensity, defined previously, equation 5.1.

Estimate of experimental error values

The microsphere samples immersed in aqueous media had a greater sample depth than the silica pellet samples investigated in Chapter 3, but have better heat transfer properties,

therefore, it was considered reasonable to use the measured temperature variation in the silica samples as the error in the measured temperature for the microsphere samples, ± 0.2 K. Greater accuracy was not required for differentiating the pore sizes determined from cryoporometry. For a temperature error of ± 0.2 K, the calculated error in pore size was a maximum of ± 0.05 nm within the range of interest. Changes seen in pore size were generally much greater than this error.

Repeatability of cryoporometry cycles

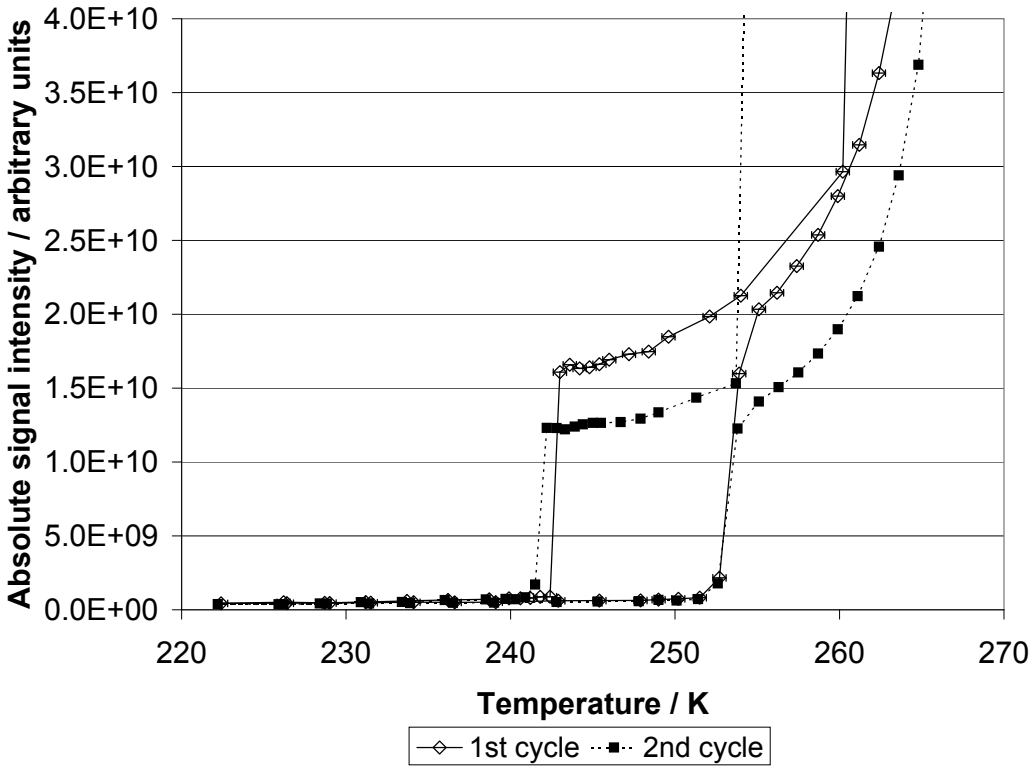

Figure 5.5: Repeat cryoporometry cycles for microsphere batch MS043 at day 1 after immersion

After initial immersion in aqueous media consecutive cryoporometry cycles were conducted to establish the repeatability of the cryoporometry cycles. Figure 5.5 shows two cycles for microsphere batch MS043 at day 1 of immersion, good agreement is seen on the thawing curve suggesting that the structure has not been disrupted by the freeze-thaw process, and that salt exclusion is not present. After the bulk and 'bubble' pore containing water has frozen, it can be seen that there is a shift in the freezing curve toward a lower temperature for the second cycle, corresponding to a smaller neck size. Between the two cycles there is a short period of time, a few hours, in which the aqueous medium is in the

liquid state, therefore, the shift of the freezing curve observed is assigned to a change in the pore neck sizes during this early stage of immersion. As discussed previously in Chapter 4, a significant change in the diffusion behaviour and the estimated cavity size is seen in the early immersion studies of PLGA microspheres. It is understood that polymer chains relax in aqueous media and the polymer is said to swell (Messaritaki et al., 2005), this would affect the arrangement of the polymer chains and, therefore, the structure that is observed at the nanometer scale. The magnitude of the change is small but still significant, as the change in freezing temperature seen is greater than twice the experimental error expected in the temperature measured, ± 0.2 K, as shown by the error bars on cycle 1.

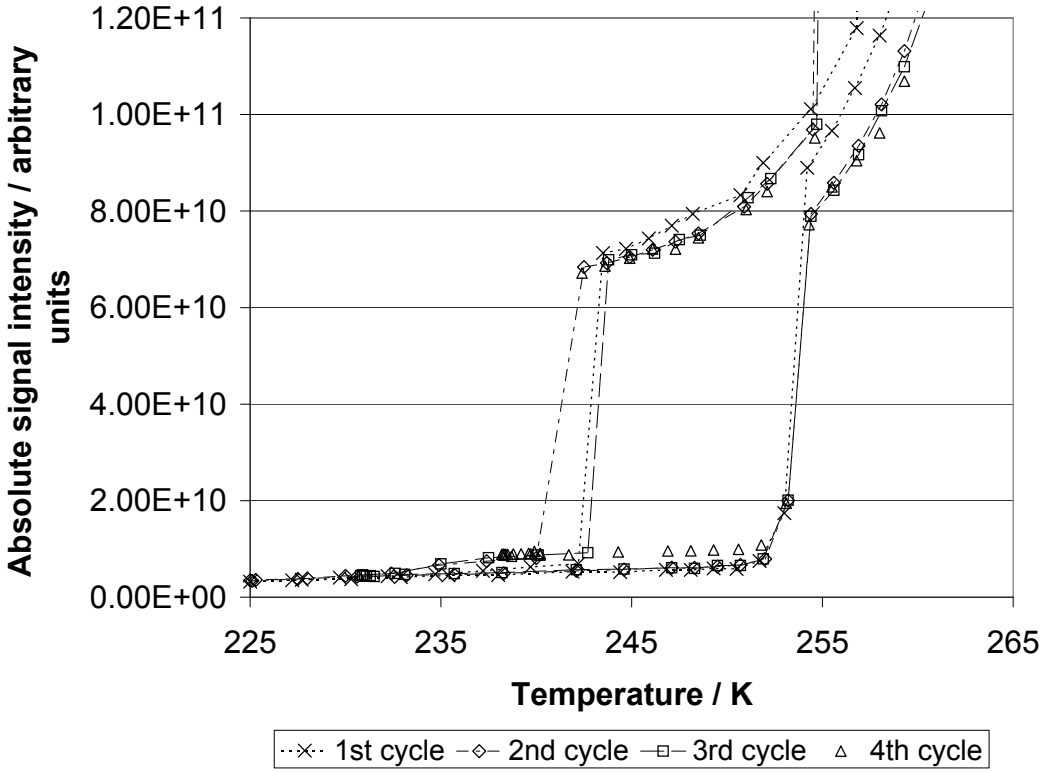

Figure 5.6: Repeat cryoporometry cycles for microsphere batch MS045 at day 1 after immersion

Consecutive freeze-thaw cycles on day 1 after immersion for a second batch of microspheres, MS045, are shown in Figure 5.6. For this batch, a time delay of 7 hours between the first and second cycles was experienced, when the microspheres were immersed in fully molten aqueous media. A decrease in absolute signal intensity is observed, a sign of the void fraction, or volume of water observed in the matrix has changed. The third and fourth cycles were conducted without further time delays and show excellent agreement in terms of thawing curve position and relative signal intensity. A shift in the freezing curve is seen between the second and third cycles but no change is seen between the third and fourth

cycle. This suggests that structural change occurs between the second and third cycle, but not between the third and fourth cycle. These experiments provide confidence that the results obtained show time dependent changes in structure that are not artifacts of the experimental technique. The repeatability of the cryoporometry cycle is also demonstrated when negligible change in the structure has occurred.

Intra-batch variability of cryoporometry cycles was assessed by comparing results obtained for different samples from the same batch at the same immersion time. Negligible differences were observed in those samples tested, suggesting that samples were representative of the batch from which they were taken, see Appendix Section A.2 for an example data set.

5.4.3 Time-resolved cryoporometry studies on PLGA microspheres

Time-resolved cryoporometry studies on Low molecular weight PLGA microspheres with encapsulating drug 5-FD, batch MS045

Microspheres were made with low molecular weight 50:50 PLGA by double emulsion evaporation technique, with the model drug 5-FD encapsulated in the internal aqueous phase as described previously in Chapter 4. Cryoporometry cycles were conducted on a sample of micropsheres immersed in 5 % w/v sodium chloride solution at increasing times after immersion. Freezing curves of these cycles are shown in Figure 5.7, for clarity data points have been connected by dashed lines as a guide to the eye. Also, the data is presented on two Figures, 5.7a for days 1—34, and 5.7b for days 42–109. The results for the first day of immersion are shown on both Figures 5.7a and 5.7b as a reference. As discussed in Chapter 3 the freezing curve is indicative of the network entrances, or necks, within the pore structure, therefore, any changes in the freezing curve are attributed to changes in the matrix pore necks. When describing pore necks in the matrix this refers to the gaps in the backbone of the polymer chains, or entrance points between the polymer chains, through which the water molecules may pass. It is thought that these openings provide access channels for transport of molecules through the polymer matrix. An encapsulated drug molecule must also pass through these channels if it is to traverse the matrix and eventually be released. Therefore, the size of these channels may control the route of passage for an encapsulated drug molecule.

There are two significant changes observed over time after the immersion of microspheres, firstly the change in temperature at which the majority of the matrix water freezes, and secondly, the number of stages in which the matrix contained water freezes. In Figure 5.7a it can be seen that there is a shift in the temperature at which the matrix contained

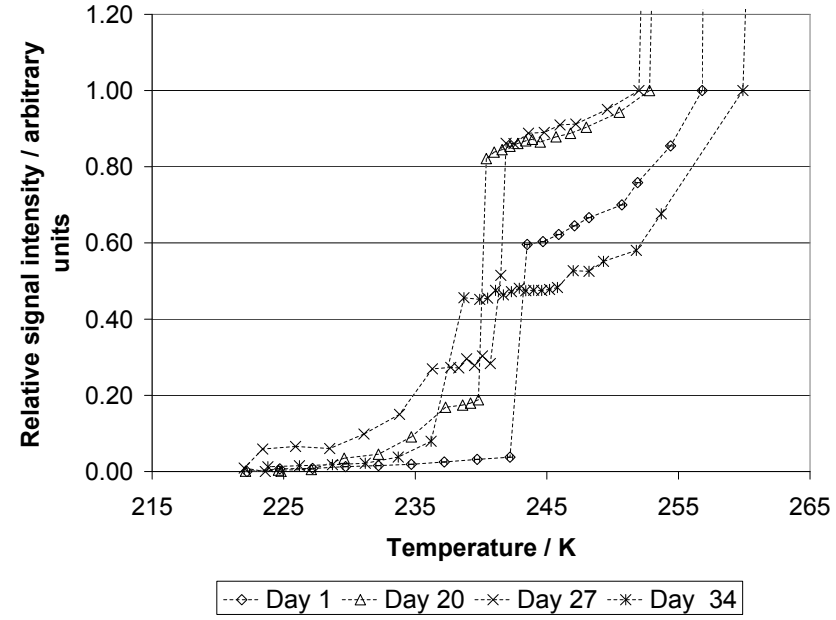

(a) Days 1—34

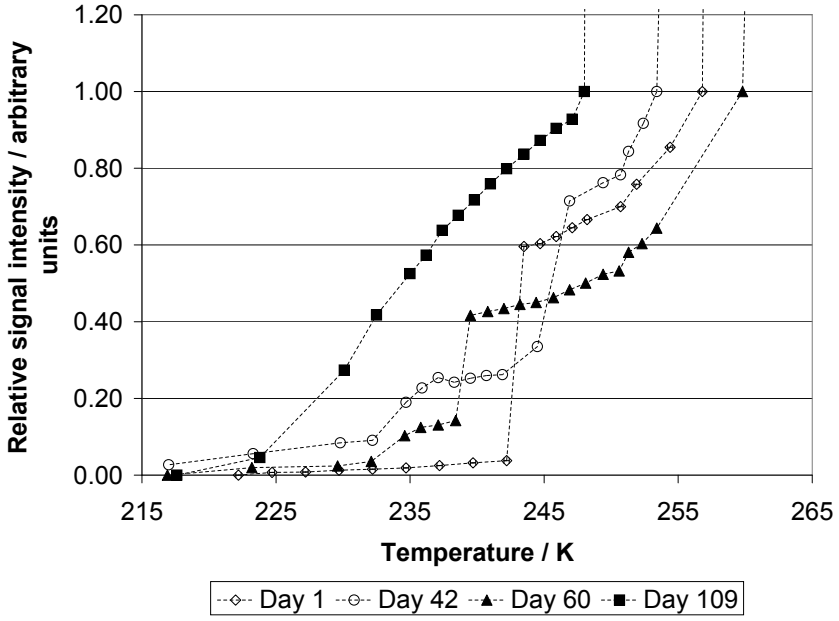

(b) Days 42—109

Figure 5.7: Cryoporometry freezing curves at increasing immersion times for microsphere batch MS045

water freezes, between days 1 and 20 the freezing temperature decreases suggesting a decrease in the modal neck size. The error bars for temperature measurement are shown for the data collected on day 1, but are the same for all days, ± 0.2 K, the changes seen are outside of experimental error and can, therefore, be discussed as structurally driven

changes. Subsequently, the freezing temperature of the matrix contained water increases between days 20 and 27, then decreases again between days 27 and 34, these changes vary in magnitude and can be seen throughout the time of immersion.

The increase and decrease in size of the pore neck suggests the pore necks, or access channels, are opening and closing with the movement of the polymer chains, in agreement with theory for burst release suggested by Allison (2008). In the context of a potential drug release mechanism the opening and closing of such access channels is an important concept. The movement, or breaking, of the polymer chains and the opening and closing of the access channels is considered to be a key factor in the control of movement of the drug molecule through, and eventually out, of the polymer matrix into the bulk fluid. This is especially the case for larger molecule drugs that are sterically hindered. The changes discussed in this section are the differences seen between observation times, additional changes may occurs between observation times that are not seen.

Another change observed in the characteristic freezing curve for the matrix contained water over time is the number of step changes in the relative signal intensity. Each step decrease in the relative signal intensity as temperature decreases, after supercooling of the bulk, is indicative of a modal neck size within the polymer matrix, for one step change such as that seen on day 1, the pore size distribution is unimodal. The change in the number of modal neck sizes can also suggest changes in the structural arrangement of the polymer chains within the matrix. At long immersion times, greater than 100 days, there is a change in the shape of the freezing curve to a more gradual freezing of the matrix contained water, without any significant step changes, this implies a continuous distribution of pore necks. Thus, suggesting a much less ordered matrix structure than at earlier immersion times where a unimodal or bimodal neck distribution is seen. The neck and body sizes observed are average values and may, therefore be affected by changes in the number of pores and the pore size distribution.

Whilst the neck size shows changes during the immersion time studied, no significant change is seen in the pore body size until long immersion times of greater than 100 days, at which point it is thought that structural degradation has sufficiently disrupted the matrix to change the spacing between polymer chains. A wider pore neck size distribution may change the complexity of the path travelled by a drug molecule. Larger pore necks provide an easier route for the encapsulated molecule, whilst smaller pore necks may prevent or divert the passage of the encapsulated the molecule. The net effect will be dependent on the size of the encapsulated molecule and any skewness in the pore neck size distribution. The complete freeze-thaw cycle at day 1, day 60 and day 109 are shown in Figure 5.8 for comparison. The repeatability of the melting curve at days 1 and 60 shows that the freeze-

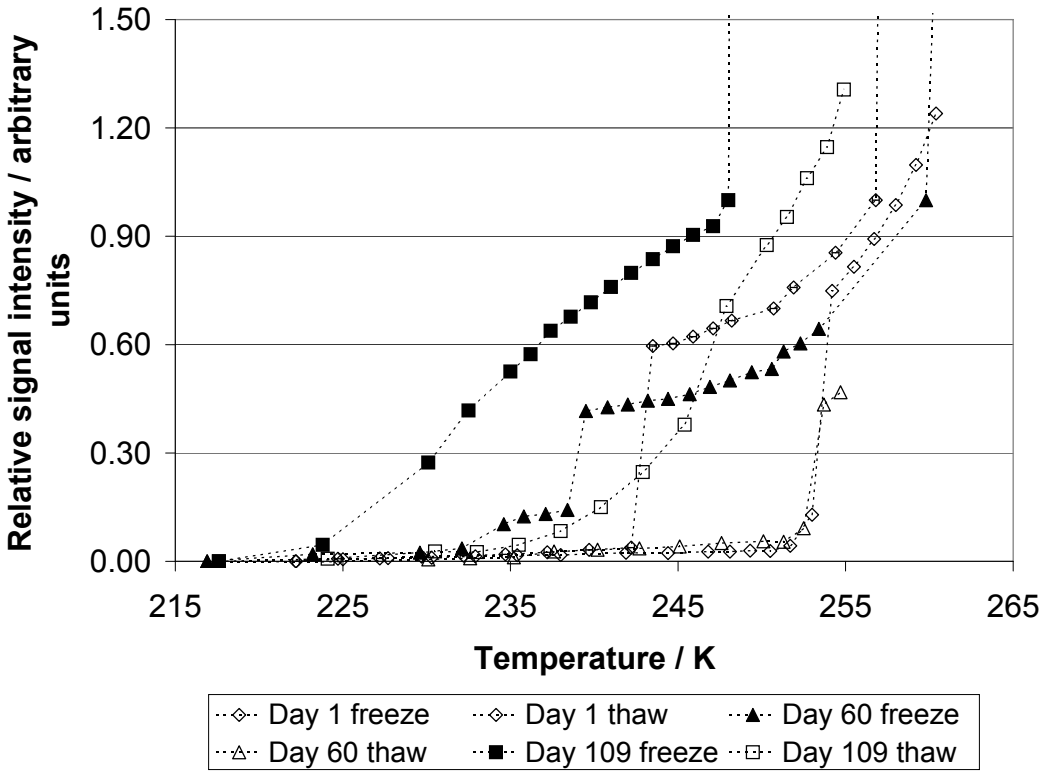

Figure 5.8: Complete cryoporometry freeze-thaw cycles for batch MS045 on days 1, 60 and 109 after immersion in an aqueous medium

thaw process does not change the structure of the microspheres, and salt exclusion does not occur, or has negligible affect. Both of these effects, if present, would cause changes to the position of the melting curve. Repeated freezing would be expected to increase the pore size due to the repeated swelling of water during the freezing process that could disrupt and fracture the polymer matrix structure. An increase in pore size would increase the observed melting temperature, such an effect is not seen. Salt exclusion effects would be different on each melting and, therefore, the melting temperature would shift both up and down in value as a result, the range of the melting curve would also be expected to change, this effect is also not observed for the matrix contained water in any samples tested in this work.

The value of the Gibbs-Thomson parameter used for the pore size estimation is that determined previously for silica in Chapter 3. Although this is not an exact value for the polymeric system, it is sufficient for the purpose of observing changes in pore size. It is not possible to determine an exact value of the Gibbs-Thomson parameter for polymer by comparison with mercury porosimetry or nitrogen adsorption, due to its fragility and large range of pore sizes. Nitrogen adsorption was attempted on a batch of microspheres and

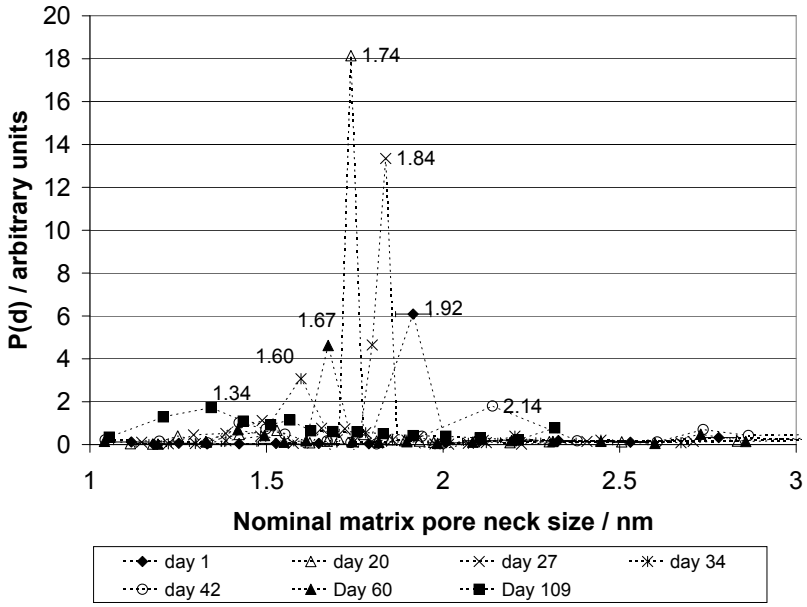

(a) Neck size

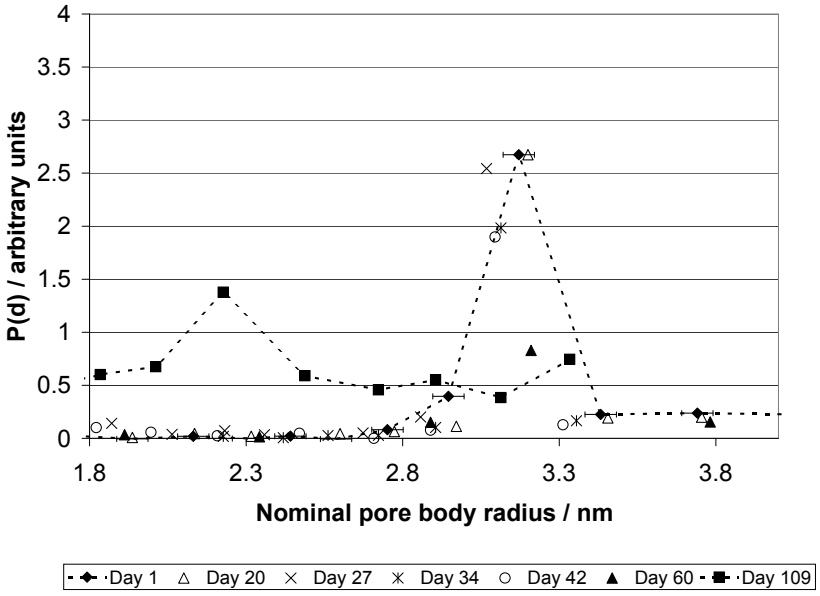

(b) Body size

Figure 5.9: Nominal pore neck and pore body size distributions determined from freezing and melting cryoporometry curves for microsphere batch MS045

despite careful preparation and handling of the microspheres to remove water traces, the nitrogen adsorption was unsuccessful, and the results are given in the appendix Section A.1. The pore neck size distribution determined from the freezing curves can be seen in Figure 5.9a, the pore body size determined from the melting curves can be seen in Figure

5.9b. Full cryoporometry cycles were conducted at days 1 and 20, where the sample was frozen and then thawed completely. After day 27 the cryoporometry cycle was modified to include a partial thaw and re-freeze of the sample after the initial freezing and before the complete thawing. This was to investigate the possible presence of shielding effects during the first freezing process of the microspheres. Evidence of shielding would suggest the presence of smaller pore necks that slow the progression of the freezing front from the external media. These smaller necks could potentially prevent the release of a large drug molecule into the external release medium, whilst larger necks within the pore matrix allow more free movement internally. Modal pore neck and pore body sizes for batch MS045 determined from freezing, re-freezing and melting curves are summarised in Table 5.1.

Time	Cycle	Neck Diameter/nm	Pore Diameter/nm	Comments
Day 1	1st full	1.92	3.17	unimodal
Day 10	1st full	1.80-1.89	3.17	unimodal
Day 20	1st full	1.74	3.20	unimodal
Day 27	1st freeze	1.84	3.06	bimodal,c. 1.5
Day 27	Re-freeze	2.6		
Day 34	1st freeze	1.60	3.11	bimodal,c. 2.2
Day 34	Re-freeze	2.6		
Day 42	1st freeze	2.14	3.10	bimodal,c. 1.4
Day 42	Re-freeze	2.6		
Day 60	1st freeze	1.67	3.21	bimodal,c. 1.4
Day 60	Re-freeze	2.6		
Day 102	1st freeze	1.21-2.31	2.22+	broad distribution
Day 102	Re-freeze	2.34		

Table 5.1: Neck and pore body sizes summary for microsphere batch MS045

The neck size shown in the first freezing process is indicative of the controlling minimum neck size between the internal polymer matrix and the release medium through which a drug molecule must pass to be released. The neck size shown by the re-freeze curve is representative of the average pore neck within the internal porous polymer matrix through which the drug molecule may travel, but does not get released to the external medium. An element of shielding is, therefore, observed for this sample of microspheres. To this end, shielding effects can be said to contribute to the observed freeze-thaw hysteresis. Other potential contributions to the hysteresis for polymer microsphere systems are discussed later in this section.

Time-resolved cryoporometry studies of high molecular weight PLGA microspheres with encapsulated drug 5-FD, batch MS043

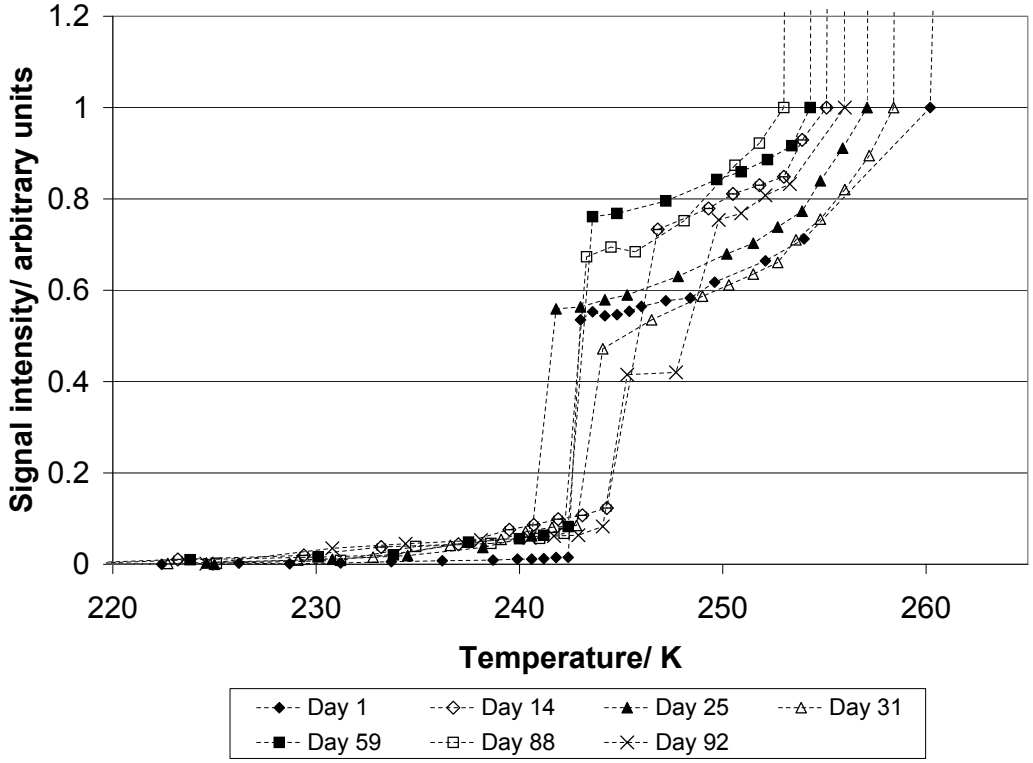

Figure 5.10: Cryoporometry freezing curve for batch MS043 from days 1 to 92 after immersion in aqueous media

A second batch of microspheres, MS043, made by double emulsion technique, with high molecular weight 50:50 PLGA and model drug 5-FD encapsulated is studied over time. Freezing curves for MS043 at increasing immersion times in aqueous media are shown in Figure 5.10. The freezing curve for day 14 shows a larger neck size than at day 1, a possible sign of the polymer swelling and the polymer chains moving position relative to one another. At day 25 the freezing curve shows a smaller pore neck size than day 1, indicating the pore necks have reduced in size. By day 31 the nominal neck size has grown again, but is smaller than at day 14. At longer immersion times, day 59 onwards the neck size appears to return to a value close to that originally observed on day 1, a similar value is also observed at day 88, possibly indicating that the polymer has settled to a steady state, with little fluctuation, over this time period. This state begins to change again after 92 days, where there appears to be two nominal neck sizes, possibly due to the start of the degradation of the polymer chains, which may provide additional access channels into and out of the polymer matrix.

Time	Cycle	Neck Diameter/nm	Pore Diameter/nm	Comments
Day 1	1st full	1.90	3.11	unimodal
Day 2	2nd full	1.85		unimodal
Day 14	1st freeze	2.13	3.22	bimodal becoming visible c.1.6
Day 14	Re-freeze	2.47		bimodal visible c.1.8
Day 25	1st freeze	1.80	3.38	bimodal visible c.2.4
Day 25	Re-freeze	2.58		
Day 31	1st freeze	1.96	3.17	
Day 31	Re-freeze	2.44		
Day 59	1st freeze	1.93	3.27	
Day 59	Re-freeze	2.69		
Day 88	1st freeze	1.91	2.95	
Day 88	Re-freeze	2.33		
Day 92	1st freeze	2.45	2.89	
Day 92	Re-freeze	2.47		

Table 5.2: Neck and pore body sizes summary for microsphere batch MS043

Nominal neck size distributions and pore body size distributions derived from the freezing and melting curves for batch MS043 can be seen in Figures 5.11a and 5.11b, respectively. A summary of the modal pore neck sizes determined from the freezing curves is given in Table 5.2.

Time-resolved cryoporometry studies of Low Molecular Weight PLGA microspheres without encapsulated drug, batch MS041

Microsphere batch MS041, made by double emulsion evaporation technique with low molecular weight 50:50 PLGA, without the model drug in the internal aqueous phase, which contained water and 0.4 % PVA, were immersed in 5 % w/v sodium chloride solution. Cryoporometry cycles were conducted at increasing immersion times for over 100 days, freezing curves are shown in Figures 5.12a and 5.12b. At earlier immersion times, less than 25 days, changes are observed in the pore neck size similar to those seen for batch MS045, also of low molecular weight, where the pore necks appear to open and close before returning to their original size. Between days 25 and 51 the pore neck size stabilizes and fluctuations observed are within experimental error, the neck size remains close to that observed at day 1. Between day 51 and 70, the pore necks increase in size and show a broader distribution, then decrease in size by day 93 and increase by day 105. Following this second

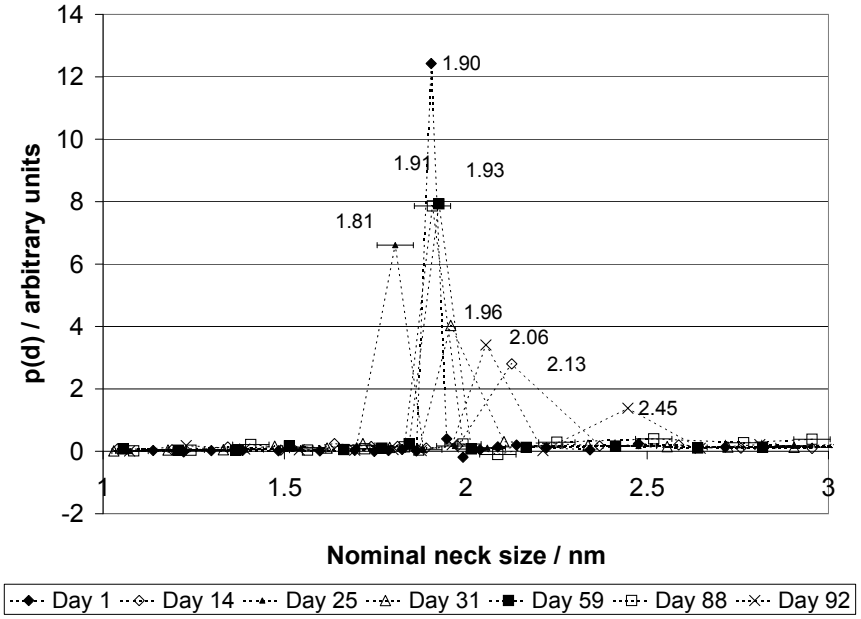

(a) Nominal neck size

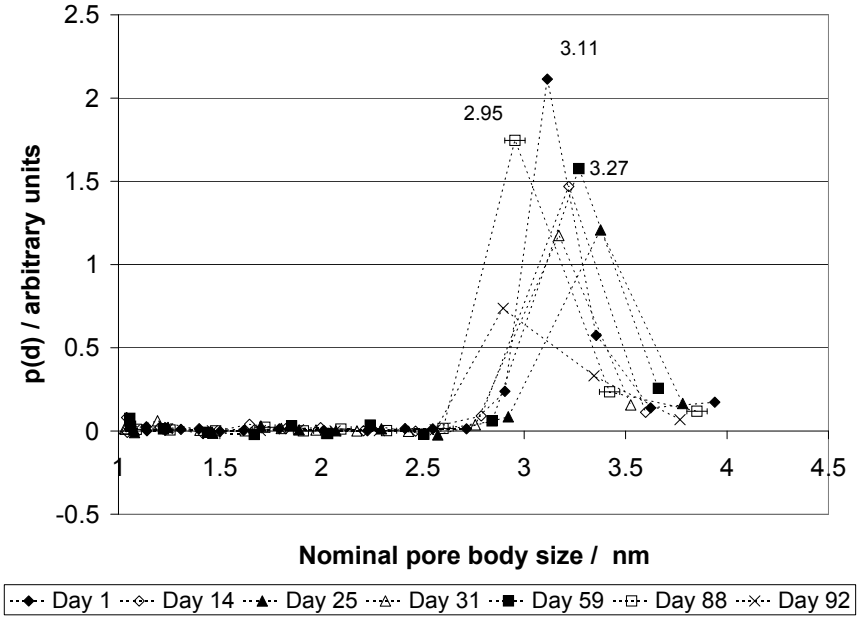

(b) Nominal pore body size

Figure 5.11: Nominal pore neck and body size distributions for microsphere batch MS043

stage of opening and closing, by day 116 there are four modal pore neck sizes across the whole range of those previously observed. The pore neck size distributions determined from freezing curve data are shown in Figure 5.13a. The pore body size also shows a change with this batch, for days 1 to 25 the body size remains constant, between days 25 and 37 the body size decreases significantly, but remains this size until day 116.The pore body

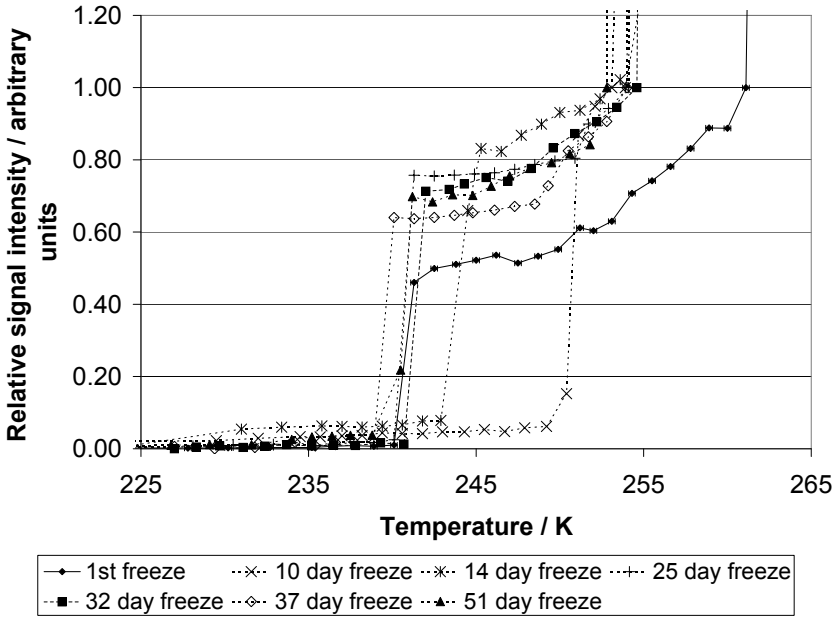

(a) Days 1–51

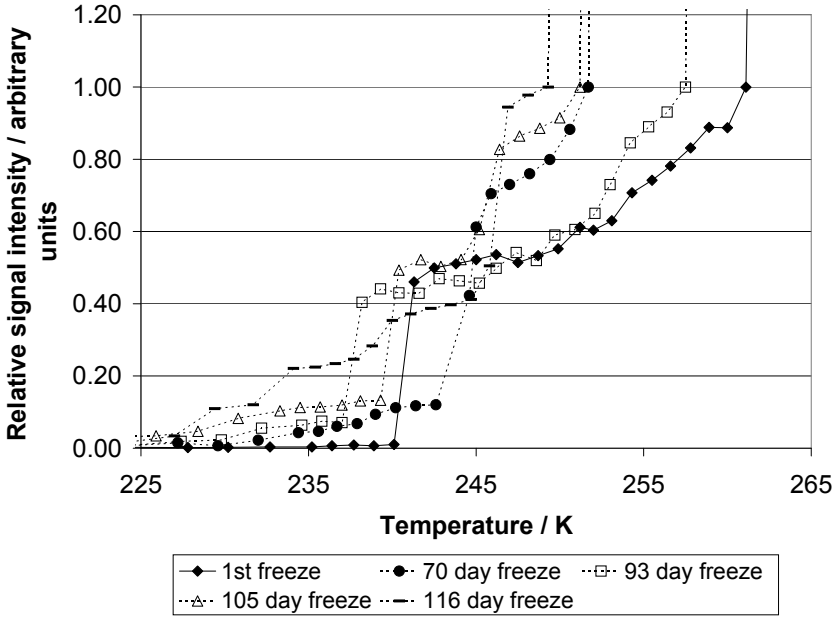

(b) Days 70–116

Figure 5.12: Cryoporometry freezing curves at increasing immersion times for microsphere batch MS041

size distributions determined from the melting curve data are shown in Figure 5.13b. A summary of the pore neck and body sizes are given in Table 5.3.

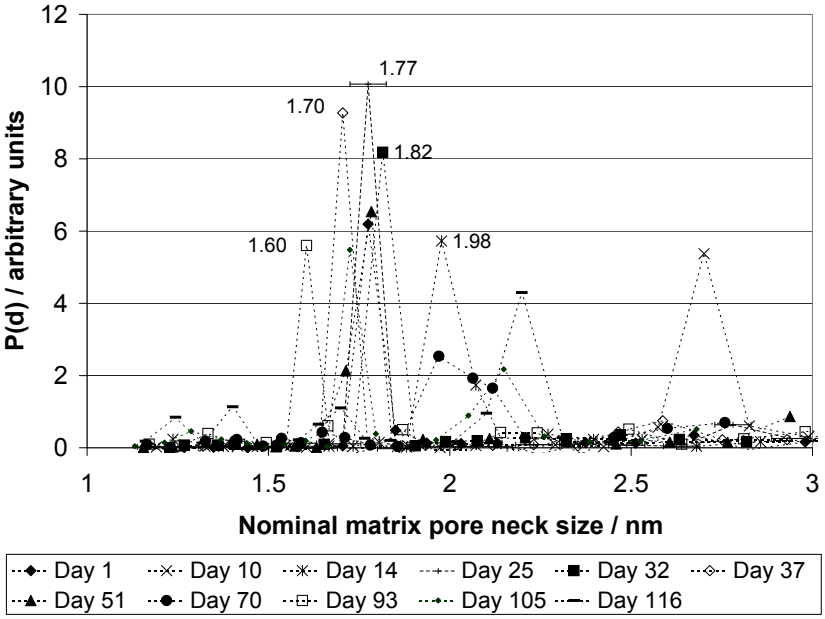

(a) Nominal neck size

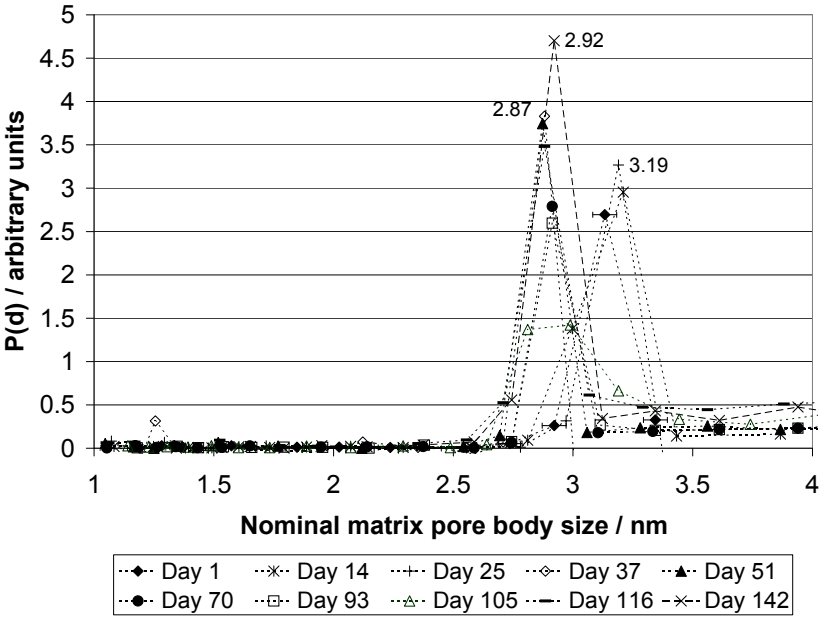

(b) Nominal pore body size

Figure 5.13: Nominal pore neck and body size distributions for microsphere batch MS041

5.4.4 Comparison of microsphere batches in terms of porosity

Nominal modal pore neck and pore body sizes at increasing immersion times for all three batches of microspheres are shown in Figures 5.14 and 5.15 respectively. For all three batches studied here the nominal pore neck sizes start at just less than 2 nm at day 1, then

Time	Neck Diameter/nm	Pore Diameter/nm	Comments
Day 1 Re-freeze	1.77 2.72	3.13	unimodal
Day 10	2.70	Not available*	unimodal
Day 14	1.98	3.21	unimodal
Day 25	1.77	3.19	unimodal
Day 32	1.82	Not available*	unimodal
Day 37 Re-freeze	1.70 2.65	2.88	unimodal, shift in pore body size
Day 51	1.78	2.87	unimodal
Day 70	Ave 1.97–2.12	2.91	modal peak widens
Day 93	1.60	2.91	Additional neck peaks at 2.14-2.24 nm
Day 105	1.72,2.15	2.81-2.99	bimodal
Day 116	2.20,1.70,1.40,1.24	2.88+	4 modes of neck size and pore size distribution change

* Not available due to premature experiment termination by equipment failure

Table 5.3: Neck and pore body sizes summary for microsphere batch MS041

the greatest initial changes are seen in the low molecular weight batches MS045 and MS041. The batch with the model drug used in the preparation, MS045, shows continual opening and closing of pore necks throughout the study, until long immersion times greater than 100 days at which point the observed structure appears to have changed at the nanometer scale. In comparison the batch without the model drug, MS041, shows an initial opening of the pore necks and then returns to the size seen at day 1, subsequent experiments suggest a relative steady state then exists for a period of around 40 days, before the necks re-open and close and the structure continues to change. The high molecular weight batch with encapsulated drug, MS043, shows some initial change in the pore necks at the early stage of the study, upto 30 days after which the necks remain unchanged. In terms of drug release potential, it is thought that the pore necks can control the release of a molecule into the release medium and the transport of the drug molecule through the matrix. Opening of pore necks provides an exit for the drug molecule to be released, closing of pore necks restricts, or prevents, passage of the drug molecule. At periods of no change in pore neck size, the drug release profile will depend on the relative size of the nominal pore neck and the drug molecule, release may be unrestricted, partially restricted or totally restricted.

Pore body sizes at the start of the study were also found to be very similar for all three

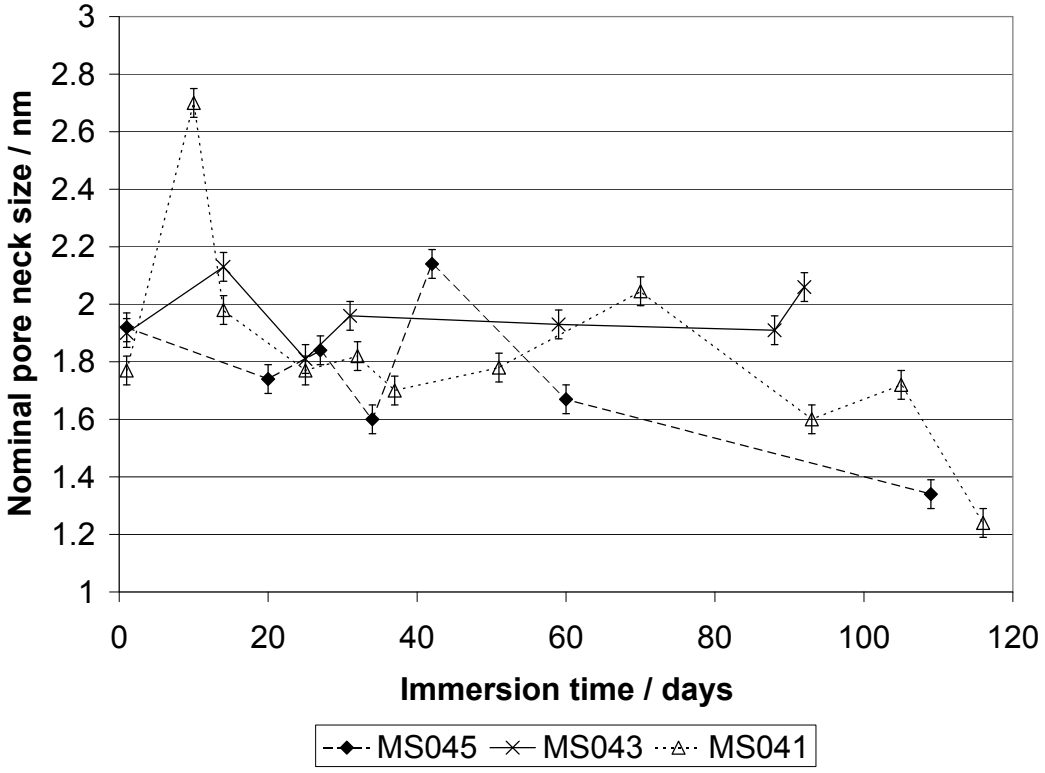

Figure 5.14: Nominal pore neck size changes with immersion time for batches MS041, 43 and 45

batches, at around 3 nm. No significant change in pore body size was seen for batch MS045 until long immersion times of more than 100 days. For batch MS041, a step change in the pore body size was seen during the period of little change in the pore neck size at around 20–37 days, therefore, suggesting a different structural evolution mechanism, where changes were occurring within the structure of the polymer matrix that did not affect the neck size. This may imply that the presence of the model drug during the preparation of the microspheres affected the polymer structure and, therefore, changing the mechanism of its evolution, as suggested in the literature (Freiberg and Zhu, 2004). In contrast batch MS043 shows more change in the pore body size than the pore neck size over the time studied. This is suggestive that the higher molecular weight polymer degradation may progress differently and have greater effect within the body of the matrix pores during the initial stages than is seen within the low molecular weight polymer. This difference could have a significant effect on the drug release profile observed.

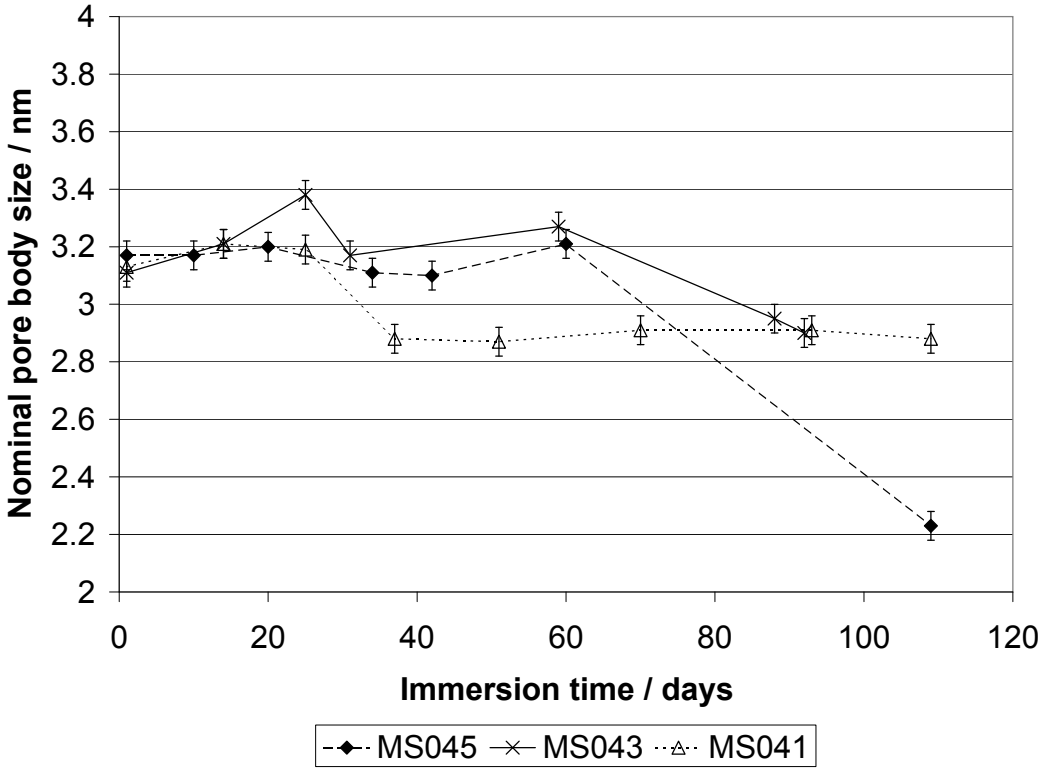

Figure 5.15: Nominal pore body size changes with immersion time for batches MS041, 43 and 45

5.4.5 Additional interpretation of cryoporometry data for matrix contained water in PLGA microspheres

Scanning loops

The partial thaw re-freeze cycle shown in Figure 5.16 can provide additional information on the shielding effects of the neck structure connecting the internal polymer matrix with the bulk or 'bubble' pore. Larger neck sizes are seen after the partial thaw, suggesting a reduction in the shielding compared to that seen during the first freezing process. In some cases it is observed that this 'unshielded' pore neck size remains constant for longer periods of time, for example for low molecular weight polymer drug encapsulated batch MS045. Changes are observed for high molecular weight polymer, again suggesting more change to the internal polymer structure for high molecular weight PLGA microspheres than seen for low molecular weight batches. The presence of larger pores which remain frozen within the matrix on initial thawing provide additional nucleation sites in the re-freeze process. In terms of drug movement within and through the matrix, this suggests there may be regions where the drug molecule can move around freely, but this movement is restricted by the matrix 'necks' that connect this region to another region, or the bulk. A drug molecule,

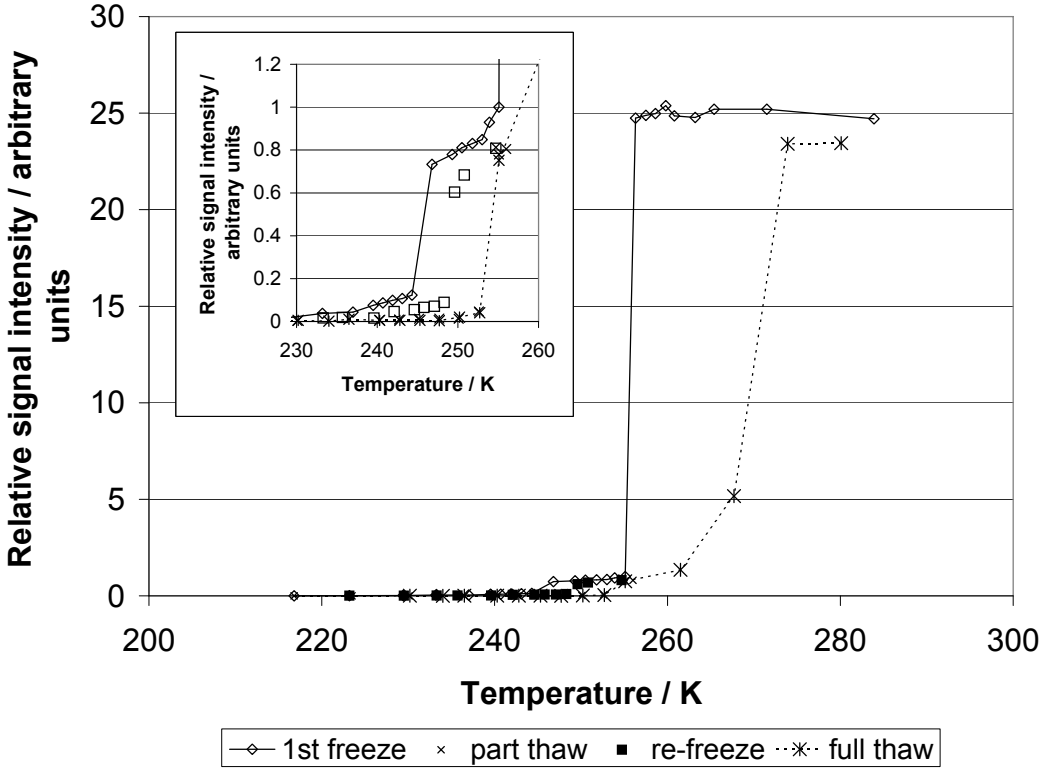

Figure 5.16: An example of the freeze, part thaw, re-freeze and thaw cryoporometry cycle for batch MS043 after 14 days immersion in aqueous media

therefore, may remain trapped within this region until the neck has opened sufficiently to allow the drug to progress to the next region of the matrix, into the 'bubble' pore or, out to the bulk. Once the drug molecule is in the bulk media, it has effectively been 'released' from the matrix. This supports earlier findings by Messaritaki et al. (2005) that different regions within the polymer matrix have different release profiles. The re-freeze pore necks observed for high molecular weight batch MS043 are similar in size to those for the low molecular weight batch MS045, however, this high molecular weight batch shows more changes with immersion time, which are not seen for MS045.

Nanometre scale geometry

As described in Chapter 3 the work of Petrov and Furo (2006) describes the hysteresis between the freezing and thawing of a liquid imbibed in a porous medium in terms of the pore shape. Applying this theory to the freeze-thaw hysteresis seen for the polymer matrix of the microsphere, the ratio of the melting point depression, ΔT_m, to the freezing point depression, ΔT_f, lies between that for cylinders $(\frac{1}{2})$ and spheres $(\frac{2}{3})$, as shown in Figure 5.17. This could suggest that the matrix contains both spherical and cylindrical pores, or

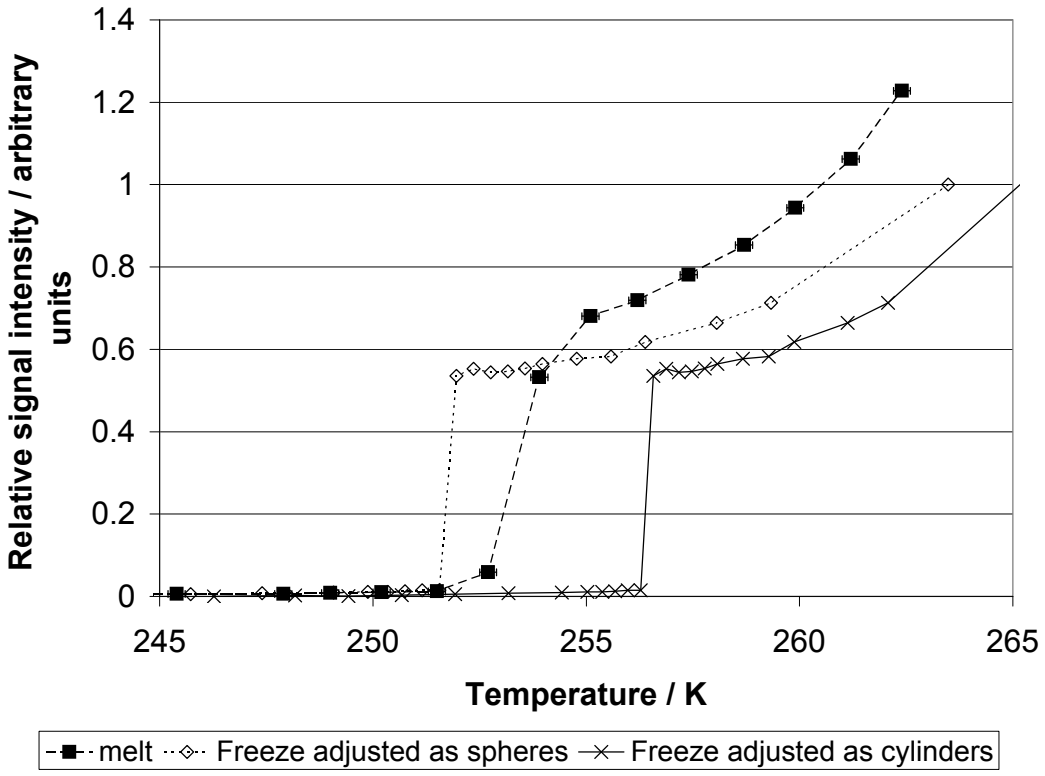

Figure 5.17: Adjusted freezing curves for cylindrical and spherical pore shapes compared to melting curve for microspheres batch MS043 after 1 day immersion

that the pores are neither spherical nor cylindrical, but some ellipsoidal shape. In either case it is concluded that the polymer matrix does not have a simple nanoporous structure. A comparison of the re-freeze curve with the melting curve also shows no correlation to simple cylindrical or spherical geometry, see Figure 5.18.

Application of percolation theory to freezing water in PLGA microsphere matrix

The application of percolation theory to the freezing of liquid imbibed in porous media is described earlier in Chapter 3. The freezing data collected for the initial freezing of the matrix is considered as being synonymous with the whole silica pellet sample, where the freezing front progression into the matrix is shielded by the small external and connecting necks. Similarly the freezing data for the second freezing of the matrix contained water after a partial thaw is considered synonymous with the powder silica sample, where shielding effects have been removed and the freezing process is affected only by pore size. This assumption is not entirely true as the distribution of the ice pockets within the polymer matrix after the partial thaw are unknown and may not fully remove the shielding effects. For the sake of this analysis, the ice pockets are considered to be in the larger matrix pores

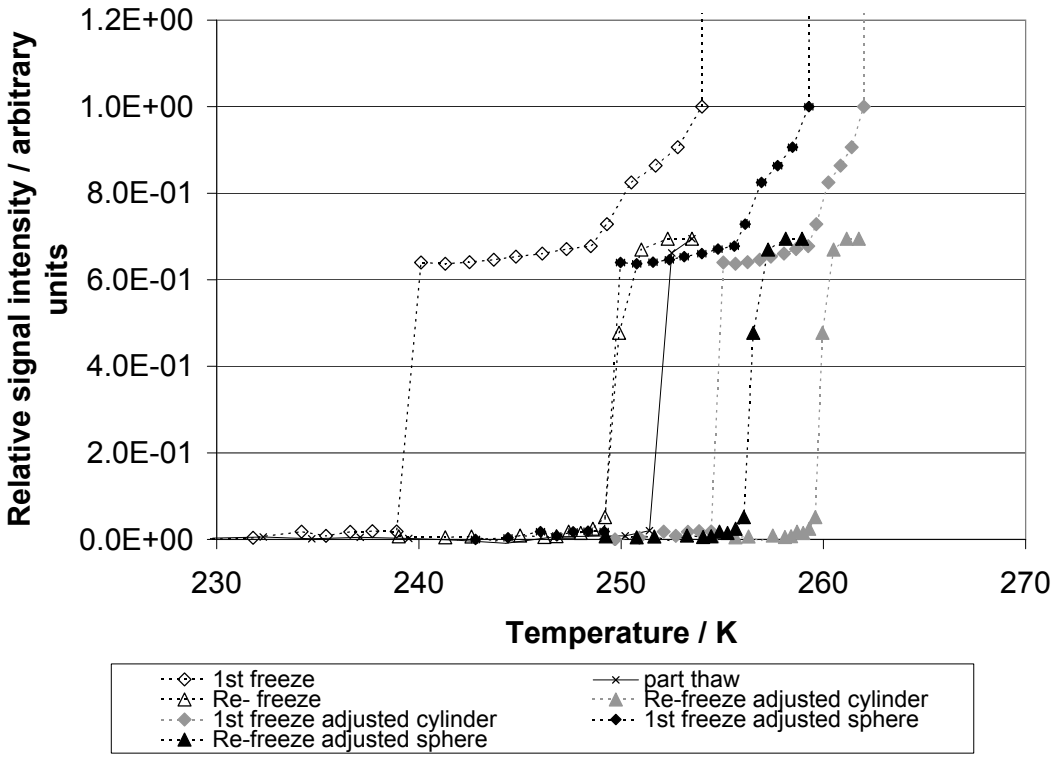

Figure 5.18: Adjusted freezing and re-freezing curves for cylindrical and spherical pore shapes compared to melting curve for microspheres batch MS041 after 37 days immersion

that could have been shielded during the initial thawing. A shift in the second re-freeze curve to larger pore sizes compared to the initial freeze is seen consistently for microsphere samples as discussed earlier in this section, providing confidence that the shielding effect is real. Percolation theory, as described for silica samples in Chapter 3, has been applied to data for all batches of microspheres studied in this chapter. An example of a typical probability of pore being frozen ,F, against probability a pore is below its freezing point, f, plot can be seen in Figure 5.19. Some freezing of matrix contained water is seen below the percolation threshold, but a significant increase in the number of pore that are frozen is seen at the percolation threshold.

A summary of the threshold values determined for different microsphere batches at similar immersion times are given in Table 5.4. The low molecular weight batches show higher values of percolation threshold compared to the higher molecular weight batch studied. A higher percolation threshold suggests poorer connectivity and, therefore, a more restricted movement and release of an encapsulated molecule. Conversely, a lower percolation threshold suggests greater connectivity which provides greater accessibility for movement through and out of the matrix for an encapsulated molecule. The change in percolation threshold

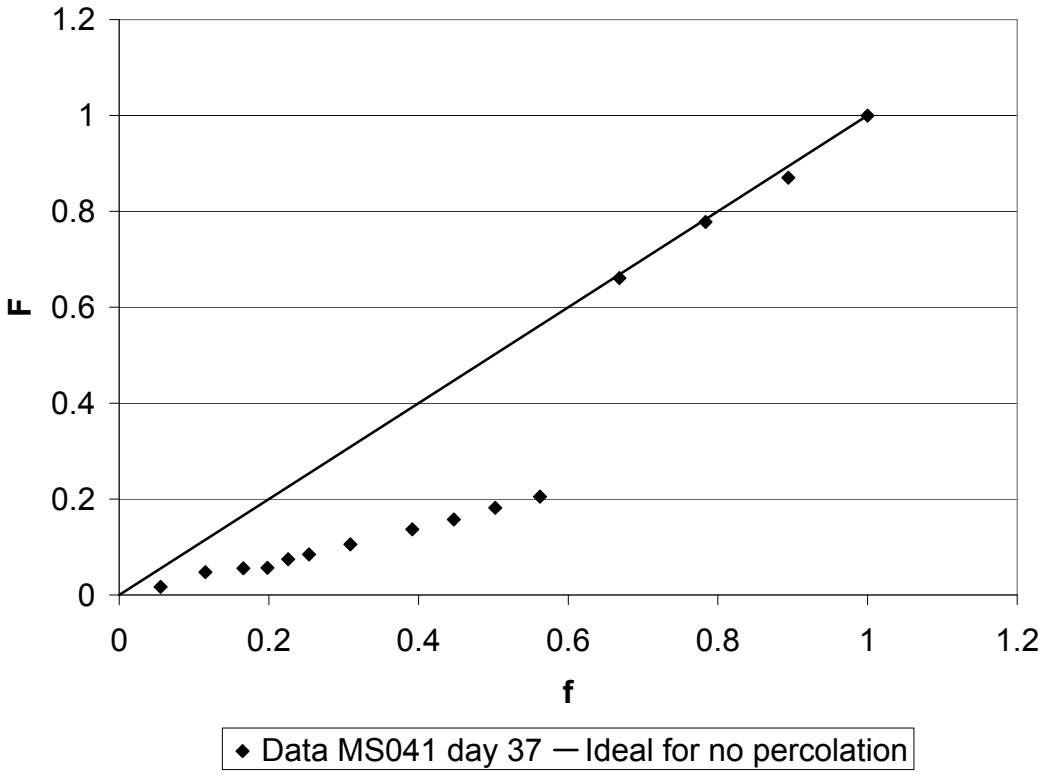

Figure 5.19: Example plot of the probability of a pore being frozen against the probability of a pore water being below its freezing point for microsphere batch MS041, 37 days after immersion

Batch	Immersion time	Percolation threshold values
MS041	1 day	0.62–0.74
MS041	37 days	0.56-0.66
MS045	27 days	0.43
MS045	34 days	0.49–0.58
MS043	14 days	0.2-0.3
MS043	25 days	0.36-0.42

Table 5.4: Approximate percolation threshold values for microsphere matrix freezing of imbibed water

over the time studied shows an increase for drug encapsulated microspheres and a decrease for microspheres without encapsulation. This observation reaffirms the need to ascertain the effect that the drug molecule of interest will have on the polymer microsphere in order to gain a full understanding of the drug release mechanism for a given system. The methods described in this chapter provide a wealth of information to assess the release mechanism in terms of structural changes in the polymer matrix at the nanometer length scale.

5.5 Conclusions

Cryoporometry has been applied to the investigation of the nanometer scale structure of PLGA microspheres for drug delivery. Changes in the polymer matrix structure over time have been observed and comparisons made between different batches of microspheres. Both the freezing and thawing characteristics of water contained in the polymer matrix have been used to determine the nominal pore neck and pore body sizes. Changes in pore neck sizes with time show the opening and closing of entrances or access channels into the polymer matrix as the freezing front progresses into the matrix from the outside. It is thought that these access channels control the release of an entrapped drug molecule from the polymer and, therefore, play a vital role in the drug release profile observed from such systems. After a partial thaw and re-freeze, the access channels restricting the progression of the freezing front are larger, the freezing front at this stage has begun within the matrix, therefore, the smaller channels seen are likely to control the release of a molecule from the matrix into the external medium rather than movement inside the matrix. The larger pore necks observed in the re-freeze cycle determine the movement of the drug molecule within the polymer matrix.

The low molecular weight batches studied initially show greater movement in the nominal pore neck size over time, than is seen for the pore body size. At longer immersion times both pore neck and pore body size distributions become broader. Some differences are seen in the observed structural changes for the drug encapsulated microsphere batch compared to that of the batch without encapsulated drug molecule. This highlights the need to consider the effects a particular encapsulated molecule may have on the formation and evolution of the polymer matrix structure. For the high molecular weight batch of microspheres, changes seen in the observed pore body size are greater than those seen in the pore neck size over the period of study and in such systems may, thus, provide additional pathways or barriers to the transport of an encapsulated drug molecule.

It has been shown that porosimetry techniques such as scanning loops and percolation theory can be applied to investigate the PLGA microsphere matrix structure. Single pore hysteresis effects were investigated and have shown that pore geometry is more complex than simple cylinders or spheres. Percolation theory has been applied and discussed in terms of differences in percolation threshold that equates to the quality of the connectivity within the pore network of the polymer matrix and, therefore, the ease of transport for the encapsulated drug molecule moving through the polymer matrix. Cryoporometry has been shown to provide a wealth of data relating to the structure of the polymer matrix, in the next chapter these findings will be combined with diffusometry studies in an effort to

further explain the causes of the drug release mechanisms and controls within the polymer microspheres over time.

References

S. D. Allison. Effect of structural relaxation on the preparation and drug release behavior of poly(lactic-co-glycolic) acid microparticle drug delivery systems. *Journal of Pharmaceutical Sciences*, 97(6):2024–2037, 2008.

S. Freiberg and X. Zhu. Polymer microspheres for controlled drug release. *International Journal of Pharmaceutics*, 282:1–18, 2004.

E. W. Hansen, G. Fonnum, and E. Weng. Pore morphology of porous polymer particles probed by nmr relaxometry and nmr cryoporometry. *Journal of Physical Chemistry B*, 109:24295–24303, 2005.

A. Messaritaki, S. Black, C. F. v. d. Walle, and S. P. Rigby. Nmr and confocal microscopy studies of the mechanisms of burst drug release from plga microspheres. *Journal of Controlled Release*, 108(2-3):271–281, 2005.

J. Mitchell, J. B. W. Webber, and J. Strange. Nuclear magnetic resonance cryoporometry. *Physics Reports*, 2008.

H. Najibi, A. H. Mohammadi, and B. Tohidi. Estimating the hydrate safety margin in the presence of salt and/or organic inhibitor using freezing point depression data of aqueous solutions. *Industrial & Engineering Chemistry Research*, 45(12):4441–4446, 2006.

O. Petrov and I. Furo. Curvature-dependent metastability of the solid phase and the freezing-melting hysteresis in pores. *Physical Review E*, 73(1), 2006. Part 1.

O. Petrov, I. Furo, M. Schuleit, R. Domanig, M. Plunkett, and J. Daicic. Pore size distributions of biodegradable polymer microparticles in aqueous environments measured by nmr cryoporometry. *International Journal of Pharmaceutics*, 309(1-2):157–162, 2006a.

A. Schreiber, I. Ketelsen, and G. H. Findenegg. Melting and freezing of water in ordered mesoporous silica materials. *Physical Chemistry Chemical Physics*, 3:1185–1195, 2001.

R. Valckenborg, L. Pel, and K. Kopinga. Cryoporometry and relaxometry of water in silica-gels. *Magnetic Resonance Imaging*, 19(3-4):489–491, 2001.

D. Vargas-Florencia, T. Edvinsson, A. Hagfeldt, and I. Furo. Pores in nanostructured tio2 films. size distribution and pore permeability. *Journal of Physical Chemistry C*, 111(21): 7605–7611, 2007.

Chapter 6

Cryodiffusometry studies of PLGA microspheres

6.1 Introduction

The diffusometry technique developed in Chapters 3 and 4 has been combined with the cryoporometry study of PLGA microspheres described in Chapter 5, cryodiffusometry. The technique has been used to investigate the longer term behaviour of PLGA microspheres in aqueous media, the interpretation of the data collected can provide information on the transport properties and structure of the porous material. The application of cryodiffusometry to porous media is relatively new (Filippov and Skirda, 2000) and the work described here contains developments made as the methods were applied to investigate the structure of polymer materials; it provides a means of investigating the polymer matrix structure at the nanometer scale. The polymer structure has been identified as an important feature in determining the drug release profile (Batycky et al., 1997) but, until now, very little has been done to investigate the structure at the nanoscale. Model interpretations of geometry and diffusion regime previously used to study materials as diverse as sedimentary rocks and dairy produce are applied to the diffusion of water within the polymer matrix. Three batches of microspheres, low molecular weight with and without encapsulated model drug, and high molecular weight with encapsulated model drug, will be compared in terms of observed structural changes and mass transport considerations.

6.2 Background and Theory

6.2.1 Diffusion models in porous systems

Chapter 4 has discussed how the non-linearity of the log-attenuation plot, determined from PFG experiments, can be explained in terms of restricted, or restrained, diffusion and anisotropy of diffusivity. By freezing the bulk water and water contained within the 'bubble' pores, the water contained within the matrix may be observed. The movement of water provides information on transport properties within the matrix that can indicate the ability of entrapped drug molecules, polymer degradation products and water to move within the polymer matrix. By examining the diffusion behaviour of water within the polymer matrix it may be possible to see the changes in tortuosity effects over time. Tortuosity is calculated from the PFG measured diffusion coefficient and the bulk diffusivity as described earlier in Chapter 3.

Restricted or constrained diffusion

According to Callaghan et al. (1979), the observed diffusion of a molecule within a porous media may be effected by the dimensional constraints of the solid. The molecule may only be able to travel in one dimension, along a tube, or in two dimensions, between two parallel planes. The signal attenuation for molecular motion in one dimension and two dimensions are given by equations 6.1 and 6.2 respectively,

$$\frac{I}{I_0} = \exp \frac{-\zeta D}{3} \tag{6.1}$$

$$\frac{I}{I_0} = \exp \frac{-2\zeta D}{3} \tag{6.2}$$

where $\zeta = \gamma^2\delta^2 g^2(\Delta - \frac{\delta}{3} - \frac{\tau}{2})$. These equations are a simplification for the condition that $\zeta D \ll 1$. If the molecule is unrestricted and able to travel in three dimensions then the signal attenuation is of the form derived by Stejskal and Tanner (1965), equation 6.3.

$$\frac{I}{I_0} = \exp -\zeta D \tag{6.3}$$

Anisotropy of diffusivity

From Chapter 4, the heterogeneity of diffusion coefficients may be expressed as a series of discrete components, or phases, each with a characteristic diffusion coefficient, equation 4.1.

6.2.2 Pore geometry

Further to describing diffusion in terms of restricted or constrained motion, diffusion studies by NMR PFG within porous media have been used to probe the geometry of the liquid containing pores (Mitra and Sen, 1992; Mitra et al., 1993; Fordham et al., 1994). Simple pore geometries of spheres, tubular and slab (flat planes) have been investigated (Mitra and Sen, 1992). A recent review of diffusometry by Stallmach and Galvosas (2007) identifies some of the work done. One dimensionally constrained diffusion described by Callaghan et al. (1979) assumes an infinitesimal separation distance between the constraining walls, such that diffusion perpendicular to the plates does not occur. In the interest of interpreting this constraint in terms of microsphere structure, an estimate of the distance between the constraining barriers is considered. To estimate the separation distance between the constraining walls further models have been investigated: For plates perpendicular to the magnetic field, the separation distance, a_s, can be calculated from the observed diffusion coefficient, D_p, for different diffusion times, Δ (Stallmach and Galvosas, 2007), equation 6.4.

$$D_p(\Delta) = \frac{a_s^2}{12\Delta} \tag{6.4}$$

The observed diffusion coefficient for the fast component adjusted for salt content can be used to estimate D_p, and a plot of the diffusion coefficient against $\frac{1}{12\Delta}$ is a straight line, of gradient a_s^2. The model is, however, limited as it considers only 'slab-shaped' pores perpendicular to the applied magnetic field. For an anisotropic arrangement of 'slab-shaped' pores, therefore, an alternative model has been applied.

Fordham et al. (1994) have investigated the separation distance between pore walls in anisotropically arranged connected slab-shaped pores within sandstone, using NMR PFG echo attenuation. The model applied that relates the signal attenuation and the distance between the pore walls, for slab-shaped interconnecting pores, is based on the work of Mitra and Sen (1992) who derived models for slab-shape, tubular and spherical pores, considering surface relaxation effects. The log of the echo attenuation is given in equation 6.5.

$$\ln \frac{I}{I_0} = -4\pi^2 q^2 D_0 \Delta + \ln F(K) \tag{6.5}$$

where $q = \frac{\gamma \delta g}{2\pi}$ and $F(K)$ is defined in equation 6.6.

$$F(K) = \int_0^1 e^{K^2 x^2}\, dx = \frac{\sqrt{\pi}}{2} \frac{erfi(K)}{K} \tag{6.6}$$

K is defined in terms of the free diffusion coefficient, D_0, and the distance travelled, perpendicular to the applied magnetic field, by a molecule, $< \frac{r^2}{2} >$, such that $K^2 = 4\pi^2 q^2 \times (D_0\Delta - < \frac{r^2}{2} >)$. The distance travelled by a molecule perpendicular to the applied magnetic field, within the anisotropic arrangement of slab shaped pores separated by a distance a_s can be approximated to $\frac{r^2}{2} \approx \frac{a_s^2}{3}[1 - \exp\frac{-3D_0\Delta}{a_s^2}]$. $erf(K)$ is the error function of K and $erfi(K) = \frac{erf(iK)}{i}$. This is approximated using the first four terms of the Taylor expansion for the error function and, therefore, $F(K)$ simplifies to equation 6.7

$$F(K) \approx 1 + \frac{K^2}{3} + \frac{K^4}{10} + \frac{K^6}{42} \tag{6.7}$$

For a given sample of microspheres, the free diffusion coefficient, D_0, within the matrix can be calculated by evaluating the change in effective diffusion coefficient at different diffusion times as shown in Chapter 3. A plot of $\ln\frac{I}{I_0} + 4\pi^2 q^2 D_0\Delta$ against K should see the data collapse onto the same line for different values of K for a given separation distance, if the pores are connected and of slab-shaped geometry.

6.2.3 Relaxation effects

The relaxation behaviour of a nucleus under investigation by NMR can be affected by the physical state of the nucleus, solid or liquid, and the environment in which the nucleus is situated. Magnetic field inhomogeneities within a sample can cause an observable change in the transverse relaxation behaviour of a nucleus, where T_2^* is the measured relaxation constant for a nucleus which would have a relaxation constant of T_2 under magnetically homogeneous conditions, and $T_2^* \leq T_2$. A liquid within a porous material is usually considered to have a combination of two relaxation time constants, a bulk relaxation constant and a relaxation constant affecting the nuclei in proximity to the wall surface. The measured relaxation constant for such a system will be an average representation of the two time constants and can be used to determine pore characteristics such as surface to volume ratio and pore size. The relationship between the measured relaxation constant in a pore, $T_{2,pore}$, and the surface to volume ratio, $\frac{s}{V}$, is given by equation 6.8, where ρ is the surface relaxivity and $T_{2,bulk}$ is the bulk relaxation constant for the imbibed liquid (Mitchell et al., 2005). An equivalent equation is true for the longitudinal relaxation constant T_1.

$$\frac{1}{T_{2,pore}} = \frac{1}{T_{2,bulk}} + \rho\frac{s}{V} \tag{6.8}$$

6.3 Experimental

Diffusometry experiments were carried out during the freezing and thawing process at similar relative signal intensities within the cryoporometry cycles. The experiments were carried out after all the bulk and 'bubble' pore contained water was frozen, and again just before it melted. Signal attenuation greater than 50 % of the original signal (or more than one half-life) is required for a good fit of an exponential curve. For the silica sample investigated in Chapter 3, increasing the gradient strength, g, with a large diffusion time, Δ, provided sufficient signal attenuation, however, similar experimental parameters gave only small changes in signal attenuation for the microsphere samples. A series of experiments were, therefore, conducted on a part frozen microsphere sample to test the optimum parameter changes to achieve a sufficient change in signal attenuation.

From equation 3.5 it is known that signal attenuation is a function of gradient strength, g, gyromagnetic radius, γ, diffusion time, Δ, the bipolar dephasing correction time, τ, and gradient length, δ, each parameter was considered in turn. The maximum gradient strength is an inherent characteristic of the spectrometer probe and could not be increased to any greater strength than that already tested. The gyromagnetic ratio is characteristic of the nucleus being studied, therefore, would require a change in solvent. This was rejected as the objective of the study was to investigate the behaviour of the microspheres in an aqueous environment. The diffusion time change showed some change in signal attenuation, however, increasing the diffusion time could change the diffusion regime observed, for example from unrestricted diffusion at small diffusion times to restricted diffusion at long diffusion times. The effect of changing the bipolar dephasing time is relatively small due to its first order relationship with signal attenuation and the small values used. Changing the length of the gradient, however, showed significant changes in signal attenuation, and providing that the condition $\delta \ll \Delta$ remains, varying δ provides a valid alternative to changing the gradient strength. For cryodiffusometry experiments, a series of 1 dimensional pulsed bipolar gradient stimulated echo with longitudinal eddy delay experiments were conducted with increasing gradient lengths, δ, in the range 0.001–0.02 s, with a fixed diffusion time, either 0.15, 0.2 or 0.25 s and a constant gradient strength of 20.229 Gcm^{-1}.

Experiment cycles were conducted immediately after microsphere immersion in aqueous media, then at varying intervals over a period upto 120 days. Batches of high (MS043) and low molecular weight (MS045) PLGA microspheres with 5-FD encapsulated, and a batch of low molecular weight PLGA blank microspheres (MS041) were tested. Modifications were made to the standard multiple temperature acquisition automatic program, *multi_zgvt*, to include multiple PFG experiments after pre-determined experiment numbers

of the cryoporometry cycle. An example of one of these modified programs is included in the appendix, Section A.8.

6.4 Results and Discussion

6.4.1 Diffusion in salt solution

Cryodiffusometry experiments were carried out during the cryoporometry experiments described in Chapter 5. The microspheres are immersed in a 5 % w/v sodium chloride solution. Consideration of the effect of salt concentration on the diffusion coefficient observed must be made. During diffusion studies it is necessary to estimate the bulk diffusion coefficient at each experimental temperature to calculate values of tortuosity within the matrix and the addition of salt affects the bulk diffusion coefficient. Above the freezing point of water the presence of salt in solution reduces the bulk diffusion coefficient, but in supercooled liquid, the presence of salt has been shown to increase the bulk diffusion coefficient (Kim and Yethiraj, 2008). The 5% w/v solution of sodium chloride is equivalent to a 0.86 M solution, and from the work of Kim and Yethiraj (2008) the diffusion coefficient adjustment factor, a, is plotted against temperature*, as shown in Figure 6.1. A second order polynomial fit to this data gives the relationship in equation 6.9, where T is the experiment temperature in Kelvin.

$$a = 1.092 \times 10^{-3} T^2 - 6.144 \times 10^{-1} T + 8.733 \times 10^{1} \tag{6.9}$$

The unadjusted free diffusion coefficient of bulk water, D_0, and the adjusted diffusion coefficient of water in the salt solution at low temperature, D_w, are related by the salt adjustment factor, a, according to equation 6.10. The adjustment factor will be used to convert the observed diffusion coefficient of salt solution in the polymer matrix, D_{PFG}, into an equivalent diffusion coefficient observed for pure water in the polymer matrix, D'_{PFG}, using equation 6.11.

$$D_0 = D_w \times a \tag{6.10}$$

$$D'_{PFG} = \frac{D_{PFG}}{a} \tag{6.11}$$

*Data extracted from the reference using software available at http://www.datathief.org/ (14th October 2008)

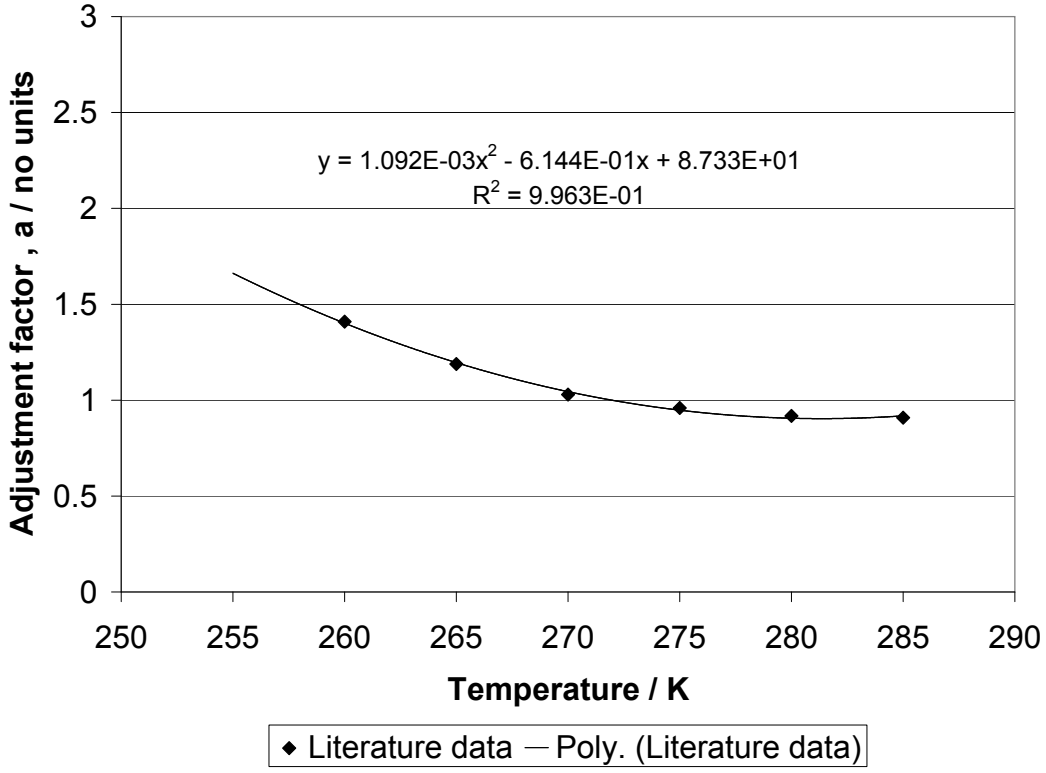

Figure 6.1: Salt solution adjustment factor as a function of temperature

Figure 6.2 shows the relationship of the estimated diffusion coefficient of free water as a function of temperature (as described in Chapter 3), the adjustment factor for diffusion coefficient as a function of temperature and the estimated diffusion coefficient adjusted for salt solution as a function of temperature. The experimental temperature range used for the cryodiffusometry experiments, 244—256 K, is marked as the region of interest on Figure 6.2 and this range alone is plotted in Figure 6.3. Both diffusion coefficient as a function of temperature, and the adjusted diffusion coefficient for salt solution as a function of temperature can be approximated as a straight line relationship within this range, both with similar gradients. It can, therefore, be said that, whilst the salt within the solution has a significant effect on the overall value of the diffusion coefficient, it has negligible effect on the relative change in the diffusion coefficient within the range of temperatures being studied. The salt adjustment factor is significant, however, for the calculation of absolute tortuosity.

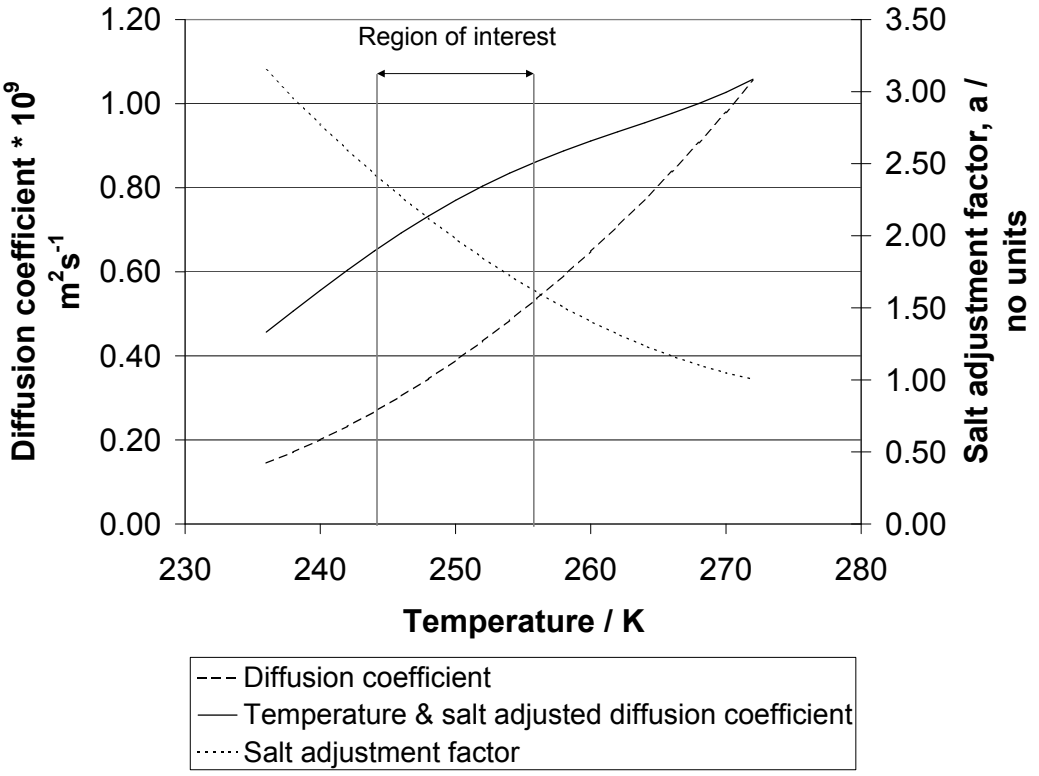

Figure 6.2: Diffusion coefficient, salt solution adjustment factor and adjusted diffusion coefficient as a function of temperature

6.4.2 Determination of diffusion model for cryodiffusometry experiments

Diffusometry was carried out at low temperature to study the diffusion of water molecules within a partially frozen salt solution imbibed in the porous polymer matrix. The collected data formed non-linear log attenuation plots, the cause of non-linearity must be determined for accurate interpretation of the results. Restricted diffusion can cause non-linearity in the log attenuation plot (Callaghan et al., 1983). Another cause of non-linearity is attributed to molecules in different environments diffusing at different rates, the log attenuation curve then has a combination of contributions from each of the different fractions of the studied nucleus (Hollewand and Gladden, 1995).

An example data set is fitted to a one component and two component model, the log attenuation plots of data and model estimates are shown in Figure 6.4. Fitting the data to a single diffusion coefficient model, as expressed in equation 3.5 provides a single diffusion coefficient, where the 'goodness of fit' is assessed by the reduced χ^2 value and the distribution of the residual values.

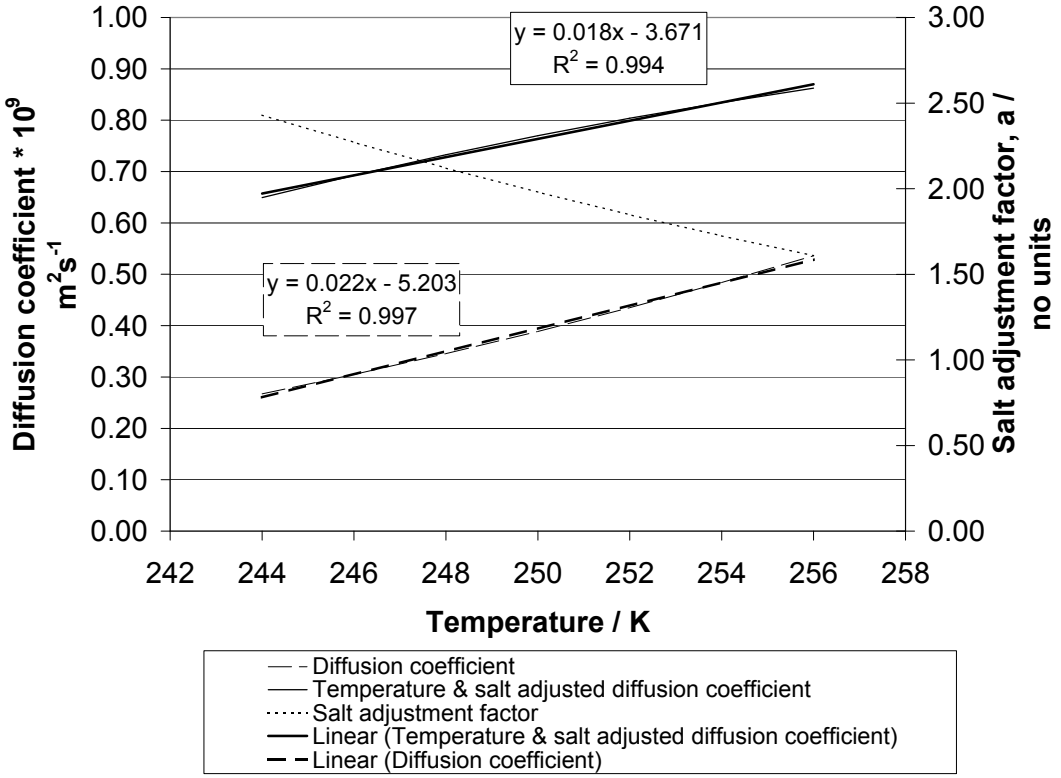

Figure 6.3: Diffusion coefficient, salt solution adjustment factor and adjusted diffusion coefficient as a function of temperature over the experimental temperature range

The applicability of a given diffusion model to the data may be assessed in terms of the 'goodness of fit', how closely the model fits the experimental data. The statistical parameter reduced χ^2 is used to compare the quality of the goodness of fit for different models. The definition of reduced χ^2, χ^2_R, is given in equation 6.12, where E is the expected value for a given data point (model), O is the corresponding observed value (experiment) and ν is the number of degrees of freedom defined by, $\nu = n - p - 1$, n is the number of observations and p is the number of fitted parameters in the model. A satisfactory fit is determined by $\chi^2_R \leq 1$ (Taylor, 1982).

$$\chi^2_R = \frac{\sum \frac{(E-O)^2}{E}}{\nu} \tag{6.12}$$

The quality of the model used to fit the unknown parameters to the experimental data is also assessed by the distribution of the residuals. The residuals are the difference values between the model data and the experimental data. A good model has both positive and negative residuals randomly distributed at increasing values of the fitted data, and any pattern in the residual values infers a systematic error within the model used.

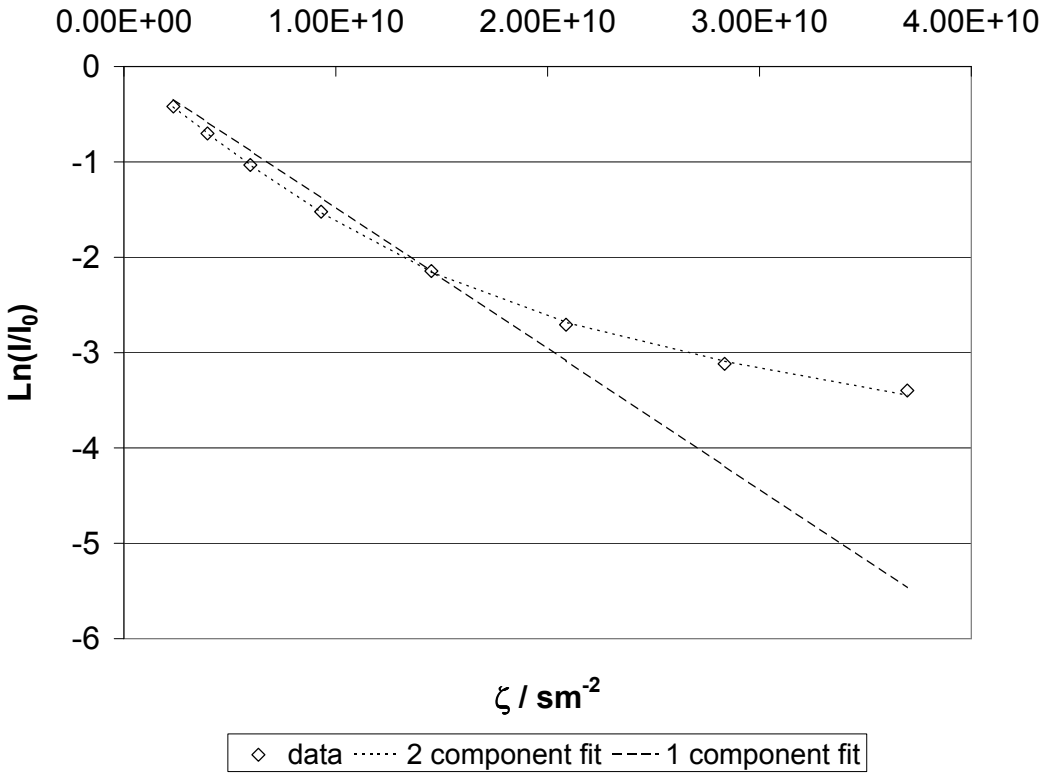

Figure 6.4: Example log attenuation plot for cryodiffusometry data collected MS041, day 37, Δ 0.20 s, freezing curve

For the single component model typical reduced χ^2 values are of the order of 0.1–0.2 and the residuals show systematic deviation from the model. A two component model fitted to the same data shows a reduced χ^2 value in the order of 0.001 and residual values distribution is less ordered. The residuals for the one and two component fit are shown in Figure 6.5. Increasing the number of variables within a model will generally improve the quality of the fit, but, to determine if this is genuinely the best model fit, the possibility of restricted diffusion of a one component model will also be considered.

To test if the curve of the log attenuation plot is due to restricted diffusion of a single fraction of molecules, a series of experiments with increasing diffusion times were carried out. If restricted diffusion is present then the Stokes-Einstein relation should hold, equation 4.2, and for an increase in diffusion time, Δ, a decrease in diffusion coefficient should be seen. A plot of the diffusion time multiplied by the diffusion coefficient against the diffusion time should be linear with a zero gradient if restricted diffusion is occurring. The linear regression analysis on data for batch MS041 showed that a zero gradient was within the 95 % confidence interval for the 1 component fit during the freezing curve, but not during the thawing curve, see Figure 6.6. The upper and lower values for the 95 % confidence

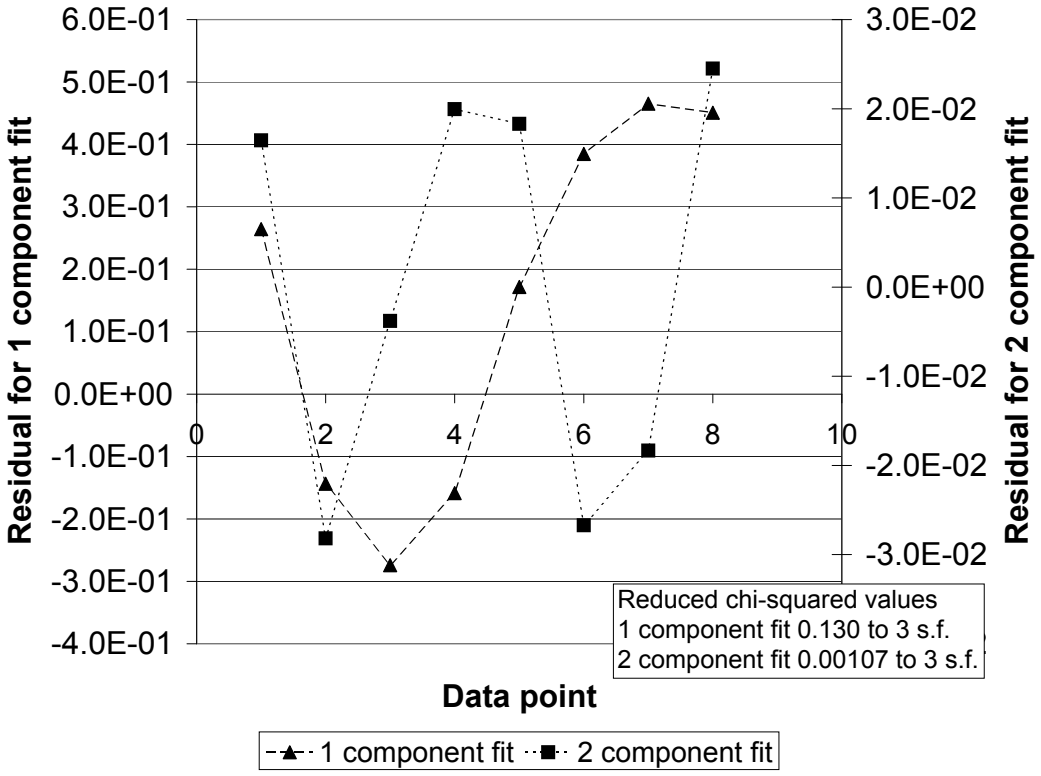

Figure 6.5: Residual values for 1 and 2 component fit to data for MS041, day 37, Δ 0.20 s, freezing curve

intervals, U_{95} and L_{95}, were determined by equations 6.13 and 6.14 respectively,

$$U_{95} = E + t_{stat}^{5,d} \times se \tag{6.13}$$

$$L_{95} = E - t_{stat}^{5,d} \times se \tag{6.14}$$

where E is the estimated value of the gradient, se is the standard error of the estimated gradient and $t_{stat}^{5,d}$ is the value of the 't' statistic for a 5 % two tailed test , with d degrees of freedom.

Whilst both freezing and thawing curve plots had similar gradients, the standard error of the gradient for the freezing curve was twice that for the thawing curve data. This suggests a greater level of error in the estimate of the gradient for the freezing data than for the thawing data. Differences seen in the diffusion behaviour during freezing to that seen during thawing should be related to the different mechanisms involved in the liquid-to-solid and solid-to-liquid phase changes. It is expected that during melting, there is a distribution of ice pockets within the pores that are not present during freezing when the freezing front

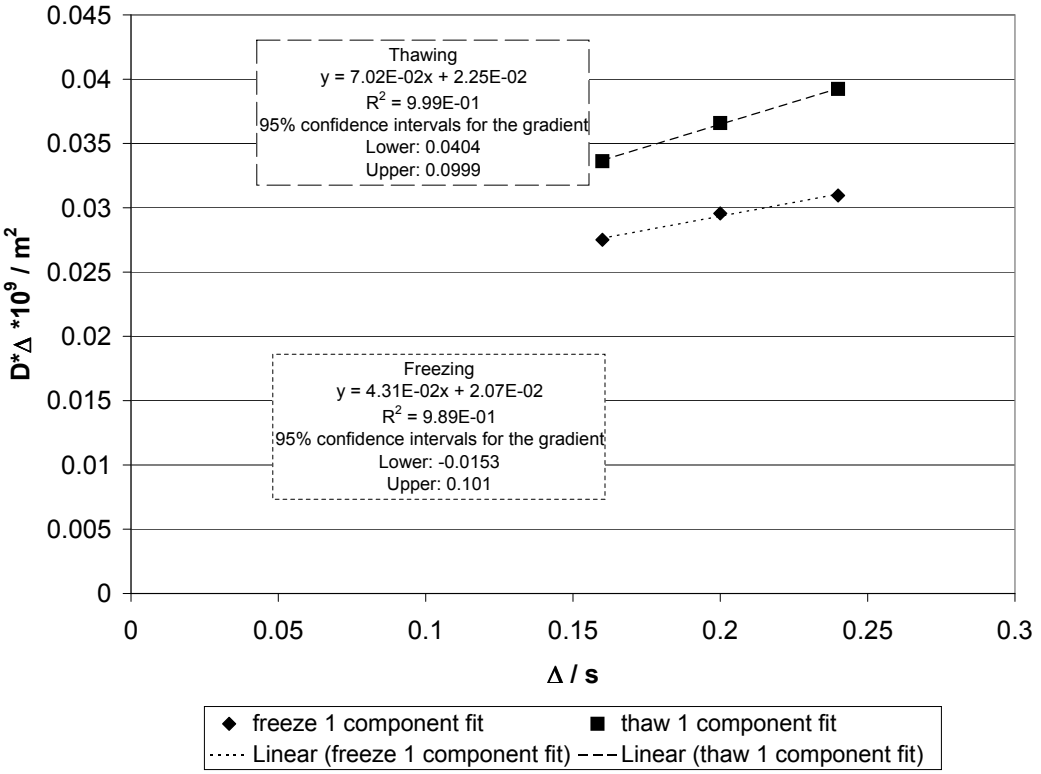

Figure 6.6: Test for restricted diffusion in freezing and thawing for a 1 component fit to data for MS041, day 37

progresses from the outside of the matrix inward. These ice pockets provide more 'walls' that restrict the motion of the water diffusing within the matrix, therefore, more restricted motion is expected during melting than during freezing. This theory is contrary to the findings suggested from the data collected. It is, therefore, proposed that the curvature of the log attenuation plot is not purely a consequence of restricted diffusion. A plot of diffusion coefficient against the square root of the diffusion time may be used to determine the free diffusion coefficient of water within the matrix material, as shown in Section 3.2.2, equation 3.10. For the one component fit of the example data set, the diffusion coefficient in the matrix estimated from the freezing data and the thawing data agree within 15 %, see Figure 6.7.

The data is now fitted to a two-component model, equation 3.5. The first component is defined as the component showing greater movement during the diffusion time. The second component is the slow component, where diffusion is comparatively slower than the first component. The two diffusion coefficients for the two components are denoted as D_1 and D_2 respectively. The fraction of water in the first component is p and the fraction of water in the second component is $(1-p)$. As mentioned previously, the residuals from the fit of

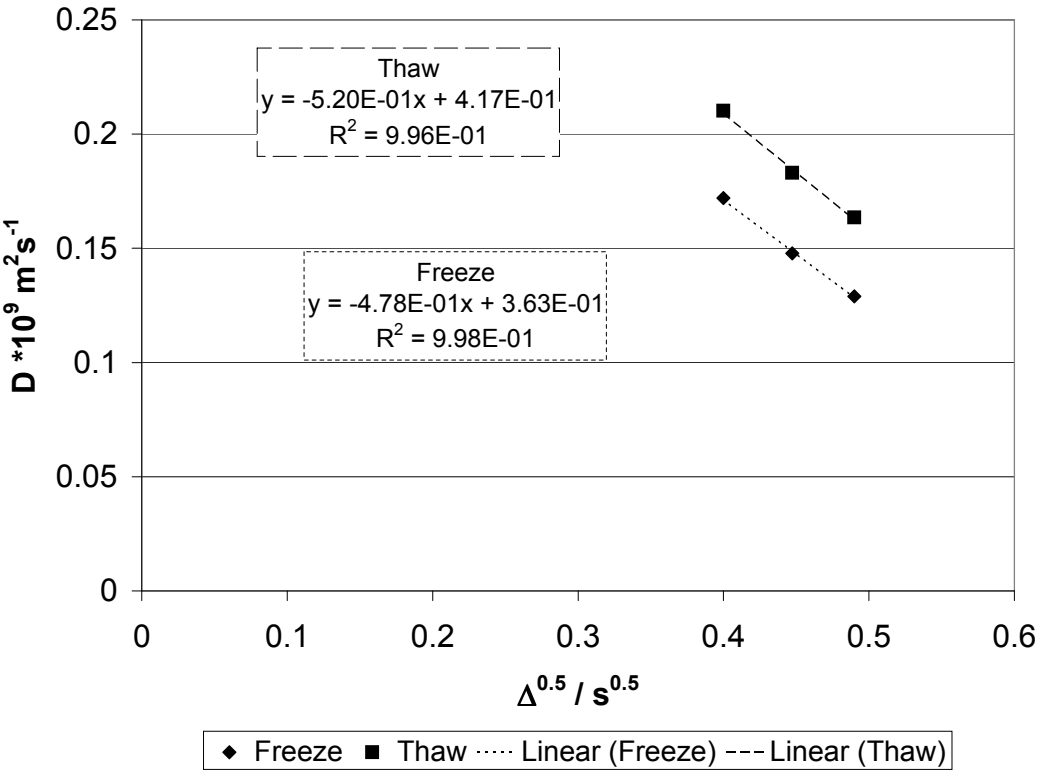

Figure 6.7: Free diffusion of water in polymer matrix for 1 component model fit to freezing and thawing data for MS041, day 37

this model shows random distribution and the reduced χ^2 value is of the order of 0.001, which suggests a better fit to the experimental data than that found from the 1 component model. The calculated diffusion coefficients for both the fast and slow component for several values of diffusion time are examined for restricted diffusion behaviour, Figure 6.8. It is found that for both freezing and thawing the fast moving component is not totally restricted, however the slow moving component is restricted and that the restricted cavity size, assuming spherical cavities, for this component is around 1–5 μm. A possible cause of this restriction may be the existence of regions of matrix material that are more dense than others. In these more dense regions the polymer chains may be more tightly arranged and, therefore, provide smaller spaces, or less, openings through which the water molecules may pass. This restricts the movement of water within this region. As the structure of the polymer changes after immersion in aqueous media, these regions change. From calculated values of diffusion coefficients for fast and slow components, tortuosity values are determined as described previously for silica materials in Chapter 3. The tortuosity for microsphere structure is defined as the ratio of the free diffusion coefficient of water, adjusted for temperature, D_B, over the estimated diffusion coefficient in the polymer matrix,

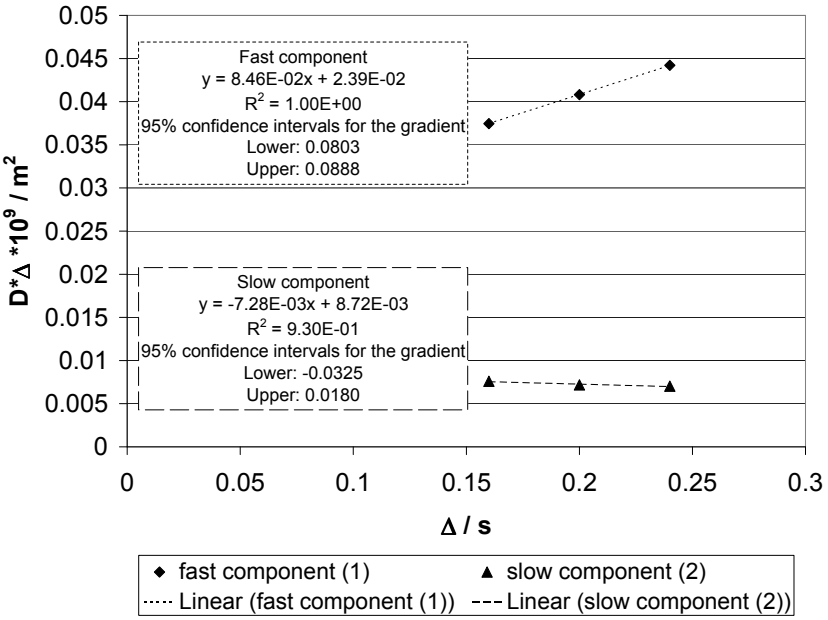

(a) Freezing

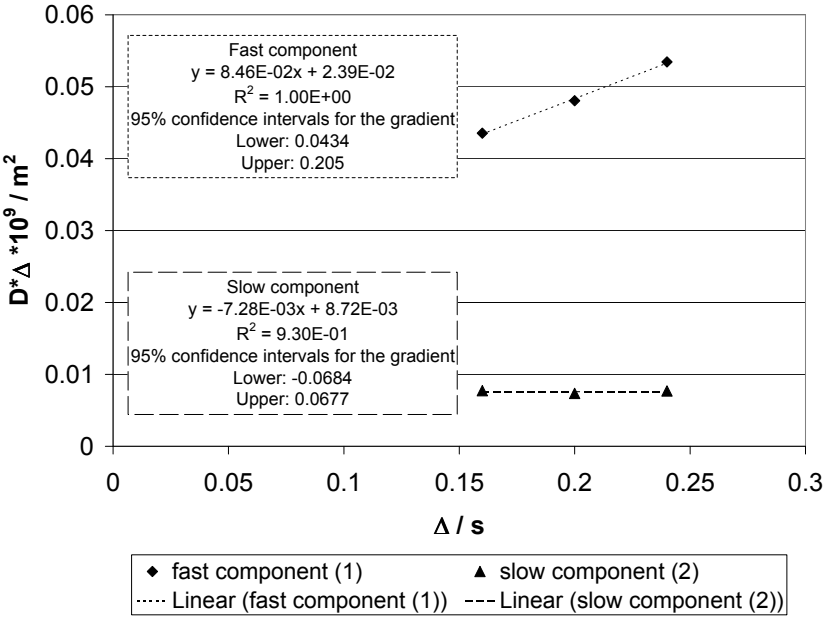

(b) Thawing

Figure 6.8: Test for restricted diffusion for 1 and 2 component fit to data for MS041, day 37, freezing and thawing

adjusted for the presence of salt, D'_{PFG}, equation 6.15. In the context of this work the tortuosity is used as a quantitative assessment of water molecule mobility within the polymer matrix.

$$\tau = \frac{D_B}{D'_{PFG}} \tag{6.15}$$

6.4.3 Temperature effects

The effect of temperature on the diffusion coefficient and signal intensity have been previously discussed in Sections 3.2.2 and 5.4.2. During the diffusion experiments on molten solution in PLGA microspheres, it was seen that the application of multiple radio frequency pulses had a small effect on the signal attenuation observed. A similar set of experiments were conducted on a partially frozen sample of PLGA microspheres, where a series of 1 dimensional experiments were conducted at increasing values of gradient length, δ, followed by a the same experiments carried out with a random order in the change of the gradient length. The results are shown in Figure 6.9, no significant difference is observed between the two data sets. The residuals between the two data sets can be seen in the insert of Figure 6.9 and are plotted in the order in which the experiments were conducted and in order of increasing gradient length. The residual values are mostly small($\ll 1\%$), only one value is significantly larger (5 %). The residuals show random distribution about zero, therefore, it can be said that the measured signal intensity is not affected by the application of increased radio frequency pulses and temperature effects of such are negligible.

The observed water diffusion coefficients are a function of temperature, salt concentration and the porous matrix in which the water is contained. Due to the freeze-thaw hysteresis during cryoporometry, there was a significant difference between the temperatures at which the freezing curve and thawing curve experiments were carried out. For a valid comparison of the diffusion behaviour an adjustment for temperature was made. The absolute tortuosity can be used as a comparative measure for change to the diffusion behaviour at different times and temperatures. The absolute tortuosity is the ratio of the free water diffusion coefficient determined from PFG experiments adjusted for temperature over the measured diffusion coefficient in the matrix, adjusted for the presence of salt. The diffusion coefficient for free water can be estimated at low temperatures, as described in Chapter 3, and the measured diffusion coefficients from PFG experiments can be corrected for salt at a given temperature as described in Section 6.4.1. A full table of the observed diffusion coefficients and calculated tortuosities for all microsphere batches studied can be found in the appendix, Section A.3.

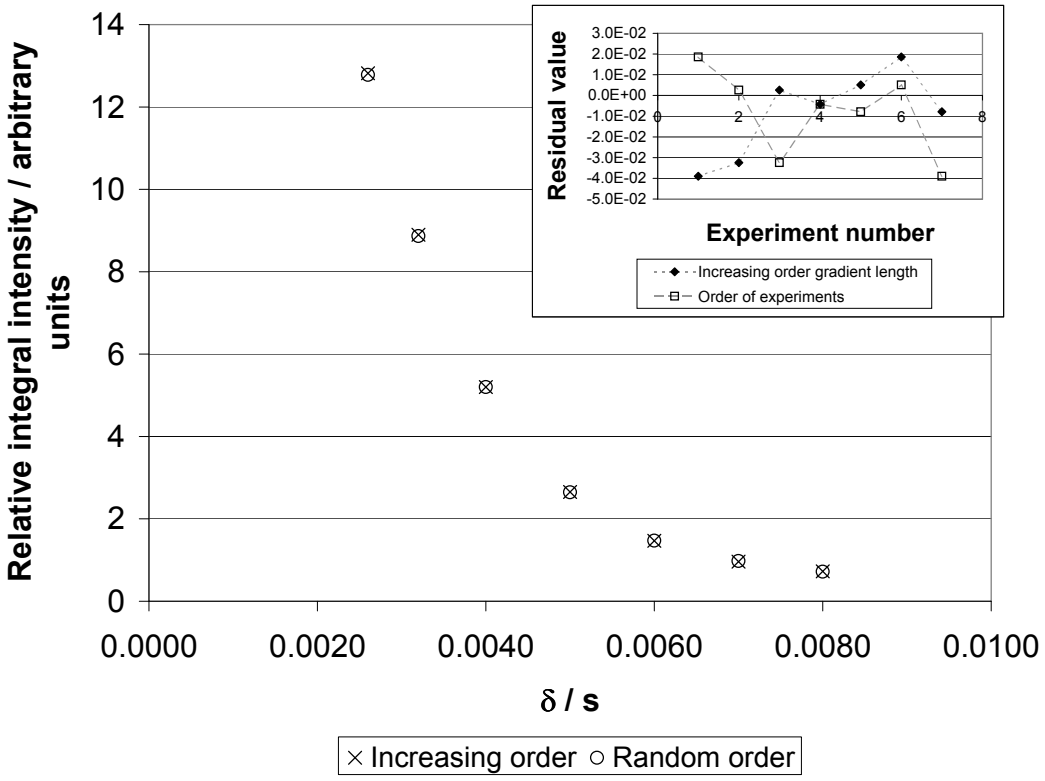

Figure 6.9: Signal attenuation measured at increasing gradient length and in random order of gradient length

6.4.4 Presence of monomers in solution

The presence of poly-lactide or poly-glycolide oligomers or monomers could also affect the observed diffusion behaviour of freezing point characteristics. To determine if there were oligomer or monomers free within solution, a two-dimensional carbon-hydrogen correlation NMR experiment was carried out. This was done at room temperature, on a sample of microspheres after a few weeks immersion in aqueous media. The hydrogen containing molecules detected showed no correlation with carbon, therefore, no oligomers or monomers could be detected in the sample.

6.4.5 Time-resolved cryodiffusometry studies of PLGA microspheres

Cryodiffusometry trial on PLGA microspheres

The first trial of cryoporometry on PLGA microspheres was after 34 days immersion on batch MS045, low molecular weight polymer with 5-FD used in the preparation method. Two experiments were conducted, one during the freezing process and one during the melting process, and the relative signal intensities on the cryoporometry curve at which the

two experiments were carried out were 0.68 for freezing and 0.55 for thawing. Firstly, the non-linear log attenuation plots were evaluated in terms of single and two component fits for the diffusion, as described in Section 6.4.2. Initial one and two component fits for this data can be seen in Figures 6.10 and 6.11, the reduced χ^2 values for these two fits were 0.57 and 0.0044 respectively. The residuals of the two fits show the same characteristics as those in Figure 6.5, systematic for one component fit and more random for two component fit.

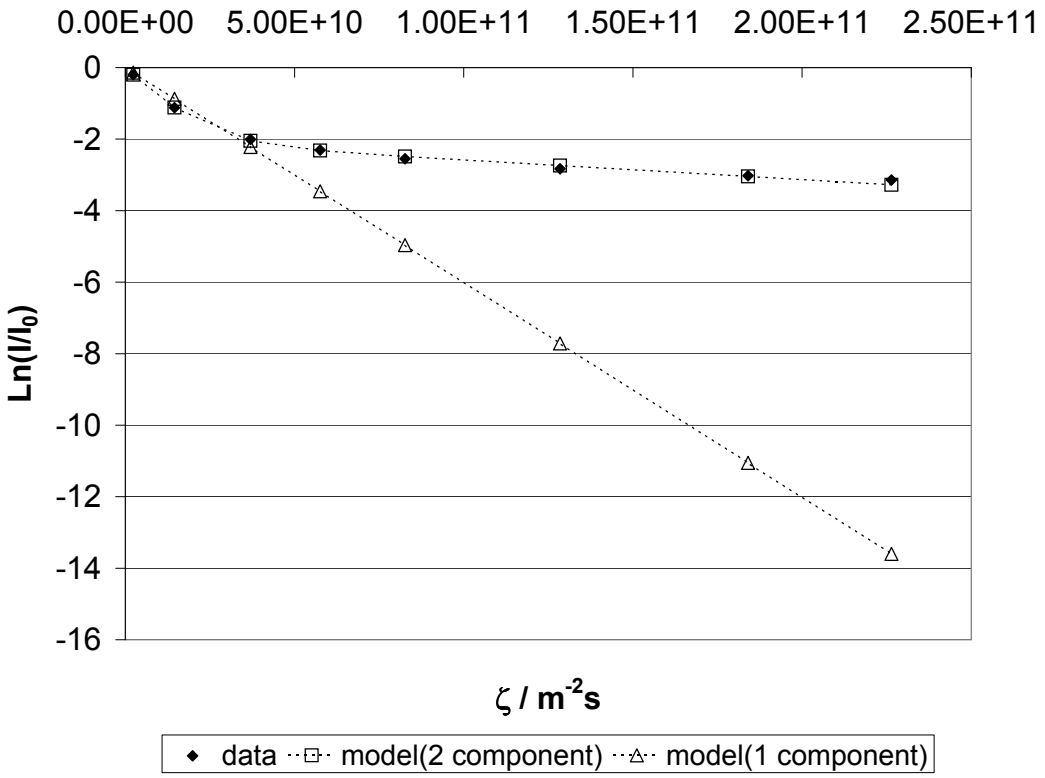

Figure 6.10: Freezing curve cryodiffusometry log attenuation plots fitted to one and two component models

The *rms* displacement of a water molecule calculated for water contained in the fast moving component is of the order of 7–15 μm and for the slow moving component around 1–6 μm. The faster moving component could, therefore, probe the wall thickness between the 'bubble' pores, and between the 'bubble' pores and the outside of the microspheres, which from SEM images were found to be of the order of 10 μm thick, see Figures 4.8a, 4.8b, 4.8c, 4.8d, 4.9a and 4.9b. Whilst the slower moving component is less likely to see the ice barriers in the 'bubble' pores and in the bulk, it could describe the structure within the polymer matrix.

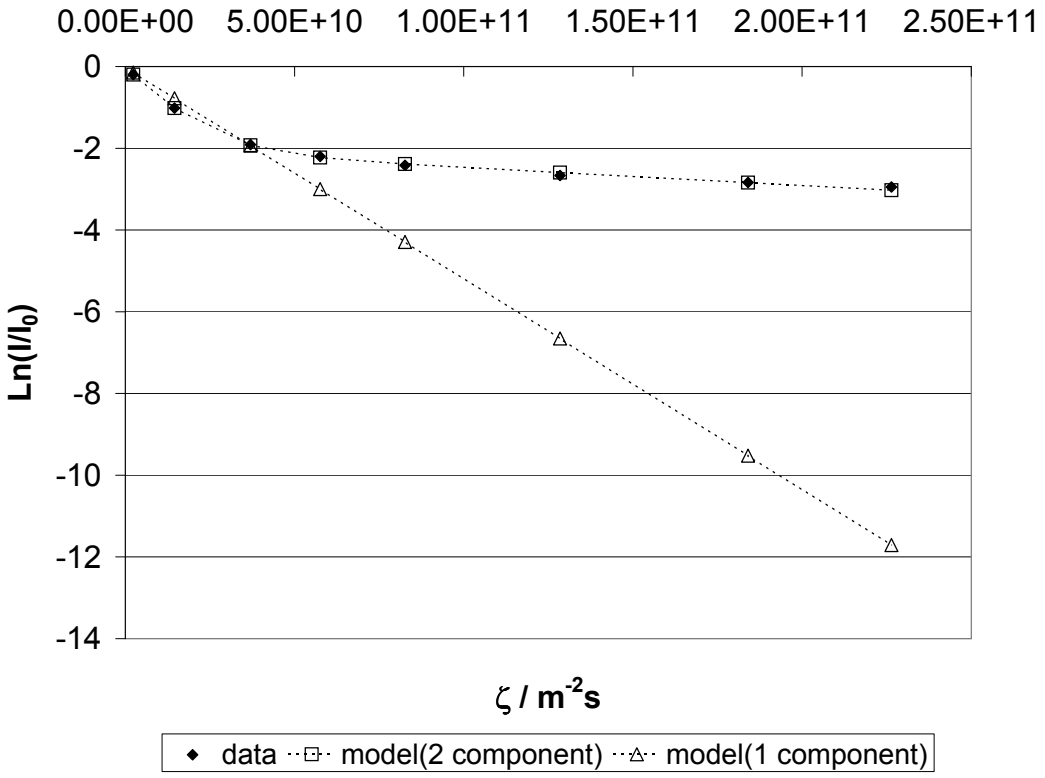

Figure 6.11: Thawing curve cryodiffusometry log attenuation plots fitted to one and two component models

Cryodiffusometry studies of low molecular weight PLGA microspheres with model drug 5-FD encapsulated, batch MS045

The calculated tortuosities for both fast and slow components of water during freezing and thawing over time are shown in Figure 6.12. Fast component tortuosities are around two orders of magnitude smaller than for slow component and the fraction of water in the slow component is upto 25 %. Also shown on Figure 6.12 are the relative signal intensities at which the experiments were carried out and the calculated fraction of water in the fast component. A relative signal intensity of 1 means all the matrix contained solution is molten, less than 1, a fraction of the matrix contained solution is frozen. The fraction of water in the fast component remains high, ≥ 80 %, of the molten solution, at shorter immersion times. On average, during this time little or equal quantities of water exchange between the two components. At long immersion times, ≈ 100 days, the fraction of water in the fast component decreases to ≤ 80 %. Two possible causes for this change are suggested. Firstly, an exchange of water from the slow to the fast component has occurred. Secondly, a greater volume of water in the slow component is observed due to a change in the fraction of molten water within the matrix during the experiment on day 109, than day 60.

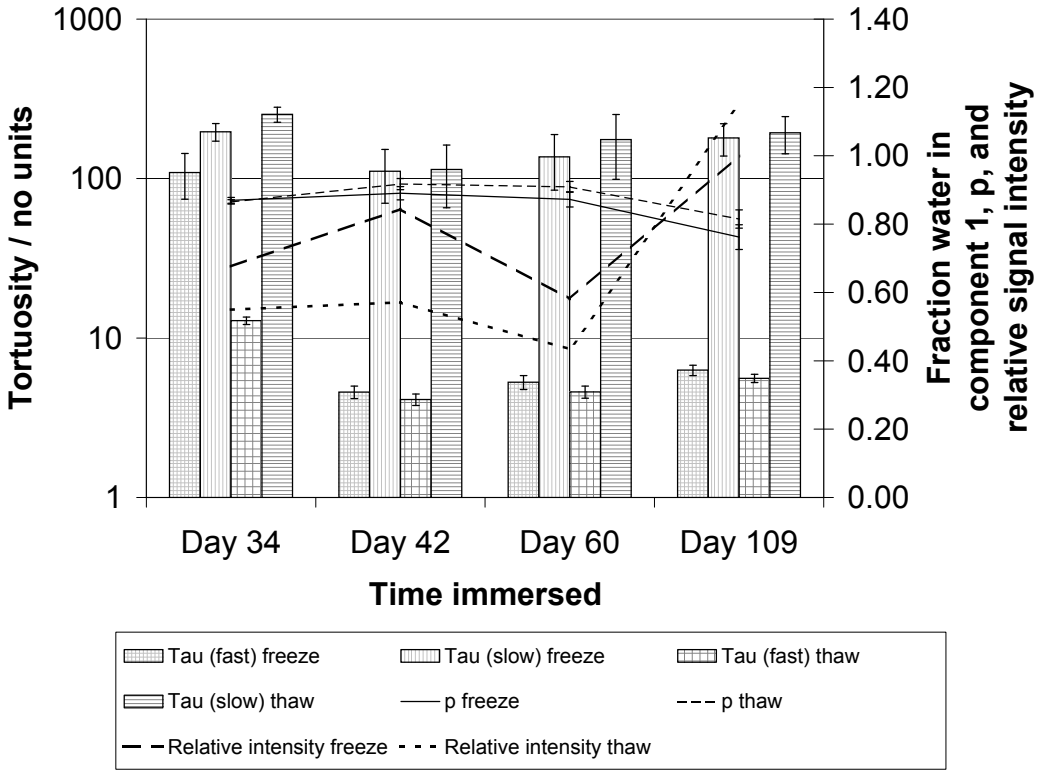

Figure 6.12: Tortuosities of fast and slow components, fraction of fast component and relative signal intensities during freezing and thawing over time for microsphere batch MS045

Figure 6.12 also shows, that despite differences in the relative intensity between freezing and thawing experiments, after 42 days the calculated diffusion coefficients are the same for the two components within experimental error. At 34 days, some difference is seen between freezing and thawing curve diffusion coefficient estimates for the fast and slow components. The relative intensity on thawing is less than on freezing, therefore, a greater fraction of the matrix contained water is frozen. The tortuosity of the fast component is significantly lower on thawing than during freezing. This suggests more free movement for the faster component during early stages of thawing than is experienced during the early stages of freezing.

The error in the estimated tortuosity is a function of the error in the measured diffusion constant, the error in the estimated diffusion coefficient of free water at the specified temperature and the error in the salt adjustment factor. For an example calculation of the errors and their analysis see the appendix, Section A.6. In addition to the individual component tortuosities, the weighted tortuosity, τ_w, can also be used as a measure of change in the average matrix structure. The weighted tortuosity can be calculated using equation 6.16,

$$\tau_w = p\tau_1 + (1-p)\tau_2 \tag{6.16}$$

where τ_1 and τ_2 are the tortuosities for the fast and slow component respectively and p is the fraction of water in the fast component. The weighted tortuosities for both the freezing and thawing curve experiments for microsphere batch MS045 are shown in Figure 6.13. The modal pore neck and pore body sizes are also shown with the weighted tortuosity values in Figure 6.13, this brings together the cryoporometry and cryodiffusometry findings to enhance the interpretation of the matrix evolution.

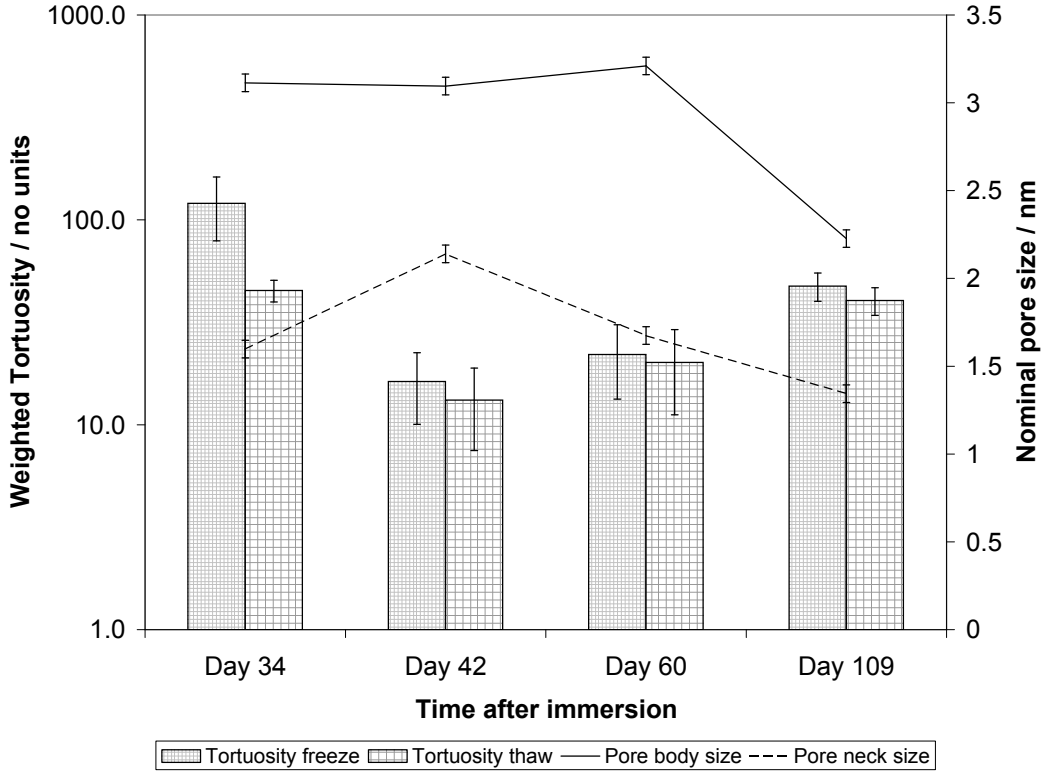

Figure 6.13: Weighted tortuosity during freezing and thawing with modal pore body and pore neck sizes over time for microsphere batch MS045

Between days 34 and 42 tortuosities in both components fall such that the weighted tortuosity decreases to approximately a third of its previous value. This change corresponds to a significant increase seen in the neck size determined from cryoporometry, as the necks 'open', the restriction of water movement within the matrix is reduced and tortuosity goes down. Between days 42 and 60 no significant changes are seen in the individual component tortuosities, the weighted tortuosity shows a slight increase, but this is within the calculated error. This time period corresponds to both a reduction in the pore necks and an increase in the pore body size, the net effect observed is no change in the mobility of the water

molecules within the matrix. Between days 60 and 109 both pore bodies and pore necks reduce in size and there is an increase in the weighted tortuosity seen. From Figure 6.12 an increased relative signal intensity is seen for day 109 compared to that for day 60 showing a smaller fraction of ice is present. The increased tortuosity seen is, therefore, a consequence of a polymer structure change rather than an increased volume of ice. In addition to this, a decrease in the fraction of water in the fast component for day 109 compared to day 60 is seen, which will have the effect of increasing the weighted tortuosity. Whilst the individual tortuosities for each component tend to follow a similar trend as the weighted tortuosity over time, the inclusion of the fraction of water in each component highlights more subtle changes in the average diffusion behaviour like that seen between days 60 and 109.

Cryodiffusometry studies of high molecular weight PLGA microspheres with model drug 5-FD encapsulated, batch MS043

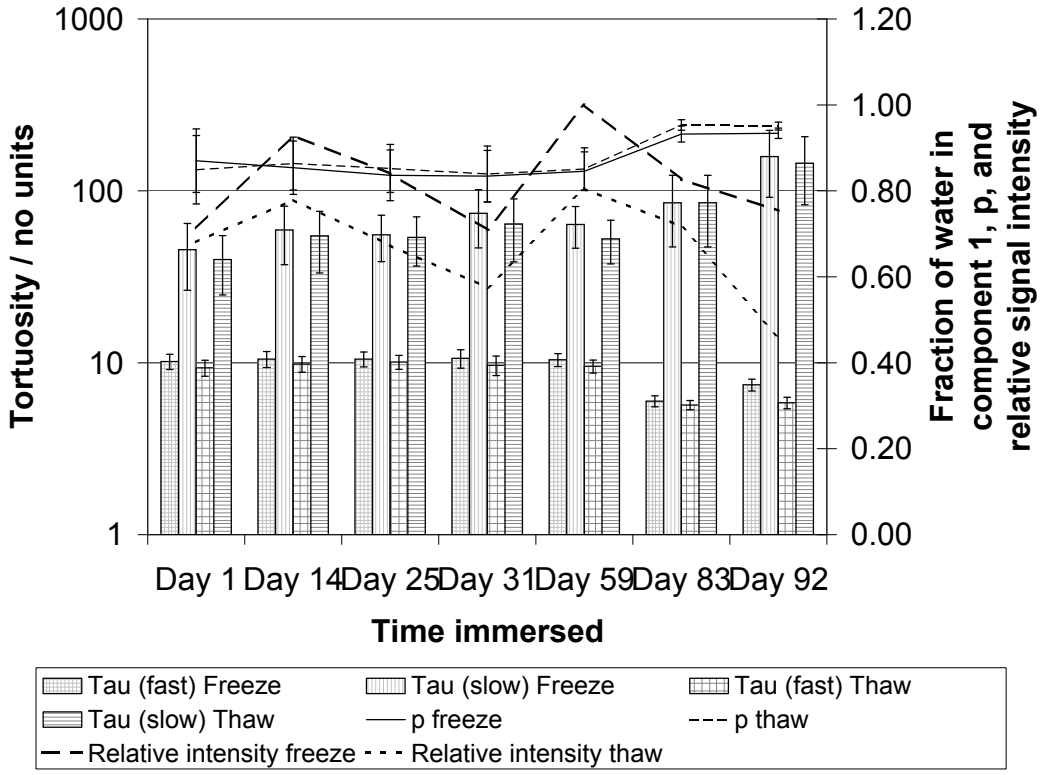

Figure 6.14: Tortuosity of fast and slow components during freezing and thawing over time for microsphere batch MS043

Batch MS043 was made with high molecular weight 50:50 PLGA by the same preparation method as MS045, which was made with the low molecular weight 50:50 PLGA. Both batches used 5-FD as a model drug for encapsulation from the internal aqueous phase

of the first emulsion. For this batch the fast component tortuosities were one order of magnitude smaller than for the slow component and the fraction of water in the slow component was less than for MS045, with values upto 15 %. Figures 6.14 and 6.15 show single component and weighted tortuosity values over time for batch MS043.

From Figure 6.14 it can be seen that there was little change in the observed slow component tortuosity values until long immersion times, where a slight increase is seen. A small, but significant decrease is seen in the fast component tortuosity at 83 and 92 days compared to earlier immersion times. This decrease corresponds in time with an increase in the fraction of water in the fast component, suggesting an increase in the average diffusion of the fast moving component. Between days 59 and 92 a significant increase is seen in the tortuosity of the slow moving component, which suggests in this time the average diffusion in the slow component has reduced.

The relative signal intensities, up until day 83, shown in Figure 6.14 show differences of upto 20 % in the molten fraction of water during the freezing and thawing curve diffusometry experiments, with no significant effect observed on the calculated tortuosity values for freezing and thawing at a given immersion time. However, at day 92, a greater difference in the relative signal intensities for freezing and thawing is seen, that coincides with a small difference seen in the corresponding fast component tortuosities for freezing and thawing. On thawing, more ice is present and the fast component tortuosity is less, implying that fast component of water is, on average, less restricted during later stages of thawing than for the initial stage of freezing. This agrees with earlier discussion for MS045 on day 34.

Figure 6.15 shows the calculated weighted tortuosities and nominal pore neck and pore body sizes at increasing immersion times. Whilst there are small changes in the pore neck, and pore body, size during the time studied, no significant changes can be seen in the weighted tortuosity. This implies that there are changes in matrix structure at the nanometer scale, but the average mass transport behaviour within the polymer matrix is unchanged, or too small to be seen within the error. Initially pore necks open and close as the average pore body size increases, after 25 days immersion, the changes in pore neck size and pore body size oppose each other. In comparison to the low molecular weight PLGA microspheres, batch MS045, the polymer matrix structure appears to be more stable over a 90 day period after immersion, changes in nominal pore size are of lower magnitude and weighted tortuosities do not show significant changes.

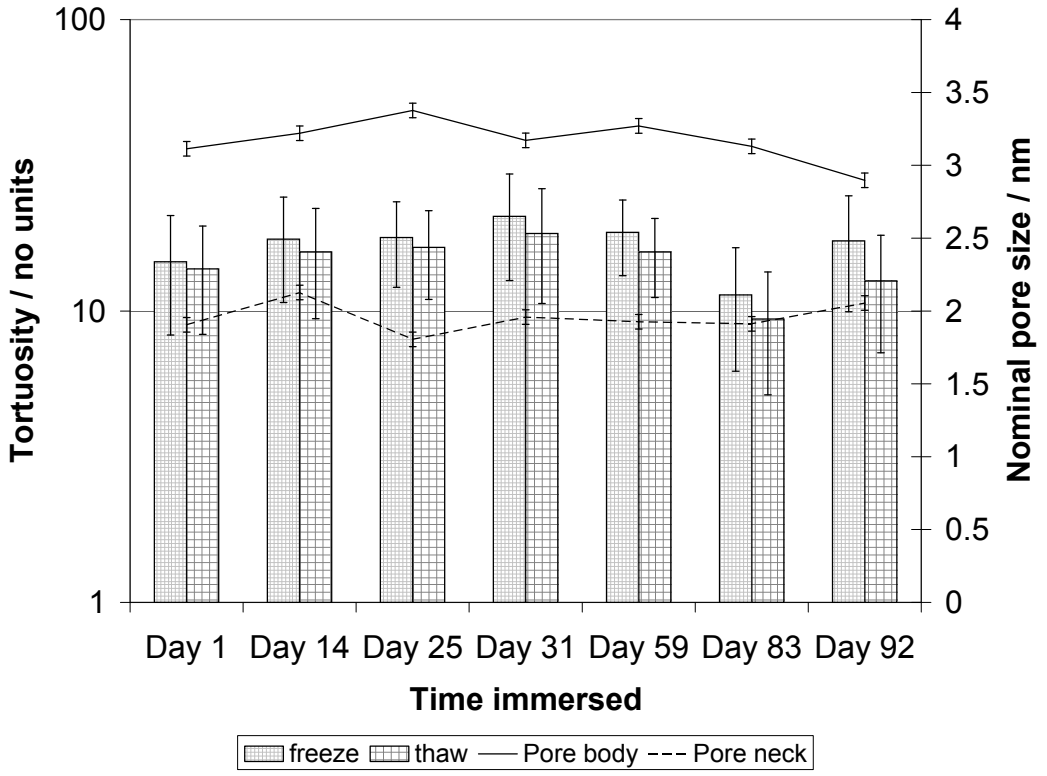

Figure 6.15: Weighted tortuosity values during freezing and thawing over time for microsphere batch MS043

Cryodiffusometry studies of low molecular weight PLGA microspheres without encapsulated drug molecule, batch MS041

A third batch of microspheres made with low molecular weight 50:50 PLGA without encapsulated drug were investigated by cryodiffusometry over time after immersion in a 5 w/v % sodium chloride solution. The tortuosity values calculated for fast and slow components over time, for batch MS041, are shown in Figure 6.16, and the weighted tortuosity values are shown in Figure 6.17. Considering the individual component tortuosities, water in the slow component showed diffusion one to three orders of magnitude slower than that in the fast component and constituted on average 11 % of the observable water. After day 1 there is a significant decrease in tortuosity for both components, but appears most prevalent in the slow component, despite the fraction of water in the slow component being very small at day 1. From day 14 until long immersion times, around 100 days, the individual component tortuosities remain constant, within the calculated error.

At day 116, a significant increase in slow component tortuosity and a decrease in the fast component tortuosity is seen during freezing and not during thawing. The relative signal intensity, fraction of water in the fast component and calculated tortuosities for day 116

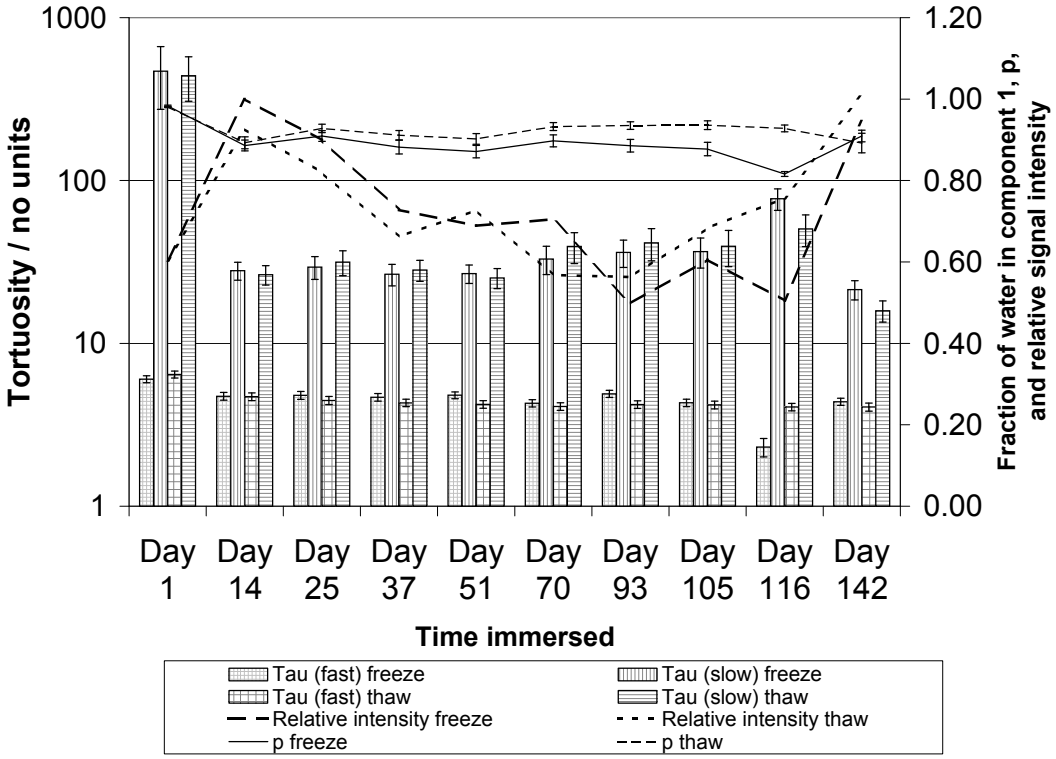

Figure 6.16: Tortuosity of fast and slow components during freezing and thawing over time for microsphere batch MS041

are summarised in Table 6.1. The difference in the observed tortuosities may possibly be

Parameter	Freeze	Thaw
Relative signal intensity	0.51	0.76
Fraction water in fast component(1)	0.82	0.93
Weighted Tortuosity	8.1	3.7
Tortuosity fast component(1)	2.3	4.1
Tortuosity slow component(2)	77	50

Table 6.1: Cryodiffusometry summary for batch MS041 after 116 days immersion

due to the different relative signal intensities at which the freezing and thawing experiments were carried out. More ice present during freezing could mean that a greater volume of one, or both, components of water is frozen and introduces additional tortuosity by the presence of more ice walls. A decreased fraction of water in the fast component during freezing is also observed, suggesting that a greater volume of the fast component water is frozen. The water that is not yet frozen has a greater average diffusion coefficient, or lower

tortuosity. The opposite effect was seen between the freezing and melting tortuosities for Batch MS043 at day 92, where the relative signal intensity was higher during freezing and a decrease in the fast component tortuosity was observed.

At day 142, a significant decrease in the slow component tortuosity is seen as the relative signal intensities increase. Compared to day 14 with similarly high relative signal intensities, there is still a significant decrease in tortuosity seen for the slow component. The decrease in tortuosity of the slow component implies that the water in the slow component has increased mobility, one cause may be that there are less restrictions within the polymer matrix, at longer immersion times.

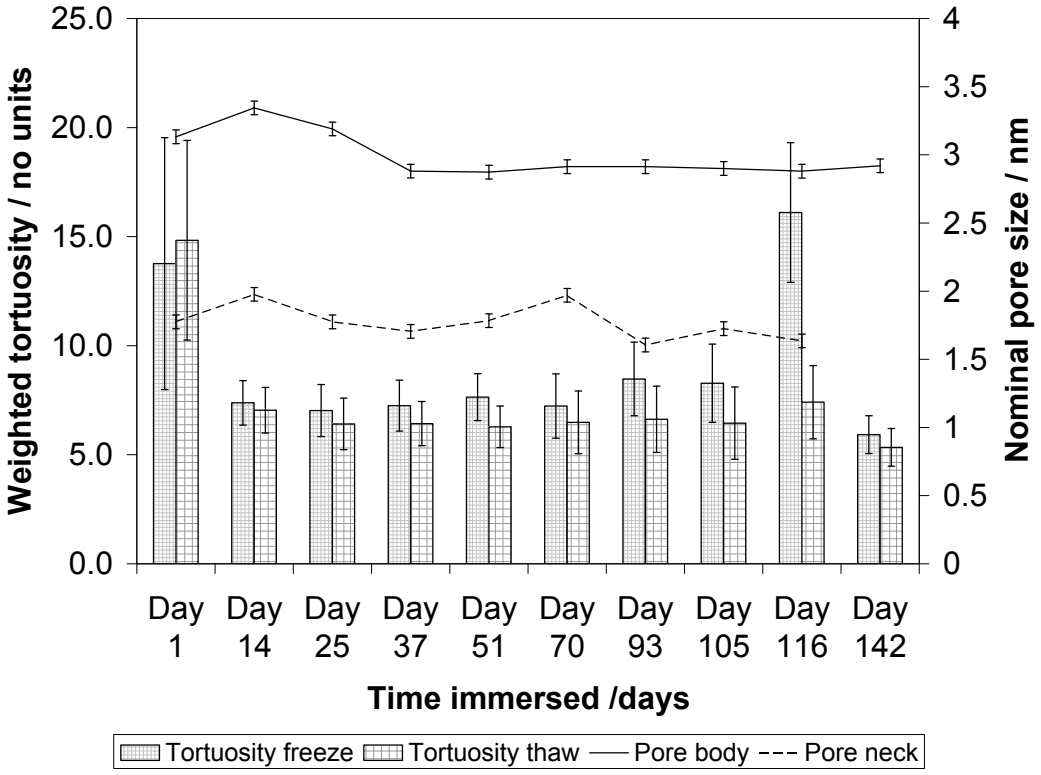

Figure 6.17: Weighted tortuosity during freezing and thawing over time for microsphere batch MS041

The weighted tortuosities and nominal pore neck and pore body sizes for batch MS041 are shown in Figure 6.17. In addition to an increase in the relative signal intensity at which diffusometry experiments were carried out, the decrease in weighted tortuosity observed between days 1 and 14 coincides with an increase in both pore body and pore neck size. At day 37 the relative signal intensity is a similar level to that of day 1, and the pore body and pore neck size have decreased to similar values to those of day 1, but no significant change is seen in the weighted tortuosity from that of day 14. Therefore, the change in

tortuosity seen between days 1 and 14 is thought to be the effect of pore size changes and an increase in the fraction of water in the slow component, rather than relative signal intensity changes. At day 116 the weighted tortuosity during freezing shows a significant increase, driven by the increased fraction of water in the slow component, and the increase in slow component tortuosity coupled with the decrease in the fast component tortuosity, as discussed above.

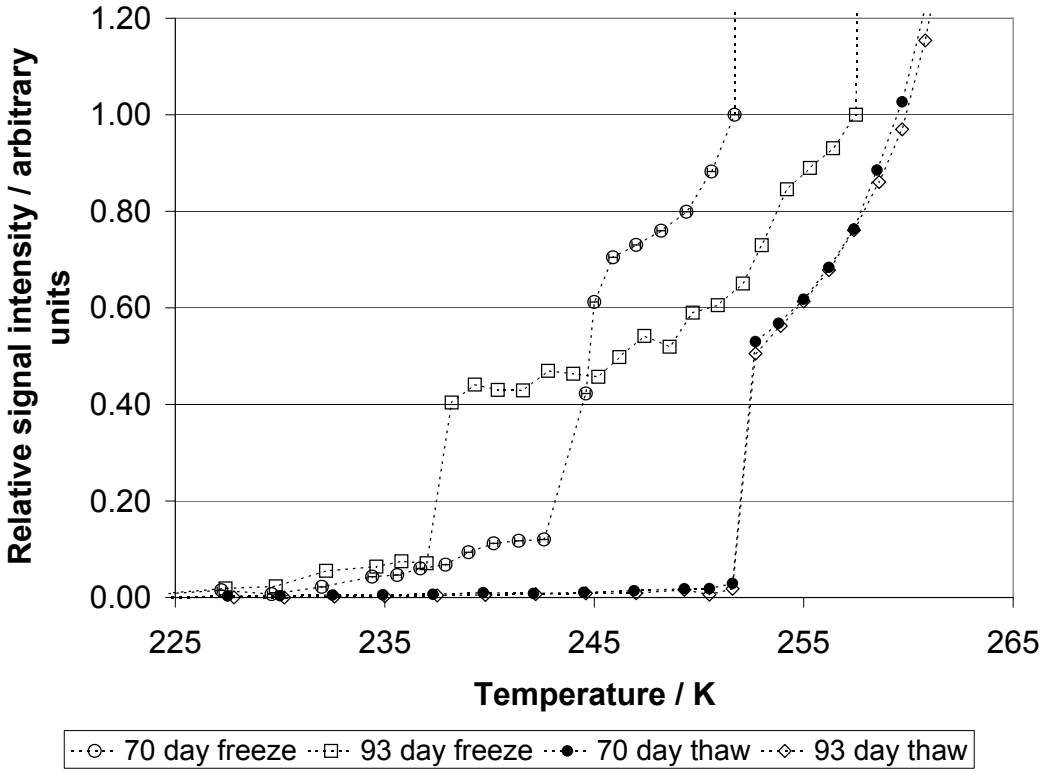

Figure 6.18: Freeze-thaw hysteresis cycles for days 70 and 93 after immersion for batch MS041

The freeze-thaw hystereses, of microsphere batch MS041, for days 70 and 93 are shown in Figure 6.18. No difference is observed in the thawing curve, whilst there is a significant change to the freezing curve between the two experiments. In Chapter 5 the changes in the freezing curve are attributed to changes in the pore neck size distribution and especially the modal pore neck size. To identify any changes in connectivity during this time, cryodiffusometry experiments were carried out at multiple relative signal intensities (molten fractions), the fast component tortuosities determined are shown in Figure 6.19. The fast component tortuosities determined at similar molten fractions at days 70 and 93 during both freezing and thawing are close in value. This suggests that the changes observed in the freezing curve are related to the pore neck size and are not a function of connectivity.

The apparent maxima of the fast component tortuosities, at a molten volume fraction

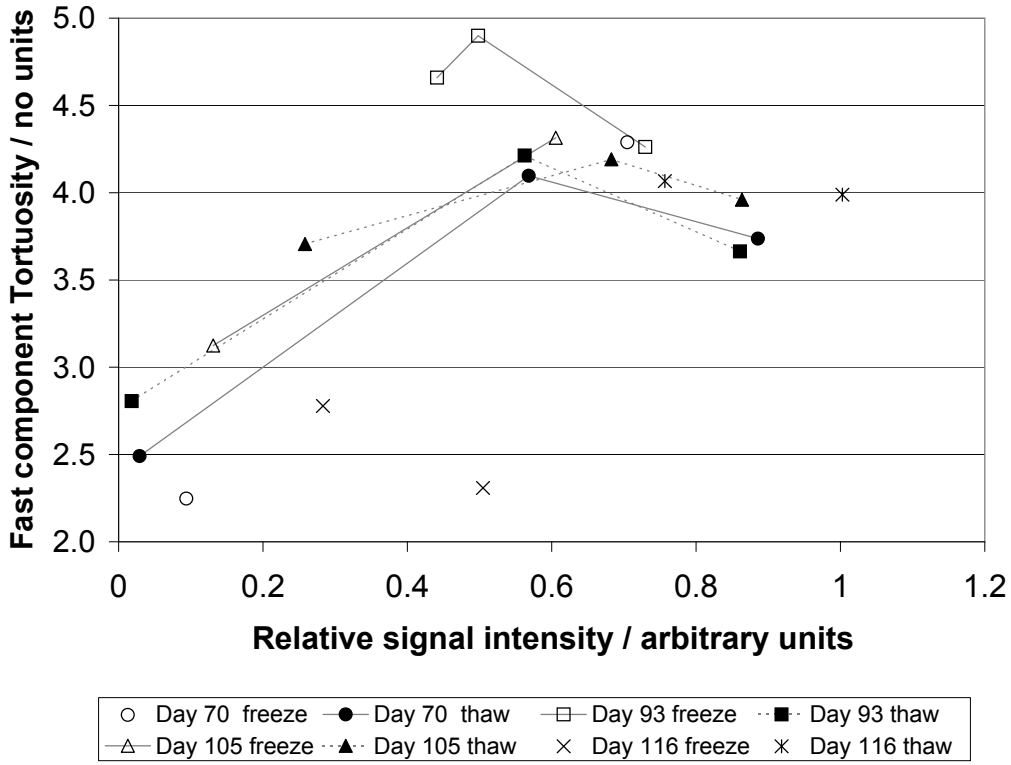

Figure 6.19: Change in the fast component tortuosity during freezing and thawing for batch MS041 at longer immersion times

of around 0.5 to 0.6, corresponds to a sharp knee feature in the melting curves for days 70 and 93, and a wide plateau in the freezing curve for day 93. This suggests the possibility of a more complex situation within the fast component, such that there are two different regions within the fast component. The first region consisting of a broad distribution of large pores, the second region consisting of a narrow distribution of well connected small pores. As the larger pore are frozen out the observed tortuosity increases, once this whole region has become ice, the tortuosity observed is dominated by the second region which has a lower tortuosity. On thawing, the tortuosity at low molten fraction is dominated by the second region, which has a lower tortuosity. Then, as the first region begins to melt the tortuosity increases to a maximum, and finally, as more of the first region melts, the tortuosity decreases again.

6.4.6 Comparison of cryodiffusometry results for three batches of microspheres

Table 6.2 gives the range of values for the calculated diffusion coefficients from PFG experiments adjusted for salt, fraction of water in the fast component and calculated tortuosities for the three microsphere batches studied. The range of calculated tortuosities for the fast component of the water, contained within the matrix, is the same order of magnitude for all three batches. However, the low molecular weight polymer batches (MS041 and MS045) show a greater range of values of tortuosity for the slower component, and are higher in value than those determined for the high molecular weight batch (MS043).

Batch	T /K	D_1 $\times 10^9/m^2s^{-1}$	D_2 $\times 10^9/m^2s^{-1}$	p	τ_1	τ_2	τ_w
MS045	248—255	0.040—0.13	0.0019—0.0042	0.76—0.93	3.4—11	62—250	13—120
MS043	253—256	0.045—0.091	0.0033—0.013	0.83—0.95	5.7—11	40—-160	9.4—21
MS041	244—256	0.064—0.13	0.00092—0.029	0.82—0.98	2.3—6.4	16—470	5.3—16

Table 6.2: Summary of cryodiffusometry parameters calculated for PLGA microsphere batches MS045, MS043 and MS041

From the SEM images, described in Chapter 4, one significant difference observed between the two batches of low molecular weight polymer, without drug encapsulated, MS041, and the drug encapsulated batch, MS045, is a comparative increase in the thickness of the matrix walls between the 'bubble' pores for the drug encapsulated batch, Figures 6.20a and 6.20b show this. Moreover, the cryodiffusometry results show a significant difference in the range of the weighted tortuosities for these two batches, the range being greater for the batch with encapsulated drug (MS045). This difference is driven by the higher value of the fast component tortuosity and larger fraction of water in the slow component for the batch with the encapsulated drug (MS045), which has thicker polymer matrix walls between the 'bubble' pores and at the external surface of the microspheres. Together these observations suggest a more significant presence of dense polymer regions within the matrix in the drug encapsulated batch than the blank batch. These dense polymer regions have, within this work, been assigned to the restricted diffusional behaviour observed as the slow component. These differences between the two low molecular weight batches highlights that changes can be seen when a model drug molecule is encapsulated within the polymer, the effect of which is thought to be drug dependent.

The batch of high molecular weight polymer microspheres with encapsulated drug molecule (MS043) shows similar characteristic ranges in weighted tortuosity and fraction of free water as those seen for the low molecular weight batch without the encapsulated drug (MS041). However, the individual component tortuosities for the high molecular

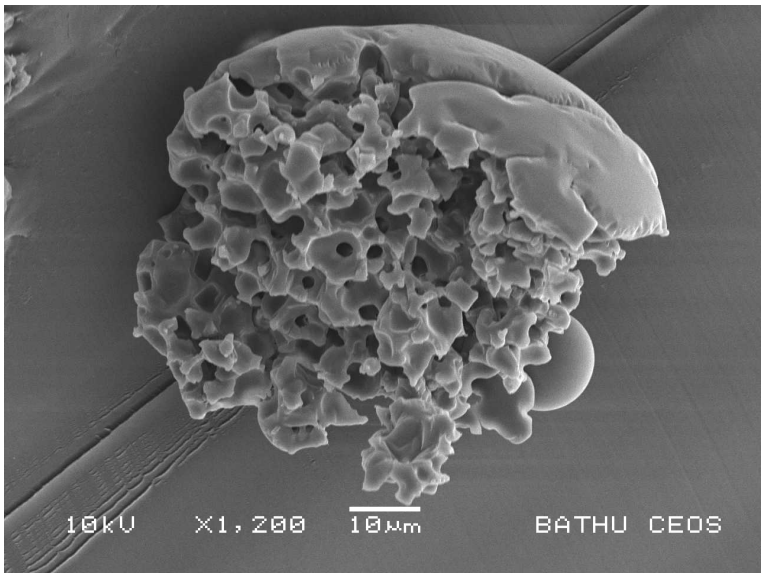

(a) MS041 without drug

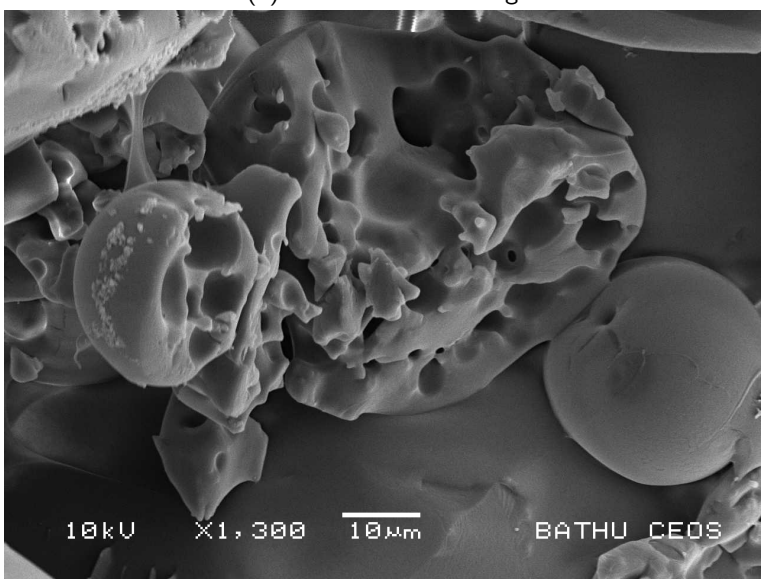

(b) MS045 with drug

Figure 6.20: SEM images of typical low molecular weight PLGA microspheres

weight batch show similar ranges as the low molecular weight batch with encapsulated drug (MS045), which shows that the difference in the weighted tortuosity is driven by the fraction of water in the fast component alone. At long immersion times the trend of the fraction of free water for the high molecular weight batch increases, whilst it decreases for the low molecular weight batch, indicating a difference in the overall degradation mechanism for the change in molecular weight of the polymer.

6.4.7 Further interpretation of cryodiffusometry results for batch MS041

The contributions to the signal attenuation made by the two components are considered separately, to assess if the diffusion of the fast component is totally free, or restrained in one, or two dimensions. From the calculation of the signal attenuation of each component, it can be seen that the fast component is dominant at lower values of ζ, and the slower component is dominant for higher values of ζ, in agreement with Callaghan et al. (1979). An estimate of free diffusion, one dimension and two dimensionally constrained models for each component are given in Figures 6.21 and 6.22.

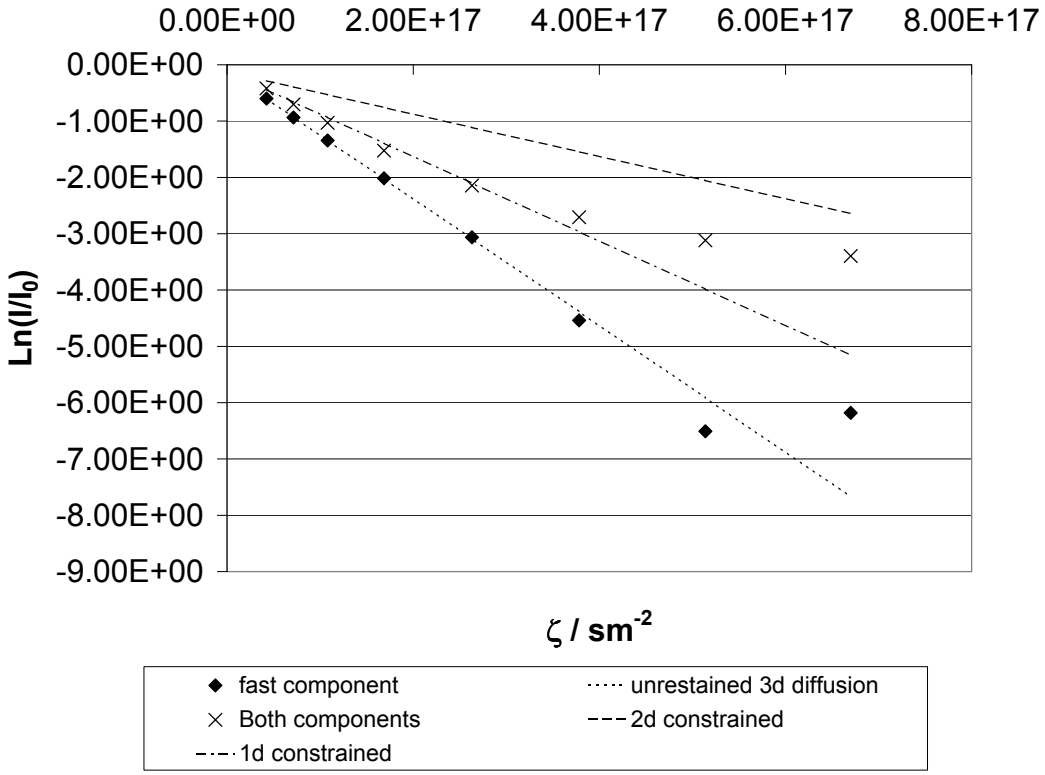

Figure 6.21: Fast component contribution to signal attenuation, comparing 1 and 2 dimensionally constrained and free diffusion models for MS041, day 37, Δ 0.20 s, freezing curve

It is observed that a good fit to the actual data comes from a 2 dimensional motion (1 dimensionally constrained) fast component for low values of ζ and 3 dimensional diffusion of the slow component at higher values of ζ, shown in Figure 6.23. The slow component diffusion, is 3 dimensional, and restricted, as determined earlier in section 6.4.2. In terms of the transport of a small molecule within the polymer matrix, this suggests the presence of two types of regions within the matrix structure. The fast component represents regions

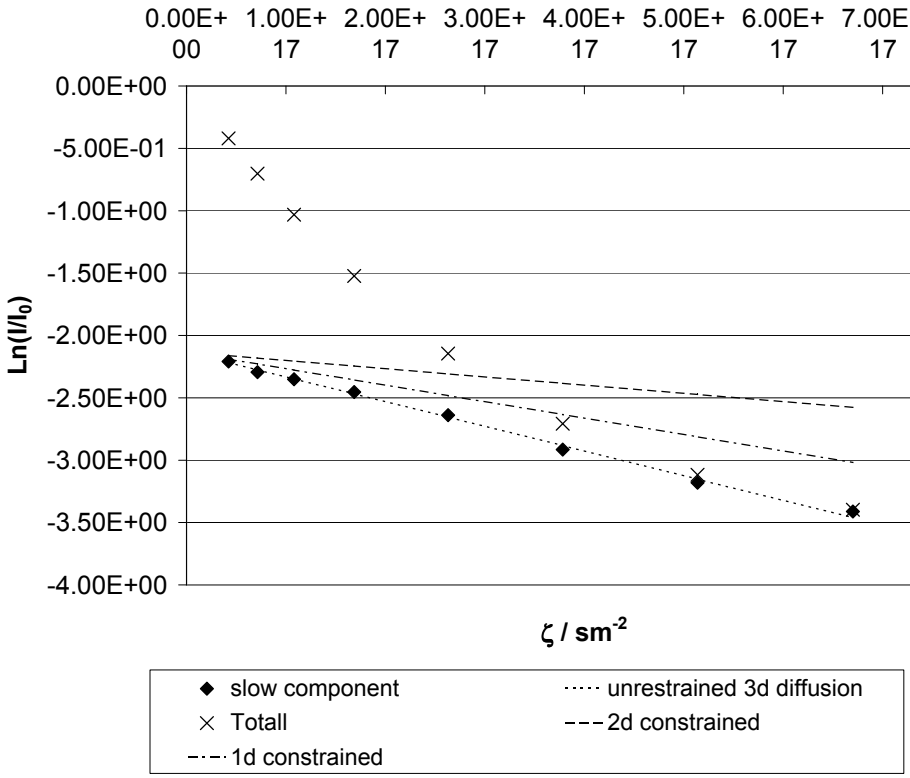

Figure 6.22: Slow component contribution to signal attenuation, comparing 1 and 2 dimensionally constrained and free diffusion models for MS041, day 37, Δ 0.20 s, freezing curve

of faster transport, better diffusion and lower tortuosity, that is restrained within planes bounded by impenetrable walls. These walls are thought to be the ice walls formed when the bulk and 'bubble' pore contained water is frozen. The other regions represented by the slower diffusion water have three dimensionally restricted motion, which are thought to be regions of more dense polymer that take longer to evolve and release the encapsulated molecule. This follows from the findings of Messaritaki et al. (2005) where different regions of polymer within the microsphere were observed to have different drug release profiles.

Modelling anisotropic slab geometry

Models for 'slab-shaped' pores or plate geometry from literature are fitted to the data collected for microsphere batch MS041 (Fordham et al., 1994) as described earlier in Section 6.2.1. Data collected on day 37 for microsphere batch MS041 is shown in Figure 6.24. It is hoped that an estimate of the slab thickness, or separation distance, between restricting walls may help to identify the scale of the fast component regions within the matrix and determine the likely source of the restriction to motion within the matrix. The corresponding separation distance is found by minimising the sum of the least squares between

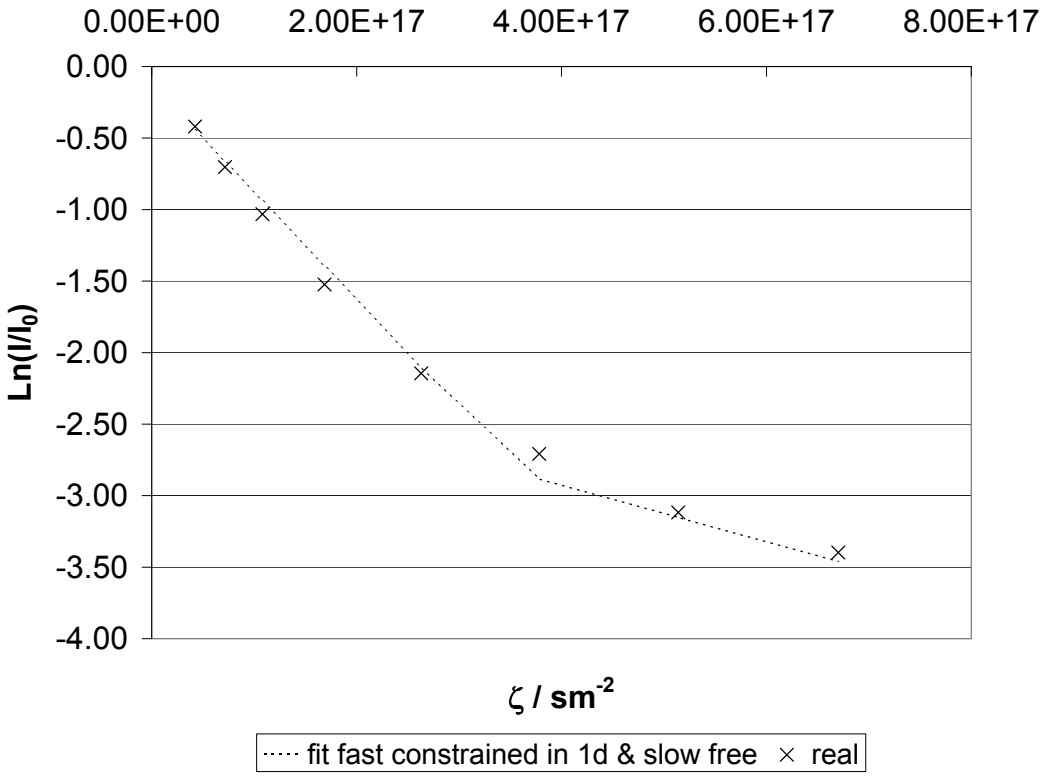

Figure 6.23: Combined signal attenuation model for MS041, day 37, Δ 0.20 s, freezing curve

the estimated log-attenuation and the observed log attenuation determined for two dimensional motion of the fast component. The slab separation distance at 37 days immersion, of MS041, is 4.8×10^{-6} m. The calculated separation distance between anisotropic plates over the first 37 days immersion of microsphere batch MS041 are given in Table 6.3. This model assumes both fast diffusion with zero relaxation at the wall, and slow diffusion with strong relaxation at the wall. An exact solution to calculate the echo signal intensity, $M(K, \Delta)$, for the slow diffusing limit was given by Mitra and Sen (1992), equation 6.17. The results of fitting this model to the data are also given in Table 6.3.

$$M(K,\Delta) = \frac{8}{\pi^2} e^{-(\frac{D\pi^2}{16a^2})\Delta} e^{-\frac{16k^2a^2(\pi-3)}{\pi^2}} \tag{6.17}$$

where $k = \gamma\delta g$.

The general trend seen in the separation distance for this batch of microspheres during the first 37 days immersion follow the trend seen in the pore neck size and pore body size for the same period of time. The separation distance determined for anisotropically arranged slab-shaped pores begins at around 3 μm which is of the order of size observed in SEM images for the matrix wall thickness between the 'bubble' pores of the dry microspheres be-

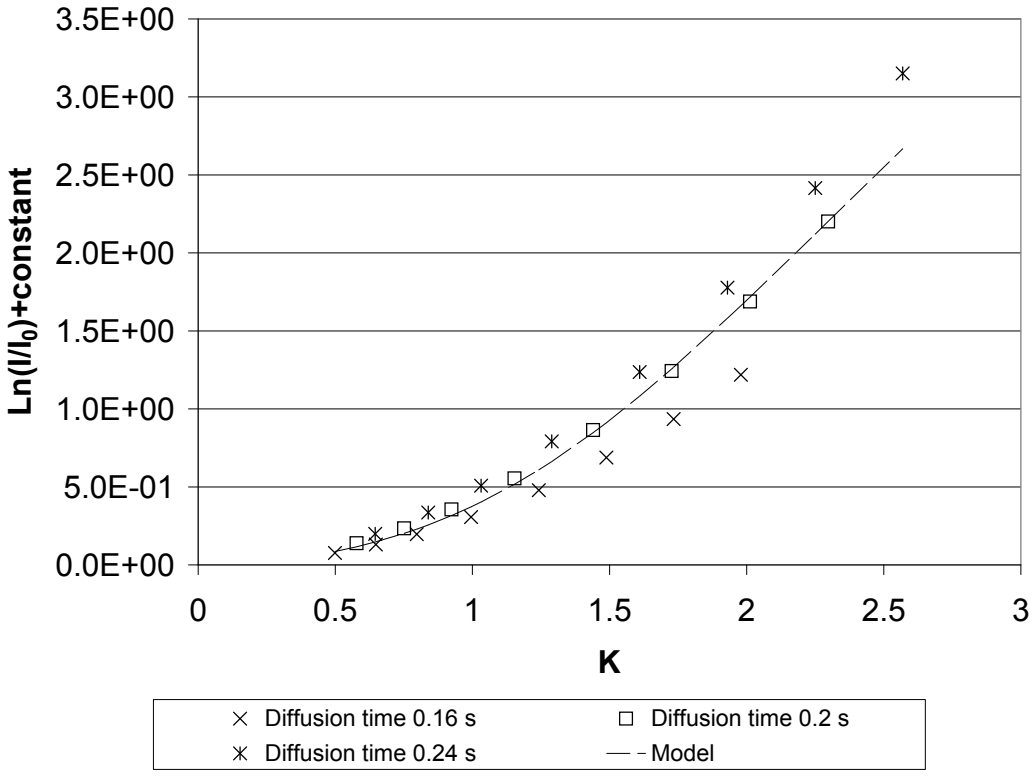

Figure 6.24: Microsphere batch MS041 day 37 plot of $\ln \frac{I}{I_0} + 4\pi^2 q^2 D_0 \Delta$ *against* K *to estimate separation distance between plates*

Immersion time	Calculated separation distance / μm (Fordham et al., 1994)	Calculated separation distance / μm Slow diffusion limit (Mitra and Sen, 1992)
Day 1	2.7	8.4
Day 14(freeze)	7.2	10.1
Day 14(thaw)	7.4	10.2
Day 25	3.9	9.7
Day 32	2.1*	7.3
Day 37	4.8	8.9

*Manual fit

Table 6.3: Separation distance determined for anisotropically arranged plates with increasing immersion times for MS041

fore immersion. There is good agreement in the estimated slab thickness values determined for day 14 during freezing and thawing. An estimate for slab thickness based on data for one value of diffusion time at day 42 for the low molecular weight drug encapsulated batch of microspheres is around 6 μm, which is similar to that for the non-drug encapsulated batch at similar immersion times. Analysis of high molecular weight drug encapsulated microspheres at days 1 and 31 indicate slab separations of 8 and 7 μm respectively; these values are also based on data for just one value of diffusion time. Caution must be taken,

however, in evaluating these results as absolute values, but at this time, a proof of concept and applicability of the models is being made. Therefore, it is possible to say that the slab separation distance calculated from cryodiffusometry data is of the correct order of magnitude to that expected from the inspection of SEM images of dry microsphere samples. A difference is seen between the estimated values of slab separation determined from the model for a range of relaxation behaviour and that of strong relaxation behaviour, but the two estimates show similar trends.

6.5 Conclusions

By combining cryoporometry and diffusometry it is possible to simultaneously study changes in the matrix structure at the nanometer scale and changes in the mass transport properties seen over time after immersion in an aqueous media. Whilst cryoporometry provides time-resolved pore size distributions in terms of pore bodies and pore necks, diffusometry experiments provide a means of investigating diffusion characteristics of water contained in the polymer matrix, after the bulk medium has been frozen. Diffusometry, using water as the probe molecule, can be used to identify the transport characteristics of a small molecule within the matrix. Water plays a vital role in the degradation process within the polymer structure, therefore, the transport of water into, within and out of the matrix is of interest in terms of polymer degradation in addition to acting as a probe molecule, or model 'drug'.

Studies on the low molecular weight batches show more changes in the neck sizes observed at early immersion times, at long immersion times, both pore neck and pore body size distributions broaden, a possible sign of structural breakdown. Both low molecular weight batches have similar values for fast component tortuosity, although the drug encapsulated batch have higher values of tortuosity for the slow moving component, suggesting a more complex path for water in the drug encapsulated batch to that seen for the blank microspheres.

For high molecular weight microspheres more changes are seen in the pore body size at earlier immersion times, possibly due to the polymer chain degradation occurring at the backbone of the polymer chain, rather than at the end of the polymer chains at this stage. The tortuosity of the fast component for the high molecular weight batch microspheres is higher than that for the low molecular weight batches. Combined with percolation analysis that suggests relatively good connectivity, this shows that the higher molecular weight polymer matrix provides more complex pathways for molecular transport which could have a significant effect on the drug release mechanism. The slow component tortuosity for high molecular weight polymer microspheres with encapsulated drug is greater than that

for blank low molecular weight microspheres and less than that for drug encapsulated low molecular weight microspheres.

The transport of water molecules through the polymer matrix is indicative of potential pathways for small drug molecules to travel through the matrix and eventually out of the matrix via the pore necks in to the release medium. This is often thought to be one of the determining factors within the drug release mechanism from such a system. Cryodiffusometry has been used to identify change in the pore openings and changes in the tortuosity for small molecule transport over time in an aqueous medium. Observable differences between the three batches of microspheres studied over time that can be related to the structural and mass transport changes within the polymer matrix have been identified and discussed. These observations relating to pore size and restricted diffusion are indicative of the different mechanisms involved in the microsphere evolution, and the subsequent drug release behaviour from such systems. By combining the two techniques a more refined understanding of the matrix structure evolution can be made than by either technique alone.

References

R. P. Batycky, J. Hanes, R. Langer, and D. A. Edwards. A theoretical model of erosion and macromolecular drug release from biodegrading microspheres. *Journal of Pharmaceutical Sciences*, 86(12):1464–1477, 1997. PLGA 50:50, double emulsion, time evolved, change in molecular weight, erosion mechanism, theoretical model.

P. Callaghan, K. W. Jolley, and J. Lelievre. Diffusion of water in the endosperm tissue of wheat grains as studied by pulsed field gradient nuclear magnetic resonance. *Biophysical Journal*, 28:133–142, 1979.

P. T. Callaghan, K. W. Jolley, and R. S. Humphrey. Diffusion of fat and water in cheese as studied by pulsed field gradient nuclear magnetic-resonance. *Journal of Colloid and Interface Science*, 93(2):521–529, 1983.

A. V. Filippov and V. D. Skirda. An investigation of the structure of a porous substance by nmr cryodiffusometry. *Colloid Journal*, 62(6):759–764, 2000.

E. J. Fordham, S. Gibbs, and L. Hall. Partially restricted diffusion in a permeable sandstone:observations by stimulated echo pfg nmr. *Magnetic Resonance Imaging*, 12(2): 279–284, 1994.

M. P. Hollewand and L. F. Gladden. Transport heterogeneity in porous pellets .1. pgse nmr-studies. *Chemical Engineering Science*, 50(2):309–326, 1995.

http://www.datathief.org/. Datathief iii, 14th October 2008.

J. S. Kim and A. Yethiraj. A diffusive anomaly of water in aqueous sodium chloride solutions at low temperatures. *Journal of Physical Chemistry B*, 112(6):1729–1735, 2008. Kim, Jun Soo Yethiraj, Arun.

A. Messaritaki, S. Black, C. F. v. d. Walle, and S. P. Rigby. Nmr and confocal microscopy studies of the mechanisms of burst drug release from plga microspheres. *Journal of Controlled Release*, 108(2-3):271–281, 2005.

J. Mitchell, S. C. Stark, and J. H. Strange. Probing surface interactions by combining nmr cryoporometry and nmr relaxometry. *Journal of Physics D-Applied Physics*, 38: 1950–1958, 2005.

P. P. Mitra and P. N. Sen. Effects of microgeometry and surface relaxion on nmr on pulsed-field-gradient experiments: Simple pore geometries. *Physical Review B*, 45:143–156, 1992.

P. P. Mitra, P. N. Sen, and L. M. Schwartz. Short-time behavior of the diffusion-coefficient as a geometrical probe of porous-media. *Physical Review B*, 47(14):8565–8574, 1993.

F. Stallmach and P. Galvosas. Spin echo nmr diffusion studies. In *Annual Reports on Nmr Spectroscopy, Vol 61*, volume 61 of *Annual Reports on Nmr Spectroscopy*, pages 51–131. Elsevier Academic Press Inc, San Diego, 2007. ISI Document Delivery No.: BID60 Times Cited: 5 Cited Reference Count: 207 Stallmach, Frank Galvosas, Petrik Review 525 B STREET, SUITE 1900, SAN DIEGO, CA 92101-4495 USA.

E. O. Stejskal and J. E. Tanner. Spin diffusion measurements: spin echoes in the presence of a time dependent field gradient. *Journal of Chemical Physics*, 42(288-292), 1965.

J. R. Taylor. *An Introduction to Error Analysis The Study of Uncertainties in Physical Measurements*. A Series of Books in Physics. University Science Books, Oxford University Press, first edition, 1982.

Chapter 7

Conclusions and future direction

7.1 Conclusions

A robust cryoporometry method has been developed which has significant improvements on the methods previously discussed in the literature. These improvements are an accurate sample temperature measurement using a 't' type thermocouple and a reduction in the temperature gradient through reducing the sample depth requirements. Both of these improvements provide confidence in the sample temperature accuracy and increase the accuracy of the pore size distribution determined from cryoporometry.

Investigations of sol-gel silica materials have shown the freeze-thaw hysteresis is repeatable after supercooling effects have been removed. By comparison of the freeze-thaw hysteresis with other porosimetry methods such as nitrogen sorption and mercury intrusion-extrusion an estimate of the Gibbs-Thomson parameter can be made. Studying whole and powder samples of the silica material it has been shown, that similar to mercury intrusion-extrusion, the causes for the freeze thaw hysteresis are attributed to single pore hysteresis and shielding effects. The single pore hysteresis for this system can be shown to follow the theory of Petrov and Furo (2006) for cylindrical pores. Heterogeneous nucleation is identified for the freezing mechanism within the silica material, such that a freezing front travels from the bulk at the surface of the pellet toward the centre of the pellet through the pore network. This mechanism has been described in terms of percolation theory. The cryoporometry freezing curve has been shown to represent the size distribution of the pore necks, or entrances, whilst the thawing curve represents the pore body size distribution. To this end, the freezing curve has been shown to provide additional information to the melting curve, previously not identified.

PLGA microspheres have been made with both high and low molecular weight PLGA,

some containing model drug molecules. SEM micrographs of different batches have been compared to identify micrometer length scale differences between batches. The presence of a model drug molecule can be seen to affect the micrometer scale structure of the microspheres. Diffusometry experiments conducted at room temperature have been used to calculate average cavity sizes for the 'bubble' pore observed in the microsphere structure. Agreement between SEM observed 'bubble' pore size and estimated cavity size, provides confidence in the application of PFG methods and their interpretation for microsphere structure investigations. Other traditional porosimetry techniques such as gas sorption and mercury porosimetry are not appropriate for analysis of microspheres, therefore, diffusometry techniques provide an alternative means for their investigation.

Cryoporometry of PLGA microspheres has identified changes in the pore neck and pore body sizes over time at the nanometer length scale. At this scale the investigations are probing the structure of the polymer matrix, the evolution of which is thought to play a key role in the release of a drug molecule. Changes in nominal pore sizes and the observed distribution of pore sizes are seen over time. Differences between batches of high and low molecular weight, and drug encapsulated and non-drug encapsulated microspheres are seen. Cryoporometry scanning loops suggest the presence of shielding effects during the freezing process of the water contained within the polymer matrix. The restricting pore structure of the microspheres that prevent the progress of the freezing front into the polymer matrix are thought to play a role in preventing the movement and release of a drug molecule out of the polymer matrix. Percolation theory has been applied to some of the microsphere batches studied and differences in the observed percolation threshold are seen between batches, and with increased immersion time.

Cryodiffusometry experiments of matrix contained water was best modelled as water contained in two components, the fast component which appeared to have free motion in two dimensions, and the slow component which appeared to suffer restricted diffusion. Applying models for anisotropically arranged slab geometry pores for the fast component, the pore width was found to be of the same order of magnitude as the polymer matrix walls between the 'bubble' pores and between the bubble pores and the external surface. The confining barriers are, therefore, thought to be the ice walls of the frozen fraction of water. The restricted cavity size determined for the slow component was smaller than the observed walls thickness and, therefore, thought to be a characteristic of regions within the polymer matrix where the matrix is more dense. Over time, after immersion, significant changes in the tortuosity of both components were seen and when compared to changes seen in the pore neck and body sizes, correlations can be seen. When put together, the cryoporometry and the diffusometry experiments carried out have shown that a wealth of information can

be gained from combining these NMR techniques. The possibility to combine techniques provides a non-invasive real time method to probe the transport and structure properties of these dynamic systems. These techniques also have potential for investigating nanoscale characteristics of other materials where structural changes are observed with time.

7.2 Future direction

The work that has been carried out on cryoporometry development and the use of cryodiffusometry to investigate drug release systems has shown that valuable information can be gained from the combination of these techniques. In this section ideas for further studies are considered.

7.2.1 Other materials

The application of cryodiffusometry to alternative materials used for drug release devices has potential to highlight the different behaviour in the structures and how they evolve in an aqueous environment with time. The methods used here could be applied to other silica or polymeric materials, or materials that are a combination of the two base materials. Provided that a material is suitable for use in a strong magnetic field, structural information can be gained from the cryoporometry and diffusometry that may be useful to identify transport properties which have an impact not only for drug delivery devices, but also, within catalysis and adsorption systems.

7.2.2 Other nuclei NMR PFG, relaxometry

The versatility of NMR techniques provides the opportunity to combine the cryodiffusometry technique developed for studying water with other NMR experiments such as relaxometry or the diffusion of alternative nuclei such as Fluorine-19 or Sodium-23. The results of a preliminary experiment looking at sodium diffusion in solution are shown in Figure 7.1.

7.2.3 Model alternative administration methods

The potential use for an oral drug delivery device with controlled release characteristics requires a more in depth study of the effect of acid conditions on the drug delivery device. The cryodiffusometry methods applied to study PLGA microspheres have been applied to investigate the early immersion behaviour of acid treated and non-acid treated microspheres to identify any initial effect of acid treatment.

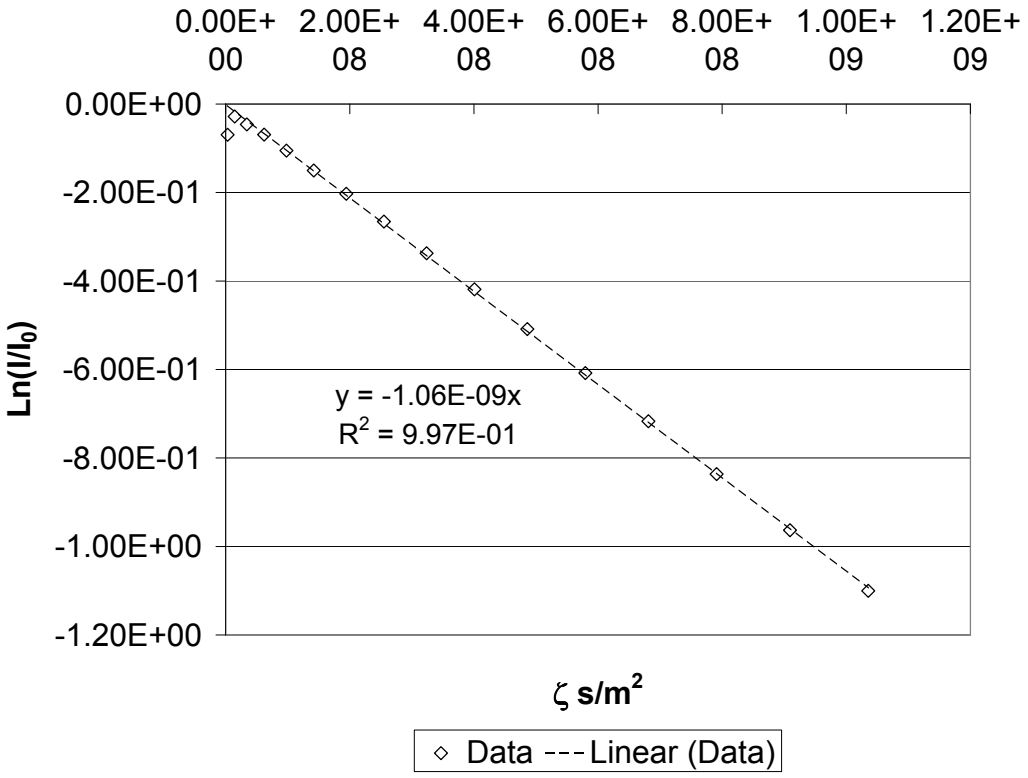

Figure 7.1: Log attenuation plot for Sodium-23 diffusion in a partially frozen PLGA microsphere sample

Microspheres (batch MS041) were pre-treated with hydrochloric acid at a pH of 2.0 for 3 hours to simulate passing through the stomach after oral delivery. For the acid treatment, a 5 ml filter pipette tip had the tip cut-off and a small magnetic stirrer was attached using sticky tape. The microspheres were placed on top of the filter and approximately 2 ml of 0.01 M hydrochloric acid was added to the pipette tip. The top of the pipette tip was sealed with parafilm and the whole tip placed inside a scintillation vial that was secured in place on a magnetic stirrer plate. The stirrer plate was switched on to half maximum speed, providing enough movement to agitate the pipette tip containing the microspheres and acid as to simulate movement within the stomach. After 3 hours of agitation, the pipette tip was removed from the vial, the stirrer bar removed and a vacuum pump was used to remove the acid through the filter of the tip, leaving the microspheres on the filter. The microspheres were then washed three times with phosphate buffer before being transferred to the 100 μl pipette tip as described previously for the microsphere cryodiffusometry experiments. The aqueous medium used for these experiments was a phosphate buffer (pH 7.4). As a control experiment, a sample of the same batch of microspheres was 'treated' with buffer solution in place of acid, non-acid treated sample. The two samples were analysed in parallel, at

varying times of immersion.

No significant difference is seen in the cryoporometry data for acid treated and non-acid treated microsphere samples at early immersion times. Diffusometry results carried out at equal signal intensities for the two samples on day 1 show a much lower relative tortuosity for the batch treated with acid than that not treated. This further demonstrates the additional benefits for combining the two techniques for the investigations of these types of system.

References

O. Petrov and I. Furo. Curvature-dependent metastability of the solid phase and the freezing-melting hysteresis in pores. *Physical Review E*, 73(1), 2006. Part 1.

Appendix A

Appendix

A.1 Nitrogen adsorption results for microspheres batch MS045

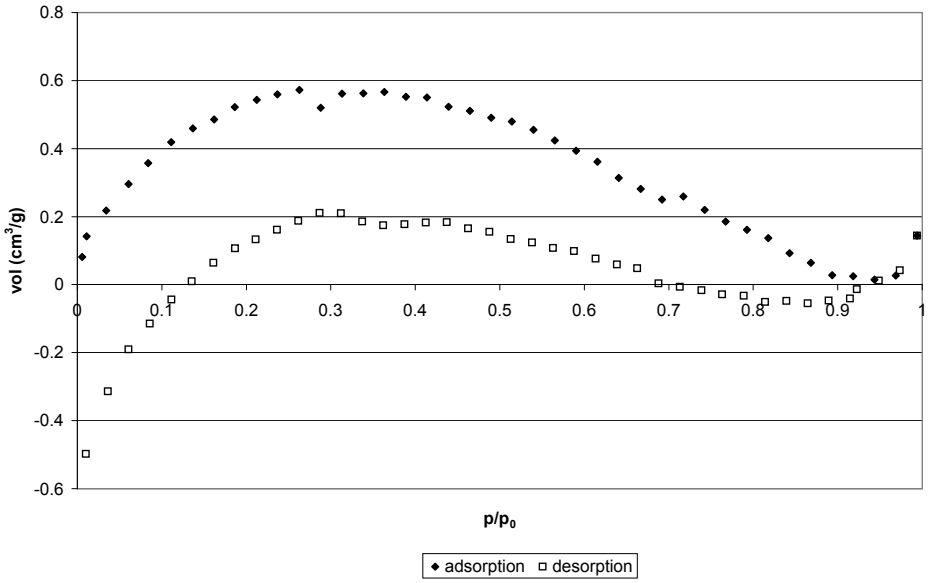

A.2 Example of cryoporometry cycles for microsphere batch MS045 one day after immersion in water for two independent samples

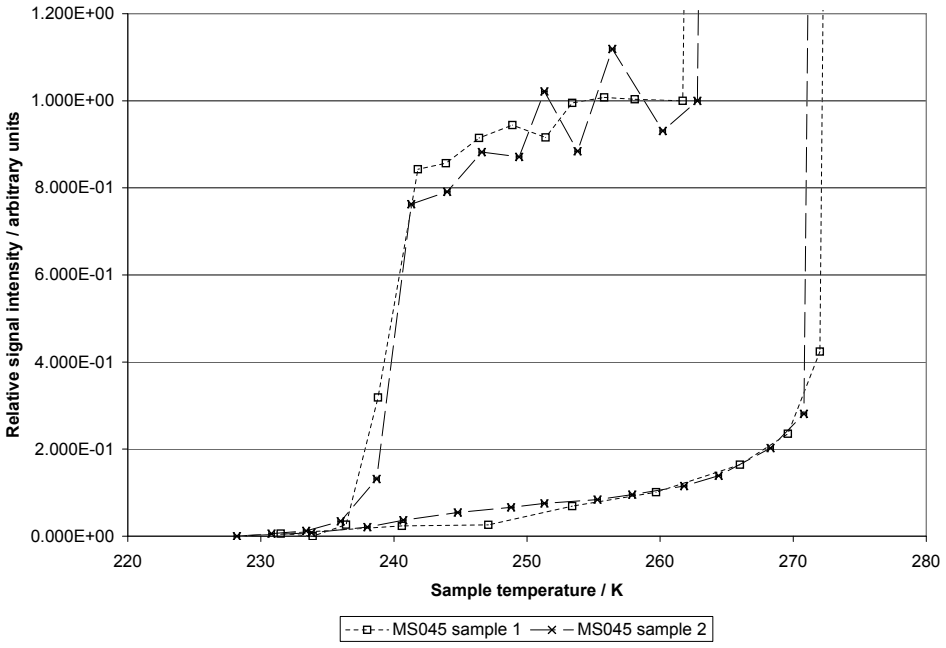

A.3 Tables of microsphere cryodiffusometry results MS045

MS045

Freeze	T /K	$D_w(T)$ / m^2s^{-1}	D_1 / m^2s^{-1}	D_2 / m^2s^{-1}	Salt adjustment, a	$D_{1(adjusted)}$ / m^2s^{-1}	$D_{2(adjusted)}$ / m^2s^{-1}	Tortuosity (1)	Tortuosity (2)
Day 34	253.7	4.77E-10	9.87E-11	5.48E-12	2.26	4.37E-11	2.43E-12	11	197
Day 42	251.3	4.19E-10	2.19E-10	9.06E-12	2.40	9.14E-11	3.77E-12	4.6	111
Day 60	251.3	4.19E-10	1.90E-10	7.35E-12	2.40	7.92E-11	3.06E-12	5.3	137
Day 73	250.2	3.93E-10	2.15E-10	7.97E-12	2.47	8.71E-11	3.23E-12	4.5	122
Day 109	248.0	3.45E-10	1.44E-10	5.05E-12	2.62	5.50E-11	1.93E-12	6.3	179

Thaw	T /K	$D_w(T)$ / m^2s^{-1}	D_1 / m^2s^{-1}	D_2 / m^2s^{-1}	Salt adjustment, a	$D_{1(adjusted)}$ / m^2s^{-1}	$D_{2(adjusted)}$ / m^2s^{-1}	Tortuosity (1)	Tortuosity (2)
Day 34	255.1	5.12E-10	8.70E-11	4.42E-12	2.18	3.99E-11	2.03E-12	13	253
Day 42	253.8	4.79E-10	2.63E-10	9.51E-12	2.25	1.17E-10	4.22E-12	4.1	114
Day 60	253.6	4.74E-10	2.34E-10	6.12E-12	2.26	1.03E-10	2.70E-12	4.6	175
Day 73	253.7	4.77E-10	2.76E-10	8.12E-12	2.26	1.22E-10	3.59E-12	3.9	133
Day 109	253.8	4.79E-10	1.93E-10	5.56E-12	2.25	8.56E-11	2.47E-12	5.6	194

A.4 Tables of microsphere cryodiffusometry results MS043

MS043

Freeze	T /K	$D_w(T)$ / m^2s^{-1}	D_1 / m^2s^{-1}	D_2 / m^2s^{-1}	Salt adjustment, a	$D_{1(adjusted)}$ / m^2s^{-1}	$D_{2(adjusted)}$ / m^2s^{-1}	Tortuosity (1)	Tortuosity (2)
Day 1	254.1	4.87E-10	1.07E-10	2.39E-11	2.24	4.78E-11	1.07E-11	10	46
Day 14	254.0	4.84E-10	1.03E-10	1.83E-11	2.24	4.61E-11	8.16E-12	11	59
Day 25	254.8	5.05E-10	1.06E-10	2.00E-11	2.20	4.80E-11	9.09E-12	11	55
Day 31	253.7	4.77E-10	1.01E-10	1.45E-11	2.26	4.49E-11	6.44E-12	11	74
Day 59	254.4	4.94E-10	1.05E-10	1.72E-11	2.22	4.75E-11	7.75E-12	10	64
Day 83	255.3	5.17E-10	1.88E-10	1.32E-11	2.17	8.65E-11	6.07E-12	6.0	85
Day 92	255.3	5.17E-10	1.51E-10	7.10E-12	2.17	6.95E-11	3.27E-12	7.4	158

Thaw	T /K	$D_w(T)$ / m^2s^{-1}	D_1 / m^2s^{-1}	D_2 / m^2s^{-1}	Salt adjustment, a	$D_{1(adjusted)}$ / m^2s^{-1}	$D_{2(adjusted)}$ / m^2s^{-1}	Tortuosity (1)	Tortuosity (2)
Day 1	255.1	5.12E-10	1.20E-10	2.81E-11	2.18	5.48E-11	1.29E-11	9.3	40
Day 14	255.0	5.10E-10	1.13E-10	2.04E-11	2.19	5.18E-11	9.33E-12	10	55
Day 25	255.7	5.28E-10	1.12E-10	2.12E-11	2.15	5.23E-11	9.85E-12	10	54
Day 31	254.7	5.02E-10	1.14E-10	1.72E-11	2.20	5.19E-11	7.81E-12	10	64
Day 59	255.3	5.17E-10	1.18E-10	2.14E-11	2.17	5.42E-11	9.85E-12	10	53
Day 83	255.3	5.17E-10	1.98E-10	1.02E-11	2.17	9.11E-11	4.67E-12	5.7	111
Day 92	255.3	5.17E-10	1.92E-10	7.75E-12	2.17	8.85E-11	3.57E-12	5.9	145

A.5 Tables of microsphere cryodiffusometry results MS041

MS041

Freeze	T /K	$D_w(T)$ / m^2s^{-1}	D_1 / m^2s^{-1}	D_2 / m^2s^{-1}	Salt adjustment, a	$D_{1(adjusted)}$ / m^2s^{-1}	$D_{2(adjusted)}$ / m^2s^{-1}	Tortuosity (1)	Tortuosity (2)
Day 1	252.4	4.45E-10	1.72E-10	2.15E-12	2.33	7.36E-11	9.21E-13	6.0	483
Day 14	254.8	5.03E-10	2.34E-10	3.96E-11	2.20	1.06E-10	1.80E-11	4.7	28
Day 25	252.0	4.34E-10	2.13E-10	3.43E-11	2.36	9.01E-11	1.45E-11	4.8	30
Day 37	249.6	3.80E-10	2.04E-10	3.59E-11	2.51	8.13E-11	1.43E-11	4.7	27
Day 51	253.0	4.58E-10	2.43E-10	4.13E-11	2.30	1.05E-10	1.79E-11	4.3	26
Day 70	246.1	3.07E-10	1.97E-10	2.60E-11	2.75	7.16E-11	9.45E-12	4.3	32
Day 93	246.4	3.12E-10	1.74E-10	2.35E-11	2.73	6.37E-11	8.61E-12	4.9	36
Day 105	245.3	2.91E-10	1.89E-10	2.26E-11	2.81	6.73E-11	8.03E-12	4.3	36
Day 116	245.9	3.02E-10	3.62E-10	1.08E-11	2.77	1.31E-10	3.89E-12	2.3	78
Day 142	250.8	4.07E-10	2.27E-10	4.77E-11	2.43	9.33E-11	1.96E-11	4.4	21

Thaw	T /K	$D_w(T)$ / m^2s^{-1}	D_1 / m^2s^{-1}	D_2 / m^2s^{-1}	Salt adjustment, a	$D_{1(adjusted)}$ / m^2s^{-1}	$D_{2(adjusted)}$ / m^2s^{-1}	Tortuosity (1)	Tortuosity (2)
Day 1	253.7	4.77E-10	1.67E-10	2.36E-12	2.26	7.40E-11	1.04E-12	6.4	456
Day 14	254.2	4.88E-10	2.32E-10	4.20E-11	2.23	1.04E-10	1.88E-11	4.7	26
Day 25	254.2	4.88E-10	2.44E-10	3.42E-11	2.23	1.09E-10	1.53E-11	4.5	32
Day 37	252.4	4.43E-10	2.40E-10	3.68E-11	2.34	1.03E-10	1.58E-11	4.3	28
Day 51	252.4	4.43E-10	2.45E-10	4.05E-11	2.34	1.05E-10	1.73E-11	4.2	26
Day 70	253.8	4.78E-10	2.63E-10	2.78E-11	2.26	1.17E-10	1.23E-11	4.1	39
Day 93	253.9	4.80E-10	2.57E-10	2.62E-11	2.25	1.14E-10	1.16E-11	4.2	41
Day 105	254.3	4.90E-10	2.60E-10	2.75E-11	2.23	1.17E-10	1.23E-11	4.2	40
Day 116	252.3	4.42E-10	2.55E-10	2.10E-11	2.34	1.09E-10	8.99E-12	4.1	49
Day 142	252.7	4.51E-10	2.59E-10	6.80E-11	2.32	1.12E-10	2.93E-11	4.0	15

A.6 Calculation of errors

Error in the diffusion coefficients of fitting PFG data to a one or two component model are determined from non-linear curve fitting function within Origin *. The standard error for each of the fitting parameters is calculated within the fitting process, $e(D_1)$ and $e(D_2)$.

Standard error in the salt adjustment factor, $e(a)$ was calculated as the standard error in the known values of temperature and adjustment factor using equation A.1, where x is the independent observation, y is the dependent observation, $\bar{x}$ and $\bar{y}$ are the mean values for x and y respectively and n is the number of observations. The value for the standard error in the salt adjustment factor was found to be 0.0844.

$$error = \sqrt{\frac{1}{n-2}[\Sigma(y-\bar{y})^2 - \frac{(\Sigma(x-\bar{x})(y-\bar{y}))^2}{\Sigma(x-\bar{x}^2)}]} \tag{A.1}$$

By combining the error in the estimated diffusion coefficient and the salt adjustment factor, therefore, the error in the adjusted diffusion coefficient for component i was calculated using equation A.2.

$$e(D_{i,adj}) = D_{i,adj} \times \sqrt{(\frac{e(a)}{a})^2 + (\frac{e(D_i)}{D_i})^2} \tag{A.2}$$

*

As discussed in chapter 3, the error in calculating free diffusion coefficient of water at low temperature, $e(D_w)$ was determined to be less than 3 % of the calculated value.Therefore, the error in tortuosity for component i, $e(\tau_i)$ is given in equation A.3.

$$e(\tau_i) = \tau_i \times \sqrt{(\frac{e(D_{i,adj})}{D_{i,adj}})^2 + (\frac{e(D_w)}{D_w})^2} \tag{A.3}$$

Similarly, the error in weighted tortuosity, $e(\tau_w)$, is given in equation A.4

$$e(\tau_w) = \tau_w \times \sqrt{(\frac{e(\tau_1)}{\tau_1})^2 + (\frac{e(\tau_2)}{\tau_2})^2 + (\frac{e(p)}{p}^2)} \tag{A.4}$$

A.7 NMR pulse sequences

- *Pulse acquire*

  The sample is subjected to a single radio frequency pulse equivalent to a 90 °flip into

Figure A.1: Pulse acquire sequence

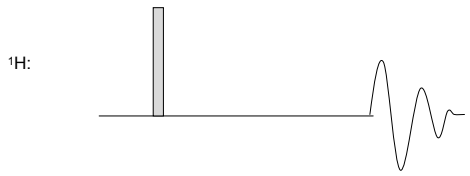

the x-y plane and after a wait period the emitted signal is acquired by the receiver coil. The disadvantage of this type of acquisition is that the signal is subject to T_2 relaxation and, therefore, may be lower in intensity.

- *Spin echo*

  In the simplest spin echo sequence the sample is subjected to a single 90 °pulse, which flips the nuclei spin into the x-y plane. The nuclei precess with different angular

Figure A.2: Spin echo sequence

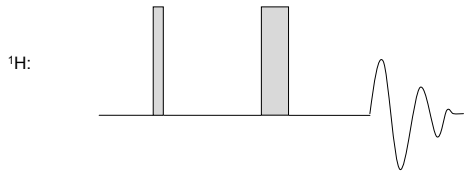

frequency and de-phase, after a short time, t, the sample is subject to a 180 °pulse, often about the y-axis, which flips the nuclei into the reverse position with respect to the z direction. After an equal time t, the nuclei have re-phased and the emitted echo signal is now acquired by the receiver coil. Thus, the spin echo maximises the signal observed by rephasing the nuclei.

- *Pulsed gradient spin echo*
  Magnetic field gradients are added to the simple spin echo, mid-way between the 90 °and 180 °pulse the magnetic field gradient is applied for a short period, the same gradient is applied mid-way between the 180 °pulse and the acquisition. The effect of the gradients is to identify locational changes during the observation time, between the two magnetic field gradients, if no diffusion has occurred the signal is the same as if the gradients had not been applied, diffusional motion of the nuclei reduces the signal intensity of the observed echo.

- *Pulsed gradient stimulated echo*
  The stimulated echo is a gradient spin echo sequence with the 180 °pulse separated into two 90 °pulses, the two gradients are separated in time by an observation time, Δ. The second 90 °pulse stores the signal in the z direction to allow for longer observation times to be used, therefore the sequence is particularly useful when $T_2 \ll T_1$ of if diffusivity is small (Hollewand and Gladden, 1995). The shape of the magnetic field gradient may be varied, for the experiments conducted in this work, the shape of the

Figure A.3: Pulsed gradient spin echo sequence

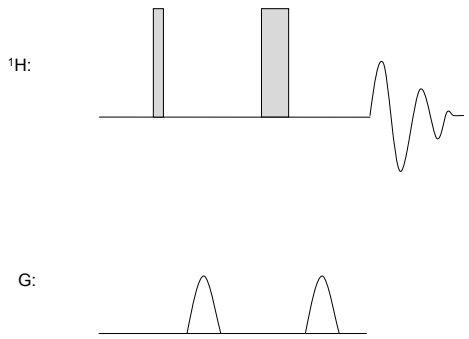

Figure A.4: Stimulated gradient spin echo sequence

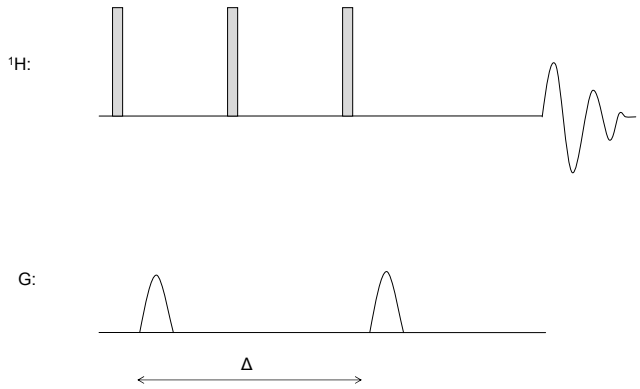

gradient is sinusoidal.

- *Bipolar pulsed gradient stimulated echo with longitudinal eddy delay*
  A development of the stimulated pulsed gradient spin echo, each applied magnetic field gradient is split into two shorter gradients of the same magnitude, first positive, then negative with an additional 180 °pulse in between the two gradients. A small time delay between the gradients is used, the bipolar correction time, τ. After the last gradient is applied, eddy currents within the sample may affect the observed signal,

Figure A.5: Stimulated bipolar gradient spin echo sequence with longitudinal eddy delay

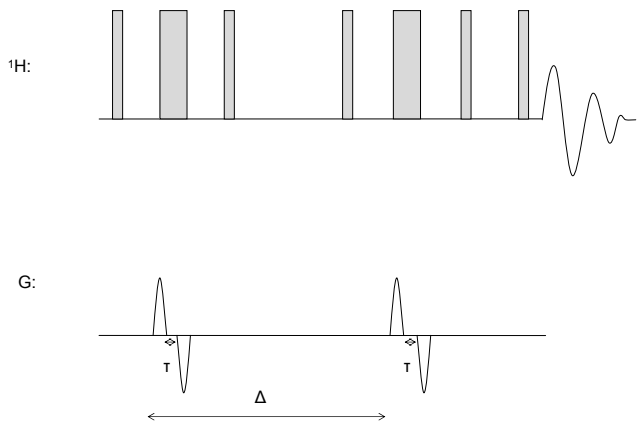

therefore, the magnetisation is stored in the z direction with the application of a 90 °pulse, and after a time delay another 90 °pulse returns the magnetisation into the x-y plane and the acquisition is taken.

- *Addition of spoil currents*

  The addition of two small gradients after each of the bipolar field gradients removes

Figure A.6: Stimulated bipolar gradient spin echo sequence with longitudinal eddy delay and spoil gradients

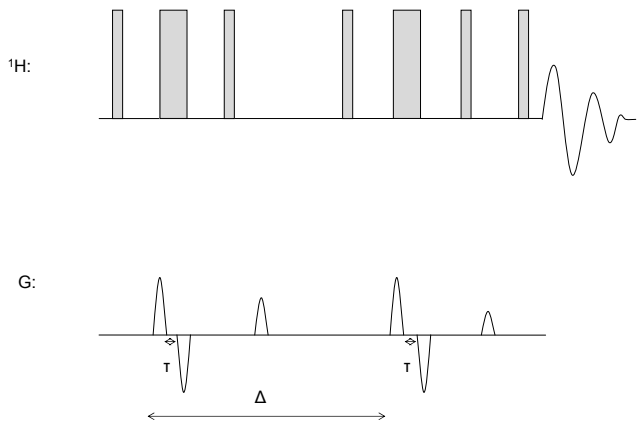

any unwanted fractions of magnetisation in the x-y plane, whilst the desired phases are stored in the z direction. This is the sequence used in PFG experiments.

A.8 Automatic programs

Multi_integtime

```
/*****************************************************************/
/* multi_integtime 12.11.2001 */
/*****************************************************************/
/* Short Description : */
/* AU program for automatic integration of a series of 1D */
/* spectra with AI calibration. The output is written in */
/* a format suitable for import in excel or similar */
/* desktop publishing programs. */
/*****************************************************************/
/* Keywords : */
/* integration of a series of data sets */
/*****************************************************************/
/* Description/Usage : */
/* AU program for automatic integration of a series of 1D */
/* spectra with AI calibration. The output is written in */
/* a format suitable for import in excel or similar */
/* desktop publishing programs. In addition, a parameter */
/* has been added to the listing. This allows to correlate */
/* the integral changes with the change of a parameter. */
/* The spectra can either be stored in a series of EXPNOs */
/* or in a series of PROCNOs. */
/* The AU program works as follows : */
/* 1. Switch to the first experiment to be integrated.  */
/* 2. Define the integral region(s) you want to use */
/*    in the interactive integration menu. Calibrate the */
/*    integrals with an appropriate calibration factor */
/*    (calibrate button) and store the intrng file (write */
/*    return button). */
```

```
/* 3. Store the intrng file with the 'wmisc' command */
/*    under a name of your choice. */
/* 5. Start the AU program. */
/* The individual integration results are stored in the */
/* file integrals.txt in each dataset, the summary of */
/* all results is stored in the file dataset-name_int.txt */
/* in the first dataset. */
/* If you want to print a different parameter than GPZ 1,*/
/* then you have to change the corresponding lines with */
/* the FETCHPARS calls. Depending on the parameter type,*/
/* you must also change the variable into which the  */
/* parameter is read (currently f1 for float). In that */
/* case, also the following sprintf lines need to be */
/* changed. */
/*****************************************************************/
/* Author(s) : */
/* Name : Mike Engelhardt */
/* Organisation : Bruker Analytik */
/* Email : eng@bruker.de */
/*****************************************************************/
/* Name Date Modification: */
/* eng 001011 created */
/* eng 001214 handle CURPRIN internally */
/* eng 011112 bug fix 2784 */
/*  E. Perkins - Combine integral output with experiment time */
/*****************************************************************/
/*
$Id: multi_integtime,v 1.3 2001/11/12 17:17:23 eng Exp $
*/
time_t t;
char *timestring;
char intrngfile[256], printname[256], newline[256];
char intresult[256], intallresult[256], dummystr[256];
double intval=0.0;
int iii, useprocnos=0;
FILE *fpnt, *fpnt2;

GETCURDATA
```

```
GETINT ("Use EXPNOs (0) or PROCNOs (1) :",useprocnos)

i1 = 1;
if (useprocnos)
{
  GETINT ("Enter first processed number :",i1)
  DATASET(name,expno,i1,disk,user)
}
else
{
  GETINT ("Enter first experiment number :",i1)
  DATASET(name,i1,procno,disk,user)
}
i2 = 16;
GETINT ("Enter number of experiments :",i2)

(void) strcpy (intrngfile,"integ-ai");
GETSTRING ("Enter name of intrng file :",intrngfile)

RMISC("intrng",intrngfile)
STOREPAR("INTSCL",1.0)
FETCHPAR("CURPRIN",printname)
STOREPAR("CURPRIN","integrals.txt")
LI
STOREPAR("CURPRIN",printname)

(void) sprintf (intresult,"%s/data/%s/%s/%s/%d/pdata/%d/integrals.txt",
disk, user, type, name, expno, procno);
fpnt=fopen(intresult, "r");
if(fpnt==NULL)
{
  Proc_err(DEF_ERR_OPT, "No integral result file :\n%s\n\
Maybe CURPRIN is not a filename ?", intresult);
  ABORT
}
(void) sprintf (intallresult,"%s/data/%s/%s/%s/%d/pdata/%d/%s_int.txt",
disk, user, type, name, expno, procno, name);
```

```
fpnt2=fopen(intallresult, "wt");
if(fpnt2==NULL)
{
  Proc_err(DEF_ERR_OPT, "No all-integral result file :\n%s",
 intallresult);
  ABORT
}

/* Get parameter to be written into the result file */

FETCHPARS("DATE", &t)

/* Discard first five lines of integral result file */

for (iii = 0; iii < 5; iii++)
  fgets(dummystr, 120, fpnt);

sprintf (newline,"%d %f ",loopcount1+1,f1);

while (fgets(dummystr, 120, fpnt) != NULL)
{
  sscanf (dummystr,"%*d %*f %*f %lf",&intval);
  sprintf (dummystr,"%f ",intval);
  strcat (newline,dummystr);
}
strcat (newline,"\n");
fputs (newline, fpnt2);

fclose (fpnt);

TIMES(i2-1)
  if (useprocnos)
  {
    IPROCNO
  }
  else
  {
    IEXPNO
```

```
  }
  RMISC("intrng",intrngfile)
  STOREPAR("INTSCL",-1.0)
  FETCHPAR("CURPRIN",printname)
  STOREPAR("CURPRIN","integrals.txt")
  LI
  STOREPAR("CURPRIN",printname)
  (void) sprintf(intresult,"%s/data/%s/%s/%s/%d/pdata/%d/integrals.txt",
disk, user, type, name, expno, procno);
  fpnt=fopen(intresult, "r");
  if(fpnt==NULL)
  {
    Proc_err(DEF_ERR_OPT, "No integral result file :\n%s", intresult);
    return(-1);
  }
  /* Discard first five lines of integral result file */
  for (iii = 0; iii < 5; iii++)
    fgets(dummystr, 120, fpnt);

  FETCHPARS("DATE", &t)

/* convert seconds into proper units */
timestring=asctime(localtime(&t));

  sprintf (newline, timestring ,loopcount1+2,f1);
  while (fgets(dummystr, 120, fpnt) != NULL)
  {
    sscanf (dummystr,"%*d %*f %*f %lf",&intval);
    sprintf (dummystr,"%f ",intval);
    strcat (newline,dummystr);
  }
  strcat (newline,"\n");
  fputs (newline, fpnt2);
  fclose (fpnt);
END

fclose (fpnt2);
```

```
(void) sprintf (text,"--- multi_integtime finished ---\n\
All results summarized in :\n%s",intallresult);
QUITMSG (text)
```

cryopfgDELTA10

Example program for multiple Δ cryodiffusometry experiments during cryoporometry freeze-thaw cycle

```
/*** ^^A -*-C++-*- ********************************************/
/* cryopfg&RTpfg&T2  15.05.2008 */
/************************************************************/
/* Short Description : */
/* Performs multiple acquisitions on increasing expnos */
/* with temperatures that are read from a vtlist file.     */
/*      At two user defined experiment numbers, pfg             */
/*      experiments are carried out with increasing gradient    */
/*      lengths, at three different diffusion times.            */
/************************************************************/
/* Keywords : */
/* serial acquisitions, variable temperature, VT , DOSY */
/************************************************************/
/* Description/Usage : */
/* This AU program performs multiple acquisitions on */
/* increasing expnos in much the same way as multizg. If */
/* datasets do not yet exist, the current dataset and its */
/* parameters are copied. If the data sets already exist,*/
/* then the experiments are executed as they are. */
/* But in addition to multizg, this AU program asks for a */
/* variable temperature list and sets the temperature for */
/* each experiment according to the list entry from the */
/* VTLIST file. */
/* The number of experiments is calculated from the number */
/* of temperature values in the VTLIST. The user can ask */
/* for a reduced number of experiments, though. */
```

```
/* A security check is implemented that asks for a */
/* confirmation of the highest and lowest temperature of */
/* the variable temperature list. */
/* Temperatures are in Kelvin K ! */
/* You will be asked for the temperature equilibration */
/* time. The AU program will wait at as long as defined */
/* by this time for the temperature to settle. */
/* The total experiment time is estimated and printed out. */
/*************************************************************/
/* This is a modification of multi_zgvt     */
/* Author(s) : */
/* Name : Emily Perkins           */
/* Organisation : University of Bath */
/* Email : E.L.Perkins@bath.ac.uk */
/*************************************************************/
/* Name Date Modification: */
/*                                  */
/*************************************************************/
/*
$Id: multi_cryo_1cycle&thaw ,v 1.0 $
*/

char vtlistname[PATH_MAX], vtlistpath[PATH_MAX], line[PATH_MAX];
char *envpnt, tmpfile[PATH_MAX];
char del[PATH_MAX], path[PATH_MAX], curp[PATH_MAX];
double sf, sfo1;
float acttemp[500], hightemp, lowtemp;
float PSH, PSP, IPS, maxpsh, maxpsp, maxips;
int noofscans, pscal_save;
int startExpno, start2Expno, start3Expno;
int fptr, fptr1, numtemp, waittime, tdiff, t, t1;
int pfgexpt, pfgexpt2;
int rem, rem2;
int ret, expTime, zgsafety;
static void PrintExpTime();

GETCURDATA;
```

```
startExpno = expno;
(void) strcpy (vtlistname,"vtlist1");
GETSTRING("Enter name of vtlist : ",vtlistname)
(void) sprintf (vtlistpath,"%s/lists/vt/%s",getstan(0,0),vtlistname);
if ( (fptr1 = fopen (vtlistpath,"r")) == NULL )
{
  Proc_err (DEF_ERR_OPT,"Could not open VT list file\n\
%s\nPlease use 'edlist vt' to check for valid files.",vtlistpath);
  ABORT
}

/* Read first temperature value, scan for highest and lowest */
/* temperature and the total number of temperature values.   */

if ( fgets (line,PATH_MAX-1,fptr1) == NULL )
{
  Proc_err (DEF_ERR_OPT,"No VT list entry found.\n\
Please check the VT list file\n%s\nwith 'edlist vt %s'.",
vtlistpath,vtlistname);
  (void) fclose (fptr1);
  ABORT
}
if ( (ret = sscanf (line,"%f",&acttemp[0])) != 1 )
{
  STOPMSG ("--- temperature list has no valid entries ---")
}
hightemp = lowtemp = acttemp[0];
numtemp = 1;

/* Check for more temperature values */

while ( fgets (line,PATH_MAX-1,fptr1) != NULL )
{
  if ( (ret = sscanf (line,"%f",&acttemp[numtemp])) != 1 )
    break;
  if ( acttemp[numtemp] > hightemp )
  {
    hightemp = acttemp[numtemp];
```

```
  }
  if ( acttemp[numtemp] < lowtemp )
  {
    lowtemp = acttemp[numtemp];
  }
  numtemp++;
}
(void) fclose (fptr1);

if ( Proc_err(QUESTION_OPT,"Highest temperature : %f OK?",hightemp) != ERR
  STOPMSG ("--- highest temperature not OK ---")
if ( Proc_err(QUESTION_OPT,"Lowest temperature : %f OK?",lowtemp) != ERR_C
  STOPMSG ("--- lowest temperature not OK ---")

do
{
  i1 = numtemp;
  GETINT("Enter number of experiments : ",i1)
} while ( (i1 > numtemp) || (i1 == 0) );

waittime = 540;
GETINT("Enter temperature equilibration period (secs) : ",waittime)

pfgexpt = 16;
GETINT("Enter experiment number for pfg experiment 1 : ",pfgexpt)

pfgexpt2 = 37;
GETINT("Enter experiment number for pfg experiment 2 : ",pfgexpt2)

expTime = 0;
TIMES(i1)
    SETCURDATA;
    STOREPAR("TE",acttemp[loopcount1]);
    expTime += CalcExpTime() + 4+ waittime;
    IEXPNO;
END
DEXPNO;
PrintExpTime(expTime, i1);
```

```
(void) sprintf (tmpfile,"%s/expt",PathSystemTemp());
(void) remove (tmpfile);

rem = pfgexpt2-pfgexpt;
start2Expno =pfgexpt+1;

rem2 = i1-pfgexpt2;
start3Expno =pfgexpt2+1;

(void) sprintf (tmpfile,"%s/expt",PathSystemTemp());
(void) remove (tmpfile);

/* Turn zg safety off if on. Turn it back on at the end. */
envpnt = getenv("UXNMR_SAFETY");
zgsafety = 0;
if(envpnt != NULL)
{
  if(strcmp(envpnt, "on") == 0)
  {
    zgsafety = 1;
    CPR_exec("env set UXNMR_SAFETY=off", WAIT_TERM);
  }
}

startExpno = 2;
expno = startExpno;
SETCURDATA;
TIMES(pfgexpt-1)
    (void) sprintf(text,"running experiment # %d (TE = %f)",
loopcount1+1,acttemp[loopcount1]);
    Show_status(text);
    sleep(4);
    TESET
    TEREADY(waittime,0.1)
    ZG;
FETCHPARS("DATE", &t)
DEXPNO;
```

```
FETCHPARS("DATE", &t1)
IEXPNO;
tdiff = t-t1;
if (tdiff < waittime)
{
TEREADY(waittime,0.1)
ZG;
}
    IEXPNO;
END

XCMD("wrpa 1110");
REXPNO(1110);
RPAR("elpDOSY1d","all");
XCMD("p30 1000");
XCMD("d20 0.20");
RGA;
ZG;

XCMD("wrpa 1100");
REXPNO(1100);
RPAR("elpDOSY1d","all");
XCMD("p30 1000");
XCMD("d20 0.20");
ZG;

XCMD("wrpa 1101");
REXPNO(1101);
RPAR("elpDOSY1d","all");
XCMD("p30 1300");
XCMD("d20 0.20");
ZG;


XCMD("wrpa 1102");
REXPNO(1102);
RPAR("elpDOSY1d","all");
XCMD("p30 1600");
```

```
XCMD("d20 0.20");
ZG;


XCMD("wrpa 1103");
REXPNO(1103);
RPAR("elpDOSY1d","all");
XCMD("p30 2000");
XCMD("d20 0.20");
ZG;


XCMD("wrpa 1104");
REXPNO(1104);
RPAR("elpDOSY1d","all");
XCMD("p30 2500");
XCMD("d20 0.20");
ZG;


XCMD("wrpa 1105");
REXPNO(1105);
RPAR("elpDOSY1d","all");
XCMD("p30 3000");
XCMD("d20 0.20");
ZG;


XCMD("wrpa 1106");
REXPNO(1106);
RPAR("elpDOSY1d","all");
XCMD("p30 3500");
XCMD("d20 0.20");
ZG;


XCMD("wrpa 1107");
REXPNO(1107);
```

```
RPAR("elpDOSY1d","all");
XCMD("p30 4000");
XCMD("d20 0.20");
ZG;



REXPNO(pfgexpt+1);
expno = start2Expno;
SETCURDATA;
TIMES(rem)
    (void) sprintf(text,"running experiment # %d (TE = %f)",
loopcount1+1,acttemp[loopcount1]);
    Show_status(text);
    sleep(4);
    TESET
    TEREADY(waittime,0.1)
    ZG;
FETCHPARS("DATE", &t)
DEXPNO;
FETCHPARS("DATE", &t1)
IEXPNO;
tdiff = t-t1;
if (tdiff < waittime)
{
TEREADY(waittime,0.1)
ZG;
}
    IEXPNO;
END


XCMD("wrpa 2110");
REXPNO(2110);
RPAR("elpDOSY1d","all");
XCMD("p30 1000");
XCMD("d20 0.20");
```

```
RGA;
ZG;

XCMD("wrpa 2100");
REXPNO(2100);
RPAR("elpDOSY1d","all");
XCMD("p30 1000");
XCMD("d20 0.20");
ZG;

XCMD("wrpa 2101");
REXPNO(2101);
RPAR("elpDOSY1d","all");
XCMD("p30 1300");
XCMD("d20 0.20");
ZG;


XCMD("wrpa 2102");
REXPNO(2102);
RPAR("elpDOSY1d","all");
XCMD("p30 1600");
XCMD("d20 0.20");
ZG;


XCMD("wrpa 2103");
REXPNO(2103);
RPAR("elpDOSY1d","all");
XCMD("p30 2000");
XCMD("d20 0.20");
ZG;


XCMD("wrpa 2104");
REXPNO(2104);
RPAR("elpDOSY1d","all");
XCMD("p30 2500");
```

```
XCMD("d20 0.20");
ZG;


XCMD("wrpa 2105");
REXPNO(2105);
RPAR("elpDOSY1d","all");
XCMD("p30 3000");
XCMD("d20 0.20");
ZG;


XCMD("wrpa 2106");
REXPNO(2106);
RPAR("elpDOSY1d","all");
XCMD("p30 3500");
XCMD("d20 0.20");
ZG;


XCMD("wrpa 2107");
REXPNO(2107);
RPAR("elpDOSY1d","all");
XCMD("p30 4000");
XCMD("d20 0.20");
ZG;


REXPNO(pfgexpt2+1);
expno = start3Expno;
SETCURDATA;
TIMES(rem2)
    (void) sprintf(text,"running experiment # %d (TE = %f)",
loopcount1+1,acttemp[loopcount1]);
    Show_status(text);
    sleep(4);
    TESET
    TEREADY(waittime,0.1)
```

```
    ZG;
FETCHPARS("DATE", &t)
DEXPNO;
FETCHPARS("DATE", &t1)
IEXPNO;
tdiff = t-t1;
if (tdiff < waittime)
{
TEREADY(waittime,0.1)
ZG;
}
    IEXPNO;
END

DEXPNO;

if(zgsafety == 1)
  CPR_exec("env set UXNMR_SAFETY=on", WAIT_TERM);

QUITMSG("--- cryopfgDELTA finished ---");

#include <inc/exptUtil>/* utilities for printing and calculation of
      experiment time */
```

References

M. P. Hollewand and L. F. Gladden. Transport heterogeneity in porous pellets .1. pgse nmr-studies. *Chemical Engineering Science*, 50(2):309–326, 1995.